

The Kynurenine Pathway: Kinetics of a Dioxygenase and Inhibitors of a Monooxygenase

A thesis submitted in the partial fulfilment of the requirements for the
award of the degree of

Doctor of Philosophy

from

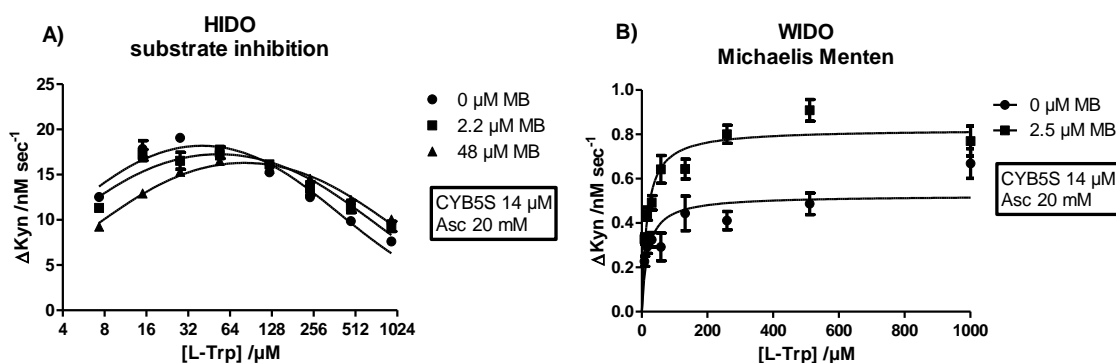
Macquarie University

by

Jason R. Smith (B.Sc., M.Phil.)

Department of Chemistry and Biomolecular Sciences

September 2016



Supervised by
A/Prof. Joanne F. Jamie
And
Prof. Robert D. Willows

Acknowledgements

No work is ever possible without the technical and administrative staff who keep the chaos of the nine hells at bay: Mark Tran, Tony Wong, Anthony Gurlica, Maria Highland, Michelle Kang, and Catherine Wong. Thanks also to Gilles Guillemin for the advice and opportunity to expand my research, and Andrew Piggott, whose effort in upgrading the analysis facilities allowed for far superior data. To Kelly Jacobs for constant effort and continued friendship, and Erin and Asha for balancing the environment. To my supervisors Joanne and Rob, for supervision, advice and patience, and perhaps a few rolled eyes, if not sleepless nights. And to the people who aren't listed here. Not because you don't deserve it, but because some stories require a pub, and shorter is always sweeter.

Declaration

I certify that the thesis entitled “The kynurenine pathway: kinetics of a dioxygenase and inhibitors of a monooxygenase” has not previously been submitted for a degree or part of a degree to any university or institution. I certify that the thesis is an original piece of research and has been written by me. Any help or assistance received during candidature has been appropriately acknowledged. I certify that work contained herein received all appropriate safety and ethics approvals prior to the commencement of work. Biosafety approval number 5201300881.

Contents

THE KYNURENINE PATHWAY: KINETICS OF A DIOXYGENASE AND INHIBITORS OF A MONOOXYGENASE.....	I
Acknowledgements	ii
Declaration	iii
Contents	v
Abstract	ix
Abbreviations	xi
 CHAPTER 1 INTRODUCTION.....	1
1.1. The kynurenine pathway and its biological significance	1
1.2. Metabolite interactions of the kynurenine pathway	1
1.3. KMO's involvement in neurodegenerative diseases	3
1.4. IDOs, TDO and the mammalian immune system	5
1.5. Interactions between IDOs, TDO, and the aryl hydrocarbon receptor	7
1.6. Research aims	8
Appendix to Chapter 1	10
 CHAPTER 2 KYNURENINE MONOOXYGENASE: STRUCTURE, REACTION MECHANISM, AND STRUCTURE-ACTIVITY RELATIONSHIP	11
2.1. KMO structure and mechanism	11
2.2. KMO's membrane association and attempts at recombinant purification	13
2.3. Yeast KMO crystal structure.....	14
2.4. KMO inhibitors.....	15
2.5. Drug discovery efforts: the gaps surrounding KMO knowledge.....	17
Appendix to Chapter 2	20
 CHAPTER 3 <i>IN SILICO</i> SCREENING AGAINST KMO	23
3.1. Drug discovery <i>via</i> screening	23
3.1.1. Pharmacophores	24
3.1.2. Docking.....	27

3.2. Results.....	30
3.2.1. Generating a KMO pharmacophore.....	30
3.2.2. Assessing the pharmacophore against known compounds.....	33
3.2.3. Linear regression of RMSD	35
3.2.4. Agreement between the pharmacophore and the yeast crystal structure.....	38
3.2.5. Docking studies in 4J36	39
3.2.6. Using the models: <i>in silico</i> screening for KMO inhibitors	43
3.2.7. In vitro and in vivo results	49
3.3. Discussion	53
3.4. Conclusion and future research.....	54
3.5. Methods	55
3.5.1. Generation of conformation libraries	55
3.5.2. Pharmacophore generation.....	55
3.5.3. Docking studies in 4J36	56
Appendix to Chapter 3	60
CHAPTER 4 CONSTRUCT GENERATION.....	69
4.1. IDO1 reaction with L-Tryptophan.....	69
4.2. IDO1 and the unresolved loop	70
4.3. Design of IDO1 mutants.....	71
4.3.1. Other residues of interest	73
4.3.2. Loop mutants	73
4.3.3. Confirmation of truncated loops in animals.....	74
4.4. Choice of recombinant expression systems.....	75
4.5. DNA manipulation systems.....	76
4.5.1. The Gibson reaction.....	76
4.5.2. Restriction-ligation method	77
4.6. Construct design	77
4.6.1. IDO1 sequences	77
4.6.2. CYB5 and CPR sequences.....	77
4.6.3. CYB5A and CYB5S	78
4.6.4. CPR and CPRS	80
4.7. Results.....	80
4.7.1. Generation of EC538 pREP4 cells.....	80
4.7.2. Attempts at assembly <i>via</i> the Gibson reaction	81
4.7.3. Optimisation of plasmid isolation	82
4.7.5. Assembly <i>via</i> restriction-ligation	90
4.8. Discussion	91
4.9. Conclusion and future research.....	92
4.10. Methods	92

4.10.1.	Reagent sources	92
4.10.2.	Stock solutions	93
4.10.3.	General protocols	94
Appendix to Chapter 4		98
CHAPTER 5 PROTEIN EXPRESSION AND PURIFICATION		105
5.1.	Introduction	105
5.2.	Results.....	106
5.2.1.	Expression of IDO1 proteins.....	106
5.2.2.	Efforts to improve isolated IDO1 proteins	110
5.2.3.	Heme spectra of IDOs	120
5.2.4.	Expression of CYB5S	125
5.2.5.	Expression of CPRS.....	128
5.3.	Discussion	130
5.4.	Conclusion and future research.....	132
5.5.	Methods	132
5.5.1.	Reagents and stock solutions	132
5.5.2.	Culturing for protein expression	134
5.5.3.	Protein purification	135
5.5.4.	Protein characterisation	135
CHAPTER 6 KINETICS OF IDO1 PROTEINS.....		137
6.1.	IDO1 as a multi-substrate enzyme	137
6.2.	Auto-oxidation of IDO1.....	138
6.3.	Methods of IDO1 reduction	139
6.4.	Models for kinetic analysis.....	140
6.4.1.	Michaelis-Menten and Briggs-Haldane kinetics	140
6.4.2.	Analysis of multi-substrate reactions – assumptions made for IDO1 analysis	142
6.4.3.	Experimental design of IDO1-based reactions.....	144
6.5.	Results.....	145
6.5.1.	HIDO kinetics	145
6.5.2.	Comparison to HIDO Δ 360-370	148
6.5.3.	HIDO and WIDO Comparisons	153
6.5.4.	Conversion of D-tryptophan	155
6.5.5.	CYB5S supported reactions	156
6.6.	Discussion	157
6.7.	Conclusion and future research.....	159
6.8.	Methods	160
6.8.1.	Stock solutions	160

6.8.2.	Reactions monitored by absorbance	161
6.8.3.	Reactions monitored by HPLC	161
CHAPTER 7 OTHER CONTRIBUTIONS.....		165
7.1.	Modification of known IDO1 inhibitors with carborane cages and their effect on IDO1 inhibition.....	165
7.2.	Mechanism of cellular uptake of the excitotoxin quinolinic acid in primary human neurons	170
7.3.	Methods	173
7.3.1.	Modification of known IDO1 inhibitors with carborane cages and their effect on IDO1 inhibition	173
7.3.2.	Mechanism of cellular uptake of the excitotoxin quinolinic acid in primary human neurons .	173
CHAPTER 8 CONCLUSIONS AND FUTURE DIRECTIONS.....		175
8.1.	KMO and drug design	175
8.2.	IDO1 and its mutants.....	176
8.3.	Kinetics of the IDO1 proteins	177
References.....		179
Publications		199

Abstract

Greater than 95% of circulating L-tryptophan is metabolised through the kynurenine pathway in mammals, with the remainder directed into protein synthesis and serotonin, melatonin, and tryptamine production. The pathway is initiated by the oxidative ring opening of L-tryptophan by one of three heme-based dioxygenases: the paralogues indoleamine 2,3-dioxygenase 1 or 2 (IDO1, IDO2), or the otherwise unrelated tryptophan dioxygenase (TDO). The role of tryptophan and its metabolites, and of the kynurenine pathway in particular, is a widespread topic of research. IDO1, IDO2, and TDO, as the initiating enzymes of the kynurenine pathway, are drug targets of great interest due to their implication in a range of pathogenic states; either directly or through the action of the wider kynurenine pathway. The first stable product of the kynurenine pathway, kynurenine, represents a branch point as it acts as the substrate for three different enzymes (kynurenine monooxygenase (KMO), kynureninase, and kynurenine amino transferases (KATs)). As such, these enzymes have received attention as candidate drug targets in order to modulate the relative flux through these branches. This study relates to the first two drug targets of the kynurenine pathway: IDO1 and KMO.

Chapter 1 provides a brief introduction to the biochemistry of the kynurenine pathway, and evidence for its role as a target for neurodegenerative and cancer related diseases. Particular focus has been given to the molecular mechanisms and evidence for IDO1 and KMO as pharmacologically relevant drug targets.

Chapter 2 reviews the current knowledge surrounding KMO's structure, kinetics and mechanism, and inhibition structure-activity relationship (SAR). From this was generated a pharmacophore based on the common feature alignment of active KMO inhibitors (Chapter 3). The pharmacophore showed excellent shape complementarity to the active site features of KMO and was able to moderately describe the relationship between the structure of KMO inhibitors and inhibitory potency (R^2 0.64, n = 39). New KMO lead molecules were screened *in silico* using the pharmacophore and docking, and 41 compounds were tested *in vitro* and *in vivo*. This yielded six molecules with an *in vitro* IC_{50} below 100 μ M and one compound with an *in vivo* EC_{50} below 20 μ M.

A study was also initiated in regards to the structure and function of IDO1, with emphasis on the possible roles that a large 20 amino acid loop might play in the binding of small molecules and protein partners. Sequence alignment also indicated that walrus IDO1 naturally possessed a truncated loop sequence and would be of interest. Mutant constructs of human and walrus IDO1s were designed, along with those of IDO1-interacting proteins cytochrome b5 and cytochrome P450:NAD(P)H reductase, as detailed in Chapter 4.

The expression and characterisation of these proteins is presented in Chapter 5, including investigations into the impact of bacterial culturing conditions. A comparison was made between different growth temperatures and different induction procedures. A method utilising weaker induction through a smaller concentration of the molecule IPTG, combined with inducing at a later phase of the culture and with reduced agitation, gave the best results as judged by size exclusion chromatography. Whilst these proteins generally gave expected results in regards to the UV-vis profiles, wild-type walrus IDO1 gave a double Soret peak in multiple instances, compared to the single Soret peak of other proteins. The Q-band region of this walrus IDO1 also behaved in an inconsistent manner compared to other heme-containing proteins when exposed to redox

reagents. This led to the hypothesis that walrus wild-type IDO1 possessed batch-specific variation in the isolated protein leading to some molecules having a heme environment protected from the actions of the bulk solvent.

Chapter 6 provides the kinetic and mechanistic background of IDO1, as an introduction to analysis of the IDO1 under different experimental conditions. The kinetics of human and walrus IDO1, and of a loop deletion mutant of human IDO1, were analysed in the presence of different redox cycling systems. Wild-type human IDO1, the human deletion mutant, and wild-type walrus IDO1 generally behaved identically under the conditions examined. A surprising exception was that wild-type walrus IDO1 showed hyperbolic kinetics with respect to L-tryptophan when IDO1 was reduced by cytochrome b5, whilst substrate inhibition was observed for all other circumstances. The possible implications of kinetic results are further discussed in Chapter 6.

Chapter 7 describes work on collaborative projects relevant to the kynurenine pathway. A carborane cage is a molecular structure made of carbons and boron in a spherical arrangement. Their use in medicinal chemistry is relatively unstudied compared to more common hydrocarbon structures such as adamantane or benzene. Collaborators synthesised a series of known IDO1 inhibitors with carborane cages in place of benzyl rings, and tested them against recombinant human IDO1. Molecular mechanics simulations were then run as part of this PhD project to visualise the differences between the benzyl rings and the carborane cages. The cages were generally well tolerated despite the apparent loss of a favourable pi-cation interaction between the benzyl analogues and an arginine at the active site entrance. Simulations indicated that this arginine performs a gating function with these types of inhibitors, as has previously been the case indicated for the substrate L-tryptophan. Also looked at was the possible interaction between quinolinic acid, a downstream metabolite of the kynurenine pathway, and the excitatory amino acid transporter 3 (EAAT3). Comparison of a structure with glutamic acid with those created through docking simulations with quinolinic acid led to the hypothesis that quinolinic acid could competitively bind in the same location as glutamic acid. This would indicate a new mechanism of quinolinic acid transport across neuronal cells, as well as a new mechanism of action for the control of neurological function *via* competition between two excitatory amino acids.

The thesis ends with Chapter 8, which summarises briefly the results obtained herein, and provides suggestions for future work of interest based on these observations.

Abbreviations

3-HK: 3-hydroxy kynurenine	IMAC: immobilised-metal affinity chromatography
AD: Alzheimer's disease	IPTG: isopropyl β -D-1-thiogalactopyranoside
AhR: aryl hydrocarbon receptor	KAT: kynurenine amino transferase
ALA: 5-aminolevulinic acid, δ -aminolevulinic acid	KMO: kynurenine monooxygenase
ALS: amyotrophic lateral sclerosis	KP: kynurenine pathway
Arg: arginine	L-Kyn: L-kynurenine
BA: benzoyl alanine	KynA: kynurenic acid
BBB: blood-brain barrier	LB: lysogeny broth
CHO: Chinese hamster ovary	LPS: lipopolysaccharide
CPR: cytochrome P450:NAD(P)H reductase	MB: methylene blue
CPRS: cytochrome P450:NAD(P)H reductase, soluble	mNBA: <i>m</i> -nitrobenzoyl alanine
CYB5A: cytochrome b5, isoform A	MOE: molecular operating environment
CYB5S: cytochrome b5, isoform A, soluble	NADH: nicotinamide adenine dinucleotide, reduced form
Cys: cysteine	NADPH: nicotinamide adenine dinucleotide phosphate, reduced form
DC: dendritic cell	L-NFK: <i>N</i> -formyl-L-kynurenine
dsDNA: double stranded DNA	NMDA: <i>N</i> -methyl-D-aspartate
DTT: dithiothreitol	PD: Parkinson's disease
EAAT3: excitory amino acid transporter 3	Phe: phenylalanine
EDTA: ethylenediaminetetraacetic acid	PMSF: phenylmethylsulfonylfluoride
FAD: flavin adenine dinucleotide	Quin: quinolinic acid
FPLC: fast protein liquid chromatography	RMSD: root-mean-square deviation
GTP: guanosine-5'-triphosphate	SAR: structure-activity relationship
HD: Huntington's disease	SEC: size-exclusion chromatography
HEK: human embryonic kidney	TDO: tryptophan dioxygenase
HIDO: human indoleamine 2,3-dioxygenase 1 (recombinant)	TEV: tobacco etch virus
His: histidine	Thr: threonine
HPLC: high performance liquid chromatography	Tris: tris(hydroxymethyl)aminomethane
IDO1: indoleamine 2,3-dioxygenase 1	Trp: tryptophan
IDO2: indoleamine 2,3-dioxygenase 2	Tyr: tyrosine
IFN- γ : interferon- γ	WIDO: walrus indoleamine 2,3-dioxygenase 1 (recombinant)
IL-22: interleukin-22	
IL-6: interleukin-6	

Chapter 1

Introduction

This chapter introduces the kynurenine pathway, a major tryptophan metabolic pathway, and highlights its biochemical significance. Particular attention was paid to the role of the enzymes kynurenine monooxygenase and indoleamine 2,3-dioxygenase 1 in health and disease, and their status as drug targets. The aims of the Ph.D. project are also presented.

1.1. The kynurenine pathway and its biological significance

Greater than 95% of circulating tryptophan is metabolised through the kynurenine pathway (KP) in mammals, with the remainder directed into protein synthesis and serotonin, melatonin, and tryptamine production [1]. The pathway is initiated by the oxidative ring opening of L-tryptophan (L-Trp) by one of three heme-based dioxygenases: the paralogues indoleamine 2,3-dioxygenase 1 or 2 (IDO1, IDO2), or the evolutionarily unrelated tryptophan dioxygenase (TDO) (Figure 1.1). The product in each case is *N*-formyl-L-Kynurenine (L-NFK), which can either spontaneously hydrolyse or be converted by formamidase to L-kynurenine (L-Kyn). Work in understanding the physiological roles of the kynurenine pathway is an expansive and ongoing endeavour, with consequences for diverse topics including: nutrition and exercise, developmental biology, circulatory, respiratory, and gastrointestinal systems, diabetes, vision, immune system function (including infection and cancers), and psychiatric and neurological diseases (See [2] and references therein).

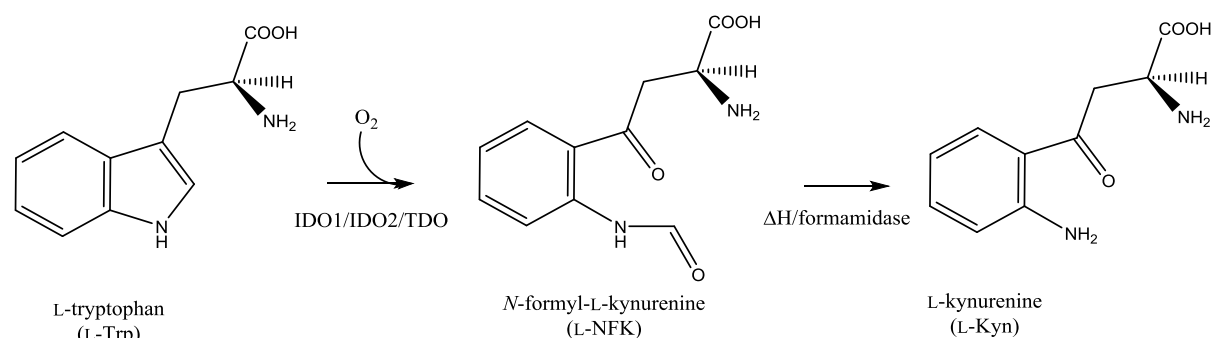


Figure 1.1. Oxidation of L-tryptophan to *N*-formyl-kynurenine is performed by IDO1, IDO2 and TDO. Hydrolysis to L-kynurenine can occur either spontaneously or enzymatically.

1.2. Metabolite interactions of the kynurenine pathway

Little is known about the biological function of L-NFK, partly due to its presumed limited lifetime. Proteinaceous tryptophan can be converted to L-NFK in the presence of light, such as in photosynthetic systems [3, 4], and it has been demonstrated that kynureninylation (the formation of adducts between proteins and KP metabolites) is a mechanism involved in cataract formation [5, 6]. The first stable product of the KP, L-Kyn, represents a branch point as it acts as the

substrate for three different enzymes [kynurenine monooxygenase (KMO), kynureninase, and kynurenine amino transferases (KATs)]. As such, these enzymes have received much attention as candidate drug targets looking to modulate the relative flux through these branches. L-Kyn (among other KP metabolites *e.g.* cinnabarinic acid and kynurenic acid [KynA]) is a ligand of the aryl hydrocarbon receptor (AhR) [7, 8], but elucidating the multiple roles of L-Kyn in the body is largely ongoing [9]. 3-Hydroxykynurenine (3-HK) and KynA readily oxidise under physiological conditions to form peroxide and hydroxyl radicals [10]. KynA is an inhibitor of the *N*-methyl-D-aspartate (NMDA), kainate, α -amino-3-hydroxy-5-methyl-4-isoxazolepropionic acid (AMPA) and α -7 nicotinic acetylcholine (α 7nAChR) receptors [11-13]. It is a ligand of the G-protein coupled receptor 35 (GPR35) [14] and AhR [15] receptors, and a scavenger of hydroxyl and superoxide radicals under some conditions [16]. Quinolinic acid (Quin) has been shown as an excitotoxin that selectively activates NMDA receptors [17, 18], and most of Quin's neurological actions can be blocked by NMDA receptor antagonists [9]. Quin also plays a role in iron-dependent oxidative effects such as the stimulation of lipid peroxidation [19, 20] and complexation with ferrous iron – auto-oxidising and producing reactive oxygen species *via* the Fenton reaction [21]. The kynurenine pathway is presented in Figure 1.2.

disease (HD) is caused by a mutated form of the huntingtin protein leading to its misfolding and aggregation [23]. Eventually, these toxic structures lead to neuronal cell death. In yeast, the toxicity induced by mutant huntingtin was rescued through the deletion of KMO [24]. KMO is localised to the mitochondrial outer-membrane, and the link between KP dysregulation and HD has been hypothesised to occur at the mitochondrial level [25]. HD is known to affect mitochondrial function [26], and mitochondrial dysregulation has been correlated with decreased KAT activity and increased Quin neurotoxicity [27]. Small-molecule or genetic inhibition of KMO activity in a fruit fly HD model increased the level of neuroprotective KynA, decreased the level of neurotoxic 3-HK, and reduced neurodegeneration [22]. Similar observations were also seen upon treatment with KynA and 3-HK, demonstrating the causative role of these molecules. Increased levels of 3-HK and Quin were observed in transgenic mouse HD models and early stage HD patients, and were concomitant with the onset of symptoms in mice [28-30]. Mouse models and HD patients also had reduced KynA levels [31, 32]. These effects were increased with the up-regulation of IDO1/TDO mRNA or activity levels in mice and HD patient's blood [33, 34]. Quin production and neuronal toxicity can be attenuated through the inhibition of KMO in mice [35, 36]. There is some debate, however, around the pharmacological result of inhibiting KMO. In one instance, administration of the KMO inhibitor UPF648 (Section 2.4) saw a lowering of 3-HK without affecting KynA levels [35], whereas the use of the KMO inhibitors Ro-61-8048 [37] or mNBA (Section 2.4) demonstrated both reduced 3-HK and increased KynA [38].

Alzheimer's disease

Alzheimer's disease (AD) is characterised by the extracellular formation and accumulation of senile plaques consisting of misfolded amyloid- β -peptides, and also intracellular phosphorylation of tau proteins leading to neurofibrillary tangles [39]. It has been shown in brain sections from AD patients that Quin co-localises with neurofibrillary tangles in neurons and that, *in vitro*, Quin increases tau phosphorylation in a dose dependent manner [40]. In the same study it was found that Quin increases mRNA of 10 genes directly associated with AD pathology, including six known to be involved in tau phosphorylation [40]. Increased IDO1, 3-HK and Quin levels have been correlated with AD stages [41-43]. Also demonstrated *in vitro* was the ability of amyloid- β peptide to induce IDO1 expression, leading to Quin production by human macrophage and microglia [44]. Zwilling *et al.* have demonstrated that treatment with a non-blood-brain barrier (non-BBB) penetrating KMO inhibitor in a mouse model of AD significantly ameliorates the symptoms and slows disease progression [45]. A number of other studies have demonstrated that peripheral administration of KMO inhibitors leads to changes in the concentrations of KP metabolites in the central nervous system (CNS) [46-49].

Parkinson's disease

Like HD and AD, Parkinson's disease (PD) neuropathology is associated with oxidative stress [50], mitochondrial dysfunction [51], protein aggregation [52], excitotoxicity [53] and inflammation (e.g. cytokine production) [54]. PD is associated with increased serum L-Kyn/Trp and brain 3-HK levels and decreased KynA levels [55-58]. Pre-treatment with KynA reduced chemically-induced neuronal cell death in a PD model [59]. Administration of L-Kyn to a PD model with simultaneous inhibition of organic acid transport (to delay clearance of L-Kyn), and inhibition of KMO and kynureninase (using a L-Kyn analogue), protected neurons from Quin-induced toxicity [60, 61].

Amyotrophic lateral sclerosis

Neuroinflammation is a hallmark of amyotrophic lateral sclerosis (ALS) [62, 63], and the KP is activated during inflammation. Most of the KP metabolites are neuroactive; some being neurotoxic (Quin) and others neuroprotective (KynA). It was demonstrated that the KP is activated in motor neuron disease patients, leading to an increase in levels of Quin and a decrease of KynA in 150 matching cerebral spinal fluid and serum samples [64-66].

Peripheral administration and central effects

The ability for peripheral KMO treatment to yield central effects is theorised to be due to the presence of selective active transport of KP molecules across the blood brain barrier (BBB) and cell specific expression patterns of KP enzymes. Only three KP metabolites: L-Kyn, 3-HK and L-Trp have been shown to be actively transported across the BBB [67]. KMO expression is low in the brain, primarily in microglia and infiltrating macrophages, whilst higher in the liver and kidney [68-71]. Meanwhile, KAT II expression is found in astrocytes and neurons [72, 73]. Thus, inhibition of peripheral KMO leads to decreased levels of peripheral 3-HK available for BBB transport, and increased levels of L-Kyn that can be centrally converted to neuroprotective KynA *via* KAT II [45].

1.4. IDOs, TDO and the mammalian immune system

Although IDO1 was investigated as an integral part of amino acid metabolism for some decades (e.g. Hirata and Hayaishi, 1972, where it was assumed to be another form of TDO [74]), it was not until the turn of the century when Munn *et al.* tested the hypothesis that a relationship existed between L-Trp depletion and maternal tolerance of concepti using an IDO1 small molecule inhibitor [75]. This IDO1-immunotolerance relationship has since been shown to have substantial therapeutic benefit in cancers when using IDO1 inhibitors, and IDO1, and more recently IDO2 and TDO, have become popular targets for development of anti-cancer therapeutics [76]. As of June 2016, IDO1 has a number of phase I-III clinical trials either proceeding or completed. A list of IDO1-related clinical trials has been provided in the appendix to Chapter 1.

TDO expression

Mammalian TDO is expressed primarily in the liver (constitutively) with some being found in the human and rodent brain [77, 78] and is increased in the placenta after bacterial infection [79]. It is upregulated by glucocorticoids, L-Trp, interleukin-1- β (IL-1 β) and by lipopolysaccharide (LPS) [80-83]. TDO is also found in gliomas, and reduces antitumor immune responses, much like IDO1 [7]. A TDO inhibitor has successfully restored immune system-mediated clearance of TDO-expressing tumours in mice [84].

IDO1 expression

Constitutive IDO1 expression is mainly confined to surface-exposed tissues such as lung, gut and skin, but is inducible, especially in antigen presenting cells, by immuno/inflammatory stimuli such as interferon gamma (IFN- γ), tumour necrosis factor, and LPS (*e.g.* [85, 86] and references therein). Whilst the induction of IDO1 through cytokines and immune challenge is well documented through the last decade of research, studies continue to find novel methods of control *in vivo*. Preliminary reports suggest that decreased methylation of the IDO1 promoter correlates with increased levels of IFN- γ -induced mRNA in breast cancer [87]. It was recently shown that lowering cellular concentrations of glutathione (GSH), through lowering the cellular uptake of the precursor cysteine, increased IDO1 production in human dendritic cells (DCs) [88] and was independent of the oxygen tension employed [89].

IDO2 expression

IDO2 is constitutively expressed in the liver, but is also found in antigen presenting cells, kidney, brain, placenta and spermatozoa [90]. This is a unique and restricted pattern compared to that of IDO1, and consistent with evidence that it performs novel and non-redundant biological activities [91, 92]. The IDO2 promoter region includes a recognition site for the transcription factor IRF-7, which is involved in control of DC maturation [93]. It is expressible in tumours *via* cytokines [91, 94-96], and can be induced or regulated in antigen presenting cells by IFN- γ , IL-10 and LPS [91, 97]. Whilst in one study IDO1 was found only in myeloid DCs, IDO2 was found in both myeloid and plasmacytoid DCs [98]. Current theory states that IDO2 may act as a set-point for self-tolerance, while IDO1 may be more inclined towards acute intervention during immune stress [92].

TDO and IDOs in vertebrates: redundant and non-redundant roles

Unicellular organisms generally contain a single protein of either the TDO superfamily or the IDO superfamily, suggesting that either is sufficient in these organisms for tryptophan catabolism [99]. Many higher organisms contain both TDO and IDO1/2 sequences, suggesting additional roles for these proteins and/or their kynurenine products requiring differential regulation (without precluding the possibility of redundancy) [99]. For example, IDO1 deficiency in the skin of mice has led to the increased production of IDO2, presumably to compensate [100]. While in

IDO1-negative mice, IDO2 was found to have attenuated function in myeloid cells due to alternative splicing producing inactive IDO2, but normal IDO2 function in liver cells [93].

1.5. Interactions between IDOs, TDO, and the aryl hydrocarbon receptor

The aryl hydrocarbon receptor (AhR) is a transcription factor acting as a sensor for a range of endogenous (and in vertebrates, exogenous) aromatic compounds [86], and is highly conserved across the animal kingdom [101]. Expressed largely in the lung, liver and placenta, low levels have also been reported in the brain, kidney and skeletal muscle [102-104]. Prior to activation, the AhR is a cytosolic resident, complexing with the heat-shock protein HSP90, the synthase/chaperone protein p23, and c-terminal Src tyrosine kinase (c-Src kinase) [105]. Upon activation by a ligand, AhR dissociates from the complex, exposing a nuclear transport sequence, initiating a signal cascade at genetic and non-genetic levels [106]. At a genetic level, nuclear translocation of AhR results in binding to, and control of, genes containing xenobiotic response elements such as the P450 enzyme, CYP1A1 [107, 108]. At a non-genetic level, the release of c-SRC kinase from the inactive cytosolic complex allows it to begin phosphorylation of target proteins, including IDO1 [83, 107]. AhR is also an E3 ubiquitin ligase, selecting proteins for degradation *via* the 26S proteasome [109, 110], which itself is responsible for AhR degradation after transportation out of the nucleus [111-113].

The precise nature of control between AhR and the adaptive immune system, and the role of TDO and IDOs during such activity, is complex and not completely clear. The specific outcome of AhR activation seems to be dependent on both the nature of the ligand and the biological context of the cell, such as cell type and developmental stage [114]. Some better understood examples can be used to highlight known interactions between AhR and the KP.

AhR, acting as a sensor of L-Kyn (an endogenous ligand that leads to further AhR expression), may constrain inflammation to a localised area *via* the generation of regulatory T-cells, and this localisation is believed to be necessary to prevent a cascading immune response that would lead to autoimmune pathology [86]. Alternatively, xenobiotic exposure at a surface such as lung or skin may result in damage to the epithelial lining and a reduction in bacterial clearance capacity [86].

AhR activation *via* this xenobiotic then initiates responses mediated by Th-17 cells (pro-inflammatory help T-cells), that prevent pathogen invasion as a result of the xenobiotic injury. Concomitant induction of IL-22 can then aid in epithelial repair, and activation of metabolism *via* P450 CYP1A1 removes the xenobiotic stressor [108]. Meanwhile, constitutive expression of IDO1

has been described in cancer cells and is AhR-mediated *via* an autocrine signalling loop involving IL-6 and STAT3 [115, 116]. Thus, not only is the presence of L-Kyn correlated with activation of AhR, leading to proteasomal degradation of IDO1, but in cancers (and perhaps elsewhere) L-Kyn and AhR activation is correlated with constitutive expression of IDO1. The causative mechanism determining whether limited or constitutive IDO1 expression eventuates after ligand activation of AhR is a matter of ongoing research.

The pharmacological mechanisms of the KP, including of IDOs/TDO and KMO, are active fields of investigation. The KP plays a role in a larger variety of biological functions, but is most notable for its effects in neurodegeneration and immune system control. These effects have complex and poorly understood regulatory mechanisms, and can lead to different physiological outcomes, especially in immune system control. Both IDO1 and KMO have demonstrated effective responses from small molecule inhibitors, with phase I-III clinical trials in progress against IDO1¹, and a pre-clinical candidate reported for KMO [49].

1.6. Research aims

Despite decades of research, there is currently a dearth of clinical candidates for KMO inhibition, with only a single class in active development as nanomolar-level pre-clinical candidates [49]. As such, a goal of this project was to search for new lead compounds as potential KMO inhibitors. The first step towards this goal would be to gain insight into how known KMO inhibitors interact with KMO, aided by an indepth knowledge of the structure and mechanism of how the KMO protein functions. This knowledge can then be used to generate *in silico* models for the screening of a commercial compound library. These *in silico* results would then need to be validated by measuring their *in vitro* and *in vivo* ability to inhibit the KMO enzyme. Therefore, Chapter 2 provides the current state of knowledge surrounding the structure, mechanism, and inhibition of KMO, with Chapter 3 utilising that information to create the *in silico* models and test selected compounds for their *in vitro* and *in vivo* inhibitory properties. The potential for the molecules to be advanced as pre-clinical candidates is then briefly discussed.

Another target of the kynurenine pathway considered in this thesis is IDO1. Prior work in this lab published the results of *in silico* screening against IDO1 [117]. In that work, the goal was to identify inhibitors with an extended structure, consisting of a core heme-binding region and, additionally, atoms that could find interactions with an apparent hydrophobic pocket described in

¹ Whilst various IDO1 inhibitors are in clinical trials, the most promising candidate – 1-methyl-D-tryptophan – likely performs the majority of its function *via* tryptophan sufficiency signalling, and not IDO1 binding (Metz *et al.*, Oncoimmunology. 2012, 1(9) p. 1460).

the crystal structures of IDO1, and supported by the SAR of some IDO1 inhibitor studies [118, 119]. Interaction with this pocket was also described as a target of other studies into IDO1 inhibitors [120, 121]. Supplementary to these inhibitor studies, Pearson *et al.* have reported changes in the shape of the kinetics of IDO1 depending on the presence of the IDO1-interacting proteins cytochrome b5 and/or cytochrome P450:NAD(P)H reductase [122]. In the same study, they report that the naphthoquinone species, menadione, inhibited IDO1 only in the absence of these proteins, and not in their presence [122]. Whilst several crystal structures of IDO1 have been published, each contains only partial resolution of a large (20 residue) flexible loop located at the active site entrance. Monte-Carlo simulations hypothesised that the loop moved to interact with substrate tryptophan upon binding [123].

It was hypothesised here then, that the loop may play a central role in several unexplored IDO1 facets. A greater understanding of the loop could answer a number questions, such as: does the loop influence the binding of small molecules such as substrates or inhibitors? Does the loop play a role in binding to either of cytochrome b5 or cytochrome P450:NAD(P)H reductase? Is the loop responsible in any way for differences seen with regards to IDO1 kinetics or inhibition in the presence or absence of these proteins? This project sought to create a tool set of protein constructs, comprised of wild-type and mutant IDO1 genes, as well as cytochrome b5 and cytochrome P450:NAD(P)H reductase constructs. These proteins could later be used in kinetic and structural experiments to examine some of these questions.

A detailed background regarding the structure, mechanism, and kinetics of IDO1 is required to properly design and analyse the results of experiments into these questions, and can be found in the introductory sections to Chapters 4 and 6. Results of the design and generation of these constructs can be found in Chapter 4. The expression, purification and characterisation of the proteins can be found in Chapter 5. Chapter 6 details the kinetics of the IDO1 proteins with reducing partners, and discusses what these results mean vis-à-vis the unresolved loop of IDO1. Chapter 7 briefly highlights other contributions to research within the context of the kynurenine pathway. Chapter 8 provides a summary of the major results and suggestions for future areas of investigation.

Appendix to Chapter 1

Current and former IDO1 clinical trial numbers

NCT01982487, NCT00919295, NCT01961115, NCT02042430, NCT02166905, NCT01822691, NCT02118285, NCT02178722, NCT02318277, NCT02118285, NCT01685255, NCT02298153, NCT01604889, NCT00567931, NCT01191216, NCT01042535, NCT00739609, NCT01792050, NCT02073123, NCT02052648, NCT02077881, NCT01560923, NCT01727531, NCT01219348, NCT01543464, NCT02048709, NCT02077114.

Further details of these trials can be found at www.clinicaltrials.gov

Chapter 2

Kynurenine Monooxygenase: Structure, Reaction Mechanism, and Structure-Activity Relationship

This chapter outlines the current knowledge with respect to kynurenine monooxygenase (KMO) and its structure and function; including the current inhibitor structure-activity relationship (SAR). This background material forms the basis for the models used for drug discovery in Chapter 3.

2.1. KMO structure and mechanism

Kynurenine monooxygenase (KMO) is a flavin adenine dinucleotide (FAD) containing monooxygenase, class A [124]. This class is typified by being encoded on a single gene containing a single FAD binding domain. The FAD in KMO is non-covalently, but tightly, bound [125, 126]. Catalysis is dependent upon FAD reduction by NADH or NADPH, and members of this class are often traceable to microbial enzymes responsible for the *ortho*- or *para*-hydroxylation of aromatic rings [127]. The KMO of *Pseudomonas fluorescens* displays 34% identity with human KMO and has been used as a proxy for the more recalcitrant human enzyme in characterisation studies [128, 129]. In addition to *P. fluorescens*, the literature has significant contributions from yeast (36% amino acid sequence identity), rodent (76% identity), and human tissue studies, due to the limited availability of high quality and quantity recombinant enzyme.

The explicit reaction mechanism of KMO's conversion of L-kynurenine (L-Kyn) to 3-hydroxy-L-kynurenine (3-HK, Figure 2.1) has not been formally elucidated, however, evidence suggests it follows the well described mechanism of related flavin-dependent monooxygenases such as *p*-hydroxybenzoate hydroxylase and phenol hydroxylase [125, 128]. After L-Kyn binds, NADPH (preferred over NADH [125]) reduces the FAD and leaves as NADP⁺ before oxygen binds and creates an L-Kyn-FAD-hydroperoxide intermediate (Figure 2.2) [128]. The oxidation of L-Kyn then proceeds, yielding water and 3-HK [128]. The reduction rate of FAD is significantly enhanced by the presence of substrate L-Kyn or L-Kyn-like inhibitors such as benzoylalanine (BA, Table 2.1) or *m*-nitrobenzoylalanine (*m*NBA, Table 2.1) – a trait commonly observed in bacterial aromatic hydroxylases [130]. The apparent K_D of NADPH is not affected by the presence of these molecules, nor is the reduction potential [128]. Bacterial hydroxylases have been proposed to undergo a dynamic shift where the FAD is in either an 'in' or 'out' conformation, and it is only in this 'out' conformation that reduction occurs [131]. It has been proposed that the substrate-induced

stimulation of FAD reduction in other proteins occurs due to it forcing the FAD to the 'out' form [132]. No direct evidence of this mechanism exists for KMO, however, distinct flavin conformations have been found during the catalytic cycle [128].

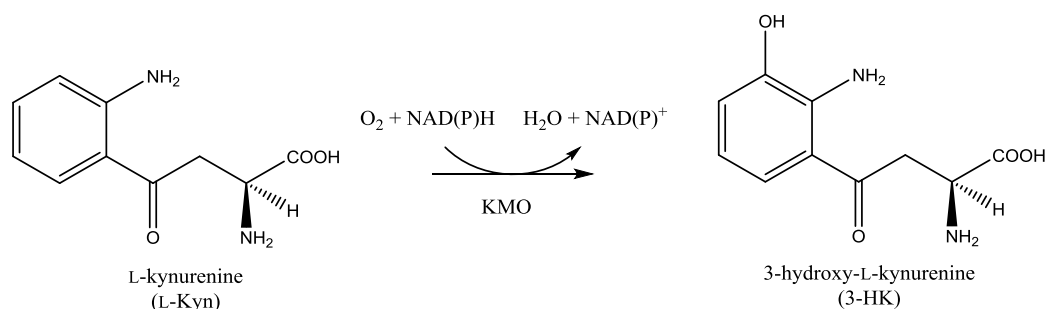
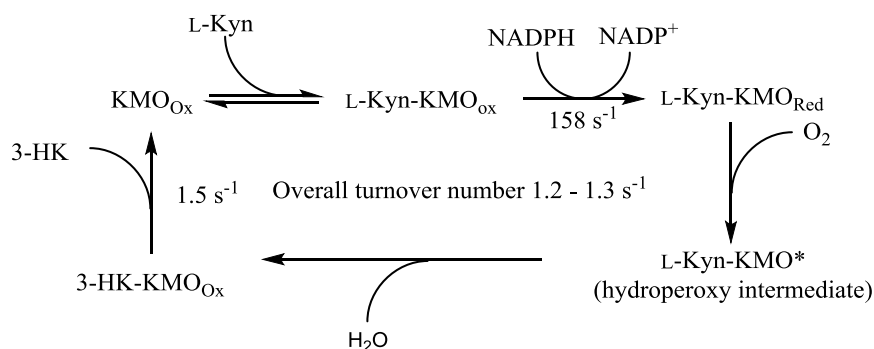


Figure 2.1. KMO's conversion of L-kynurenine to 3-hydroxy-L-kynurenine consumes oxygen and either NADH or NADPH, producing water and NAD(P)⁺.

Low levels of chloride ion have been reported to stabilise the protein during *in vitro* kinetic assays, but also to inhibit 3-HK production [128]. Spectroscopic data suggests that the chloride forces FAD into a state similar to a 3-HK bound state (although the presence or absence of a ligand has not been confirmed) [128]. Presumably, the chloride ion is either forcing the protein into this conformation (with or without a ligand) or, once the protein reaches this conformation through the normal catalytic cycle, is preventing product release. Chloride ions have been seen binding adjacent to the FAD in bacterial flavin-containing monooxygenases [131], but it has not yet been investigated whether this conserved kinetic control by monovalent ions of class A monooxygenases represents a relevant pharmacological control point in KMO action.

Inhibition by substrate mimetic molecules such as *m*NBA, BA and UPF-648 (Table 2.1) additionally yield hydrogen peroxide, likely due to the decay of the intermediate hydroperoxyflavin [126, 128]. The decay of this intermediate also fits with the lack of turnover of these mimetic molecules. At least for *m*NBA, this peroxide production was stoichiometric with NADPH loss [128]. These inhibiting molecules are structurally similar to the substrate L-Kyn, and *m*NBA and BA are known to facilitate faster FAD reduction. It may become necessary, therefore, to ensure that therapeutic development is directed towards systems that avoid such peroxide release, although peroxide production may be limited to structures highly similar to substrate L-Kyn.

A) Reaction cycle of KMO



B) Probable FAD intermediates during reaction

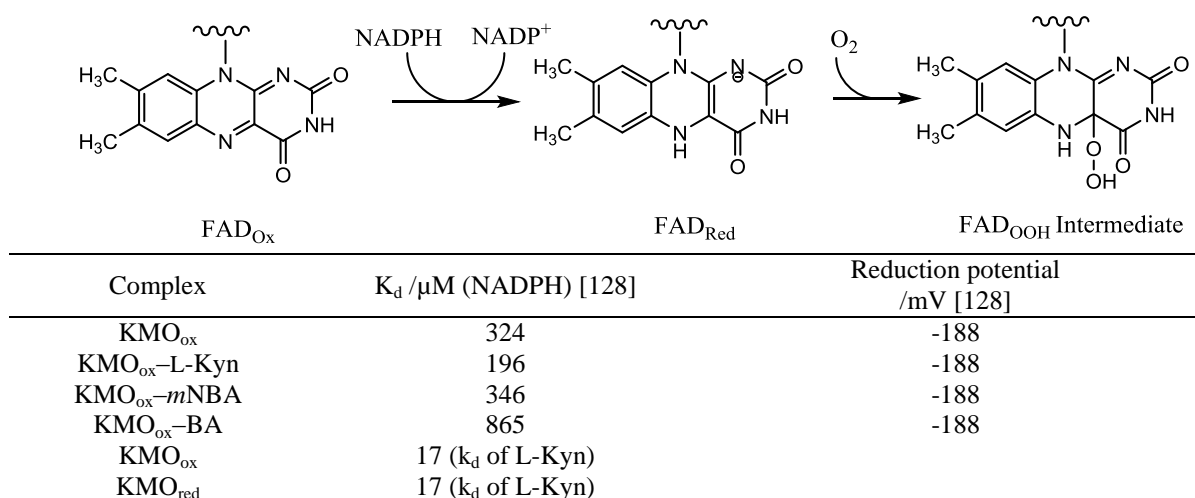


Figure 2.2. The catalytic cycle of KMO. After L-Kyn binding, NADPH (preferred over NADH [125]) binds and quickly reduces the FAD with a rate constant of 158 s⁻¹ [128]. NADP⁺ is subsequently released, allowing for dioxygen binding. This likely forms an FAD[•]-superoxide radical pair that rapidly decays to a hydroperoxyflavin structure capable of acting as the electrophile for L-Kyn oxidation [128]. Rapid dehydration of C4a-hydroxy flavin is thought to yield the oxidised flavin. The final step, 3-HK release, is rate limiting with a rate constant of ~1.5 s⁻¹, slightly faster than the overall turnover number of the enzyme of 1.2 – 1.3 s⁻¹ [128, 129]. The K_D for NADPH is constant within an order of magnitude regardless of ligand presence, whilst the rate of reduction is enhanced by three orders of magnitude in the presence of saturating L-Kyn [128]. All values are from *P. fluorescens*, 5 °C.

2.2. KMO's membrane association and attempts at recombinant purification

The C-terminus of KMO contains a putative outer-mitochondrial membrane targeting sequence [25] and this portion of the molecule is required for both pig and human enzyme function [133, 134]. A human polymorphism in this region, resulting in an Arg452Cys mutation, has been statistically linked to bipolar disorder and schizophrenia, with increased central KynA levels and reduced KMO expression – further cementing the importance of this sequence [135, 136]. Purification attempts by Hirai *et al.* on pig KMO resulted in the co-elution of cytochrome b5 and the β sub-unit of monoamine oxidase. Attempts at their removal yielded little to no enzyme activity [134]. Likewise, recombinant human KMO expressed in an *E. coli* system co-eluted with

the β sub-unit of tryptophan synthase and an unidentified protein with putative GTP-binding properties [133]. Presumably the hydrophobic C-terminal of KMO will form complexes or aggregates with other proteins during purification in the absence of an appropriate lipid environment. The inability to remove the proteins with detergents suggests a particularly tight association, and points to a C-terminal domain that requires a hydrophobic environment in order to properly function. This was supported by attempts to solubilise the C-terminal domain with a highly hydrophilic 3xFLAG sequence. The majority of protein was present in the membranous pellet fraction, even after repeated ultra-centrifugation and solubilisation steps [133].

2.3. Yeast KMO crystal structure

Five KMO structures from the yeast *Saccharomyces cerevisiae* (*E. coli* expressed) were released in 2013 (PDB: 4J2W, 4J31, 4J33, 4J34 and 4J36) [126]. The sequence employed was a C-terminal truncation of the full yeast KMO, missing the membrane-targeting region. Unlike pig and human KMO, the truncated yeast KMO obtained was enzymatically active. Structures 4J34 and 4J36 are most relevant in drug design efforts as they describe the KMO molecules in the absence (apo) and presence (holo) of a bound inhibitor: UPF-648 (a.k.a. PNU-165853), respectively (Figure 2.3). Significant structural changes are apparent between the two. In 4J34, the upper roof of the active site – directly above the FAD molecule – is made up of the flexible and highly conserved sequence 321-PFYGGG-325 (*S. cerevisiae* numbering. Human and rat PFYGGG). However, in the inhibitor-bound form, this sequence of residues was displaced by the 3,4-dichloro moiety of UPF-648 (Figure 2.3). This rotation of the Pro321 – Gln325 chain was not evident in a short molecular dynamics simulation involving substrate L-Kyn within the active site of KMO, suggesting an adaptive cavity [126]. Nearby to the active site entrance, a flexible loop exists in the sequence Tyr97 – Ile104. This is conserved among vertebrates with a consensus sequence of YGX₁KX₂QYI. X₁ in particular is almost exclusively a hydrogen bond donor such as lysine or threonine (a multiple sequence alignment is available in the appendix to Chapter 2). It should be noted that 4J34 is the only structure with a ligand in the active site, and as a direct result of this, the only one that doesn't have Phe322 blocking access to the FAD co-factor.

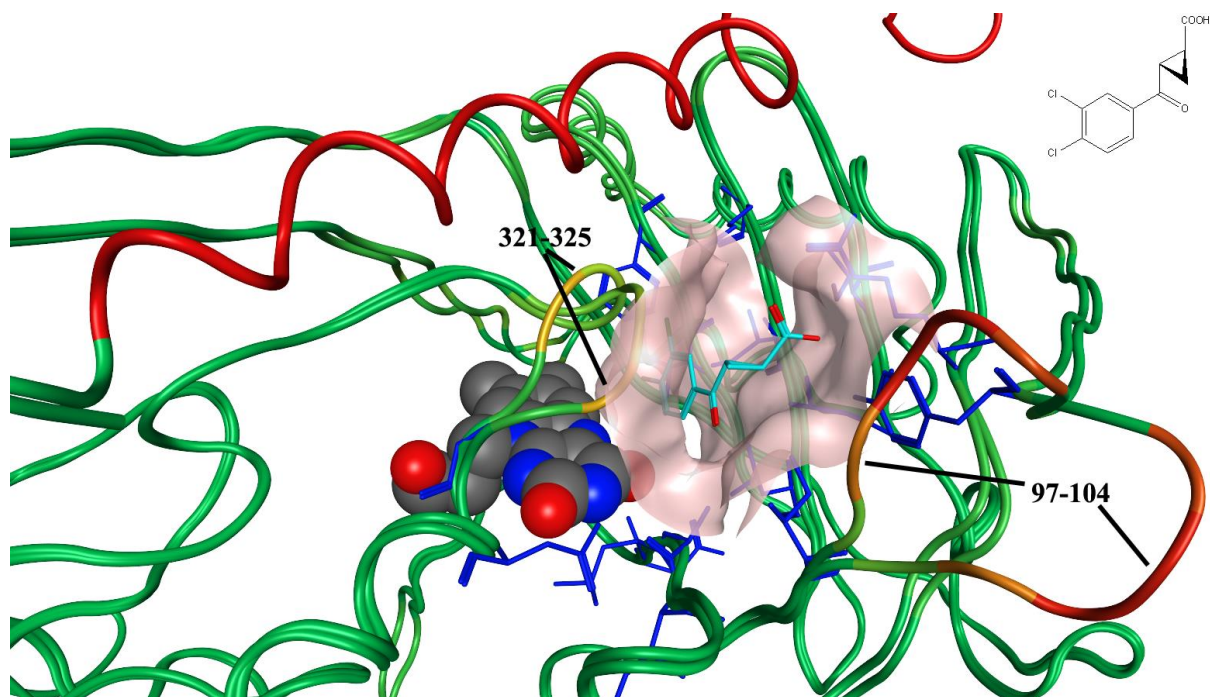


Figure 2.3. Superposition of the KMO structures 4J34 (apo) and 4J36 (holo). The backbone is coloured according to RMSD where green > yellow > orange > red. Active site atoms of 4J36 are shown (dark blue with a pink interaction surface). Co-crystallised UPF-648 is shown with light blue carbons and red oxygens and also inset. Part of FAD is also shown in space-filling mode with grey carbons, blue nitrogens and red oxygens. To the immediate left of UPF-648 are the displaced loops 321-325. Immediately to UPF-648's right are the loops 97-104. The red alpha helix shown at the top is from 4J34. In 4J36 these residues are unresolved due to displacement by residues 321-325 [126].

2.4. KMO inhibitors

4-Aryl-4-oxobutanoic acids

Early KMO inhibitors were substrate analogues that can be collectively described as derivatives of 4-aryl-4-oxobutanoic acid. For these derivatives, use of ring deactivating chloro- and nitro- groups yield sub-micromolar inhibitors (Table 2.1, *m*NBA and **1**) [137-139]. The carboxyl is obligatory for inhibition (**5**) but the amine is not (**2**), being replaceable with a hydroxyl group (**3**) or a methylene bridge (UPF-648) [139, 140]. This suggests that the amino interaction contributes roughly the same amount of inhibition as the entropic cost of binding the flexible alkyl chain. This alkyl linker between the benzoyl and carboxyl groups can also be replaced with dihydroisoxazole (Table 2.1, **27 – 30**) [141]. Replacement of the amine with thioether groups suggest the presence of a hydrophobic pocket as there is a trend of increasing inhibition with increasing size for these substituents (Table 2.1, compounds **18-21**) [142, 143]. Benatti *et al.* replaced the FAD binding benzene ring with a thiophene (Table 2.1, **31**), however no inhibition data was reported [144]. Carboxyl glycosylation of scaffold **II**, to which UPF-648 belongs, demonstrated an unchanged *in vitro* IC₅₀, but improved CNS penetration in rats at 50 mg/kg [48].

Sulfonamides

The sulfonamide structural analogues of the substrate L-Kyn are inhibitors with nanomolar IC₅₀s (Table 2.1) [46, 47, 145]. They contain an FAD-binding benzene ring (ring **A**, Table 2.1), a 5- or 6-membered aromatic ring as linker, a sulfonamide as amino-acid bioisostere, and an extendable benzene ring (ring **B**) that may be hitting the same hydrophobic pocket as the thioethers. Significant differences in inhibition was seen with modification of the linking ring, with minimal inhibition from 6-membered rings ($\leq 25\%$ at 10 μM) [47]. Of the 5-membered ring systems, the thiazole was significantly more potent [46]. The phenylthiazole benzenesulfonamides in particular are well explored (Ro 61-8048 and compounds **6** – **11**) [46]. Small substituents on both benzene rings are required for optimal *in vitro* binding, with methoxy and smaller groups being preferred. The majority of such inhibitors, such as those listed in Table 2.1, had equivalent IC₅₀s (within error) of 80 – 20 nM. They possess very poor BBB penetration but showed evidence that peripheral inhibition was enough to produce pharmacologically relevant results [45].

6-Phenylpyrimidines

The phenylpyrimidines were first investigated as KMO inhibitors after isosteric alignment with the 4-aryl-4-oxobutanoic acid scaffold [49]. The FAD-binding benzene ring is hypothesised to bind in the same manner as the co-crystallised UPF-648, and the 3,4-disubstituted system shows the greatest activity (Table 2.1). In particular, 3-chloro-4-alkyl/alkoxy groups show good *in vitro* and cellular activities (Table 2.1, compare **12** – **15**) [49]. N4 is needed more than N1 (**16** vs. **17**), but both are needed for optimal activity. Peripheral administration of **15** led to an increase of plasma L-Kyn, kynurenic and anthranilic acids, and concomitant decrease in 3-HK and Quin in rat, as expected from the peripheral inhibition of KMO. BBB penetration of the compound was poor, but was observed in the striatum at levels equivalent to the observed EC₅₀ for rat microglial cells [49]. Increased brain extracellular levels of L-Kyn, kynurenic acid and anthranilic acid were observed as was a relatively modest increase in 3-HK – much smaller than that observed from the administration of exogenous L-Kyn. This provides indirect evidence that peripheral and central inhibition are both taking place, as otherwise it would be expected that 3-HK levels should increase in a manner similar to that of exogenous L-Kyn administration [49].

Phenyloxadiazoles

The phenyloxadiazoles KMO inhibitors were first reported by Milne *et al.* [146], and tested further by Wilkinson *et al.*, [147]. Some important differences were observed in the phenyloxadiazoles compared to the structurally similar phenylpyrimidines. In the phenylpyrimidines, carboxylates were highly active, whilst in the phenyloxadiazoles, the carboxylates were inactive (Table 2.1, compounds **32** – **33**). Activity was not obtained until the carboxylates were converted to benzamides (**34**). It is also worth noting that in the same study, the benzenesulfonamide Ro 61-

8048 gave a much higher K_i of 1 μM in *P. fluorescens* compared to the nanomolar values reported by Röver *et al.* in rat kidney KMO [46]. This may highlight a greater need to investigate the interspecies differences among KMO enzymes for the purposes of drug discovery.

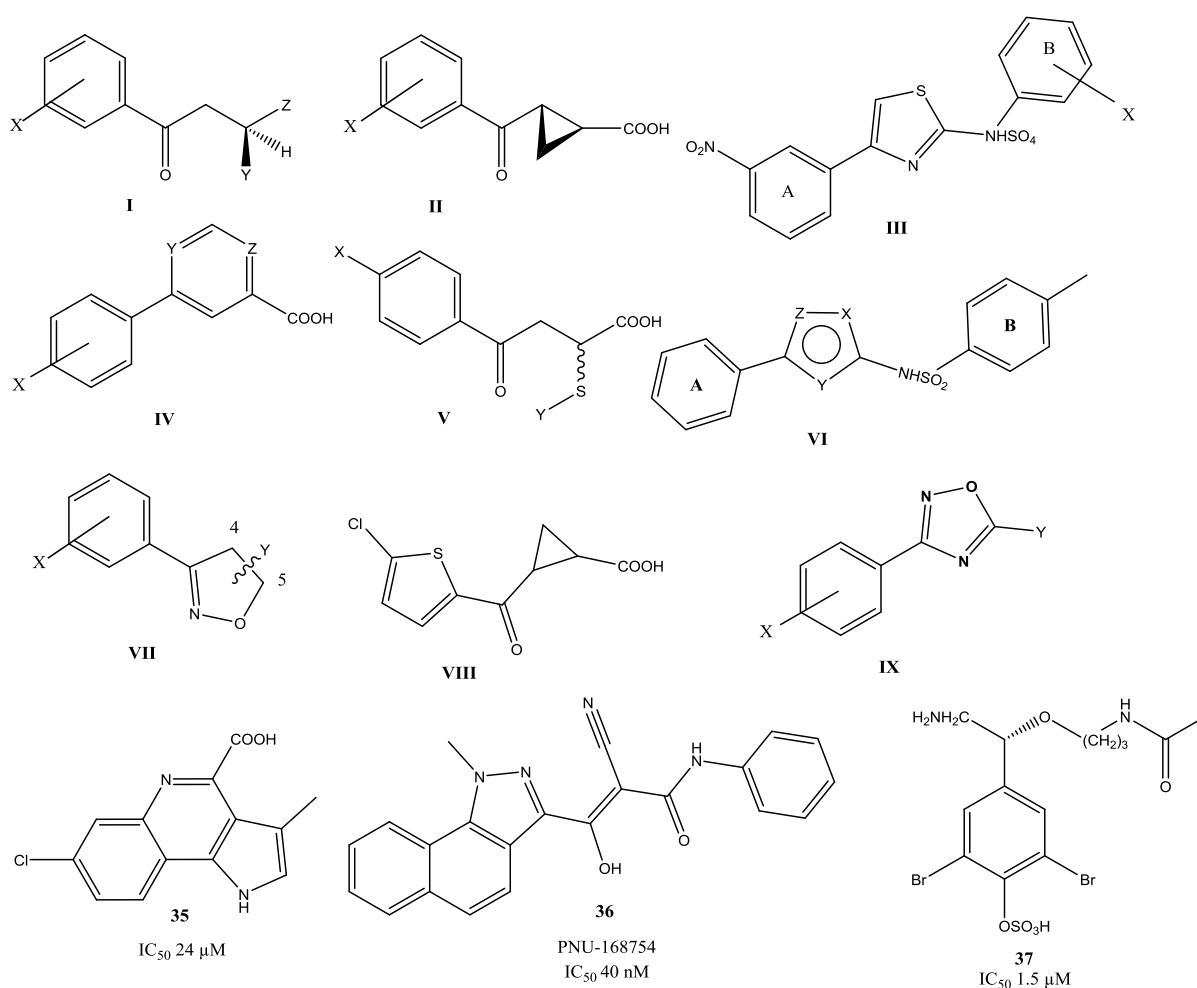
Other scaffolds

Heidempergher *et al.* reported a limited KMO inhibitor SAR of the modestly active pyrroloquinolines, the strongest of which is shown in Table 2.1 (compound **35**) [148]. Removal of the carboxylate group negates inhibition even at 100 μM . Removal of the pyrrole ring from compound **35** results in negligible activity, as does saturation of the benzene ring. A series of 3-oxo-propanenitrile molecules were separately patented and described with 40 nM IC_{50} (Table 2.1, compound **36**) [149], though no SAR is available. More recently, the marine sponge amine ianthellamide A was reported with an IC_{50} of 1.5 μM in *in vitro* assays and gave a 3-fold increase in rat brain kynurenic acid levels when administered at 200 mg/kg (Table 2.1, compound **37**, [150]).

2.5. Drug discovery efforts: the gaps surrounding KMO knowledge

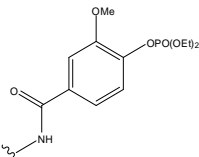
A number of inhibitor scaffolds have been reported for KMO, most of which can be described as substrate-mimetic bioisosteres. Despite this, no molecules have so far proceeded to clinical testing. Crystal structures are available for yeast KMO, with a bound substrate mimetic ligand, and these structures can be useful during docking studies. However, there is evidence of considerable conformational rearrangement to accommodate ligand binding; with the ligand-bound structure (PDB: 4J34) missing electron density of an α -helix that makes up part of the active site roof, and two loops showing significant movement (Figure 2.3, above). Additionally, the proposed mechanism of KMO turnover involves a number of binding and unbinding steps of NADPH and oxygen species, prior to the binding of substrate L-Kyn. As such, there may be other druggable structures besides those observed so far. Additionally, the structure is of yeast KMO, and not human. Whilst the residues in and surrounding the active site are largely conserved, with the exception of a tyrosine/phenylalanine substitution, there may still be subtle differences in optimising molecules for each species to consider. The mechanistic and inhibitory structure-activity relationship covered in this section provide a foundation for the development of models in Chapter 3.

Table 2.1. Selected SAR of KMO inhibitors.



Scaffold	X	Y	Z	IC_{50} / μ M	Source	Cmpd	Ref
I	<i>m</i> -nitro	NH ₂	COOH	0.5	Rat liver	<i>m</i> NBA	[139] ^a
I	H	NH ₂	COOH	16	Rat brain	BA	[151]
I	3,4-dichloro	NH ₂	COOH	0.33	"	1	[139] ^a
I	3,4-dichloro	H	COOH	3.9	"	2	[139] ^a
I	3,4-dichloro	OH	COOH	0.42	"	3	[139] ^a
I	3,4-dichloro	CH ₂ Ph	COOH	2.3	"	4	[139] ^a
I	3,4-dichloro	NH ₂	H	None	"	5	[139] ^a
II	3,4-dichloro			0.18	"	UPF-648	[140] ^a
III	3,4-dimethoxy			0.037	Rat kidney	Ro 61-8048	[46] ^b
III	4-amino			0.040	"	6	[46] ^b
III	4-methoxy			0.051	"	7	[46] ^b
III	4-chloro			0.084	"	8	[46] ^b
III	3,4-dichloro			0.120	"	9	[46] ^b
III	H			0.200	"	10	[46] ^b
III	4- <i>iso</i> -propyl			0.990	"	11	[46] ^b
IV	3-chloro	N	N	0.005	Human liver	12	[49] ^b
IV	3,4-dichloro	N	N	0.006	"	13	[49] ^b
IV	H	N	N	0.038	"	14	[49] ^b
IV	3-chloro-4-cyclopropoxy	N	N	0.005	"	15	[49] ^b
IV	3,4-dichloro	CH	N	0.032	"	16	[49] ^b
IV	3,4-dichloro	N	CH	0.090	"	17	[49] ^b

Table 2.1. Continued from previous page.

Scaffold	X	Y	Z	I%, 10 μM	Source	Cmpd	Ref
V		cyclohexyl		19	Rat liver	18	[142] ^b
V		phenyl		30	"	19	[142] ^b
V		<i>p</i> -chlorophenyl		65	"	20	[142] ^b
V		β-naphthyl		77	"	21	[142] ^b
VI	S	N	C	470 nM (IC ₅₀)	Rat kidney	22	[46] ^b
VI	S	N	N	78	"	23	[47]
VI	N	S	N	72	"	24	[47]
VI	O	CH	N	31	"	25	[47]
VI	NCH ₃	CH	N	0	"	26	[47]
VII	3,4-dichloro	4-CH ₂ COOH		100	Human recombinant from CHO ^c cells	27	[141] ^b
VII	3,4-dichloro	5-CH ₂ COOH		93	"	28	[141] ^b
VII	3,4-dichloro	4-CH ₂ COOCH ₃		100	"	29	[141] ^b
VII	3,4-dichloro	5-CH ₂ COOCH ₃		88	"	30	[141] ^b
VIII	-	-		NR	NR	31	[144]
IX	<i>m</i> -nitro	COOH		0	<i>P. fluorescens</i>	32	[147]
IX	<i>m</i> -nitro	CH ₂ CH(NH ₂)CO OH		0	"	33	[147]
IX	3,4-dichloro			17 nM (K _i)	"	34	[147]

^aL-Kyn at 25 μM. ^bL-Kyn at 100 μM. NR: not reported. ^cCHO: Chinese hamster ovary.

Appendix to Chapter 2

KMO multiple sequence alignment

```

P_fluorescens 1 -----MTA--D--NA--QVTTIG--AG--
S_cerevisiae 1 -----MSESVAIIIG--AG--
X_tropicalis 1 -----MEIQGNRKKTVSIVG--GG--
D_rerio 1 -----METAFSHPPQSSSSKRVIAVG--GG--
O_anatinus 1 -----MPSIDPRDQKVAVIG--GG--
M_gallopavo 1 -----MKSSNVQKKVAIVG--GG--
S_harrisii 1 -----MAGRRKAQDVQAGPGGQCNSLVGKRRRRERYMVPGEFGGD
B_taurus 1 -----MDSSDIQRKNIAIIG--GG--
S_scrofa 1 -----MKNTSAVMDSSDIQRTSIAVIG--GG--
M_musculus 1 -----KDRKTSACRTESSDLNRGVLEAMASSDTQCKRVAVIG--GG--
G_gorilla 1 MNALGLGQYKNSEKPVCRHRNQCHSVTEATIIVKNTSAVMDSSVQRKKVAVIG--GG--
H_sapiens 1 -----MDSSVQRKKVAVIG--GG--

```

```

P_fluorescens 17 -----LAGTILVARLLARNGQVNLFFERRPDPRIT--ETGARGRSINLALAERGAHAL
S_cerevisiae 12 -----LVGCLALAFSKEGVNVTLYDFRQDPRLDTTKNKNLSINLAISARGIDAL
X_tropicalis 18 -----LVGSLNACFFAKKGFQVLYEAREDIRY--ARMVSGRSINLALSHRGRQAL
D_rerio 26 -----LVGSLNACFLAKRGDFVEVYESREDIRQ--AKVVGRSINLALSHRGRQAL
O_anatinus 18 -----LVGNLNACFLAKRGFQVDIYEAREDIRV--AKVARGRSINLALSHRGRQAL
M_gallopavo 18 -----LVGALNACFFAKRGFIVDVYEAREDIRV--SSFARGRSINLALSHRGRQAL
S_harrisii 43 FRQXXXXFSEVGLNACFFAKRGFQVDVYEAREDIRV--AKFARGRSINLALSHRGRQAL
B_taurus 18 -----LVGSLNACFLAKRNFQVDIYEAREDIRV--TKSARGRSINLALSYRGRQAL
S_scrofa 25 -----LVGSLNACFLAKRNFQVDVYESREDIRV--AEFARGRSINLALSYRGRQAL
M_musculus 40 -----LVGALNACFLAKRNFQVDVYEAREDIRV--AKSARGRSINLALSYRGRQAL
G_gorilla 58 -----LVGSLNACFLAKRHFQIDVYEAREDIRV--ATFTRGRSINLALSHRGRQAL
H_sapiens 18 -----LVGSLNACFLAKRNFQIDVYEAREDIRV--ATFTRGRSINLALSHRGRQAL

```

```

P_fluorescens 66 RLAGLE--REVLAELAVMMRGRM/HVPGTPPNLQPYGRDDSEVIWSINRRLRNRLILDCAE
S_cerevisiae 63 KSLDPDACEHILQDMIPMKGRMIHDKGRQESQLYGLH-GEAINSNRSLVNLNSLLDELE
X_tropicalis 67 KAVGLD--EKTAAMGIPMRARMIHSVKGKSSIPYCKQ-HQYILSDRANLNKELLAAE
D_rerio 75 KHVGME--DKTISKGIPMHARMIHNVNGKRSPIPYCKK-QQYILSDRANLNKELLTAAE
O_anatinus 67 RSLGLE--DQIVSQGIPMRARMIHSLSGKKSAPYCKK-NQYILSISREILNKELLTEVE
M_gallopavo 67 QAVGLE--EQIVSKGIPMHARRIHPDGKKYSIPYCKK-NQYILSDRANLNRELLTAAE
S_harrisii 101 KAVGLE--DQIVSQGIPMRARMIHSLSGKKTAPYCTK-NQYILSISREHLNKDLLNAVE
B_taurus 67 KAVGLE--DQIVSQGIPMRARMIHSLSGKKSAPYCTK-SQYILSISRENLNKDLLTAVE
S_scrofa 74 KAVGLE--DQIVSQGIPMRARMIHSLSGKKSAPYCTK-SQYILSISRENLNKDLLTAVE
M_musculus 89 KAVGLE--DQIVSKGIPMRARMIHSLSGKKSAPYCNK-SQYILSISRENLNKDLLTAVE
G_gorilla 107 KAVGLE--DQIVSQGIPMRARMIHSLSGKKSAPYCTK-SQYILSISRENLNKDLLTAAE
H_sapiens 67 KAVGLE--DQIVSQGIPMRARMIHSLSGKKSAPYCTK-SQYILSISRENLNKDLLTAAE

```

YGKK-XQYI

```

P_fluorescens 124 A-AGASIHFNGLDSVD-FARQRIT--LSNVS-GERLEKRFHLLIGADGCNSAVRQAMAS
S_cerevisiae 124 K-STTELKFGHKLNKIEWTDDKOICHFAIGEDLKTPHTEKYDFVIGCDGAYSATRSQMR
X_tropicalis 124 KYSNVTMHFEHKLKRDGN-VDSGTMT--FLNNM-ENIEKKADLIVGCDGAFSVVRKQFMR
D_rerio 132 AYPNTRINFNHLKLDWS-PKTGTMT--FIGSD-GQKTETQADLIVGCDGAFSAVRKQELR
O_anatinus 124 KYPNAKVHFGHKLKCR-PEEGVIT--VLGSN-DGEVEIACDLIVGCDGAYSTVRKQLLK
M_gallopavo 124 KYSNTKLYFGHKLKCN-AELGTIT--IKRSG-QPLEVITYDLIVGCDGAFSTVRKQFMR
S_harrisii 158 KYPTAKVHFGHKLKCK-PEEGVIT--VLGSN-QVPEVTCTDLIVGCDGAYSTVRKQFMR
B_taurus 124 KYSNAKVHFGHKLKCR-PEEGVIT--VLGQD-KVPKDVTCDLIVGCDGAFSTVRYLMK
S_scrofa 131 KYPNAKVHFGHKLKCR-PETGVIT--LLGPD-KVPKDIACDLIVGCDGAYSTVRTHLMK
M_musculus 146 SYANAKVHFGHKLKCI-PEEGVIT--VLGPD-KVPRDVTCDLIVGCDGAYSTVRAHLMK
G_gorilla 164 KYPNVKMHFNHRLKCN-PEEGVIT--VLGSD-KVPKDVTCDLIVGCDGAYSTVRSHLMK
H_sapiens 124 KYPNVKMHFNHRLKCN-PEEGVIT--VLGSD-KVPKDVTCDLIVGCDGAYSTVRSHLMK

```

```

P_fluorescens 179 VVDLGEHLETQPHGYKELQITPEA-----SAQENLEPNALHIWPHGDMCIALPNLDIS
S_cerevisiae 181 KVEMDSQEYNLRYIELYIPPTTEEFKPNYGGNFAPDHLHIWPRHKFMIALANSDBGS
X_tropicalis 180 KSRFNYSHVYIPHGKELTIPPR-----KGDFAMEPNYLHIWPRNTFMMIALPNMDKS
D_rerio 188 QSRFNYSQTYIPHYGMELTIPPK-----DGDFAMEPNYLHIWPRNTFMMIALPNLDRT
O_anatinus 180 QPRENYSQQYISHGYMELTIPPK-----NGDFAMEPNSLHIWPRNTFMMIALPNANKS
M_gallopavo 180 QTRFNYSHEYIPHYGMELTIPPK-----DGDFAMEPNYLHIWPRNTFMMIALPNMDKS
S_harrisii 214 RPRENYSQQYIPHYGMELTIPPK-----NGDFAMEPNYLHIWPRNTFMMIALPNQNKs
B_taurus 180 KPRFDYSQQYIPHYGMELTIPPK-----NGDFAMEPNYLHIWPRNTFMMIALPNMNKS
S_scrofa 187 KPRFDYSQQYIPHYGMELTIPPO-----NGDFAMEPNYLHIWPRNTFMMIALPNMNKS
M_musculus 202 KPRFDYQQYIPHYGMELTIPPK-----NGDFAMEPNCLHIWPRNTFMMIALPNMDKS
G_gorilla 220 KPRFDYSQQYIPHYGMELTIPPK-----NGDFAMEPNYLHIWPRNTFMMIALPNMNKS
H_sapiens 180 KPRFDYSQQYIPHYGMELTIPPK-----NGDFAMEPNYLHIWPRNTFMMIALPNMNKS

```

P_fluorescens	233	FTVTLFLHHQSPAAQPASPCFAQLVDG-HAARRFFQFQFDLSPML--DSLEQDFEHHPT
S_cerevisiae	241	FTSTFFGSKDQ-----ISDLTTSKSRVREFLIENFPDIINIMDLDDAVKRFITYPK
X_tropicalis	233	FTCTLFMPFED-----FEKLRTG-DQVLDFFKTYFPDSIELIGEKKLTEDFFLLP
D_rerio	241	FTCTLFMPFED-----FEKLRTG-DEILRFFHKYFPDSVPLIGVEALKQDFFRLPA
O_anatinus	233	FTCTLFMPFED-----FESLRTG-SEVLDFFKFNFPDSIPLIGEQALKRDFFLLPA
M_gallopavo	233	FTCTLFMPFEE-----FEKLRTG-EQVLDFFKTYFPDSIPLIGERELKHDYFLLPA
S_harrisii	267	FTCTLFMPFEN-----FEKLRTG-SDVLDFFKYFPDSIPLIGVEALKQDYFLLPA
B_taurus	233	FTCTLFMPFEE-----FEKLRTS-SDVLDFFKYFPDSIPLIGEQALVQDFFLLPA
S_scrofa	240	FTCTLFMPFEE-----FEKLRTS-RDVLDFFKYFPDSLHLIGKEALAQDFFRLPA
M_musculus	255	FTCTLFMPFEE-----FEKLRTS-SDVLDFFKYFPDAIPLIGEQALMRDFFLLPA
G_gorilla	273	FTCTLFMPFEE-----FEKLRTS-NDVVDFFQKYFPDAIPLIGEKLLVQDFFLLPA
H_sapiens	233	FTCTLFMPFEE-----FEKLRTS-NDVVDFFQKYFPDAIPLIGEKLLVQDFFLLPA

P_fluorescens	290	GKATLRLTTWHV-GGQAVLLGDAAHFVVPFHGQGMNCALEDAVALAEH-QSAADNAS-
S_cerevisiae	292	ESLVCVNCKPYDVPGGKATLLGDAAHAVVPFYGQGMNCGFEDVRLMALLLKKHSGDRSRA
X_tropicalis	283	QAMISVKCSSFCI-DHKCVLMGDAAHAVVPFYGQGMNAGFEDCLVFSELMEQYQNNLRIC
D_rerio	291	QAMISVKCCPYHL-FEKCVMGDAAHAVVPFYGQGMNAGFEDCLVFDEIMDQFNENLVAV
O_anatinus	283	QSMIAKCSSFHL-SSKCLMGDAAHAVVPFYGQGMNAGFEDCLVFDELMDKFNNDLCIC
M_gallopavo	283	QAMISVKCSSYHL-SSRCVLMGDAAHAVVPFYGQGMNAGFEDCLVFDELMQFHNDLGAC
S_harrisii	317	QPMIAVKCSFHH-GSHCVLMGDAAHAVVPFYGQGMNAGFEDCLVFDELMDKFNNDLSAC
B_taurus	283	QSMISVKCSSFHF-KSHCLMGDAAHAVVPFYGQGMNAGFEDCLVFDELMDKFNNDLSNC
S_scrofa	290	QPMISVKCSSFHF-NSHCVLMGDAAHAVVPFYGQGMNAGFEDCLVFDELMDKFNNDLSNC
M_musculus	305	QPMISVKCSSFHL-KSHCVLMGDAAHAVVPFYGQGMNAGFEDCLVFDELMDKFNNDLSNC
G_gorilla	323	QPMISVKCSSFHF-KSHCVLLGDAAHAVVPFYGQGMNAGFEDCLVFDELMDKFNNDLSIC
H_sapiens	283	QPMISVKCSSFHF-KSHCVLLGDAAHAVVPFYGQGMNAGFEDCLVFDELMDKFSNDLSIC

PEFGQC

P_fluorescens	348	LAAFTAQRPDALATQAMALENYEMSSKVASPTYLLEELGQIMAQROPTRFIPRYEMV
S_cerevisiae	352	FTEYTQTRHKDLVSIHELAKRNYKEMSHDVTSKRFLRKKLDALEFSIMKDKWIPLYTMV
X_tropicalis	342	LHEFSRLRPDDHAISDLAMYNKEMRAHVNSKWFIFRKOVDNILLHFMPEKTIPLYTMV
D_rerio	350	LQETTRVRPDDHAISDLAMYNKEMRAHVNSKYFIFRKYLDNILLHFMPEKTIPLYTMV
O_anatinus	342	LPEFSRLRPDDHAISDLAMYNKEMRSHVNSRWFIERTYLDRLVLAIMPSTFIPLYTMV
M_gallopavo	342	LPEFSRLRPDDHAISDLAMYNKEMRSHVNSTWFIERKQINNLLHIMPSTFIPLYTMV
S_harrisii	376	LPEFSRLRIPDDHAISDLAMYNKEMRAHVNSRWFIQKNIEKCLHAIMPSTFIPLYTMV
B_taurus	342	LPEFSRLRIPDDHAISDLAMYNKEMRAHVNSRWFIERKNIERLLHAIMPSTFIPLYTMV
S_scrofa	349	LPEFSRFRIPDDHAISDLAMYNKEMRSHVNSRWFIQKNIERCLHIMPSTFIPLYTMV
M_musculus	364	LPEFSRFRIPDDHAISDLAMYNKEMRAHVNSRWFIQOKLLDKFLHAIMPSTFIPLYTMV
G_gorilla	382	LPVFSRLRIPDDHAISDLAMYNKEMRAHVNSRWFIQKNMERFLHIMPSTFIPLYTMV
H_sapiens	342	LPVFSRLRIPDDHAISDLAMYNKEMRAHVNSRWFIQKNMERFLHAIMPSTFIPLYTMV

P_fluorescens	408	TF-SRIPYAQAMARGQIQEQLLKFAVANHSDLTSSN--LDAVEHEVTRCLPPLSHL-C
S_cerevisiae	412	SFRSDISYSRALERAGKOTRILKFLESITLGMLSIGG-YKLFKFLRERS
X_tropicalis	402	TF-SRIRYHEVILRWQKKIINVGLFTVGTGSGVAYLVIKYLPFNKY--IEHV-G
D_rerio	410	TF-IRTRYNDVNRWQKKVITRGLNLGCFVSAAGGTYYLVKNSHKLPSISAEQL-W
O_anatinus	402	SF-SRIRYHEVVRWQKKVVKGLMCGSLSALSAYLLTRSLWQS---VPR-L-W
M_gallopavo	402	TF-SRIRYHEALRWQKKIINRGLFIMCA-AGIGCTYLLIKRLRDWYFFIPNL-W
S_harrisii	436	TF-SRIRYHEALRWQKKVINKGLEFFGTATASGTCLFVTYMSPKVQ--LKML-W
B_taurus	402	TF-SRIRYHEAVLHWQKKVINGGLEFLTGTLIASGTYLLMRYKSPSPLDYLRP-S
S_scrofa	409	TF-SRIRYHEAMLRWQKKVINTALEFFGTLLVALSTTYLLTGPTFRSSLGCLRRS-W
M_musculus	424	AF-SRIRYHEAVLRWQKKVINRGLFVLGSLIAIGGTYLLVHLLSRPLEFLRRPW
G_gorilla	442	TF-SRIRYHEAVQRWQKKVINKGLEFLGSLIAISSTYLLIHYMSPRPFLRLRP-W
H_sapiens	402	TF-SRIRYHEAVQRWQKKVINKGLEFLGSLIAISSTYLLIHYMSPRSFCLLRP-W

Apparent consensus sequences of active site loops are highlighted in green. Box shading provided by the BoxShade server:
(http://www.ch.embnet.org/software/BOX_form.html).

Alignment performed using MOE 2012, Chemical computing group (Montreal, Canada) using a Blossum62 algorithm with a tree-based pairwise build-up, gap start penalty of 7 and a gap extend penalty of 1.

NCBI protein accession numbers

NP_009454 - Saccharomyces cerevisiae, yeast
CAA73613 - Homo sapiens, Ape
Q84HF5 - Pseudomonas fluorescens, Gram-negative bacteria
NP_001006690 - Xenopus (Silurana) tropicalis, frog (amphibian)
XP_003207386 - Meleagris gallopavo, wild turkey (North America) (Bird)
EDL13209 - Mus musculus, house mouse, rodent

XP_003767836 - *Sarcophilus harrisii*, Tasmanian devil, marsupial
XP_001514157 - *Ornithorhynchus anatinus* (platypus), monotreme
Q1RLY6 - *Danio rerio* (Zebra fish), fish
NP_001230227 - *Bos taurus* (cow)
NP_999241 - *Sus scrofa* (wild boar)
XP_004028713 - *Gorilla gorilla gorilla*

Chapter 3

In Silico Screening Against KMO

This chapter introduces some basic concepts of molecular modelling for early drug discovery, with a focus on high throughput in silico screening techniques to identify potential hit compounds as kynurenine monooxygenase (KMO) inhibitors. It also presents in vitro and in cell data of a small number of compounds that were purchased as possible KMO inhibitors.

3.1. Drug discovery *via* screening

High throughput drug discovery involves the synthesis or purchase of a large variety of compounds, and the addition of these compounds to some form of enzyme, cell, tissue, or even whole organism assay. An assessment is then made as to the impact of the test compound on the physical, chemical, or biological properties of the system. For example, screening for antibiotics typically involves the screening for compounds capable of inhibiting specific bacterial enzymes (target-based screening), or inhibiting bacterial processes such as cell proliferation or biofilm formation (phenotype screening) [152-155]. Until very recently, the vast majority of screening for KMO inhibitors was performed by measuring the hydroxylation by KMO of L-kynurenine in rodent mitochondrial isolates (Section 2.4). Screening *via* this method therefore requires a significant investment not only in designing and obtaining the compound library, but also in the preparation of sufficient mitochondrial tissue. Whilst more recent technologies have allowed greater quantities of recombinant human KMO to be produced by insect or bacterial expression systems, KMO screening by such methods still represents a large investment in resources. Hit rates of unbiased compound libraries (*i.e.* a library not biased towards activity at the specific target by any foreknowledge) are commonly less than 1% (e.g. [156, 157]). This can be further compounded by the difficulty in differentiating true and false positives, and in prioritising true candidate molecules over promiscuous molecules or “common hitters” – molecules that may have a higher propensity for failure during later stages of drug development due to off-target actions [152, 158-160].

In silico screening is the act of assessing a molecule’s potential as a drug through the use of computer models. At its heart, it is the use of computational methods to enrich an unbiased library through the removal of true negatives, and ideally the identification of true positives [161]. Resources spent creating a biased library of compounds are ideally recuperated by not screening molecules unlikely to bear fruit. In order to realise this goal, balance must be attained between the computational cost incurred and the accuracy required of the results. This can be achieved by adjusting the granularity of the information used to describe both the compound library and (in target-based screening) the target macromolecule. At the higher end of data granularity, chemical

and physical information is retained to the highest level of theory currently known (quantum mechanics). At the lower end of data granularity, molecules may be stripped of three dimension information, and only atom identity and connectedness is retained (*e.g.* topological indices, MACCS keys [162]). In this work, the balance between resource cost and accuracy of results was achieved using, sequentially, pharmacophores and docking. Initially, high speed, low complexity, pharmacophores were employed to screen through a database of 420, 000 commercial molecules. Once the number of molecules had been reduced, slower, more information rich, docking techniques were used. Such sequential methodologies have been used with success previously against a range of drug targets with improved hit rates compared to the screening of unbiased libraries. [117, 163, 164].

3.1.1. Pharmacophores

Pharmacophores can be broadly separated into the categories of either 1-, 2- or 3-dimensional, based on whether they are derived from/operate on 1-, 2-, or 3-dimensional representations of molecules. 1-Dimensional examples of chemical structures include the oft-cited and variously implemented MACCS keys, which act by encoding a string of bits to represent the presence or absence of defined chemical features (*e.g.* is there are heteroatom? Is there a nitrogen in a ring? *Etc.*) [165]. 2-Dimensional representations include the umbrella term of topological indices, which generally extend on this idea by including how the bits are connected and sees particular use in combination with machine learning approaches (see for example, [166-169]). 3-Dimensional pharmacophores, look to encode not just what types of chemistries are present and how they are connected, but also their relative orientation in space – usually by using the 3-dimensional conformations of the compounds themselves. Biovia Discovery Studio (formerly Accelrys Discovery Studio) has a number of algorithms to do with elucidating pharmacophores from a dataset of compounds (*e.g.* HypoGen) [170]. These algorithms may take into account the features that are common to both highly active, and those that are common to inactives – but missing from active – compounds. This information is used to construct a number of hypotheses of functional group combinations that are either required or detrimental to activity [170-172]. Similarly, the software package used in this work, MOE, provides different though similar functionality in elucidating pharmacophores based on the 3-dimensional alignment of known ligands. The representation of these 3-dimensional pharmacophores is generally *via* defining regions of space as spheres (called pharmacophore features), and defining the types of molecular functional groups (*e.g.* hydroxyl groups, amines, carboxylates, *etc.*) that are allowed to exist within them as part of a potential ligand. Therefore, for any given ligand (or by definition, any given binding site) the steric properties of a molecule is defined by the 3-dimensional positioning

of pharmacophore features, and the electronic properties are defined by the list of functional groups assigned to each feature.

The following list provides examples of how pharmacophoric functional groups are defined in the software employed in this work, Molecular Operating Environment (MOE, Chemical Computing Group, Montreal, Canada), and includes those features used in this KMO study:

- Ani: explicitly anionic
- O2: carboxyl/sulfonyl centroid
- Cat: explicitly cationic
- CN2: imidamide centroid
- Don: hydrogen bond donor
- Don2: hydrogen bond donor vector
- Vol: a special region of space that is either an inclusion or exclusion zone. Inclusion zones must have a non-hydrogen atom within it. An exclusion zone cannot have one within it.
- Acc: hydrogen bond acceptor
- Acc2: hydrogen bond acceptor vector
- Aro: aromatic centroid
- PiR: pi ring centre (non-aromatic)
- PiN: normal (90°) vector of PiR or Aro
- Hyd: hydrophobic centroid

One or more of the above functional group definitions are applied to the pharmacophore features, and individual molecules can be assessed for their ability to 'satisfy' the pharmacophore through the answering of some simple questions: 1) Are there atoms within the pharmacophore feature? 2) Do these atoms constitute a desired functional group? 3) How close to the centre of the feature is the functional group? Specifically how these questions give rise to numbers for use in the screening is dependent on the program being used, but MOE calculates them as a root mean square deviation (RMSD) from a perfect fit (described in more detail in the next section).

Some examples of molecules aligned to pharmacophore features are presented in Figure 3.1. Protonated 4-(2-aminoethyl)cyclohexan-1-ol (left) satisfies the hydrogen bond acceptor feature (F1:Don) by having a hydroxyl group within it. The F2:Don2 feature is satisfied by having the projection of the hydroxyl's O-H bond pass through it. The F3:Hyd feature is satisfied by having a cyclohexyl ring within it. While the F4:Cat feature is satisfied by having an explicitly cationic amine within it. An uncharged amine would not satisfy F3:Cat in this work.

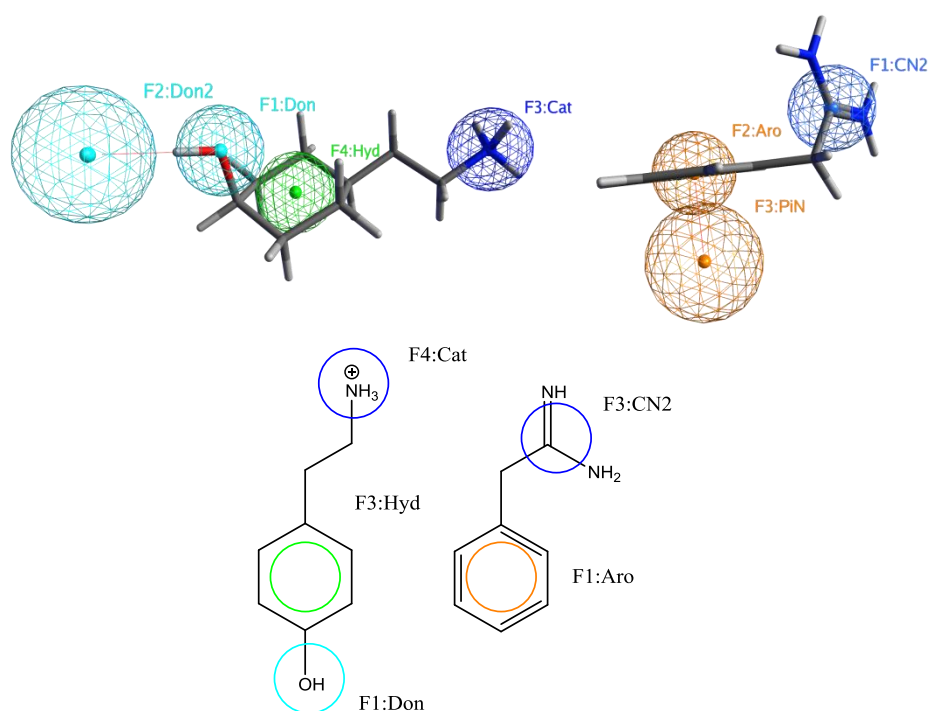


Figure 3.1. Example molecules and potential pharmacophore features that can be used to define them. **Left:** 4-(2-Aminoethyl)cyclohexan-1-ol. The F1:Don feature is occupied by a hydroxyl group, and is connected to the F2:Don2 feature *via* a red line. For F2:Don2 to be satisfied, the projection of the O-H bond must pass through F2:Don2. For F4:Hyd to be satisfied, a hydrophobic group must be placed within it, in this case the centre of mass of a cyclohexane ring. In order for F3:Cat to be satisfied, cationic atoms must be residing within it. **Right:** 2-Phenylacetimidamide. The F1:CN2 feature is satisfied by having an imidamide group within it, The F2:Aro group is satisfied by having an aromatic ring such as benzene within it, and the F3:PiN is satisfied by having the vector of the normal plane of the aromatic ring in F2:Aro passing through it. The equivalent two dimensional representation of each molecule and pharmacophore is also given at the bottom. These are theoretical compounds generated by the candidate for discussion purposes only.

Understanding the fit of a molecule with a pharmacophore in MOE

Some functional groups can satisfy multiple of the above definitions, while others might be subsets for another definition. For example, a hydroxyl group can be both a hydrogen bond donor or acceptor, whilst the definitions used within MOE mean that all anionic groups are also hydrogen bond acceptors (though a cation is not by default a hydrogen bond donor unless it happens to have a hydrogen). Thus, a given molecule might fit within the definition of a given pharmacophore in a number of ways, depending on the complexity and conformation of each.

As such, each conformation has an associated root mean square deviation (RMSD), which describes the deviation of functional groups from perfect, across the whole of the molecule. For example, the molecules in Figure 3.1, above, sit within their native pharmacophores. Their fit is perfect and they have an RMSD of 0 because each molecular functional group sits at the centre of the respective feature, and each vector passes through the centre of their respective feature. Deviation from this is measured in angstroms (from the centre of the sphere) and presented as an RMSD across all features. In Figure 3.2, the pharmacophore shown is that of the aminodibenzofuran acid (grey atoms). Its RMSD is therefore 0. An isosteric ring expansion yields

the analogous phenanthrene amino acid (gold atoms). This molecule cannot sit in the exact centre of the three pharmacophore features, and therefore has an RMSD of 0.4 Å. In this work, all features were given equal weighting. Therefore, the fit of each molecule is dependent only on the RMSD across the features, and not the identity of the feature or the functional group within it.

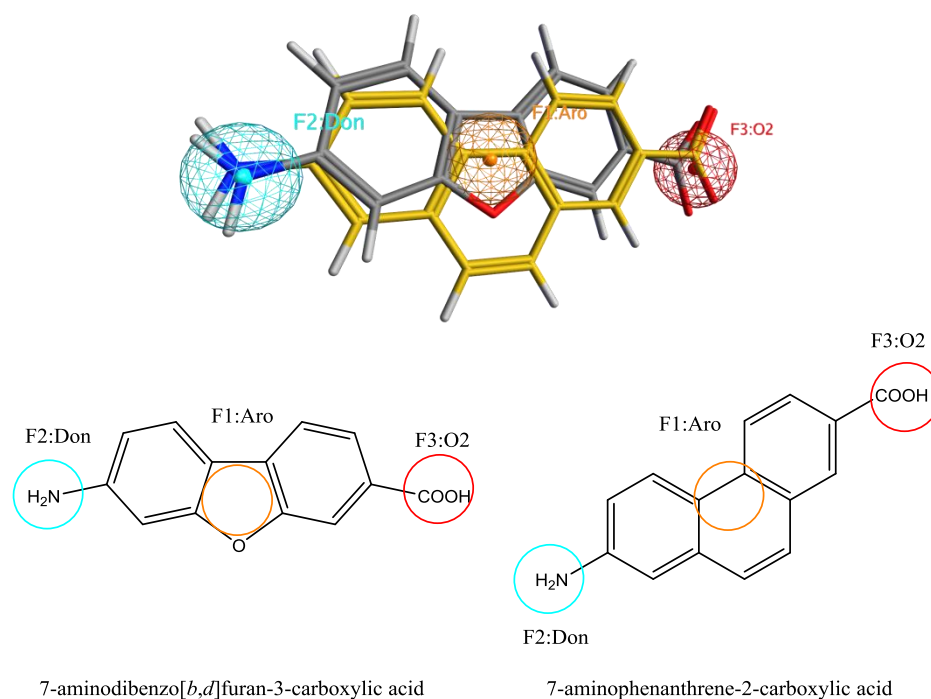


Figure 3.2. Use of RMSD to compare the fit of two molecules to the same pharmacophore. Although the phenanthrene (gold atoms) places its aromatic, amino and carboxylate groups within each sphere, they do not sit at the exact centre of each sphere, and thus it has a higher RMSD compared to the perfect fit (RMSD = 0 Å) of the dibenzofuran.

3.1.2. Docking

The purpose of docking is to find the lowest energy binding pose between a receptor and an effector. In this work the effector is always a small molecule, but protein-protein and protein-nucleic acid docking is also possible. Conversely to pharmacophores, docking results provide an atomistic view of information, where molecules are defined by their constituent atoms. Most commonly (though not always), docking programs do this by using force field definitions of atoms. The atoms possess a 3-dimensional co-ordinate in space, and the effect that each atom exerts on other atoms is represented by classical physics. Electrons do not exist in this definition of an atom. Instead, the atoms are given a point-charge that is (usually) not polarisable based on the distance to other atoms [173]. The geometry and electrostatic charge of each atom are defined based on the connectivity of the atom, referred to as ‘atom typing’. For example, the nitrogen of aliphatic amines (sp^3 , tetrahedral), aromatic amines (sp^2 , slightly tetrahedral) and amide nitrogens (sp^2 , planar) are given different values that define their varied geometries, electronic properties and interactions.

At a simplistic level, docking programs can be split into two categories: those that use force fields to generate and/or assess docking poses, and those that do not. Independently of this, different programs will treat flexibility differently. Depending on the program used, some or all of the covalent bond lengths, bond angles, and rotation around bonds may be held rigid or flexible (either on the receptor and on the ligand). Popular stand-alone docking programs include Gold, Glide, Dock, and AUTODOCK, in addition to commercial software suites which may either integrate with these stand-alone programs, and/or provide their own docking algorithms (*e.g.* OpenEye, Biovia (formerly Accelrys), Chemical Computing Group, and Schrödinger), and each performs docking *via* different methods.

During docking, there are a number of problems that each algorithm must overcome, and they directly impact the efficiency and accuracy of the experiment. These can split up as problems in sampling all of the relevant poses, the scoring (and therefore ranking) of the poses, and the screening power [174]. The sampling problem is the ability of the procedure to generate the ‘true’ pose that exists in nature. The scoring problem is the ability of scoring functions to attribute a physically relevant number to each pose and thus rank them in some meaningful way, such that the ‘more true’ pose(s) can be identified. The screening power is the ability to use all of these factors to efficiently screen a virtual database and discriminate between true positives and inactive molecules. A key problem in the field with the latter part (independent on whether one is talking about docking or any other virtual screening method) is the concept of an activity cliff. This cliff exists between two molecules that superficially look structurally very similar, but that have a large difference in their affinity to the target [175].

One of the major factors influencing all of these problems, is receptor flexibility. Whilst the purpose of docking is to find the 3-dimensional complex between receptor and ligand, the purpose of virtual screening is to find novel, high affinity, ligands. However, it can be difficult for a static representation of binding such as docking to accurately depict a highly dynamic process such as binding – due in large part to flexibility. The flexibility of the receptor, the ligand, and the solvating water all play a large role in determining the ΔG of binding.

Flexibility is difficult to deal with because it substantially increases the search space, and because there are currently no easy ways to accurately assess the energy of receptor and ligand re-organisation (*i.e.* the energy required to move from the unbound native state to the complexed state, including desolvation and entropy terms) [176]. Further, it is unlikely that a one-size-fits-all approach to treating flexibility in a receptor is possible using current docking methods. Under the induced-fit paradigm of ligand-receptor interaction, the holo- and apo- forms of the receptor are

unique. The native holo-form is converted to the apo-form upon binding of the ligand [176]. KMO may be an example of this, in that all current crystal structures without a bound ligand contain a phenylalanine occupying the binding site. In order to bind, the ligand must move the phenylalanine out of the way, which in turn causes a large movement in an adjacent helix² [126]. Alternatively, evidence exists for another paradigm known as conformational polymorphism [177-179], whereby the unbound receptor exists as an ensemble of structures in equilibrium, and the binding of a ligand to one of these structures shifts the equilibrium of the ensemble (*i.e.* a conformation of the receptor exists that naturally complements the ligand's shape as part of the equilibrium, and the ligand binds to this conformation) [180-183]. It is likely that many proteins exist somewhere on the spectrum between the different paradigms [184]. More complicating still, different stages of binding may exist, where the ligand binds to form an initial complex that undergoes a slower re-arrangement to a more favourable receptor-ligand complex. Therefore, not only is the affinity of the ligand to the initial receptor conformation a factor, but also the energy surface of the subsequent re-arrangement [185-187]. Clearly then, in a docking system where the receptor backbone is held rigid, it is less likely that a correct pose can be obtained when the receptor's starting conformation is significantly different from that of the bound form.

Different approaches may be taken during docking with regards to receptor flexibility. FlexE, for example, attempts to automatically produce ensembles of receptor structures during the docking run, creating a unified receptor structure generated from several input structures [188, 189]. Alternatively, docking may be performed on a range of receptor structures, and in this case can be program independent – the user need only start the docking experiment for each structure [176, 190]. The question then becomes whether to rank the results based on all of the receptor-ligand complexes, or just the best one(s) [191]. A number of hybrid methodologies also exist, where both docking and molecular dynamics are performed (*e.g.* [192, 193]). For example, during candidature, the docking of naphthoquinones to IDO1 was followed by low-mode molecular dynamics simulations [194] and allowed for the visualisation of differences of conformations between interacting residues [195] (Section 7.1). This methodology was not appropriate for a high throughput screen of KMO inhibitors due to its much greater computational cost compared to a traditional docking method, but may be more useful during structure-optimisation work.

How docking works in MOE

Specifically within MOE (the software used in this thesis), docking works by creating a library of conformations for each small molecule and then placing each within the defined binding site of

² It is for this reason that cross-docking is currently impossible in KMO, as there is only a single crystal structure capable of accepting a ligand into its active site.

the receptor in random orientations (using rotations and translations) [196]. This occurs thousands of times to adequately sample the possible combinations between ligand and receptor. These initial poses may then be taken directly, or energy minimised according to the force field. During energy minimisation, the receptor may be held rigid or allowed to flex, to simulate an induced fit. There is no limit to the number of atoms that may be defined as flexible or rigid, although most methods keep backbone atoms rigid [196]. The energy minimisation process itself entails that small perturbations in space are applied to the atoms of the ligand and receptor, the energy of the system is then calculated based on this new conformation. If it is lower it is retained, otherwise it is rejected and the previous conformation is retained. This occurs iteratively until no further improvements can be made to the conformation, or until a preset iteration limit is reached.

3.2. Results

3.2.1. Generating a KMO pharmacophore

At the initiation of this Ph.D. study, no KMO crystal structure was available. Therefore, the SAR of KMO inhibitors, reviewed in Chapter 2, was used to guide the identification of a likely pharmacophore. As all ligands bind to the same receptor (presumably in the same place), they should be able to achieve conformations with a very similar alignment of functional groups in space. This common pharmacophore should equate to the complement of the KMO binding site. This pharmacophore was then investigated for its ability to rationalise other reported inhibitors. After the release of the crystal structure, it was also rationalised within the KMO binding site [126]. The three molecules used (a sulfonamide, an oxobutanoic acid and an oxopropanitrile, all with nanomolar IC_{50} s) are shown in Figure 3.3 [46, 139, 149]. Although the pyrimidine class of inhibitors has since been reported with nanomolar IC_{50} s, this information was not available at the time. The sulfonamides, oxobutanoic acids and pyrimidines have been reported as competitive inhibitors of L-Kyn, indicating that binding is occurring at the same site for all molecules (the oxopropanitrile series has not had its mode of binding reported, but was assumed to be an active site ligand) [46, 49, 139].

A conformational library was generated of each of the three molecules, and individual conformations from each molecule were superimposed in space by MOE so as to maximise their pharmacophoric overlap. Shown in Figure 3.3 is the alignment with greatest overlap obtained. The oxopropanitrile is shown with green carbons, the sulfonamide with fuchsia carbons and the 4-oxobutanoic acid with grey carbons. F2:Aro and its vector, F6:PiN, describes the benzene ring of the substrate-analogous 4-aryl-4-oxobutanoic acid, and thus of substrate L-kynurenine, and

therefore must interact with FAD (as the physical site of benzene hydroxylation (Section 2.1)). As the site of action for catalysis, this feature was considered to be obligatory for high affinity binding to KMO. F1:Acc and its vector, F7:Acc2, is common to all three (Figure 3.3). This corresponds to the carboxylate of the oxobutanoic acids, and has been shown to be obligatory for inhibition [139]. In the same study, the amino group (occupying F3:Don in the oxobutanoic acid molecule, Figure 3.3) was replaced with a proton and suffered only a 10-fold loss of inhibition, indicating that whilst not obligatory, such a group is advantageous to binding. F5:Aro is not satisfied by the oxobutanoic acid, because it has no such second aromatic ring to do so, and thus was considered as advantageous, but not obligatory, in the same way as F3:Don. F4:Aro|Hyd (aromatic or hydrophobic) is satisfied by heteroaromatic rings of the oxopropanitrile and sulfonamide, and the carbonyl carbon of the butanoic acid. This perhaps describes a preference for sp^2 structures to link the obligatory F1:Acc and F2:Aro regions. As a final step, the Van der Waals surface from the overlaid molecules was expanded by 1.5 Å in all directions to create an inclusion volume as an approximation to the active site size and shape (Figure 3.4).

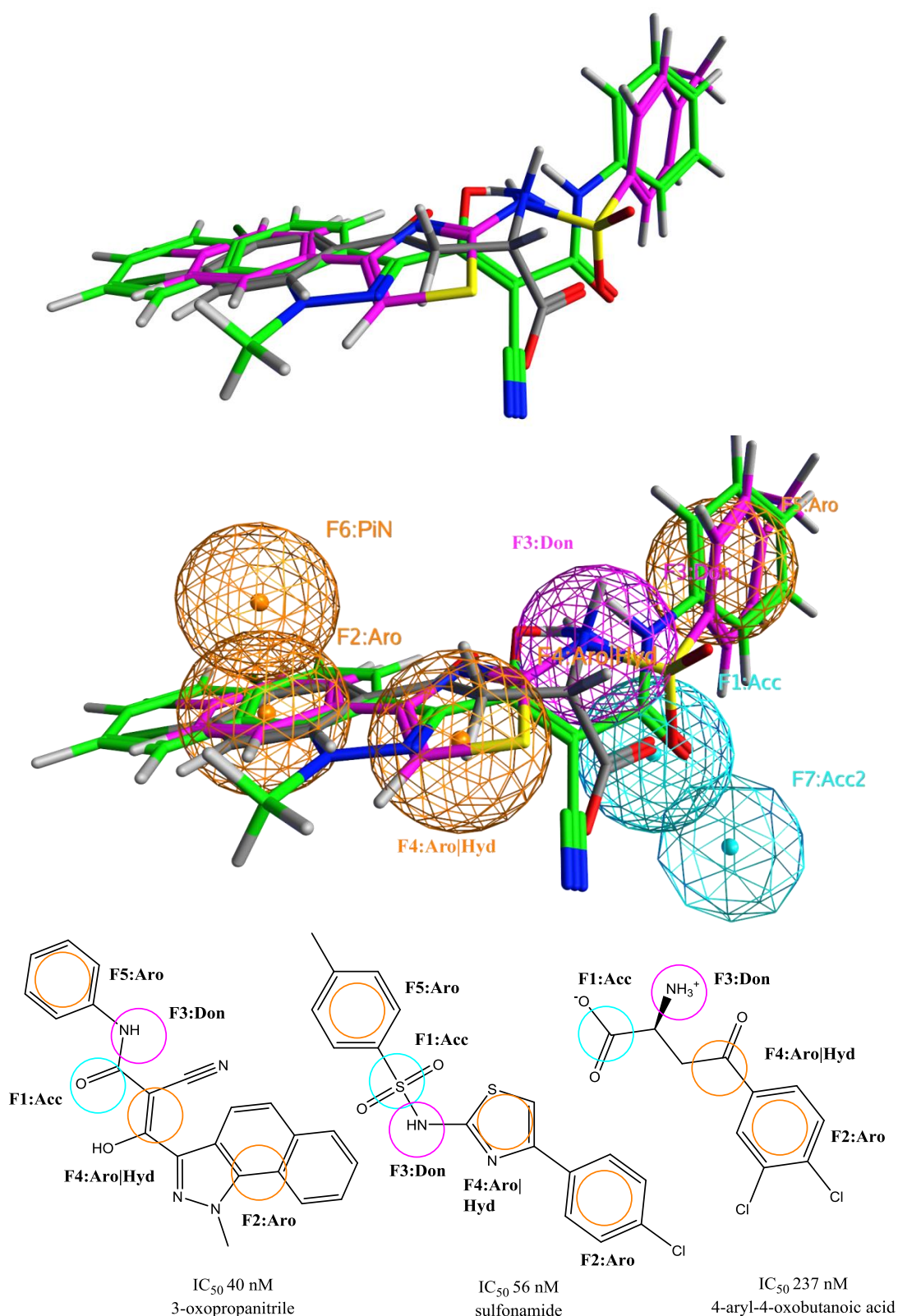


Figure 3.3. Upper: Nanomolar KMO inhibitors aligned in three dimensional space to provide maximum overlap of their pharmacophoric features. **Middle:** The molecular alignment along with the pharmacophoric features used to search the database. **Lower:** Two dimensional representation of pharmacophore and inhibitor structure. IC₅₀ values are for rat liver mitochondrial KMO [46, 139, 149].

3.2.2. Assessing the pharmacophore against known compounds

The pharmacophore was used to qualitatively assess 108 known KMO inhibitors using the sulfonamide, pyrimidine, oxobutanoic acid and pyrroloquinonline scaffolds and the oxopropanitrile and ianthellamide molecules (Section 2.4 [46, 47, 139-142, 144, 150, 151]). Approximately two-thirds of these molecules had only been reported as percent inhibition at 10 μ M, making it impossible to meaningfully compare pharmacophore fit and inhibitor potency, especially as the pharmacophore was created from molecules with nanomolar IC_{50} s. Some of the 108 molecules do not contain a second aromatic feature, and cannot satisfy the full pharmacophore, but were able to satisfy the expected subset of features. However, some of the sulfonamides, which did contain all features found in the pharmacophore, did not satisfy the pharmacophore. Upon inspection, these molecules failed because they were too large to fit within inclusion volume generated during the pharmacophore generation stage. When this volume was increased by 20%, all molecules were able to satisfy the pharmacophore. An example of this is shown in Figure 3.4. Representative molecules are presented in Figure 3.5 for how these molecules fit with the pharmacophore.

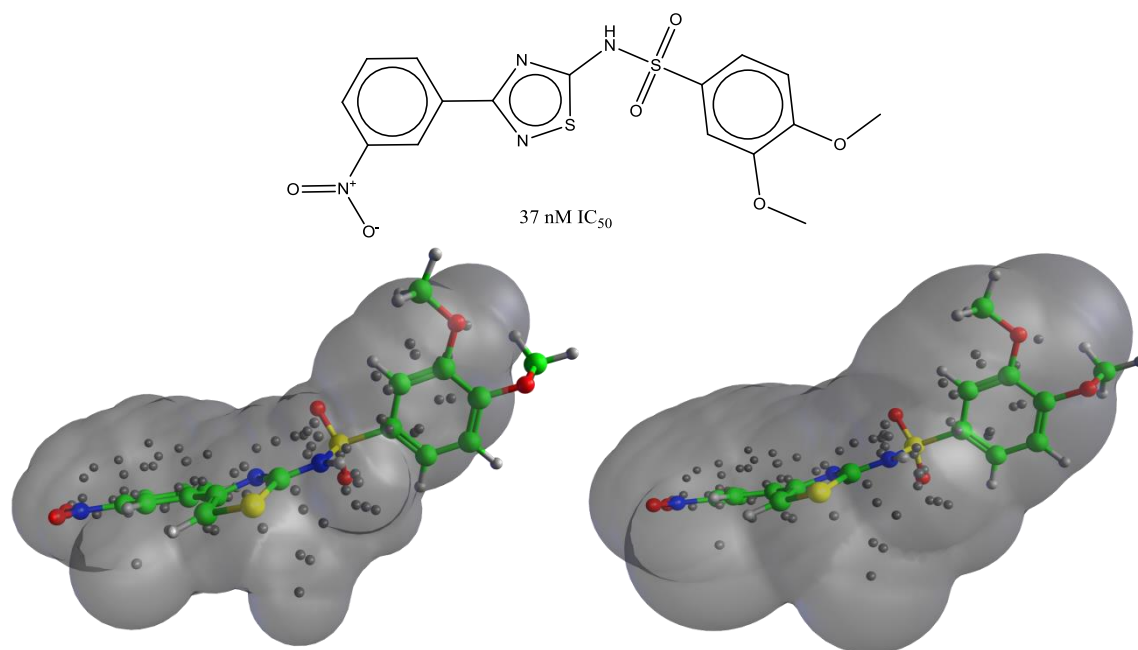


Figure 3.4. The grey surface on the left is the inclusion volume obtained from the initial pharmacophore generation, with one of the methoxy groups outside the inclusion volume. On the right is the increased volume used during screening [46]. Hydrogens are not counted as heavy atoms, and so are allowed to extend beyond the surface.

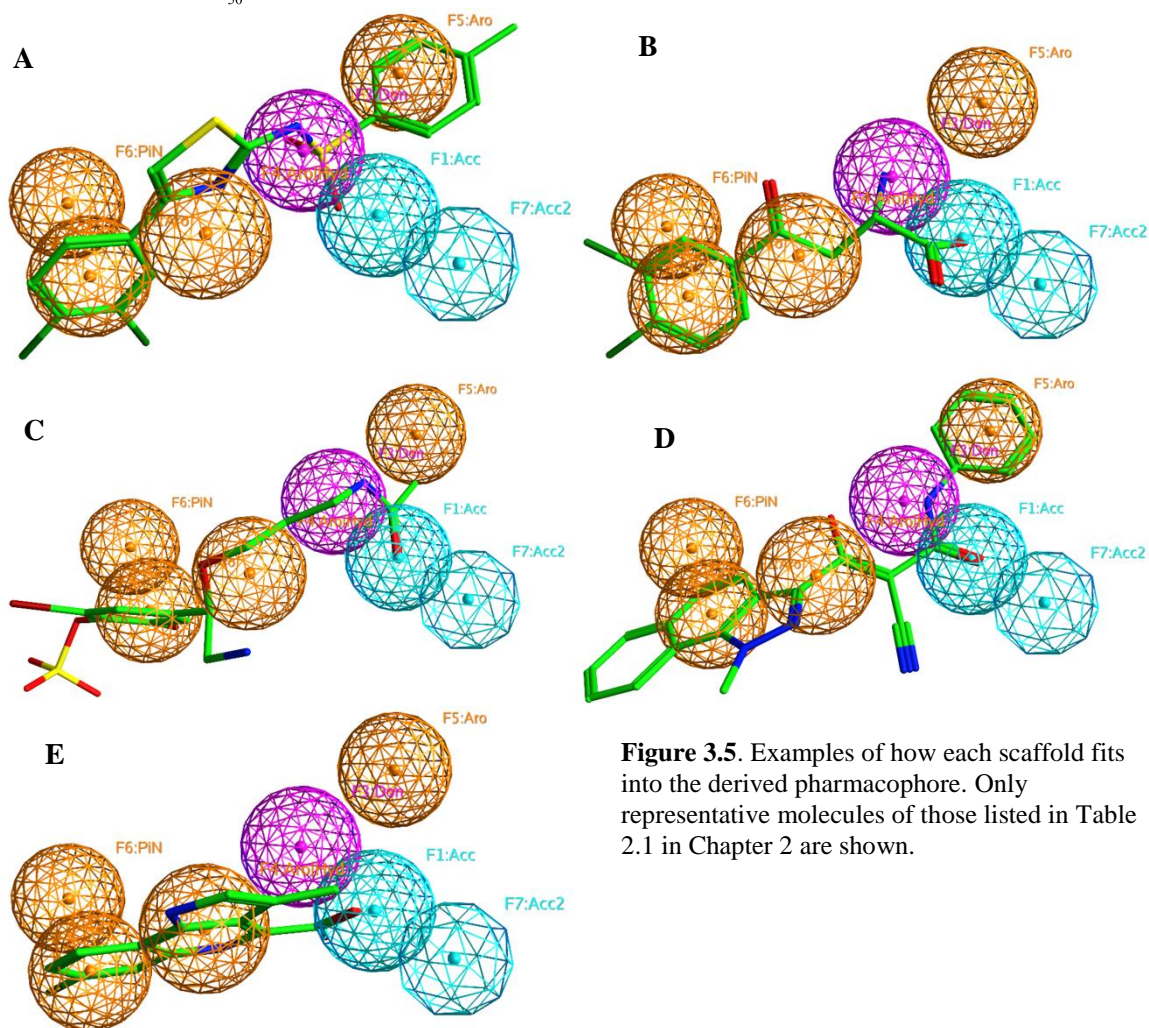
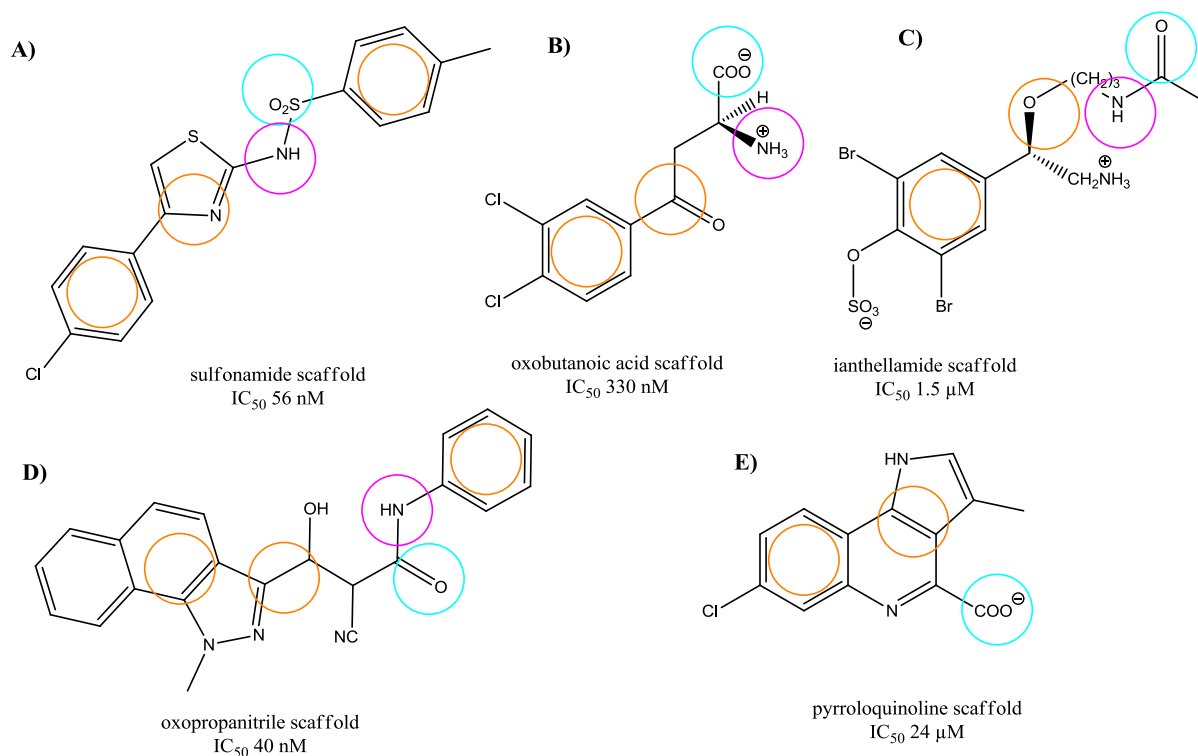


Figure 3.5. Examples of how each scaffold fits into the derived pharmacophore. Only representative molecules of those listed in Table 2.1 in Chapter 2 are shown.

3.2.3. Linear regression of RMSD

A linear regression between the results of the pharmacophore and literature IC_{50} values was performed. A conformer database was created using 39 molecules for which there was IC_{50} data (see appendix to Chapter 3). Both the sulfonamides (15 molecules) and the oxobutanoic acids (19 molecules) span ~ 2 log units of inhibition each. Four additional pyrroloquinolines with IC_{50} data were reported and were used, as was the ianthellamide molecule (no further IC_{50} data was available at this time) [46, 139, 148, 150]. The three molecules used to create the pharmacophore (Figure 3.3) were not used to generate the linear regression, although their data is shown in Figure 3.6. The final spread of activities ranged from \log_{10} (nM) 1.2788 – 4.9868, and their relationship with RMSD to the pharmacophore, including the linear equation, is provided in Figure 3.6. The R^2 value was 0.64. The adjusted R^2 is a measure of correlation independent of sample size and was 0.63. The regression in Figure 3.6 shows a significant, though moderately sized, correlation between the pharmacophore's RMSD output and the literature inhibition values. Figure 3.7 shows a plot of predicted and measured IC_{50} s, with a slope ($\log_{10} IC_{50}$) of 0.63.

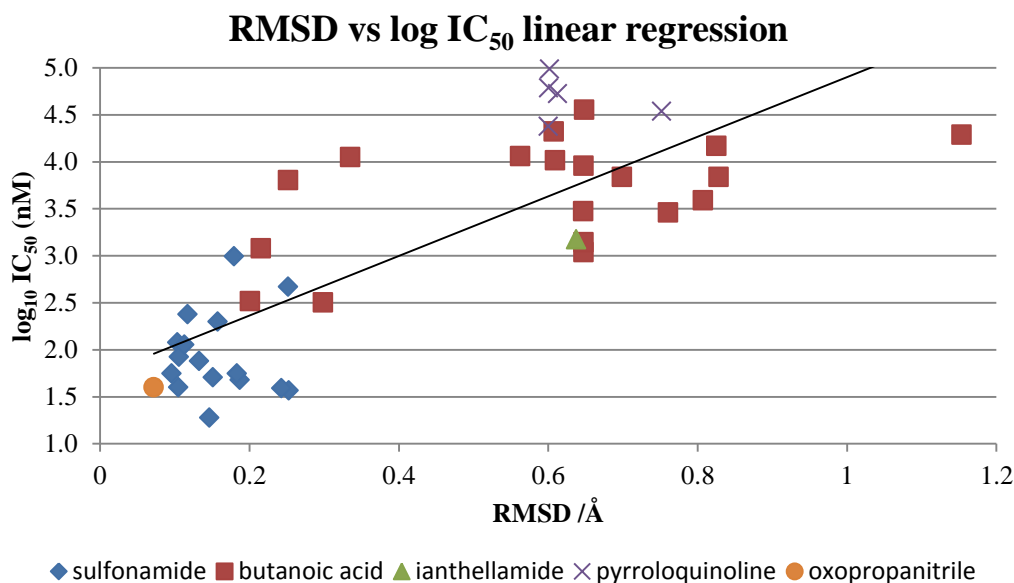


Figure 3.6. Correlation between RMSD from the pharmacophore and measured $\log_{10} IC_{50}$ values. The equation obtained was: $\text{Log}_{10} IC_{50} = 1.73 (\pm 0.39) + 3.17 (\pm 0.77) \cdot \text{RMSD}$, R^2 0.64, R^2_{adjusted} 0.63, $n = 39$, where numbers in parentheses indicate the 95% confidence interval of each coefficient.

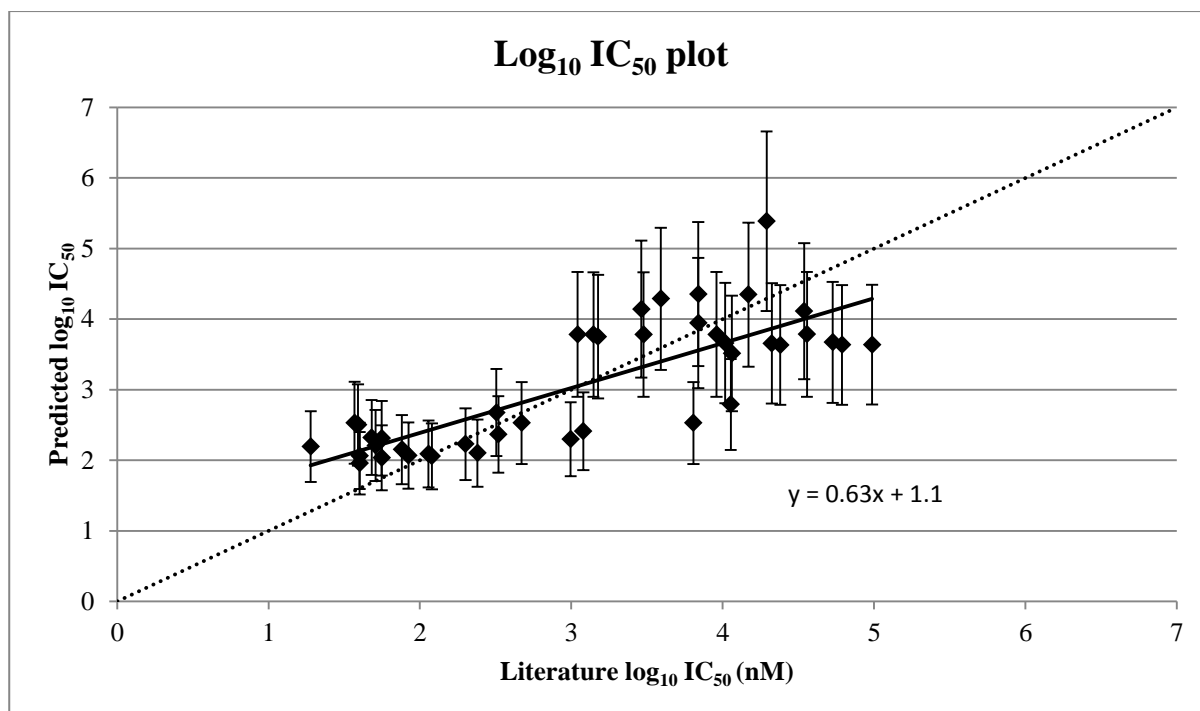


Figure 3.7. Plot of predicted and literature $\log_{10} \text{IC}_{50}$ values, with a dotted line of $y = x$. The slope is less than 1, indicating a tendency to under-estimate the inhibition activity of good inhibitors and over-estimate the inhibition by poor ones. The R^2 is 0.64.

Statistical tests on the linear correlation

A randomisation test was performed such that RMSD data was randomly re-assigned to different molecules for a total of fifty new models. The 99% confidence interval for these R^2 values was 0.02 ± 0.01 , with the highest observed being 0.17, and demonstrated that the chance of finding a model with as good an R^2 value randomly was $<1\%$ [197]. A leave-one-out analysis was also performed to test the coefficients of the linear regression. This was performed such that one molecule of the 39 was removed from the data set, leaving 38. These 38 were then used to create a new regression and predict the activity of the 39th molecule. This was performed systematically for all 39 molecules. The goodness-of-fit between these 39 predicted values and the measured values (q^2) was 0.60, and the coefficients of each of these 39 models fell within the 95% confidence intervals for the original regression equation. Outlier molecules were also searched for by investigating the residuals (the difference between the measured inhibition and the predicted inhibition from each of the 39 models). All residuals were within 2.2 standard deviations of the mean of the residuals, *i.e.* they were all within the predicted 95% confidence interval for residuals. Therefore, no individual molecule appeared to be an outlier with respect to the other molecules, and each model created fell within the 95% confidence interval of the initial model.

ROC analysis

Receiver-operator characteristic curve are a method of visualising the rate at which an enrichment method, such as virtual screening, identifies true positives, versus the rate at which it

identifies false positives. First, the database of compounds is ranked based on their *in silico* score (in this case, the RMSD to the pharmacophore), and at each data point a count is taken as to the number of true positives and false negatives identified to that point [198, 199]. A plot is then created by dividing the true positive count by the total number of positives in the database (y-axis), and then also the number of false positives divided by the number of negatives (x-axis). A resulting curve that lies on the line of $x = y$ is equivalent to random chance, meaning that the *in silico* method is no better at identifying compounds than a coin. A curve that lies significantly to the left of $x = y$, means that the method is selecting for true positives faster than it is searching for false positives. The global enrichment achieved is calculated from the area under the curve (AUC), and is interpreted as the probability associated that a given active molecule will score better than an active one. For the random case, where $x = y$, the AUC is 0.5, with higher numbers meaning higher global enrichment. Figure 3.8 shows the ROC curve produced from the pharmacophore, using KMO compounds with IC_{50} data at the time of model generation. A true positive was defined as a molecule with a both a measured and predicted IC_{50} of 200 μ M or less, and a false positive was defined as a molecule with a predicted IC_{50} of 200 μ M or less, but a measured IC_{50} higher. The ROC curve (diamonds) lies significantly to the left of the $x = y$ line, and the AUC is 0.7. It should be noted that the predictive error (the level of confidence one can have that a retrospective screen can predict future screening performance) is directly proportional to the size of the dataset being used [199]. This is a small dataset of ~40 molecules, and validation is normally performed on dataset containing hundreds, or preferably thousands, of molecules tested against the target. With such a small dataset to work on in KMO, the use of a ROC curve to validate the predictiveness of the pharmacophore is tenuous at best.

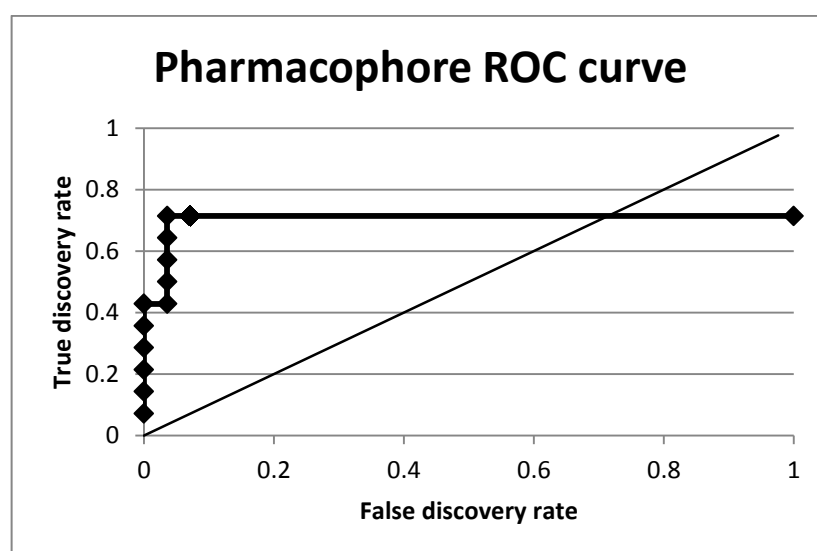


Figure 3.8. ROC curve of enrichment due to the pharmacophore. The area under the curve was calculated as 0.7, which means that a given molecule has a 70% chance of obtaining a better RMSD compared to inactive compounds. In this work, an active was defined as an IC_{50} of 200 μ M or less.

3.2.4. Agreement between the pharmacophore and the yeast crystal structure

A yeast KMO crystal structure was released soon after the pharmacophores presented above [126]. This allowed for the comparison of the pharmacophore with active site structure, without foreknowledge having biased the pharmacophore generation stage. Figure 3.9 shows the manual alignment of the pharmacophore within the crystallised KMO binding site. The feature F2:Aro corresponds well to the FAD interacting benzene ring as predicted. The F4:Aro|Hyd feature sits in a narrowing section of the active site, which is consistent with its apparent preferences for aromatic rings and the sp^2 carbonyl group of oxobutanoic acids. The F1:Acc group aligns with the carboxylate group of the kynurenine mimic co-crystallised with KMO. The F3:Don feature sits over the top of the cyclopropane ring, which is an amino group in the substrate kynurenine. Lastly, the F5:Aro sits just outside the active site, near a flexible loop and bulk solvent, and implicates this portion of the inhibitors in interaction with a dynamic portion of the protein, such as the loop consisting of residues 97-104 (Section 2.3).

The proposed pharmacophore displays a clear qualitative trend (R^2_{Adjusted} 0.63) with inhibitor potency of individual molecules, and possesses substantial geometric consistency with the active site of the crystal structure, allowing for confidence in the notion that it can be meaningfully employed during *in silico* investigations. With the release of the crystal structure at this time, efforts were focused toward gaining further insight concerning the binding of inhibitors to KMO *via* docking methodologies.

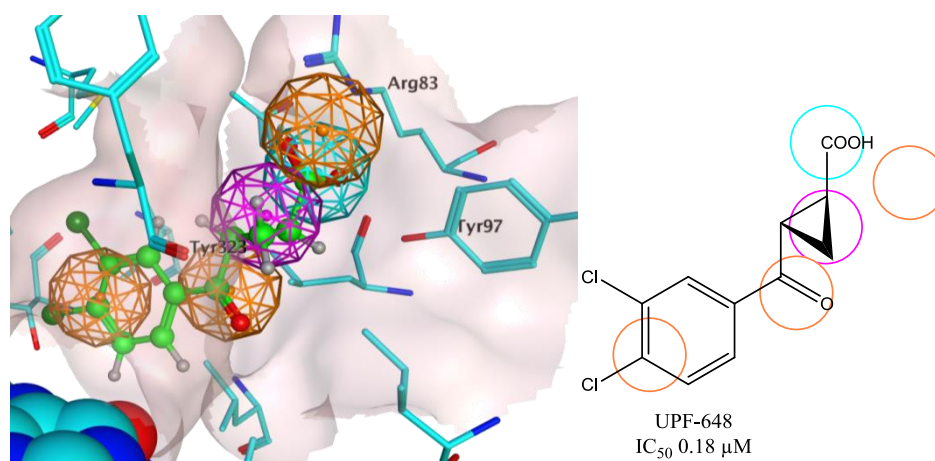


Figure 3.9. Alignment of the pharmacophore (Figure 3.3) within the active site of the yeast KMO crystal structure, 4J36 [126], showing agreement between positioning of the pharmacophore features, and the crystallised inhibitor. The benzene ring of UPF-648 occupies the same space as the aromatic feature, F2:Aro. The perpendicular vector of the benzene ring was also consistent with F6:PiN of the pharmacophore (not shown). The carbonyl oxygen resides in the F4:Aro|Hyd feature, the cyclopropane ring (which replaces an aliphatic amine in the substrate) occupies the F3:Don feature, and the carboxylate occupies the F7:Acc feature. Ligand carbons are shown in green and KMO carbons in cyan. Sulfur, oxygen and nitrogen are shown in yellow, red and blue, respectively.

3.2.5. Docking studies in 4J36

UPF648 and other kynurenine mimetics

Docking was performed on the 4J36 structure of yeast KMO [126]. First, re-docking of the co-crystallised ligand was performed to ensure that the protocol could reproduce the experimental result (Figure 3.10), followed by the docking of other known KMO inhibitors in order to elucidate common binding patterns among the inhibitors. The 4J36 structure contains UPF-648 as a co-crystallised ligand (green atoms, Figure 3.10 A [126]). The crystal structure describes the benzene ring close to the FAD, in proximity to the bridge carbon that hosts the reactive hydroperoxy intermediate during catalysis (Section 2.1). The carboxylate group is interacting with an omega nitrogen of Arg83 and the phenol group of Tyr97. Re-docking the ligand (purple atoms) gives an almost identical result, with some small differences in distances (given in the caption). Substrate L-Kyn was also docked under the same conditions and gave results consistent with UPF-648, placing the reactive site in proximity to FAD (Figure 3.10 B). The amino group of the substrate was in good proximity to the carbonyl oxygen of Tyr323. Similarly, the α -thioether mimics also showed a consistent binding pose, placing the second ring structure outside the active site, into bulk solvent (Figure 3.10 C) [142].

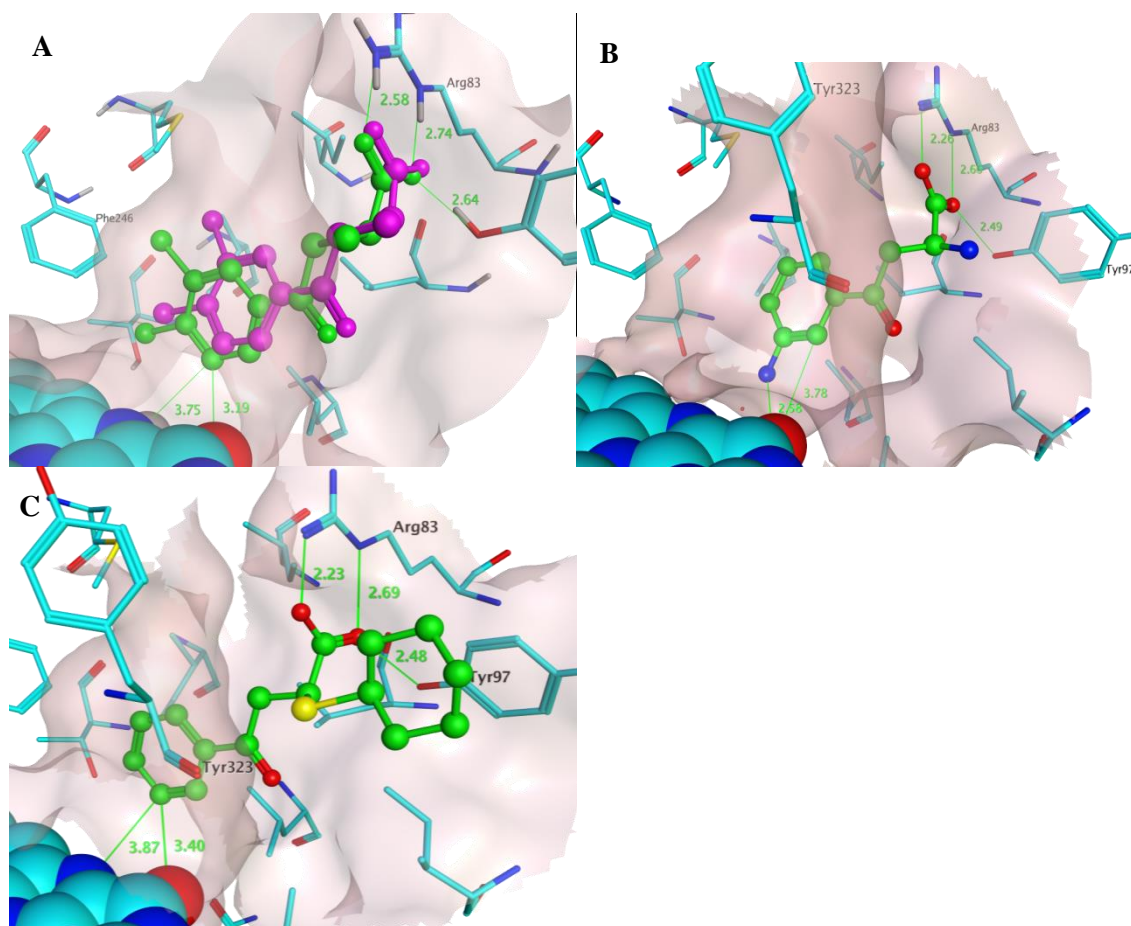


Figure 3.10. **A)** Re-docking of UPF-648 into KMO (PDB: 4J36) was able to reproduce the original pose to an RMSD of 0.8 Å. Distances, in angstroms, are shown in green for the co-crystallised molecule. Those distances become 3.75→3.94, 3.19→3.36, 2.58→2.53, 2.74→2.65, 2.64→2.77 for the docked UPF-648. **B)** Docked pose of substrate L-kynurenine. **C)** An α -thioether example of a 4-aryl-4-oxo-butanoic acid inhibitor (20% inhibition at 10 μ M [142]) showing a similar pose to that of the more potent UPF-648 (IC_{50} 0.18 [46]). Ligand carbons are shown in green and KMO carbons in cyan. Sulfur, oxygen and nitrogen are shown in yellow, red and blue, respectively.

Docking non-oxobutanoic acid inhibitors

Consistent with the sulfonamide moiety being a popular bioisostere of amino acids, the KMO sulfonamide inhibitors [46] docked in an essentially identical manner to that of the substrate analogues, with the sulfonyl oxygens also finding interactions with Arg83 and Tyr97 (Figure 3.11 **A**). The dimethoxy benzene group was placed outside the active site. This group was not in any direct contact with any other residues, but was pointing towards a loop that is open in the 4J36 structure and closed in the 4J34 structure (Section 2.3). It was found for the pyrimidine class of molecules [49] that N1 donates its lone pair to the Arg83 interaction, while one of the carboxyl oxygens takes the remaining Arg83 and Tyr97 position (Figure 3.11 **B**). The replacement of the carboxylate in this molecule with a tetrazole (Figure 3.11 **C**) decreased the IC_{50} by 10-fold [49]. Docking showed a larger distance between Arg83 and the isosteric tetrazole and a loss of interaction with the phenolic group of Tyr97. Interestingly, both the pyrimidine carboxylate and the pyridine carboxylate (Figure 3.11 **B** vs. **D**), see a good distance between the oxygens and

Arg83 and Tyr97, albeit with slightly worse distances to FAD. This single nitrogen to carbon change resulted in a 100-fold decrease in IC_{50} [49]. Docking of the two pyrroloquinolines (Figure 3.11 E and F, 24 vs 61.4 μ M [148]) showed reduced interactions between FAD and benzene carbons, that may in part explain the reduction in potency.

For oxopropanitrile, only poses where the naphthalene ring was present inside the active site, maximising the FAD interaction surface, are presented. A single bond rotation was found to yield either the hydroxyl group or the nitrile group in proximity to Arg83. Presumably, the oxygen possesses a better interaction energy due to being a more electronegative atoms and having a better geometry with respect to its lone-pair of electrons, however, these docking experiments do not contain sufficient information to answer such questions (Figure 3.12, A and B).

The marine natural product, ianthellamide A, possesses a unique structure compared to other KMO inhibitors [150]. The mode of inhibition is unknown at this time, but it has been shown to inhibit the hydroxylation of L-Kyn to 3-hydroxy-L-kynurenine in homogenised rat liver tissue and in live rats [150]. This unique structure was highlighted in the docking results, where no pose was found that placed both the aromatic ring in proximity to the FAD, and an acceptor close to the Arg83. Instead, a pose was found where the sulfonyl ester was able to have interactions with Arg83, with an aliphatic amine hydrogen bonded to the carbonyl of FAD (Figure 3.12, C). In this pose the aliphatic tail occupied the same space as a helix in structure 4J34, which is displaced in the 4J36 structure used for docking. (Section 2.3). An alternative pose was to have this aliphatic tail exiting the active site into bulk solvent, although the same interactions were seen with regards to Arg83 and the FAD (Figure 3.12, D). Based on this, ianthellamide A appears to exploit a novel interaction fingerprint compared to other molecules and is worth investigating from an SAR perspective in the future.

Based on the observations from docking, a common fingerprint identified among KMO inhibiting molecules was interaction between FAD and an aromatic ring, and interaction between a carboxyl or isostere with Arg83 and Tyr97. The notable exception to this was the natural product, ianthellamide A, which may forgo the aromatic FAD interaction in favour of a hydrogen bonding interaction with the FAD carbonyl oxygen. Final compound selection therefore focused on molecules that could give short distances between a benzene ring and FAD, and oxygen-centred interactions with Arg83. An extra aromatic feature outside the active site would be advantageous.

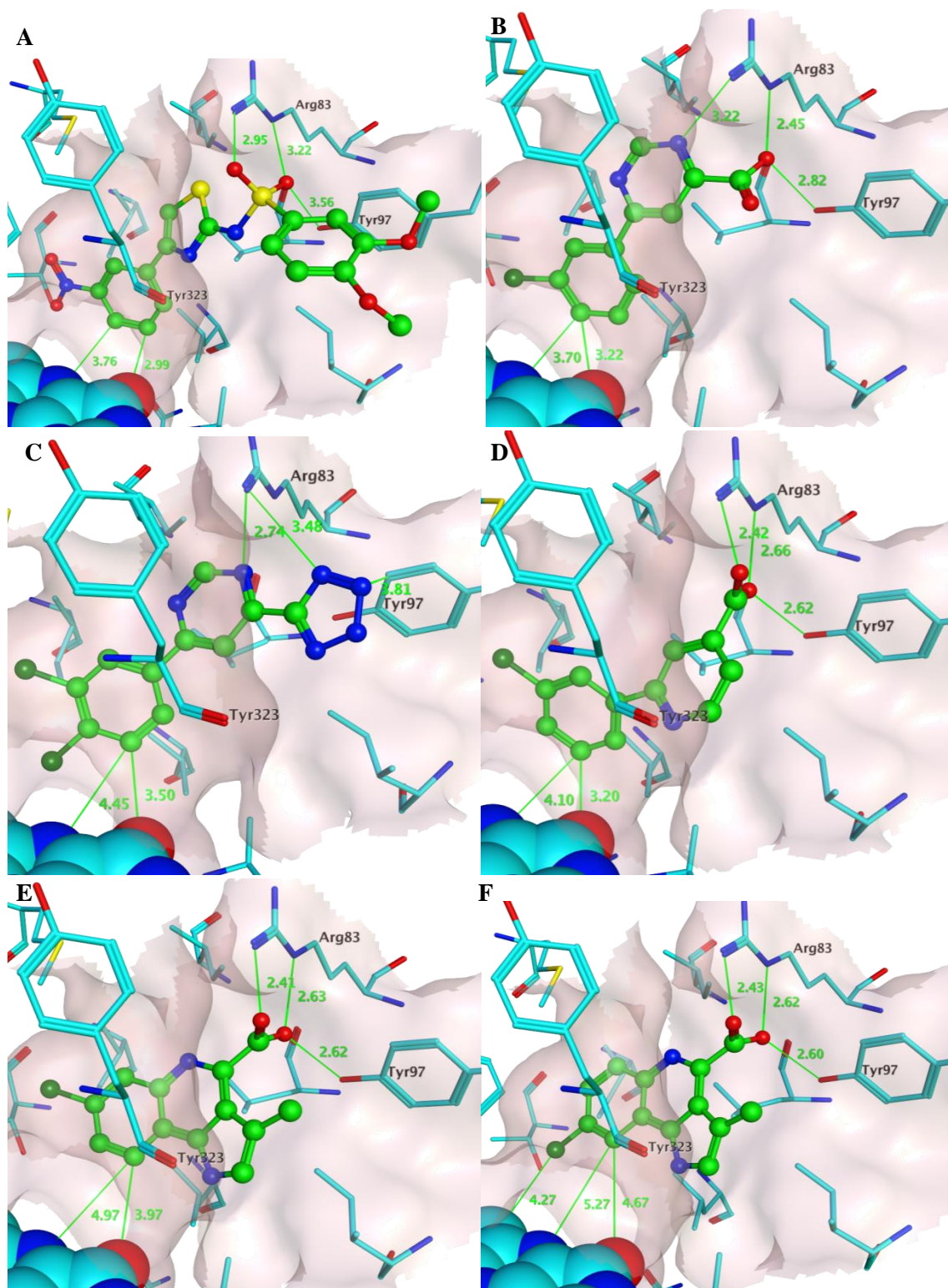


Figure 3.11. Example docked poses (A – F) from each scaffold of KMO inhibitor in the yeast crystal 4J36 [46, 49, 126, 148]. Ligand carbons are shown in green and KMO carbons in cyan. Sulfur, oxygen and nitrogen are shown in yellow, red and blue, respectively. Distance measurements are in angstroms. In light pink shading is the van der Waals surface of the active site.

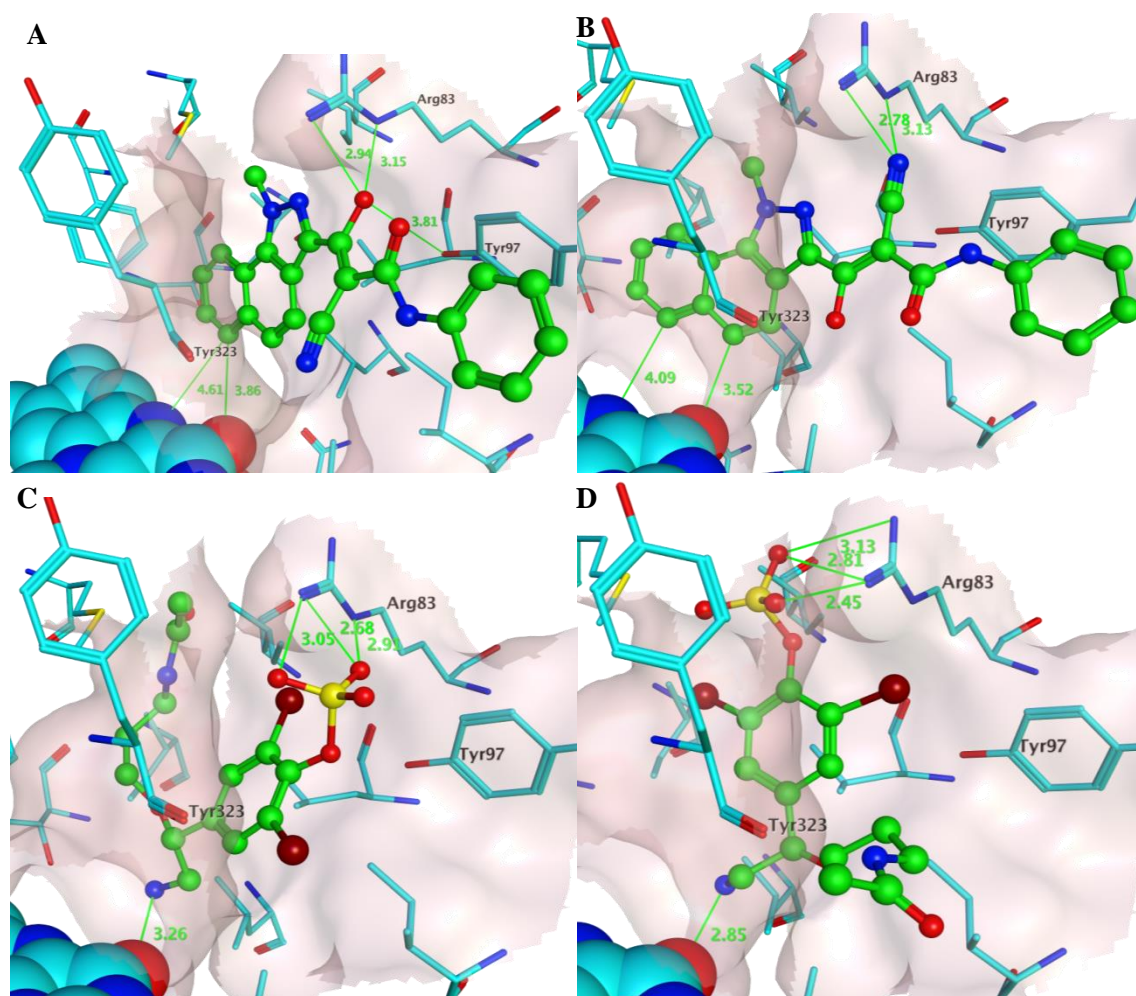


Figure 3.12. Proposed binding of oxopropanitrile (A and B) and ianthellamide A (C and D) molecules within the yeast structure of 4J36. Ligand carbons are shown in green and KMO carbons in cyan. Sulfur, oxygen and nitrogen are shown in yellow, red and blue, respectively. Distance measurements are in angstroms. In light pink shading is the van der Waals surface of the active site.

3.2.6. Using the models: *in silico* screening for KMO inhibitors

420,000 compounds from the Aldrich Market Select catalogue (First quarter, 2013. Sigma-Aldrich) were screened using the pharmacophore presented in Figure 3.5. This yielded approximately 100,000 hit molecules. The SMARTS [200] structural query language was then used to select those compounds containing groups identified through docking as interacting with Arg83 (shown in Figure 3.13). From each of these five subsets, 2000 molecules with the lowest RMSD to the pharmacophore were submitted to docking using the GridMin method in MOE. This is a faster, but potentially less accurate method of minimising the energy of the docking poses compared to full-force field docking [196]. Results from this were then ordered based on the distance between a polar atom of the hit compound, and an omega nitrogen of Arg83, as well as distances between the FAD co-factor and an aromatic atom of the ligand. The aggregate of these distances (smaller is better) was then used to rank the poses. This resulted in 63 compounds being manually selected from the results. An additional 20 compounds were manually built. These were built by isosteric

replacement of groups interacting with Arg83 or FAD, using scaffolds from the 63 hit compounds. For example, a molecule with a thiophene interacting with FAD, may have been replaced by one with a benzene ring, instead. This resulted in 83 compounds being selected and investigated by force field docking. From these results, the 83 molecules were again ranked based on their aggregate distances to the FAD and Arg83. The 41 highest ranked molecules, that were also immediately available from suppliers, were purchased for testing. The moieties interacting with Arg83 consisted of 16 molecules with carboxyl groups joined to an aliphatic atom, 8 with carboxyl groups joined to an aromatic atom, 24 containing a sulfonyl group, 9 with carbonyl groups, 2 with phenol groups, 4 with cyano groups, and 20 heteroaromatics (*e.g.* pyrimidines, tetrazoles) not fitting into any of the above categories. Some examples of these compounds are presented in Figure 3.15 and Table 3.1. A complete list of molecules that were tested can be found in the appendix to Chapter 3. Figure 3.16 shows a number of compounds that were desired but were unavailable at the time of purchase. Figure 3.14 shows the selection process as a flow diagram.

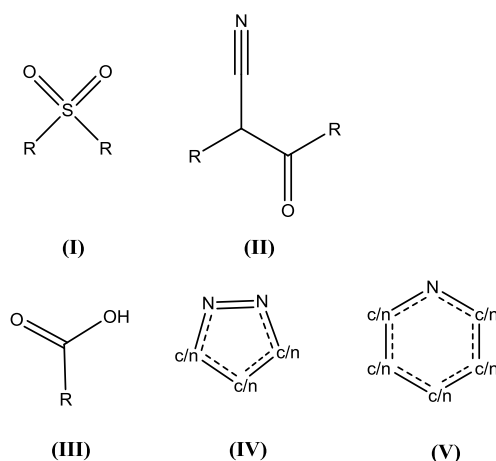


Figure 3.13. The SMARTS query language [200] was used to select initial hits that contained as part of their structures, the drawn functionalities, where “R” was any atom, “a” was any aromatic or sp^2 atom, and “c/n” was any aromatic or sp^2 carbon or nitrogen. Approximately 100, 000 compounds were selected by the pharmacophore roughly split. Of these, the sulfones, group I, accounted for ~8,000, the oxopropanitriles, group II, accounted for ~5, 000, the carboxylates, group III, accounted for ~20, 000, and the heteroaromatics, groups IV and V, accounted for ~ 33, 000 each.

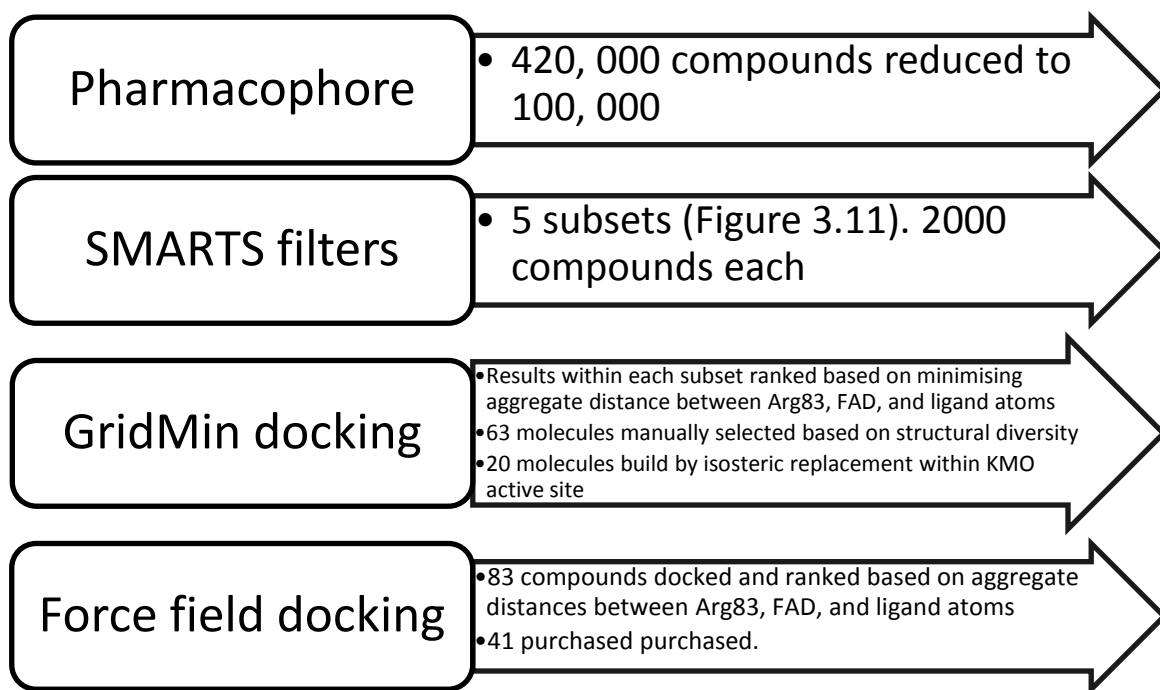


Figure 3.14. Flow diagram for the virtual screening and selection of compounds employed in this work.

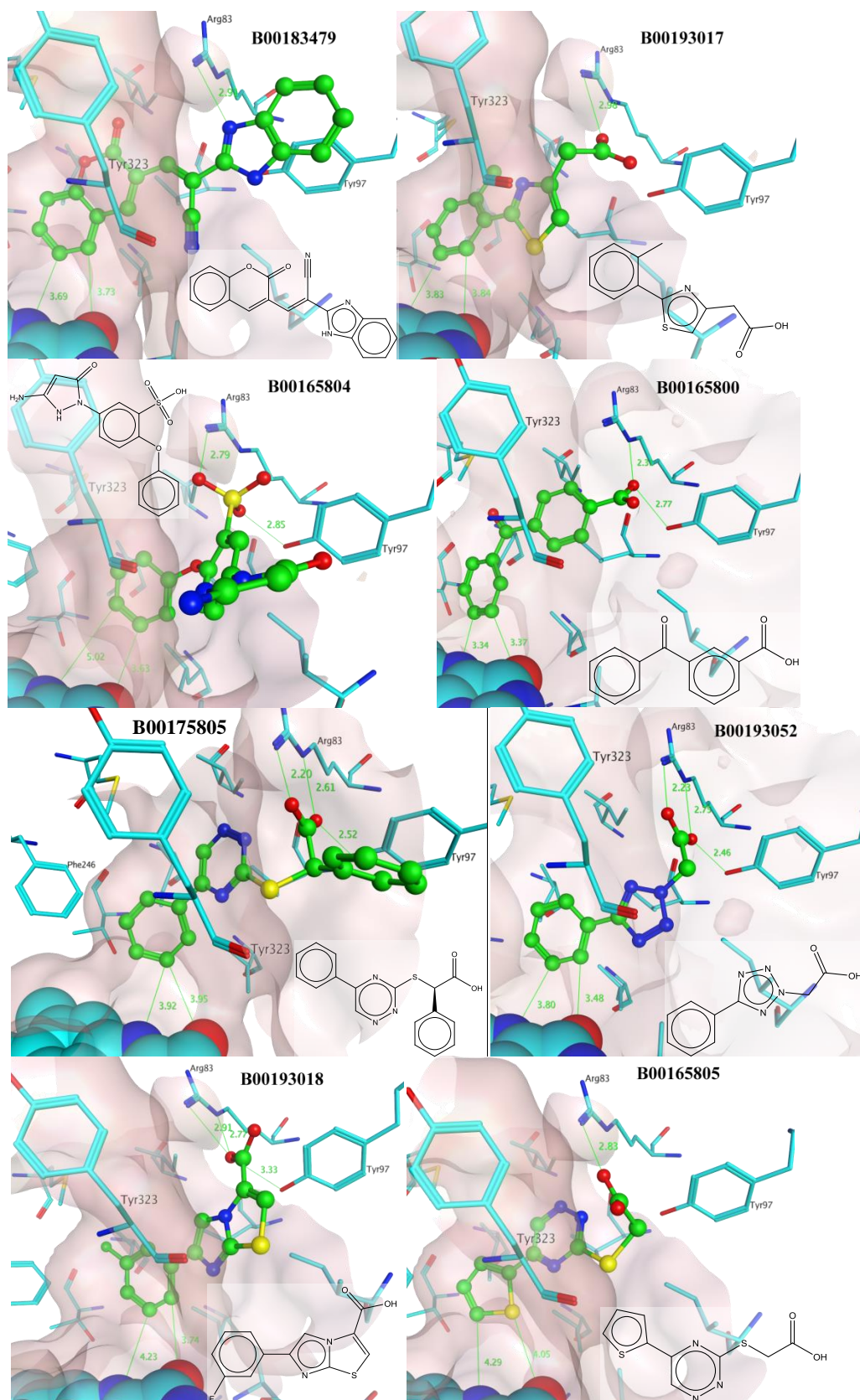


Figure 3.15. Examples of force field-docked hit compounds. Ligand carbons are shown in green and KMO carbons in cyan. Sulfur, oxygen and nitrogen are shown in yellow, red and blue, respectively. Distance measurements are in angstroms. In light pink shading is the van der Waals surface of the active site.

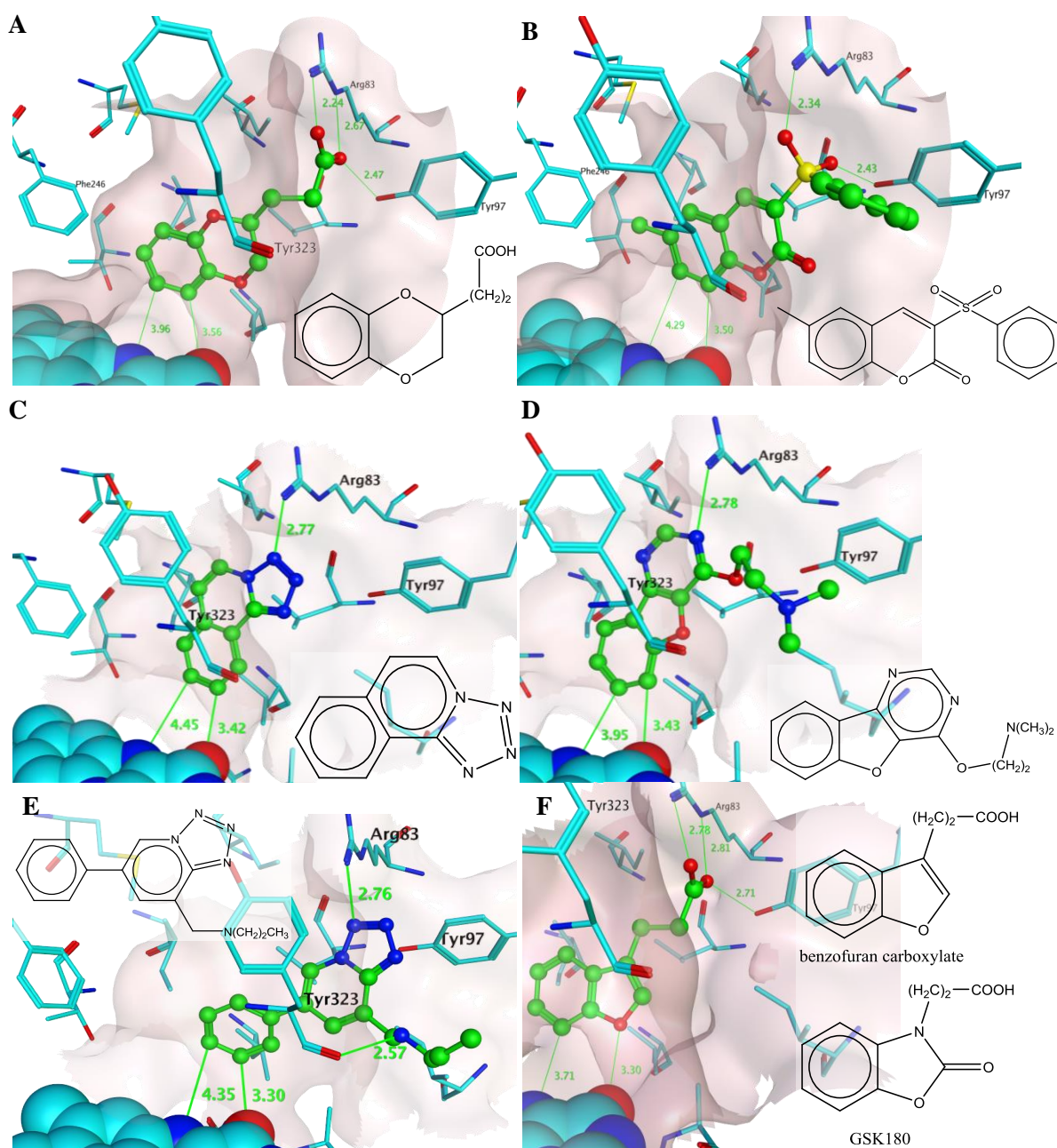


Figure 3.16. *In silico* hits that could not be sourced at the time of purchase. The benzofuran carboxylate (**F**) is particularly interesting as it differs by just a few atoms from GSK180, reported as an inhibitor in the final stages of writing [201].

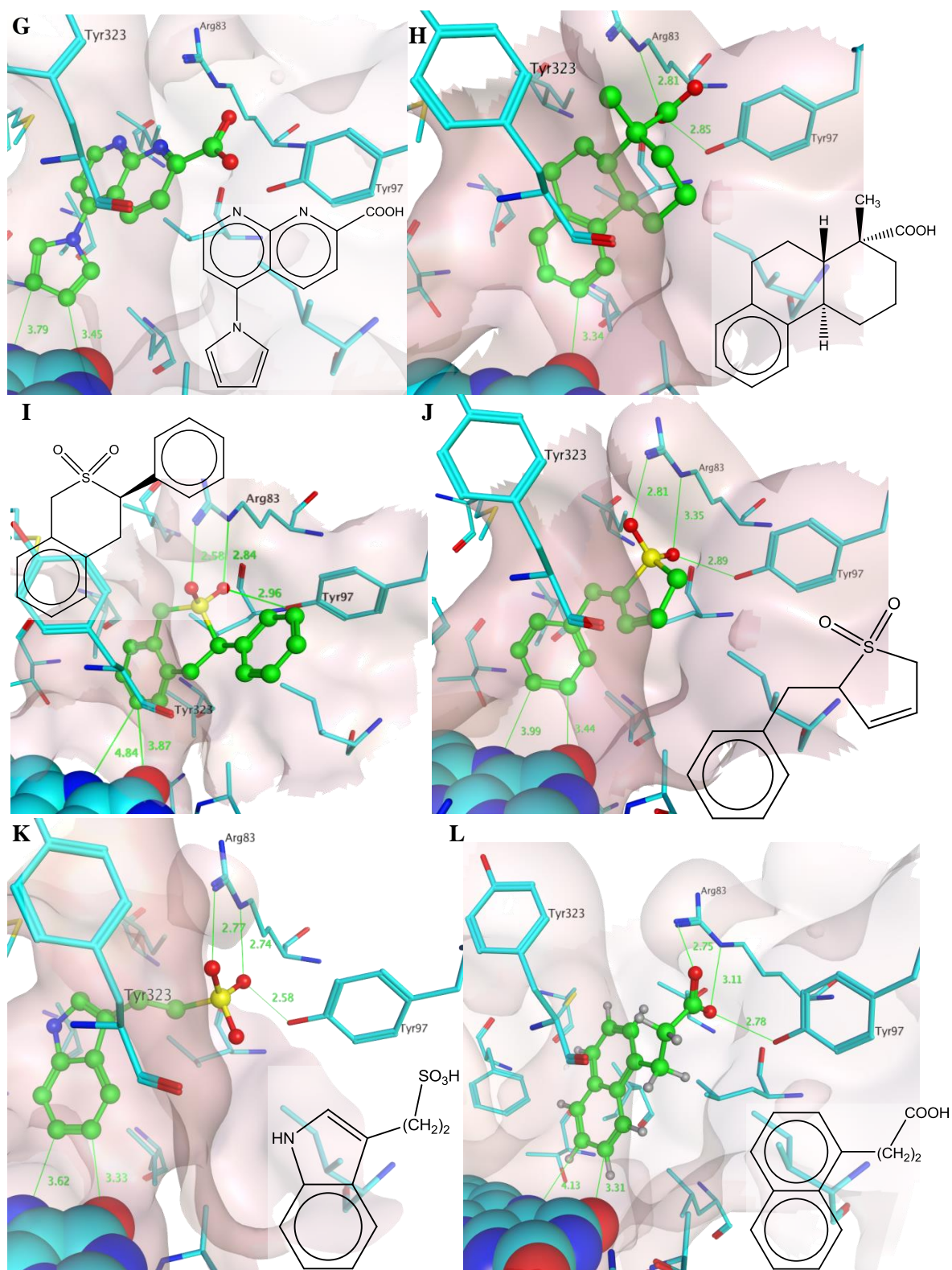


Figure 3.16. Continued from previous page.

3.2.7. In vitro and in vivo results

In vitro and in vivo KMO experiments were conducted by Kelly Jacobs, a Ph.D. candidate supervised by Gilles Guillemin and David Lovejoy, in the Neuroinflammation Group, Faculty of Medicine, Macquarie University, Sydney, Australia. The analyses of in vitro and in vivo KMO data, including the graphs contained in Figure 3.17, were performed by Kelly Jacobs. Section 3.2.7 was written by Jason Smith with input from Kelly Jacobs.

In vitro inhibition testing of the 41 compounds selected in Section 3.2.6 was achieved using recombinant human KMO (sourced commercially from baculovirus infected insect cells, R&D systems, United States, Cat# 8050-KM-25), with HPLC quantification of L-kynurenine loss and 3-hydroxy-L-kynurenine formation. From this, several active compounds were also tested against human embryonic kidney (HEK-293) cells (genetically modified to overexpress human KMO in the Guillemin lab), with quantification also by HPLC. The toxicity of the compounds was assessed by measurement of cell lysis, normalised by the amount of cellular respiration in controls samples. That is, the amount of cell lysis was normalised to the actual amount of cell metabolism, in an effort to control for day-to-day differences in cell numbers and growth rates. Specifically, the amount of cell lysis was assessed by the level of lactate dehydrogenase (LDH) activity in the supernatant. Such activity is only possible if the enzyme has escaped the cell due to lysis, which occurs after cell death. Respiration was followed colourmetrically by the control cells' ability to metabolise the tetrazolium salt of the MTS assay ([3-(4,5-dimethylthiazol-2-yl)-5-(3-carboxymethoxyphenyl)-2-(4-sulfophenyl)-2H-tetrazolium salt, Promega, Australia, Cat #G3580). Therefore, as the ratio of LDH activity to MTS activity increases, the tested compounds can be seen as more toxic *via* an increased amount of cell lysis. All assays were performed by Kelly Jacobs of the Guillemin lab, using commercially sourced kits.

Experiments were ongoing at the time of writing, and only available data is presented. Initial screening was performed at a single concentration of 10 μ M, with subsequent IC₅₀ independent replicates (Figure 3.17 and Table 3.1, with the appendix to Chapter 3 showing the remaining results). Six of these gave IC₅₀ values of <100 μ M (Table 3.1). This is in the expected range of inhibitors for a study of this nature – where diverse scaffolds from different studies and different labs are used to generate models with emphasis on the identification of novel structures, rather than on absolute potency (*e.g.* [117, 157, 163, 164, 202, 203]). Most importantly, the scaffolds, particularly B00165800, B00165805, B00183479 and B00193018 (Figure 3.17), offer novelty compared to current literature.

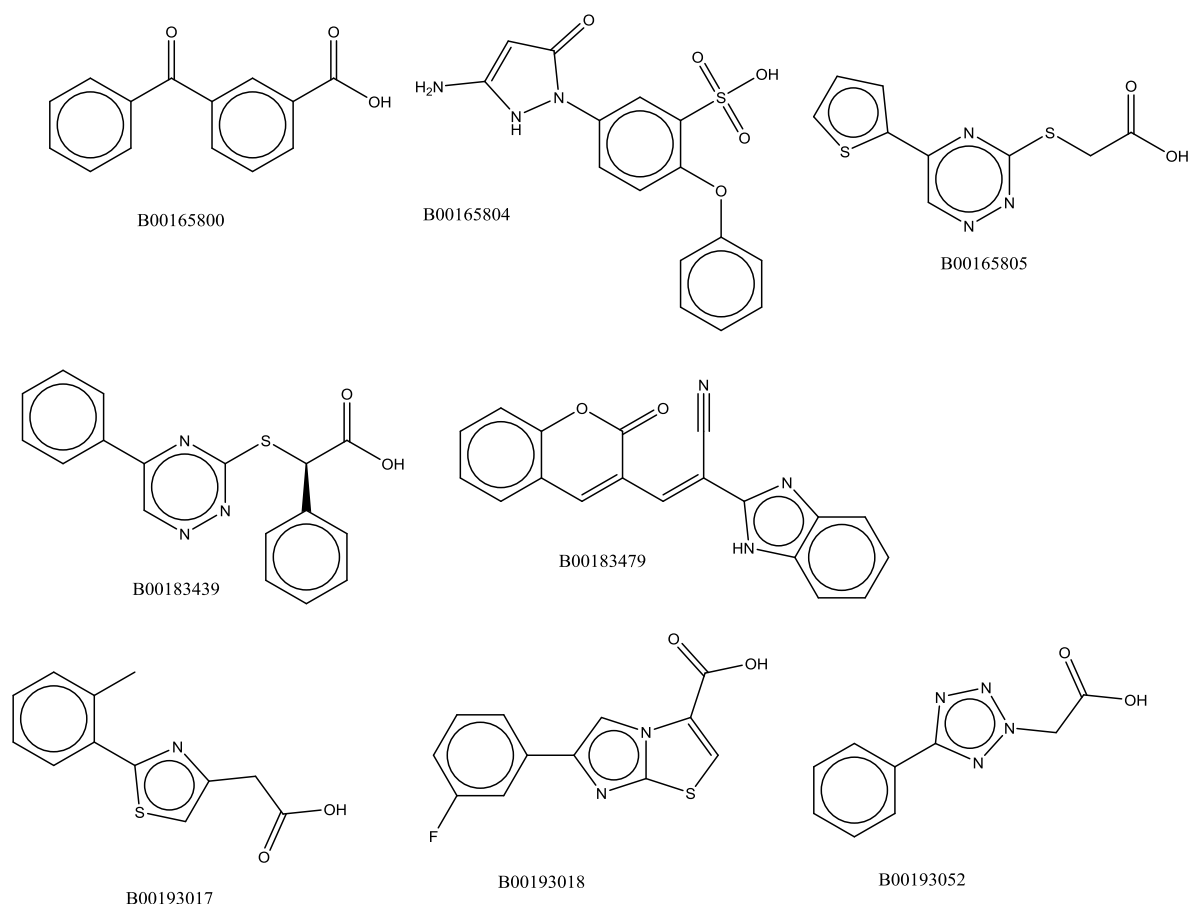


Figure 3.17. The eight compounds selected for IC₅₀ and toxicity studies. Inhibition data can be found in Table 3.1.

Table 3.1. Inhibition values of hit compounds against human recombinant KMO.

Compound	% inhibition at 10 μ M	IC ₅₀ / μ M		EC ₅₀ , HEK-293 cells / μ M
B00183479	45	6.0	NI ^a	19 \pm 2
B00193017	15	19	38	~1000
B00165804	22	38	57	not yet tested
B00165800	23	44	36	~2000
B00183439	24	58	73	270 \pm 2
B00193052	17	73	77	not yet tested
B00193018	8	100	130	~750
B00165805	10	480	520	~5000
RO-61-8048 (Control)	100	4.0	2.9	< 5
UPF-648 (Control)	100	not tested	0.085	not yet tested

^aNo inhibition (NI) due to degradation during storage (DMSO). IC₅₀ values are independent (interday) replicates (dose-response experiments) using isolated recombinant human KMO. Reactions contained 300 μ M L-kynurenine, 0.6 mM NADPH at 37 °C for 30 minutes. Cellular EC₅₀s are the average \pm standard error of three independent experiments.

Toxicity data is presented in Figure 3.18. Three compounds possessed sub-millimolar cellular IC₅₀s, B00183479, B00183439, and B00193018. The ordering of these compounds did not change between the *in vitro* and *in cell* experiments, with IC₅₀s of 6, 60 and 115 μ M vs. 19, 270 and 750 μ M, respectively. All three of these molecules possessed similar toxicity profiles to that of

RO-61-8048, with LDH:MTS ratios of 5 – 10 at 500 μ M. This demonstrates that the molecules have cell penetrating capabilities, but have a poor therapeutic index by virtue of both their moderate inhibition and toxicity levels. B00193017 and B00165800 possessed poor cellular inhibition (IC_{50} s >1 mM) and displayed no significant toxicity, suggesting the compounds are either metabolically unstable or unable to penetrate the cells.

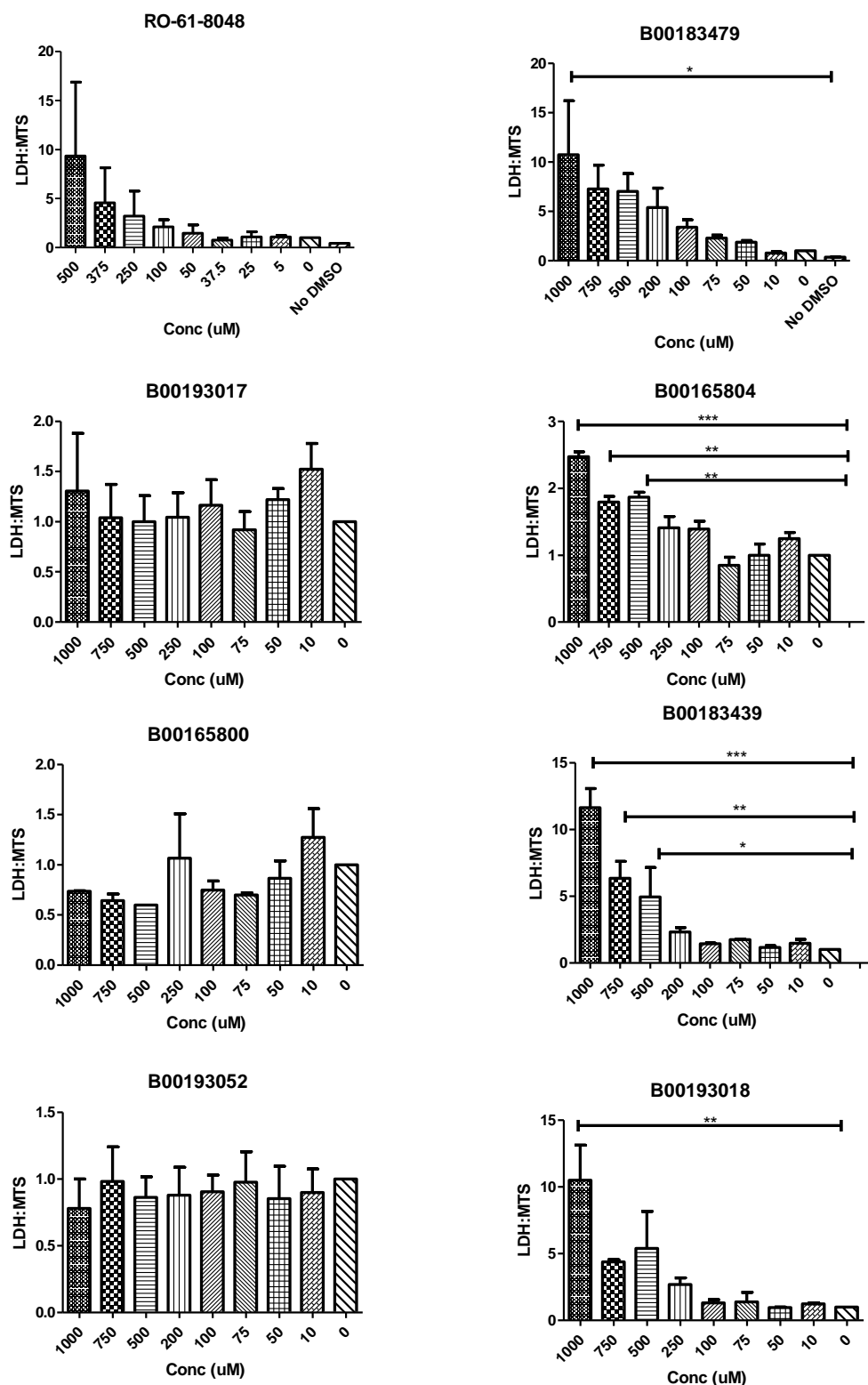


Figure 3.18. Cell toxicity data using human embryonic kidney (HEK) cells. LDH:MTS is the ratio between the activity of lactate dehydrogenase in the media and a tetrazolium-formazan assay for cell proliferation. A higher number equates to higher toxicity at the specified concentration. Results are the average \pm standard error of triplicate experiments. Significance levels (p-values) are: * (0.01 – 0.05), ** (0.001 – 0.01), *** (<0.001).

The measured IC_{50} values (using human recombinant enzyme in buffer) relative to the predicted IC_{50} values (for rat liver enzyme in isolated mitochondria) based on the pharmacophore fit alone are presented in (Figure 3.19). The predicted 95% confidence intervals for these molecules was ± 1 log unit, while the measured data possessed an average residual and an average standard deviation of 0.7 log units, respectively, indicating that this small sample was within the interval expected of the pharmacophore, but with a large amount of variance (relative to the predicted value).

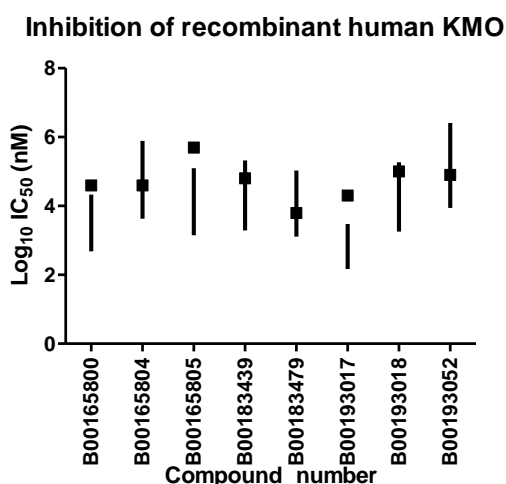


Figure 3.19. *In vitro* results of compound testing against recombinant human KMO. Squares indicate the measured activity, while vertical bars represent the 95% confidence interval predicted by the RMSD to the pharmacophore.

3.3. Discussion

In this work, computational models were employed to find new inhibitor lead compounds for KMO. This resulted in the testing of forty-one compounds *in vitro* against recombinant human KMO, and the testing of five (at the time of writing) of these against transgenic HEK-293 cells, overexpressing human KMO. During the *in silico* screening, emphasis was placed on the high throughput of a pharmacophore screen as the first step. The generated pharmacophore, created from the common features of literature inhibitors, provided a qualitative trend with respect to IC_{50} values, and was easily rationalised within the active site of KMO. A leave-one-out analysis and randomisation test were performed on the linear regression between the pharmacophore and literature IC_{50} values to assess randomness of the model and its dependency on single data points. This showed that the model was non-random and not unduly dependent on individual molecules. The pharmacophore produced an R^2_{adjusted} of 0.63, and a predicted 95% confidence interval of 1 log unit. Although the correlation is relatively weak (0.6), this level of correlation and accuracy is common in the literature, with studies reporting R^2 values (between predicted and

measured) activities of 0.6 – 0.8, and average residuals against hit compounds of 1 log unit (see for example [171, 204-206]). Part of this weakness lies in partial clustering of congeneric molecules as shown in Figure 3.6. The clustering indicates that the model is weak at differentiating activity within scaffolds. These may represent activity cliffs – defined as a sharp difference in activity between two apparently structurally similar molecules. Instead, the spread of scaffolds across activity ranges is likely the driving force of the regression line. That is, the data describes mostly the average activity of a scaffold, but struggles to explain the activity changes caused by peripheral functional groups.

Subsequent docking results of literature KMO inhibitors were in agreement with the pharmacophore – producing a pattern of aromatic groups interacting with FAD, and hydrogen bond acceptors with Arg83. The crystal structure was able to accommodate all scaffolds of KMO inhibitors, although the scoring functions employed were not able to quantifiably account for activity differences within each congeneric series. This is a clear limitation of the docking results presented here, and was the reason behind the use of distance metrics during final compound selection. Taken together, the models employed in this work struggle to quantifiably handle small changes among molecules, but should instead be deployed to screen for new scaffolds – with multiple examples of each scaffold being tested to better account for the variance within each congeneric sequence. However, this also represents a large increase in costs during testing.

3.4. Conclusion and future research

This chapter sees the first example of KMO inhibitors identified after an *in silico* screening campaign. The pharmacophore generated matched well with the crystal structure of yeast KMO and both pharmacophore and docking results supported the same interaction “hotspots”. Due to a lack of literature data at the time of model generation, they appear to struggle with differences in activity caused by subtle structural changes, such as atom substitution in aromatic rings and small substituents placed on aromatic rings. This also makes formal validation by ROC curve analysis difficult. Further work can be performed to potentially improve the quantitative nature of this modelling. The recent release of structure-activity data for the pyrimidine-containing inhibitors can be used to investigate the causes of activity changes within a single scaffold [49]. This information could then be translated onto other scaffolds to develop those into more potent inhibitors. Another avenue relates to the limited validation that can be performed on the lone crystal structure. The generation of other structures, either *via* simulation or empirical methods, will allow for cross-docking validation and ensemble docking methodologies to be employed. Depending on the amount of flexibility within KMO, this may produce sufficiently different

structures that the dynamic requirements of the binding site can be observed. Such ensemble methods have been used to overcome limitations in very low resolution $\alpha\beta$ -tubulin structures [207], to quantitatively explore the flexibility inherent in a tyrosine kinase and how that flexibility interacts with diverse scaffolds of inhibitors [208], provide rationale for structure-based design of selective inhibitors in a family of phosphodiesterase enzymes [209].

The literature inhibitor values used in this work were rat liver KMO in mitochondrial membranes, and these were used to generate models, in part, using the yeast KMO structure. The measured inhibition activities reported here were obtained from human recombinant KMO in buffer. This provides evidence that sufficient structural and functional similarities exist between these various enzymes to be useful during early drug discovery stages. This is also the first report of KMO inhibitors coming from an *in silico* screening platform, and validates the 4J36 crystal structure as a useful starting point for future human KMO drug development work. A success rate (defined in this work as molecules with an IC_{50} below 100 μ M) of 6/41 (15%) is commensurate with other studies of similar size [171, 204-206]. These compounds represent new hit compounds for future SAR work into KMO inhibition.

3.5. Methods

All computational modelling for drug discovery took place in the Molecular Operating Environment (MOE version 2011.10) by Chemical Computing Group (CCG, Montreal, Canada) unless otherwise stated.

3.5.1. Generation of conformation libraries

All conformation libraries were generated in MOE using the *Conformation Import* protocol and the AM1-BCC force field with the generalised Born solvation model. In the protocol settings, all “input filters” and “constraints” were removed except that “strain” and “fragment strain” limits were increased to 20 kcal/mol (*i.e.* conformations were only discarded if they were more than 20 kcal/mol higher in energy than the lowest energy conformation found for that molecule). All other settings were left at default. For the library containing 108 known KMO inhibitors and the library of 83 hits from the Aldrich Market Select catalogue (Section 3.4), the 250 lowest energy conformations were retained for each molecule. For all other libraries, the 50 lowest energy conformations were retained.

3.5.2. Pharmacophore generation

Three nanomolar-level KMO inhibitors ((*Z*)-2-cyano-3-hydroxy-3-(1-methyl-1*H*-benzo[*g*]indazol-3-yl)-*N*-phenylacrylamide [IC_{50} 40 nM], *N*-(4-(4-chlorophenyl)thiazol-2-yl)-4-methylbenzenesulfonamide [IC_{50} 56 nM], and (*S*)-2-ammonio-4-(3,4-dichlorophenyl)-4-

oxobutanoate [IC₅₀ 237 nM]) [46, 139, 149] were flexibly aligned in space using MOE's *Flexible Alignment* function. This protocol creates a stochastic conformational library of each molecule prior to aligning them in space based on their pharmacophoric features. The *Similarity terms* for this alignment were hydrogen bond donor, hydrogen bond acceptor, hydrophobe, aromatic and volume of the molecule. The alignment with the greatest pharmacophoric overlap (assessed by *Flexible Alignment*'s F-score output) was used subsequently. This alignment was passed through the *Flexible Alignment* protocol again, this time with the "refine existing alignment" option activated, which acts as a minimisation procedure to ensure the most finite overlap has been found. A common feature pharmacophore was then generated from this refined alignment by using MOE's *Consensus Pharmacophore* panel, with default settings. The features listed in Section 3.2.1 were then manually selected and the rest discarded.

Using the pharmacophore against known KMO inhibitors

Section 3.2.1 describes the pharmacophore in full. For the passing of the 108 KMO inhibitors through the pharmacophore, all of the described features were considered as mandatory. In order for a molecule to hit the pharmacophore it must satisfy every specified feature. A number of the molecules could not do this due to not being sufficiently large enough. These molecules were separately passed through the same pharmacophore except only F1:Acc and its vector F7:Acc2, F2:Aro and its vector F6:PiN, and the inclusion volume were mandatory. Molecules that could fill other features would do so and receive a boost in their RMSD. All molecular-pharmacophore alignment pairs were then manually inspected to ensure that the software had been capable of finding the most satisfactory alignment (*e.g.* if a molecule could be manually aligned within the complete pharmacophore, that the software had also been able to achieve a similar alignment).

Using the pharmacophore for screening the Aldrich Market Select catalogue

Section 3.2 describes the pharmacophore in full. The following features were defined as mandatory: F1:Acc and its vector F7:Acc2, F2:Aro and its vector F6:PiN, F5:Aro, and the inclusion volume. The features F4:Aro|Hyd and F3:Don were present, but optional. The conformation library of the Aldrich Market Select catalogue, created in Section 3.2.6, was passed through the pharmacophore using MOE's pharmacophore search function, with hit conformations being exported to a separate database, along with RMSD values.

3.5.3. Docking studies in 4J36

The KMO structure, 4J36, was downloaded from the RCSB Protein Databank (www.rcsb.org). The protein was protonated by using MOE's *Protonate 3D* protocol with default settings except the van der Waals calculations used the Lennard-Jones 6-12 function. The Amber10:EHT force field

was used with AM1-BCC charges for the FAD co-factor. No receptor energy minimisation was performed due to missing structural information in a helix making up part of the active site roof. As such, it was possible that Arg83 may have been allowed to move too much if energy minimisation was used. For the same reason, all docking was performed on a rigid receptor.

GridMin docking

GridMin docking runs were setup using MOE's *Dock* panel by selecting "GridMin" as the refinement method. The pocket was defined as the space occupied by the co-crystallised ligand. The electrostatic cut-off distance was 5.5 Å and the van der Waals cut-off distance was 4 Å and used a Lennard-Jones 4-8 potential. Charges of the ligands in the database were calculated from AM1-BCC.

Poses from this process were assessed by calculating their interaction energy (between ligand and receptor) and adding it to the strain energy of the ligand. Any poses with positive numbers were discarded. Poses were then ranked on their distance between any ligand polar atom and the closest omega nitrogen of Arg83 using the "dock_measuredist" script written by CCG and available to licensed users upon request from CCG. Similarly, distances between aromatic atoms of the ligands and the nearest nitrogen or oxygen of FAD were measured in the same fashion. Poses without a polar atom within 3 Å of the Arg83 omega nitrogen and an aromatic atom with 5 Å of the FAD atoms were discarded.

Force field docking

Force field docking was used for known KMO inhibitors and the 83 hit compounds as detailed in Section 3.2.5. Force field docking runs were setup using MOE's *Dock* panel by selecting "force field" as the refinement method. The pocket was defined as 9 Å within the space occupied by the co-crystallised ligand. The Amber10:EHT force field was used with the generalised Born solvation model and AM1-BCC charges for ligands and FAD. The gradient cut-off for energy minimisation was 0.01 with a maximum of 500 iterations per conformation. Assessment of these poses was performed in the same manner as described for GridMin docking.

Curating the Aldrich Market Select catalogue

The Aldrich Market Select (Q1, 2013) catalogue was obtained from Sigma-Aldrich Australia, consisting of ~6 million compounds. The database did not contain three dimensional information and additionally contained many species not suited to typical medicinal chemistry (e.g. very large or small, reactive functionalities). The database was curated as follows: The entries were desalted by using MOE's *Wash* function, retaining only the largest molecular species from each entry (discarding, for example, sodium, chloride, formate ions, etc.). The *Wash* protocol was then used to fill empty valencies with explicit hydrogen atoms. Entries smaller than 180 amu and larger than

600 amu were discarded. Reactive functional groups using the SMARTS query language were then selected and removed, to minimise assay interference [200]. Use of this query language allows for the identification of database entries that contain the specified substructures. For example, the query “cccccc”, specifies six aromatic carbon atoms joined together (either linearly or in a single ring), and could be used to select any molecule that contains this as part of its structure such as benzophenone, indoleamine, 1,7-naphthyridine (naphthalene with positions 1 and 7 being nitrogens), *etc.* Table 3.2 gives a basic introduction to the language and Table 3.3 specifies the queries used on the database and the order in which they were applied.

Table 3.2. Basic operators and query examples of the modified SMARTS query language implemented in MOE. Hydrogens are implicit.

Operator	Interpretation	Operator	Interpretation
;	AND logical operator	upper case letter (e.g. C, N, O)	non-aromatic element symbol
,	OR logical operator	lower case letter (e.g. c, n, o)	aromatic element symbol
!	NOT logical operator	A	any aliphatic non-hydrogen atom
()	collects structural arguments together for a branched species e.g. N(CC)CC is diethyl amine while NCCCC is <i>n</i> -butyl amine	a	any aromatic non-hydrogen atom
[]	collects logical arguments together	R	preceding structural argument is part of a ring
~	any bond (single, double, triple)	[C;R]	an aliphatic carbon AND part of a ring
=	double bond	[C,R]	an aliphatic carbon OR any atom in a ring
#	triple bond	[C;!R]	an aliphatic carbon AND NOT part of a ring
H2	has two hydrogens attached. <i>E.g.</i> [C,N;H2] is any aliphatic carbon OR nitrogen AND has 2 hydrogens.	[C;!R]=[C;!R]	an aliphatic carbon, which is not part of a ring, joined by a double bond to an aliphatic carbon which is not part of a ring

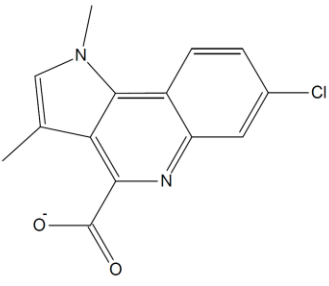
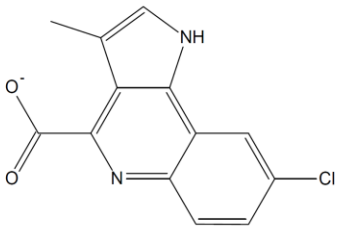
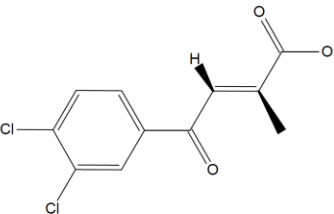
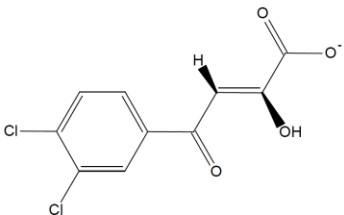
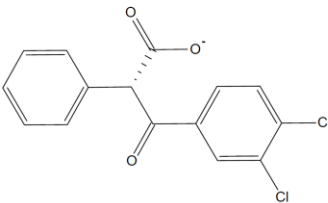
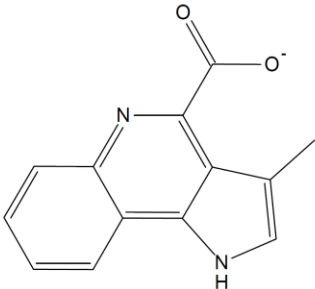
Table 3.3. Queries used to remove potentially reactive molecules from the database prior to screening.

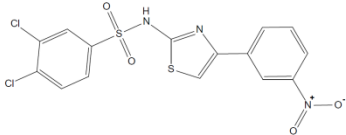
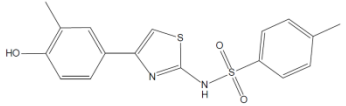
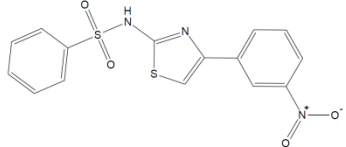
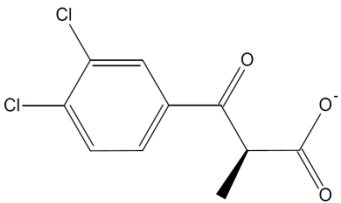
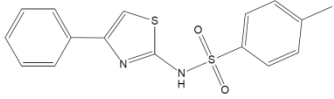
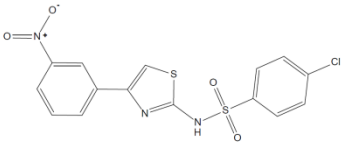
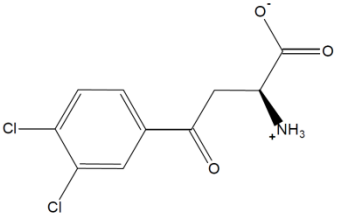
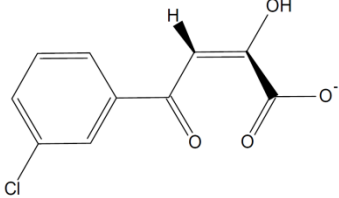
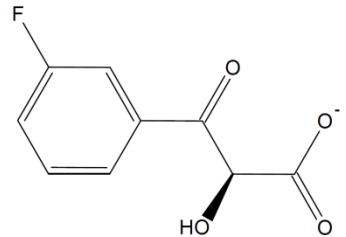
Query	Substructure	Query	Substructure
<chem>[C;!R](=O)C(=O)</chem>	linear 1,2-dicarbonyls	<chem>[C;!R]=[C;!R][C;!R]=O</chem>	linear Michael acceptors
<chem>[O,N,S;!R]~[O,N,S;!R]</chem>	bonded aliphatic heteroatoms not in a ring.	<chem>C#C</chem>	alkynes
<chem>N=N=N</chem>	azides	<chem>C[Br,Cl,I]</chem>	aliphatic halides except fluorides
<chem>O=[C;!R][O,S;!R][C,S,O;!R]</chem>	linear esters and thioesters	<chem>[C;H2]=C</chem>	terminal alkenes

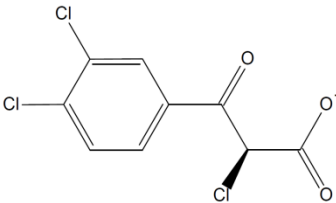
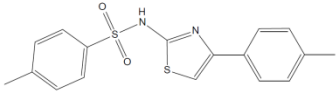
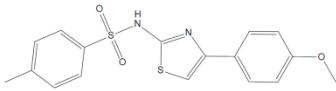
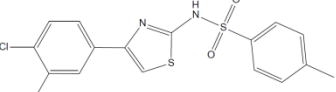
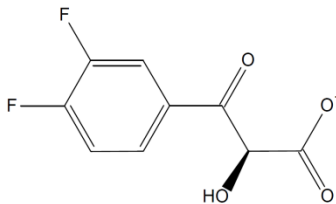
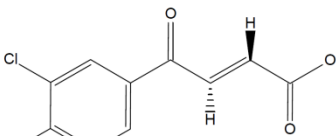
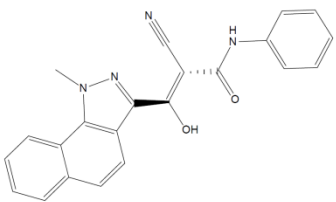
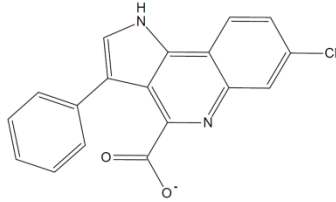
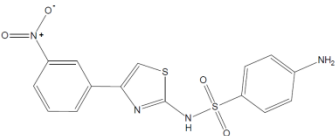
The remaining structures (~ 4 million), were ordered by a random number generator and 420, 000 were used to generate a library. The *Wash* function was then used to (sequentially) rebuild the three dimensional coordinates, add hydrogens, and protonate/deprotonate strong bases and acids. A conformational library was then generated as detailed in Section 3.2.6.

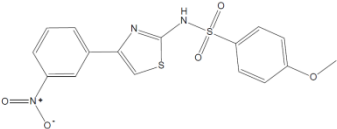
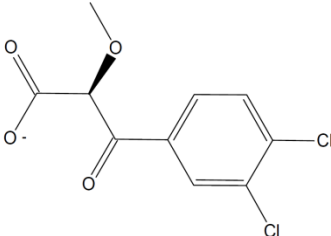
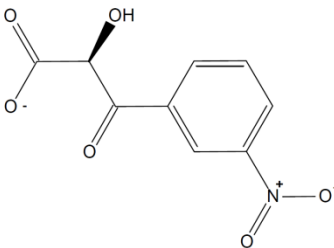
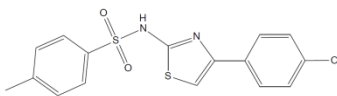
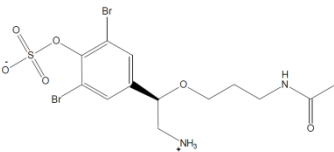
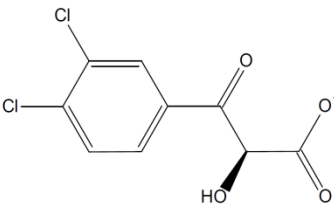
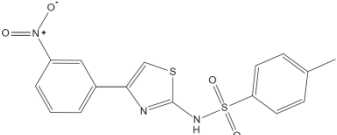
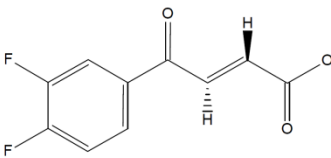
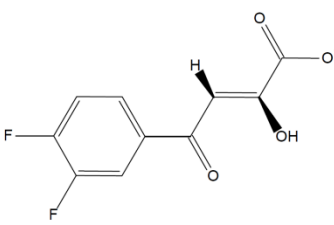
Appendix to Chapter 3

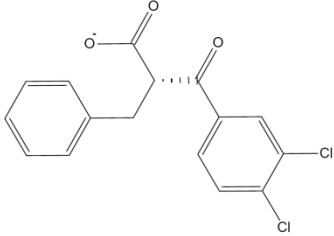
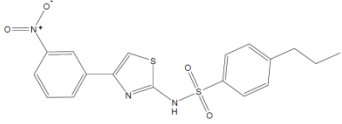
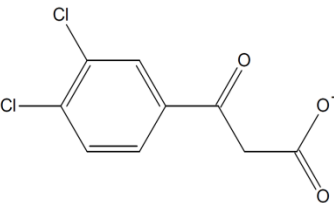
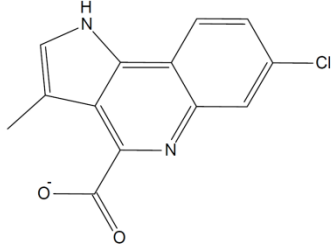
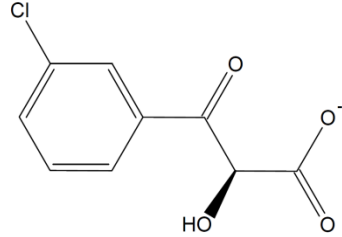
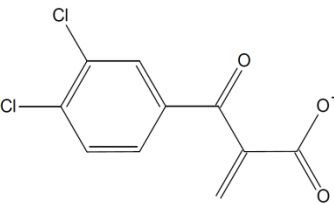
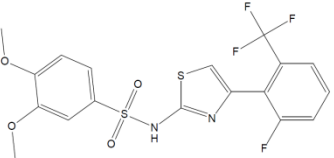
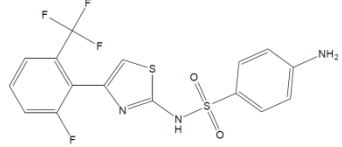
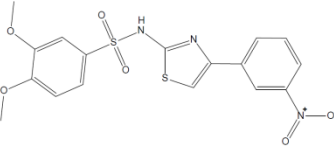
KMO inhibitors used in the linear regression model

<p>RMSD: 0.6125</p>  <p>Log IC₅₀: 4.7267 Predicted IC₅₀: 3.6744</p>	<p>RMSD: 0.6006</p>  <p>Log IC₅₀: 4.7882 Predicted IC₅₀: 3.6368</p>	<p>RMSD: 0.3347</p>  <p>Log IC₅₀: 4.0531 Predicted IC₅₀: 2.7935</p>
<p>RMSD: 0.2515</p>  <p>Log IC₅₀: 3.8062 Predicted IC₅₀: 2.5296</p>	<p>RMSD: 1.1534</p>  <p>Log IC₅₀: 4.2900 Predicted IC₅₀: 5.3899</p>	<p>RMSD: 0.6018</p>  <p>Log IC₅₀: 4.9868 Predicted IC₅₀: 3.6404</p>

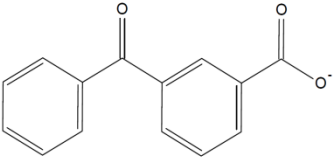
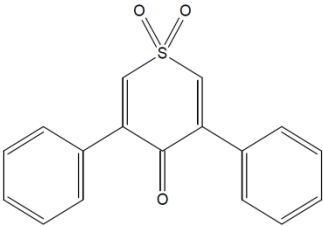
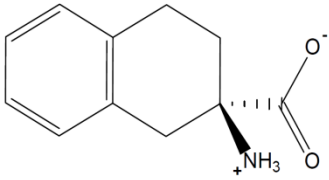
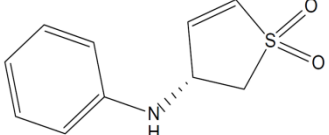
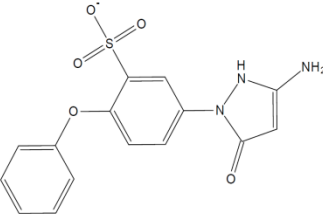
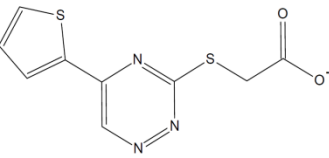
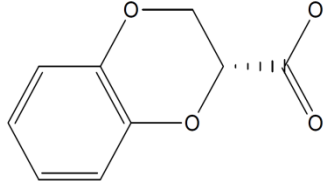
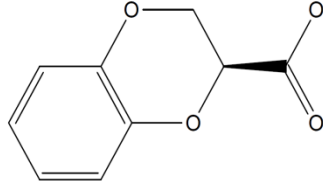
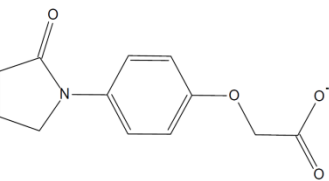
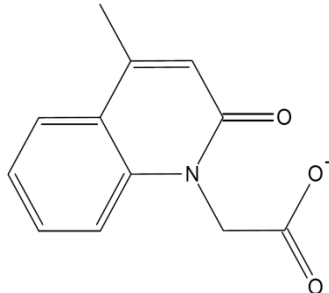
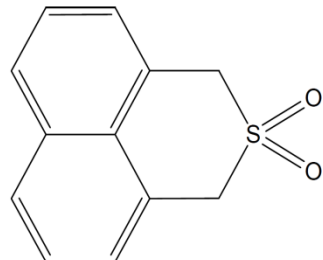
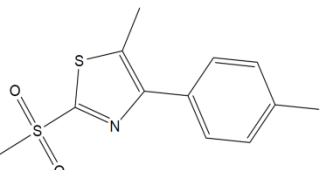
<p>RMSD: 0.1032</p>  <p>Log IC50: 2.0792 Predicted IC50: 2.0591</p>	<p>RMSD: 0.1128</p>  <p>Log IC50: 2.0569 Predicted IC50: 2.0898</p>	<p>RMSD: 0.1574</p>  <p>Log IC50: 2.3010 Predicted IC50: 2.2310</p>
<p>RMSD: 0.6984</p>  <p>Log IC50: 3.8388 Predicted IC50: 3.9469</p>	<p>RMSD: 0.2516</p>  <p>Log IC50: 2.6721 Predicted IC50: 2.5300</p>	<p>RMSD: 0.1056</p>  <p>Log IC50: 1.9243 Predicted IC50: 2.0669</p>
<p>RMSD: 0.2007</p>  <p>Log IC50: 2.5185 Predicted IC50: 2.3683</p>	<p>RMSD: 0.2983</p>  <p>Log IC50: 2.5051 Predicted IC50: 2.6781</p>	<p>RMSD: 0.6473</p>  <p>Log IC50: 3.9590 Predicted IC50: 3.7850</p>

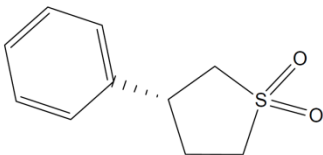
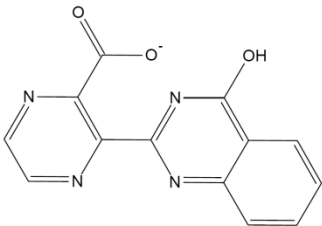
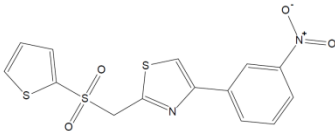
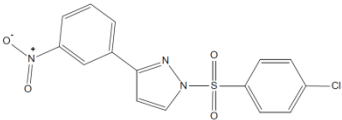
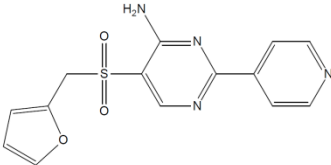
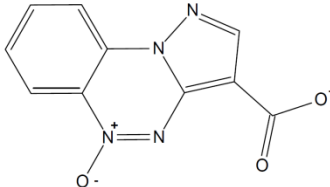
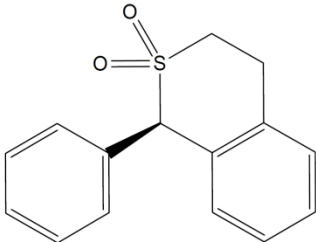
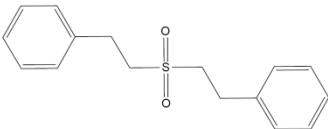
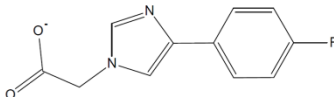
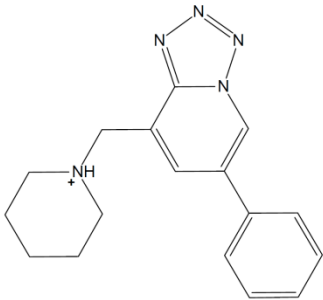
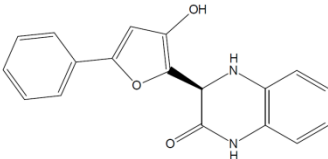
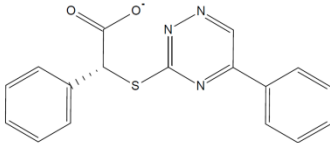
<p>RMSD: 0.8252</p>  <p>Log IC50: 4.1703 Predicted IC50: 4.3491</p>	<p>RMSD: 0.1326</p>  <p>Log IC50: 1.8808 Predicted IC50: 2.1526</p>	<p>RMSD: 0.1170</p>  <p>Log IC50: 2.3802 Predicted IC50: 2.1030</p>
<p>RMSD: 0.0958</p>  <p>Log IC50: 1.7482 Predicted IC50: 2.0357</p>	<p>RMSD: 0.6466</p>  <p>Log IC50: 3.4771 Predicted IC50: 3.7827</p>	<p>RMSD: 0.6090</p>  <p>Log IC50: 4.0170 Predicted IC50: 3.6634</p>
<p>RMSD: 0.0717</p>  <p>Log IC50: 1.6021 Predicted IC50: 1.9592</p>	<p>RMSD: 0.7519</p>  <p>Log IC50: 4.5378 Predicted IC50: 4.1167</p>	<p>RMSD: 0.1046</p>  <p>Log IC50: 1.6021 Predicted IC50: 2.0637</p>

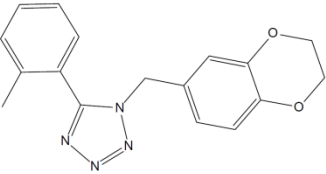
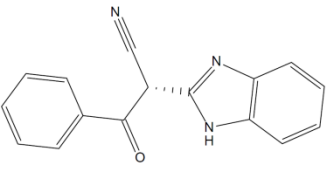
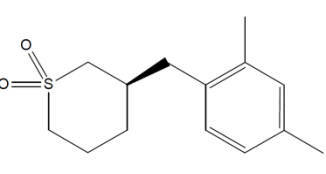
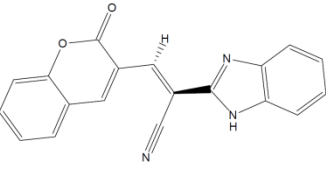
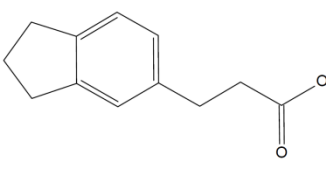
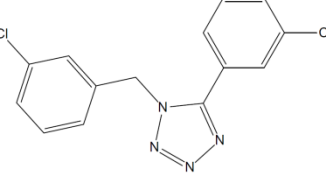
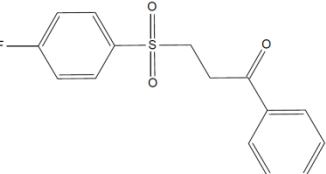
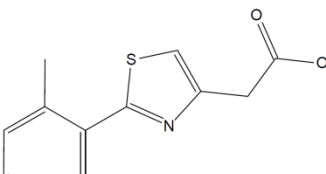
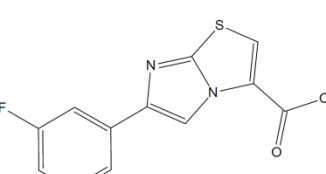
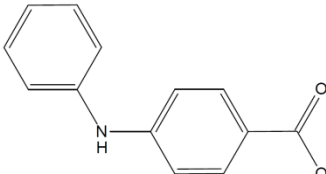
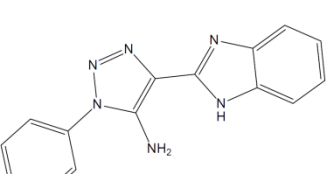
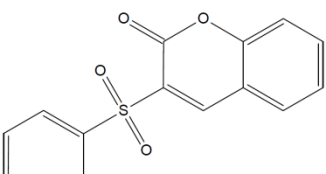
<p>RMSD: 0.1508</p>  <p>Log IC50: 1.7076 Predicted IC50: 2.2102</p>	<p>RMSD: 0.8279</p>  <p>Log IC50: 3.8388 Predicted IC50: 4.3577</p>	<p>RMSD: 0.5625</p>  <p>Log IC50: 4.0607 Predicted IC50: 3.5160</p>
<p>RMSD: 0.1831</p>  <p>Log IC50: 1.7482 Predicted IC50: 2.3127</p>	<p>RMSD: 0.6372</p>  <p>Log IC50: 3.1761 Predicted IC50: 3.7530</p>	<p>RMSD: 0.6470</p>  <p>Log IC50: 3.1461 Predicted IC50: 3.7840</p>
<p>RMSD: 0.1868</p>  <p>Log IC50: 1.6812 Predicted IC50: 2.3245</p>	<p>RMSD: 0.6075</p>  <p>Log IC50: 4.3243 Predicted IC50: 3.6587</p>	<p>RMSD: 0.2150</p>  <p>Log IC50: 3.0792 Predicted IC50: 2.4138</p>

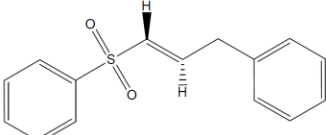
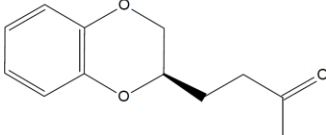
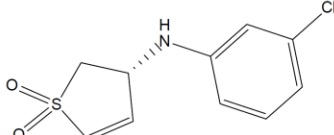
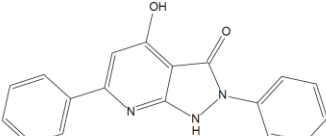
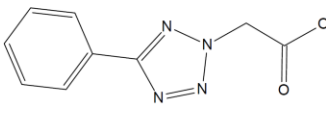
<p>RMSD: 0.7604</p>  <p>Log IC50: 3.4624 Predicted IC50: 4.1435</p>	<p>RMSD: 0.1792</p>  <p>Log IC50: 2.9956 Predicted IC50: 2.3004</p>	<p>RMSD: 0.8069</p>  <p>Log IC50: 3.5911 Predicted IC50: 4.2909</p>
<p>RMSD: 0.6000</p>  <p>Log IC50: 4.3802 Predicted IC50: 3.6350</p>	<p>RMSD: 0.6474</p>  <p>Log IC50: 3.0414 Predicted IC50: 3.7852</p>	<p>RMSD: 0.6481</p>  <p>Log IC50: 4.5563 Predicted IC50: 3.7874</p>
<p>RMSD: 0.2428</p>  <p>Log IC50: 1.5911 Predicted IC50: 2.5020</p>	<p>RMSD: 0.1463</p>  <p>Log IC50: 1.2788 Predicted IC50: 2.1959</p>	<p>RMSD: 0.2523</p>  <p>Log IC50: 1.5682 Predicted IC50: 2.5320</p>

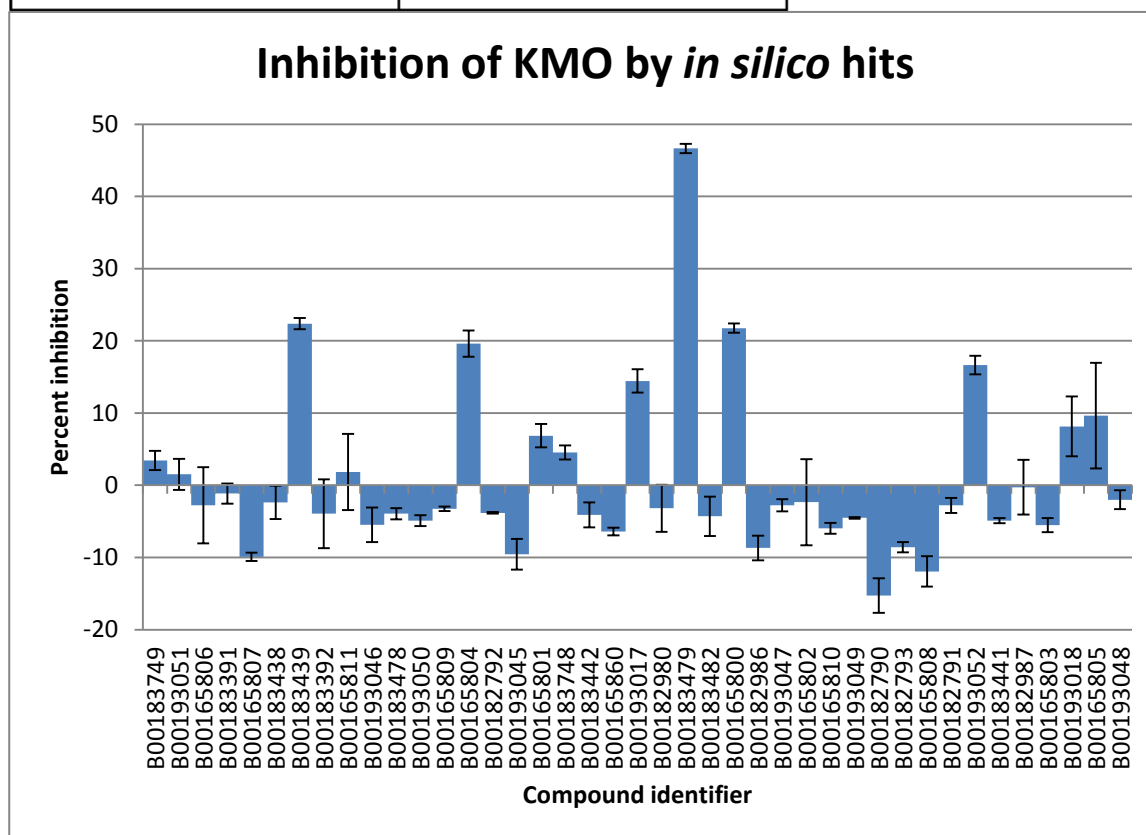
Compounds tested against KMO in vitro

<p>Barcode: B00165800</p> 	<p>Barcode: B00165801</p> 	<p>Barcode: B00165802</p> 
<p>Barcode: B00165803</p> 	<p>Barcode: B00165804</p> 	<p>Barcode: B00165805</p> 
<p>Barcode: B00165806</p> 	<p>Barcode: B00165807</p> 	<p>Barcode: B00165808</p> 
<p>Barcode: B00165809</p> 	<p>Barcode: B00165810</p> 	<p>Barcode: B00165811</p> 

<p>Barcode: B00165860</p> 	<p>Barcode: B00182790</p> 	<p>Barcode: B00182791</p> 
<p>Barcode: B00182792</p> 	<p>Barcode: B00182793</p> 	<p>Barcode: B00182980</p> 
<p>Barcode: B00182986</p> 	<p>Barcode: B00182987</p> 	<p>Barcode: B00183391</p> 
<p>Barcode: B00183392</p> 	<p>Barcode: B00183438</p> 	<p>Barcode: B00183439</p> 

<p>Barcode: B00183441</p> 	<p>Barcode: B00183442</p> 	<p>Barcode: B00183478</p> 
<p>Barcode: B00183479</p> 	<p>Barcode: B00183482</p> 	<p>Barcode: B00183748</p> 
<p>Barcode: B00183749</p> 	<p>Barcode: B00193017</p> 	<p>Barcode: B00193018</p> 
<p>Barcode: B00193045</p> 	<p>Barcode: B00193046</p> 	<p>Barcode: B00193047</p> 

Barcode: B00193048 	Barcode: B00193049 	Barcode: B00193050 
Barcode: B00193051 	Barcode: B00193052 	



Data are the average of independent duplicate experiments. Error bars represent one standard deviation. Test compounds were 10 μ M with 300 μ M L-kynurenine, 0.6 mM NADPH at 37 $^{\circ}$ C, 30 minutes.

Chapter 4

Construct Generation

This chapter provides background on the structure of IDO1 and the use of this information in designing mutants of IDO1. These mutants were designed to investigate the role of the unresolved loop of IDO1 with small molecules and with protein binding partners. The results of producing these constructs are presented.

4.1. IDO1 reaction with L-Tryptophan

IDO1 is a heme-containing enzyme that catalyses the oxidative cleavage of L-tryptophan (L-Trp) to *N*-formyl-L-Kynurenine by addition of dioxygen across the C2-C3 bond (Figure 4.1 A). Under typical experimental conditions, this reaction only occurs with IDO1 in the ferrous state, and is electron neutral (ferrous heme remains after reaction) [210]. The electronic structure of the active binary complex (dioxygen bound to ferrous IDO1, prior to tryptophan binding) is best described as ferric-superoxide in nature, where the electron primarily resides on the dioxygen ($\text{Fe}^{3+}\text{-O}_2^-$) [211, 212]. Displacement of this superoxide by water yields an inactive ferric enzyme (Figure 4.1B) [212, 213]. Due to this auto-oxidation, IDO1 reactions are carried out in the presence of a reducing system. Typical electron transfer agents include dye molecules such as methylene blue, or proteins such as cytochrome b5 (CYB5) or cytochrome NAD(P)H:P450 reductase (CPR) [214, 215]. The catalytic mechanism and reaction conditions are discussed in greater detail in Chapter 6).

A) Oxidation of L-tryptophan by IDO

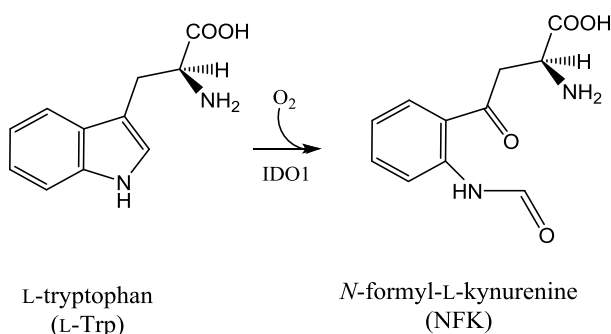
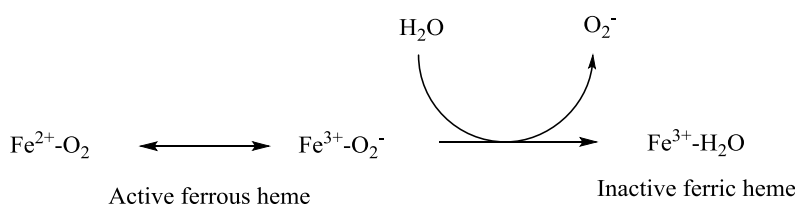


Figure 4.1. A) Oxidative bond cleavage of L-tryptophan to yield *N*-formyl-L-Kynurenine. B) Water mediated auto-oxidation of active ferrous to inactive ferric IDO1.

B) Autooxidation of ferrous IDO1



4.2. IDO1 and the unresolved loop

There are currently 9 crystal structures of IDO1 in the protein databank (www.rcsb.org) of 2.0 – 3.45 angstrom resolution, all of them human (Figure 4.2) [119, 216-218]³. There are no IDO2 crystal structures. All IDO1 structures are crystallised as homodimers, with 8 of them containing a single disulfide bond between Cys308 of each monomer. In structure 5EK4 the dimers are still in the same relative position, but without the disulfide bond being present. There is no evidence that this bond occurs in nature, but by inference from its prevalence, likely confers stability to the protein's structure under crystallisation conditions. Some recent studies have used a Cys308Ser human IDO1 mutant, without observable differences in catalytic activity [210, 219]. All evidence to date suggests that IDO1 operates as a monomer, although the possibility of a hetero-oligomer under specific experimental conditions has also been raised (discussed further in Section 6.3) [122].

Currently, all crystal structures are missing electron density from a 20 amino acid loop (residues 360-380) due to a high level of disorder. The 18 monomers are essentially identical on the large scale, with an average root mean square deviation (RMSD) of 0.68 Å across backbone heavy atoms (Figure 4.2). The majority of these differences are present at the *N*- and *C*-terminal. Bound in these structures are non-substrate-like inhibitors such as cyanide, phenylimidazole, or larger imidazothiazoles (Figure 4.3). Smaller inhibitors also co-crystallise with *N*-cyclohexyl-2-aminoethanesulfonic acid (CHES) buffer molecules in the active site entrance. The lack of a resolved loop in these structures implies that the loop is not involved in locking these particular inhibitors in place. This does not preclude the possibility that the loop is involved in transient interactions with these inhibitors during their passage into the binding site, or that they possess interactions only with substrate-mimetic molecules.

Early coarse-grained, Monte-Carlo, computer simulations on the 2D0T partial structure of human IDO1 (*i.e.* no loop atoms were present) suggested that the loop may move in a manner consistent with a gating action upon tryptophan binding [123]. This type of simulation was designed to explore the conformational space of a protein-ligand complex, and does not give any details of the relative energy of each state. Thus, whilst a closed gate conformation appeared energetically feasible, the study could not comment on the thermodynamic relevance of the motion. During writing, Álvarez *et al.* showed that Thr379 was required for substrate binding in human IDO1, and likely involves interaction with the substrate tryptophan's α -amino group [220].

³Two Structures (4U72, 4U74) have been deposited in the protein databank, but have not been published by peer-review at the time of submission.

As well as interaction with substrate molecules, it was hypothesised during project design that the loop might have an important role in interacting with some inhibitors (*e.g.* those that appear to compete for binding with CHES molecules during crystallisation), or with reducing partners such as methylene blue. Especially of interest was the possibility of interactions between the IDO1 loop and proteins involved in IDO1 reduction such as cytochrome b5 (CYB5) and cytochrome P450:NAD(P)H reductase (CPR). Thus, efforts were directed towards creating *E. coli* expression systems of these proteins, as well as IDO1 loop mutants, to investigate such possibilities.

4.3. Design of IDO1 mutants

As a first step in the design of IDO1 loop mutants, other mammalian IDO1 sequences were identified through an NCBI blastp search⁴ and aligned using Clustal Omega⁵. The alignment of the loop region is shown below (Figure 4.4). In the vicinity of the anchor points (residues 360 and 380 using human numbering), each sequence displays generally high conservation, with less apparent conservation appearing in the rest of the loop. Notably, three organisms have a portion of

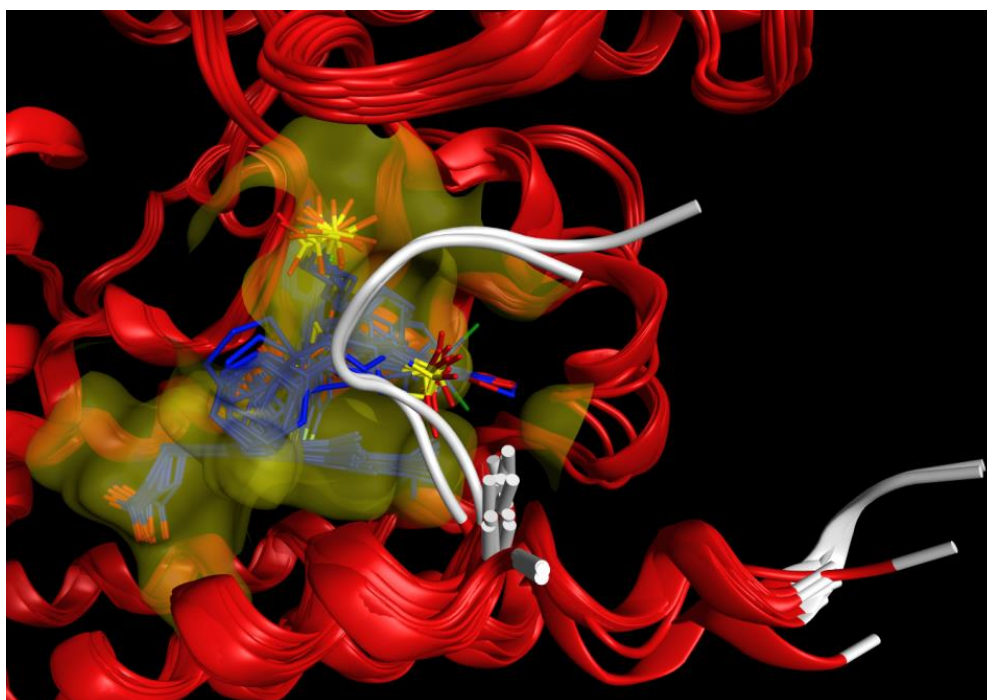


Figure 4.2. Superposition of the 18 IDO1 monomers from all 9 crystal structures present in [119, 216-218]. PDB codes can be found in Figure 4.3. Shown in yellow is the Van der Waals surface of the binding site. In blue are heme and other bound ligands as detailed in Figure 4.3. The white ribbon shows atoms of the loop sequence 360-380, if present, with the remainder of the protein in red. Two of the structures have slightly more of the loop resolved than the other structures. These are from structure 5EK2 and 5EK3. Only one monomer from each of these dimers has these extra atoms, with no other differences that could be apparent causes. 5EK4, from the same study, did not manage to resolve these atoms in either monomer.

⁴ blast.ncbi.nlm.nih.gov/Blast.cgi

⁵ www.ebi.ac.uk/Tools/msa/clustalo

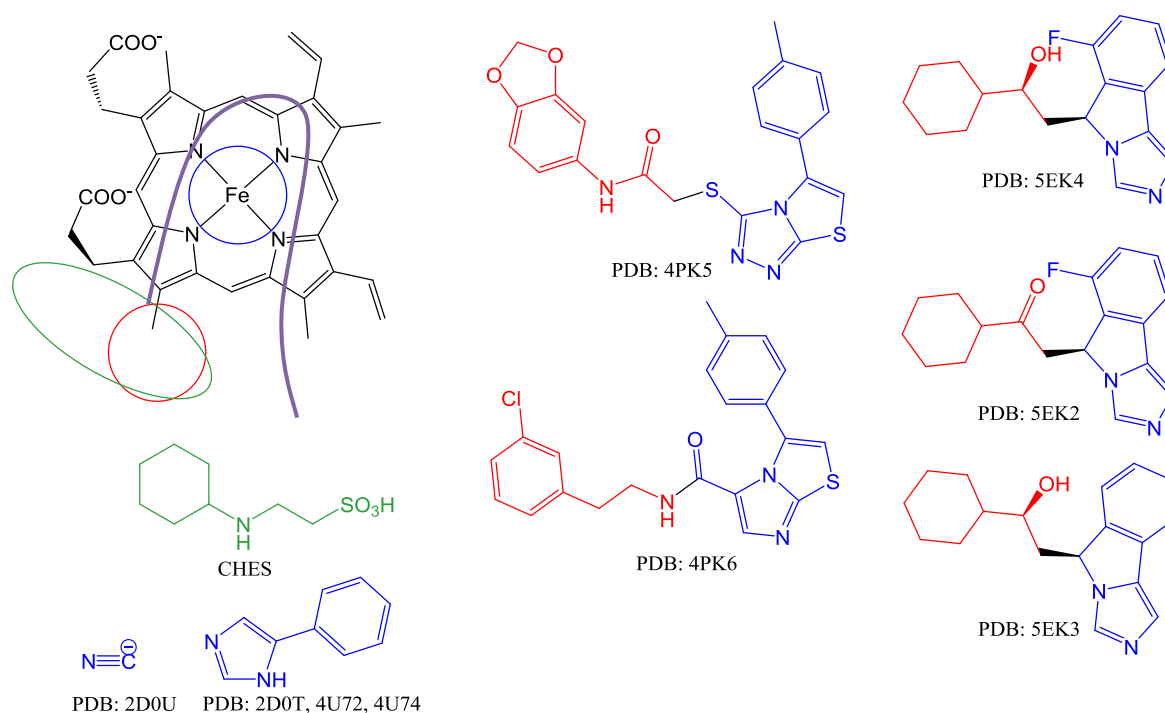


Figure 4.3. Co-crystallised ligands with human IDO1. A top-down schematic representation of the binding pocket showing heme (black) and inhibitor binding regions. The purple line represents the approximate shape of the binding pocket. The blue circle above iron represents the common region where all inhibitors bind. The red circle represents the binding region occupied by inhibitors large enough to prevent buffer co-crystallisation. The green oval is a region occupied by two *N*-cyclohexyl-2-aminoethanesulfonic acid (CHES) buffer molecules in PDB: 2D0U, 2D0T, 4U72, and 4U74 only. The ligands are coloured according to their binding region.

the loop absent: pacific walrus, giant panda and domestic ferret (the full sequence alignment and accession codes are available in the appendix to Chapter 4). Assuming that these sequences are truly lost in the general population for these animals, it raises the question of whether the loop (or at least part of it) is needed for IDO1 function, or whether in these organisms its role is modified, unnecessary, or supplanted by another system.

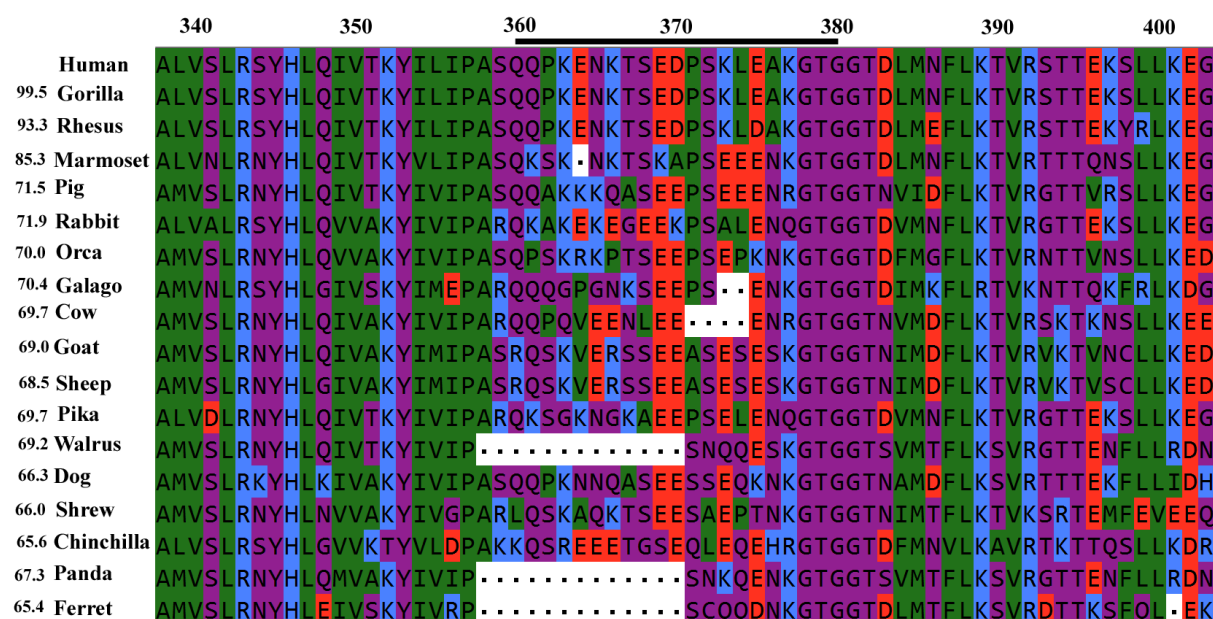


Figure 4.4. Multiple sequence alignment of 18 mammalian IDO1s, ordered by percent identity to human. The human sequence is numbered across the top, with the loop region indicated by a black line. Residues are coloured according to their properties: lipophilic (green), hydrophilic (purple), acidic (red), and basic (blue). The full sequence alignment with accession codes is available in the appendix to Chapter 4.

4.3.1. Other residues of interest

As IDO1 binds to other proteins, the loop might be needed to recruit and/or stabilise the binding of these partners, and other residues surrounding the periphery of the active site might also be involved in such interactions. In the crystal structures, the charged or aromatic residues that line the periphery of the active site entrance are F227, R231, K238, H287, F291, D383, and F387. Using the alignment, Table 4.1 details additional point mutations that might be of interest in investigating protein-protein interactions in future work, but were not considered at this time.

Table 4.1. Aromatic and charged residues (human) making up the periphery of the active site entrance.

Residue	Notes
Phe227	Mostly Phe, some Tyr. Required for catalytic turnover [119]
Arg231	Conserved – needed for catalytic turnover [119]
Lys238	Conserved – not investigated in the literature. The region in general has high conservation
Phe291	Complete except for galago (miniature monkey) which has Ile
Phe387	Complete except for chinchilla (rodent) which is Val

4.3.2. Loop mutants

In addition to the possibility that individual residues might be needed for interaction with protein partners, it may be that more general aspects of the loop, such as size, charge or dipole, are the properties governing function. In such a case, point mutations may not have a large enough impact on those properties to see significant changes in IDO1 function. Rather than working at the single residue level, it was decided to independently delete the first or second half of the loop in mimicry of the walrus, panda and ferret sequences. These deletion mutants are herein referred to as HIDOΔ360-370 and HIDOΔ371-380, respectively. Additionally, walrus IDO1 (WIDO) was chosen for expression as it has the greatest sequence identity to human IDO1 (HIDO) of the three

animals. As a control measure for the HIDO and WIDO proteins, chimeric sequences of each were designed: human main sequence with a walrus loop (termed HCHIM) and the walrus main sequence with a human loop (termed WCHIM). These sequences were chosen as controls for separating the effects of the loop and extra loop sequences. The loop region sequences are shown in Figure 4.5.

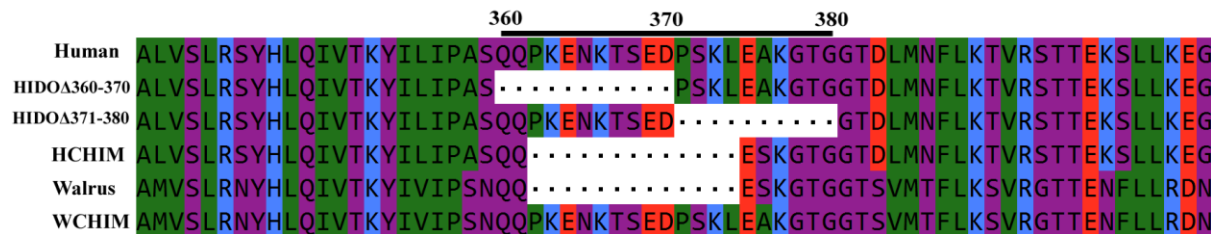


Figure 4.5. The loop region of each IDO1 sequence is shown using the same colouring and numbering as Figure 4.4. HIDOΔ360-370 and HIDOΔ371-380 is human IDO1 with either the first or second half of the loop deleted, respectively. HCHIM is human IDO1 with the walrus loop sequence. WCHIM is walrus IDO1 with the human loop sequence.

4.3.3. Confirmation of truncated loops in animals

Of the three animals with the smaller loop sequences, mRNA data could be found only for ferret in a transcriptome study of animals infected with an influenza virus [221]. From this dataset (which identified both IDO1 and IDO2), contig (a section of experimental sequencing data) number 5000 covers the *N*-terminal, and contig 426 the *C*-terminal of IDO1; where the loop sequence can be found. Contig 426 was compared to the non-redundant nucleotide database using NCBI's blastn⁶ and gave 99% identity to a number of predicted IDO1 ferret sequences (with the next highest overlaps found for walrus and panda IDO1 sequences, respectively). After alignment, the contig was different only at two positions compared to the predicted sequence used (accession XM_013048534.1). The first was the addition of an A at position 141 in the contig sequence due to a poly A region, and this was removed under the assumption that it was a result of the sequencing technique failing to adequately measure the length of a poly A region. Secondly, an A in the contig sequence is a C in XM_013048534.1. This would lead to a premature TAA stop codon prior to the heme-ligating His, and therefore must be de-activating. Assuming that this too was a read quality error (this was a high throughput, shotgun transcriptomic study), then the translated mRNA sequence aligns almost identically: with Leu→Ser and Thr→Ile residue changes being distant from the loop and active site in space, according to the crystal structures. The alignment of the translated sequences are shown below in Figure 4.6. This is not conclusive evidence for the existence of shortened loops in these animals, but does make it more likely. Whilst it would be possible to obtain ferret samples for confirmation of the sequence, it was not deemed necessary in this project as the primary question to be answered was whether loop

⁶blast.ncbi.nlm.nih.gov/Blast.cgi

mutations affect IDO1 function – which is somewhat independent of whether the sequences exist in nature. It is interesting to note that no shortened forms of IDO2 were found in any organism (either in mRNA or genomic data). This may have implications in understanding the differing roles of IDO1 and IDO2 during evolution.

```

XM_013048534.1> EDQNAL
Contig426>      EDQNAL

QKALRYIASSLKQARKEFEKMHKYVDPNTFYNVLRIRYLSGWKNSSKLPKGLKYEFGSDTPREYAGGSAAQSSIFQCFDVL
QKALRYIASSLKQARKEFEKMHKYVDPNTFYNVLRIRYLSGWKNSSKLPKGLKYEFGSDTPREYAGGSAAQSSIFQCFDVL

LGIQQKSGEESAARFLQEMRKYMPPAHREFLLSLESGPSVREFVLKGDTELQADYNECVKAMVSLRNYHLEIVSKYIVR
LGIQQKSGEESAARFLQEMRKYMPPAHREFLLSLESGPSVREFVLKGDTELQADYNECVKAMVSLRNYHLEIVSKYIVR

PSCQQDNKGTGGTDLMTFLKSVRDTTKSFQLEK
PSCQQDNKGTGGTDLMTFLKSVRDTTKSFQLEK

```

Figure 4.6. Translated alignment between predicted ferret sequence XM_013048534.1 and the adjusted mRNA sequence (Contig426) from Camp *et al.* [221]. The two point mutations are boxed, as is the ferret loop sequence. The point mutations are distant from the loop and active site in space.

4.4. Choice of recombinant expression systems

The production of recombinant *N*-tagged-6xHis human IDO1 has been reported [222, 223]. It was shown to possess highly similar kinetic and structural properties to protein isolated from human placenta and has been the staple form of IDO1 used in the literature for mechanistic, structural and drug screening studies [117, 119, 224]. Its expression uses a non-commercial strain of *E. coli*, EC538, containing the expression vector pQE9 and the helper plasmid, pREP4, both from Qiagen. pQE9 uses a T5 promoter and is under control of the *lac* operator. Selection is conferred *via* ampicillin and chloramphenicol resistance genes. pREP4 encodes the *lacI* repressor protein and is neomycin/kanamycin resistant. For IDO1 sequences, the decision was made to continue working in the EC538 system rather than a commercially available system, to maintain consistency with previous work. For CYB5 and CPR proteins, involved in the reduction of IDO1, the commercially available and more commonly employed BL21 (DE3) *Star* expression host was chosen, along with the pET15b and pET28a expression vectors (Novagen). Both vectors are *lac* controlled with resistance to either ampicillin or kanamycin, respectively. Additionally, these vectors have an *NcoI* restriction site as part of their start codon for protein expression. This allows the removal of the vector's own affinity tag sequences (consisting of metal affinity, and antibody and protease recognition sites), and replacement with desired tags in a straight forward manner. This was regarded as particularly useful for adjusting the position and size of the metal-affinity His-tag relative to the membrane anchoring region of CYB5 and CPR, should it prove necessary. CYB5 requires an *N*-terminal His-tag to avoid interference with the *C*-terminal membrane anchor, whilst CPR contains an *N*-terminal anchor and requires a *C*-terminal His-tag.

4.5. DNA manipulation systems

All constructs were designed such that they could be ordered from Integrated DNA Technologies (IDT, USA) as linear double-stranded DNA (dsDNA) in forms compatible with either the Gibson reaction or restriction-ligation methodologies.

4.5.1. The Gibson reaction

The Gibson reaction (New England Biosciences, NEB) provides a means to ligate multiple pieces of double stranded DNA together so long as they have terminal sequences capable of annealing. For this work, it was possible to design DNA sequences for each half of the protein of interest, with terminals having annealing capacity for either the vector or to each other, to create the desired final sequence (Figure 4.7). The Gibson reaction mix consists of an exonuclease that digests the terminals of single stranded DNA in the 5'→3' direction only. This reveals complementary sequences that allows annealing. The ratios of enzymes and DNA in a Gibson reaction has been optimised such that the annealed sequences are generally 25-50 bases, compared to a typical restriction-ligation reaction which usually has 2-4 bases for annealing [225]. This make the annealed DNA very resistant to detachment once annealing has occurred. Whilst annealed, the excised DNA bases are replaced by a polymerase, which results in annealed, nicked, double stranded DNA. Finally, these nicks are joined through the action of a ligase to yield circular double stranded DNA. The reaction is one-pot at 50 °C.

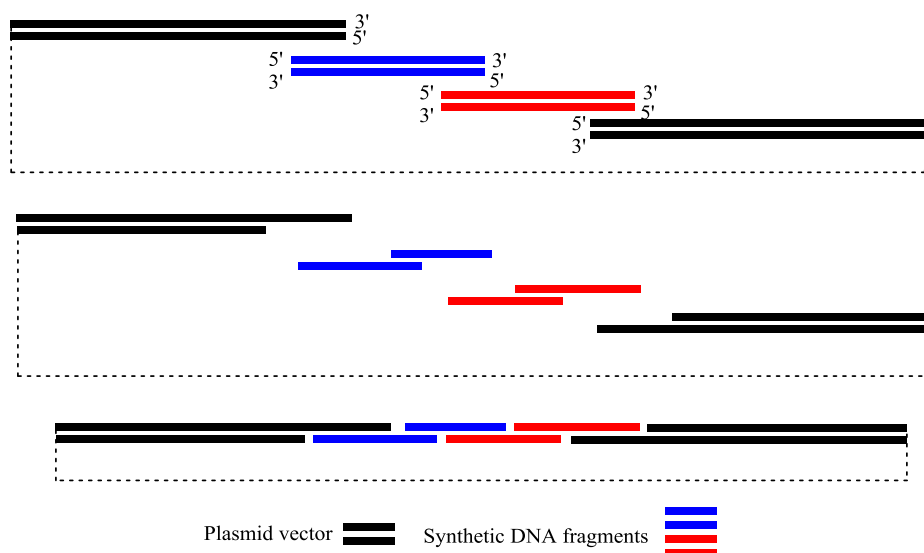


Figure 4.7. The Gibson reaction contains an exonuclease that works only in the 5'→3' direction, allowing for overhangs to be created that can then anneal. Not shown: the polymerase then fills in the DNA bases removed by the exonuclease, using the alternate strand as a template. In the final step, ligase activity yields a circular plasmid ready for transformation into a host.

4.5.2. Restriction-ligation method

At the onset of this work, the length of linear dsDNA available for order was limited to 500 bp in length. Advancing technology later increased this to 2000 bp. This meant that sequences ordered at this later stage were a single piece of dsDNA. Suitable restriction sites were placed 6 bp in from either terminal of the dsDNA, to ensure higher binding between the restriction enzyme and the DNA. T4 ligase was then used to ligate the linearised plasmid and insert to create transformable circular plasmid, by-passing the Gibson reaction.

4.6. Construct design

Ordered DNA sequences and the translation of sequenced plasmids have been provided in the appendix to Chapter 4.

4.6.1. IDO1 sequences

The IDO1 genes were inserted into pQE9 at identical positions for each plasmid, to maintain distance between the protein and 6xHis-tag. Thus, all IDO1 DNA sequences are 5'-ATG-6xHis-BamHI-Sall-IDO1-Stop-HindIII-3', which translates to: MRGS-HHHHHH-GSVD-IDO1.

4.6.2. CYB5 and CPR sequences

Both CYB5A and CPR are membrane bound proteins. The expression, purification and characterisation of membrane bound proteins is a more difficult, though often still tractable, task relative to their soluble forms. Both proteins have been shown by a number of groups to work in truncated form [226-228]. Therefore, soluble forms were engineered in this study, in addition to their full-length counterparts. This served the purpose of having an easier system to start with that could be used to aid in designing later liposomal experiments. It also allows for the investigation of possible functional differences between liposomal and soluble assays during future work. For example, the same hydrophobic portions of the proteins that lead to membrane insertion, could be required for interaction between CYB5A or CPR and other binding partners [229, 230]. Herein, full length CYB5A refers to standard nomenclature for protein naming (CYB5, isoform A), while CYB5S will be used to denote the truncated (soluble) form of CYB5A. Likewise, CPRS will denote the truncated form of CPR. After plasmid assembly these proteins have the sequence structure shown in Figure 4.8. Where TEV is an amino acid sequence specifically recognised by the tobacco etch virus (TEV) protease. This would allow the cleavage of the His-tag from the protein after purification in the event that it was interfering with the protein's function.

CYB5A and CYB5S:

NcoI(ATG)-SalI-8xHis-TEV-CYB5-Stop-BamHI-HindIII

CPR and CPRS:

NcoI(ATG)-SalI-CPR-TEV-10xHis-Stop-BamHI-HindIII

Figure 4.8. Sequence structure for the constructs of the cytochrome b5 (CYB5A, CYB5S) and cytochrome:P450 NAD(P)H reductase (CPR, CPRS) proteins. TEV is an amino acid sequence specifically recognised by the tobacco etch virus (TEV) protease. When placed into a pET28-based vector, the ATG codon of the NcoI recognition site additionally acts as the start of transcription.

4.6.3. CYB5A and CYB5S

The sequences used here for CYB5 and CPR were obtained from consensus coding sequences (CCDS) utilising the NCBI CCDS project⁷. The CCDS project is a collaborative effort between NCBI, ENSEMBL and the Sanger Institute to identify the core human coding regions that give rise to protein products, with high quality annotations.

Human cytochrome b5 may refer to two genes, each with multiple potential splice variants. The gene *CYB5A* on chromosome 18 has the protein product cytochrome b5, type A, (CYB5A) and is associated with the cytoplasmic side of the endoplasmic reticulum [231]. The gene *CYB5B* on chromosome 16 gives rise to cytochrome b5, type B, and is associated with the cytoplasmic side of the outer-mitochondrial membrane [232]. Coincidentally, this is the same membrane location as KMO, and mitochondrial dysfunction in general has been implicated in a number of KMO-linked pathologies.

CYB5A is associated with three CCDS splice variants: CCDS12004.1, CCDS12005.1 and CCDS54188.1 whose products are 134, 98 and 124 residues long, respectively. *CYB5B* is associated with a single CCDS, CCDS10880, comprising 150 residues. Additionally, *CYB5A* is associated with a coding splice variant of 60 residues and *CYB5B* is associated with 4 other splice variants ranging from 146 to 64 residues long. These latter variants are not associated with CCDS entries and were not considered further in this work. The accession numbers of these sequences can be found in Table 4.2.

⁷ www.ncbi.nlm.nih.gov/CCDS/CcdsBrowse.cgi

Table 4.2. Transcript variants for human cytochrome b5.

Gene	Transcript ID	Amino acid length	CCDS	Reference sequence (RefSeq)
CYB5A	ENST00000340533	134	CCDS12004	NM_148923
	ENST00000494131	98	CCDS12005	NP_683725
	ENST00000397914	124	CCDS54188	NM_001914 NP_001905
	ENST00000299438	60	-	-
CYB5B	ENST00000307892	150	CCDS10880	NM_030579 NP_085056
	ENST00000512062	146	-	-
	ENST0000015314	131	-	-
	ENST00000561792	140	-	-
	ENST00000568237	64	-	-

Pearson *et al.* detailed some of the kinetics of human recombinant IDO1 in the presence of recombinant CYB5A and CPR [122]. The CYB5 reported to be used was from Sigma-Aldrich (catalogue number C1427) recombinantly expressed from *E. coli* as a His-tagged protein. The product datasheet⁸ lists it as the ER bound form (His-tagged) with a molecular mass of 16, 080 Da. Assuming a 6xHis-tag is used, CCDS12004 (134 a.a.) corresponds with this mass. This CCDS was elected for use to maintain consistency with the previous work of Pearson *et al.*, however, the co-localisation between CYB5B and KMO (the next major enzyme of the kynurenine pathway and a major target for neurodegenerative drug research) may warrant further investigation between IDO1 and IDO2, and CYB5B in the future – in both *in vitro* and cellular contexts.

The expression and purification of membrane bound proteins can have difficulties compared to equivalent cytosolic proteins. Therefore, constructs were designed for both full-length CYB5A, and a truncated form (CYB5S) that is cytosolically located and known to still perform its function with other cytosolic proteins [227]. The CCDS12004 sequence is shown below (Figure 4.9). Beck von Bodman *et al.*, engineered a soluble form of rat CYB5A that was physically and kinetically similar to native CYB5A solubilised through trypsin treatment [227]. The rat and human sequences were therefore aligned and the construct was truncated at the same place as the sequence of Beck von Bodman *et al.* The conservation between human and rat sequences is very high, allowing for easy identification of the equivalent human residues. Figure 4.9 outlines the CYB5A sequence and highlights the truncated position used to obtain the soluble form.

⁸ Document number: KAA, RBG, MAM 03/08-1

```

Human  MAEQSDEAVKYYTLEEIQKHNHSTWVILHHKVYDLTKFLEEHPGGEEVLREQAGGDATENFEDVG
Rat    MAEQSDKDKVYYTLEEIQKHKDSKSTWVILHHKVYDLTKFLEEHPGGEEVLREQAGGDATENFEDVG
      *****
Human  HSTDAREMSKTFIIGELHPDDRPKLNKPPETL
Rat    HSTDARELSKTYIIGELHPDDRSKIAPSETL
      *****
Human  ITTIDSSSSWWTNWVIPAISAVAVALMYRLYMAED
Rat    ITTVESNSSWWTNWVIPAISALVVALMYRLYMAED
      ***

```

Figure 4.9. Sequence alignment between human (CCDS12004.1) and rat (AAH86945.1) CYB5A. Underlined residues are present in full length (CYB5A) but not the soluble (CYB5S) protein used in these experiments. Asterisks show identical residues.

4.6.4. CPR and CPRS

The CPR gene is associated with only a single CCDS: CCDS5579 (RefSeq NP_000932) which encodes a 680 residue product. However, this sequence represents the longer of two in-frame sequences. A second start codon produces a protein truncated by three amino acids at the *N*-terminal, but is otherwise identical. This second start codon is annotated as having a stronger Kozak sequence (a consensus mRNA sequence involved in initiation of translation *via* ribosomal recognition) widely conserved outside of primates⁹. *In vivo* protein sequencing suggests that this shorter sequence is the primary product present and was therefore selected [233]. Hayashi *et al.* [226] have performed investigations using a truncated form of rat CPR, shortened by 56 residues at the *N*-terminal, which is the membrane binding region. Here, human CPR has been truncated in the same spot to form CPRS.

4.7. Results

4.7.1. Generation of EC538 pREP4 cells

Before placing another pQE9 plasmid into EC538 cells, the resident pQE9-HIDO plasmid first needed to be removed. Hill and Carlisle reported the loss of plasmids from *E. coli* after treatment with SDS at 44.5 °C [234]. Therefore, the HIDO expressing cells underwent heat shock in the presence of 0.1 g/L SDS, and cells were selected for resistance to kanamycin (pREP4) but sensitivity to ampicillin (pQE9) on agar plates (Figure 4.10). Twenty four colonies showed kanamycin resistance, of which two also displayed ampicillin sensitivity. Restriction analysis of these colonies confirmed that this was due to pQE9 loss, and not just loss of the resistance gene (Figure 4.11). pQE9 has a single *Sall* site, giving rise to a single 3.4 kb fragment. pREP4 has two *Sall* sites, giving rise to 2.5 and 1.2 kb fragments.

⁹ http://www.ncbi.nlm.nih.gov/nuccore/NM_000941

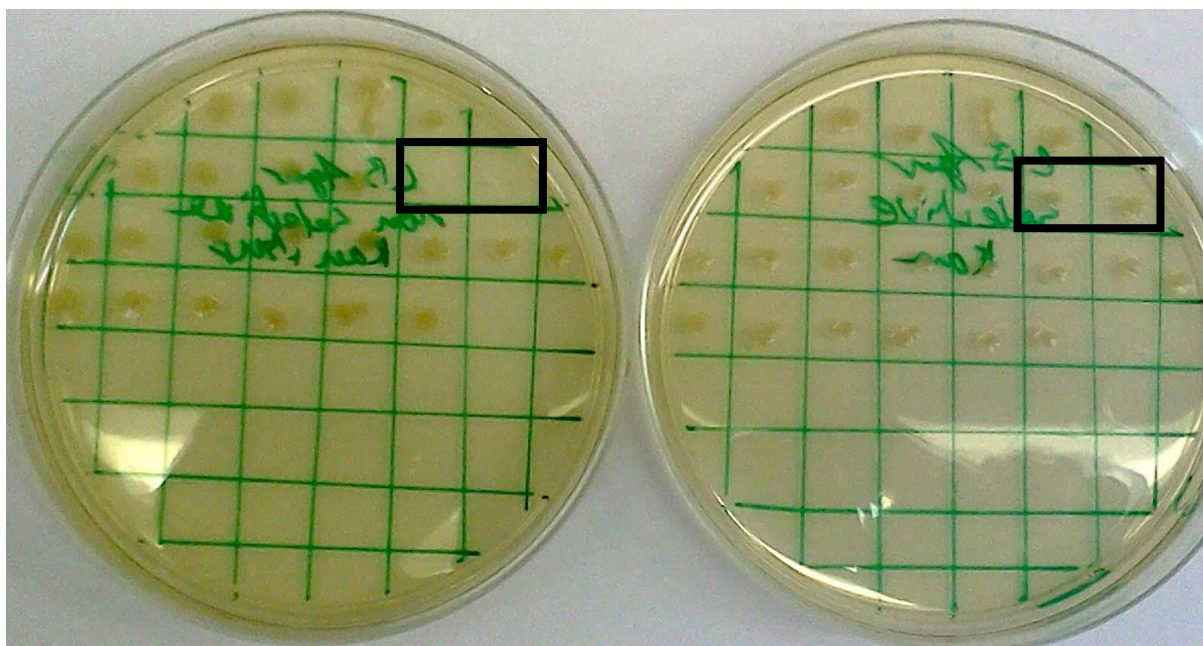


Figure 4.10. Left: Kanamycin and ampicillin plate. **Right:** kanamycin only plate. Boxed region shows stab points for two colonies that were sensitive only to ampicillin, indicating loss of pQE9 and retention of pREP4. These two colonies were streaked again onto plates for confirmation of resistance loss. Restriction analysis also confirmed the loss of pQE9-HIDO.

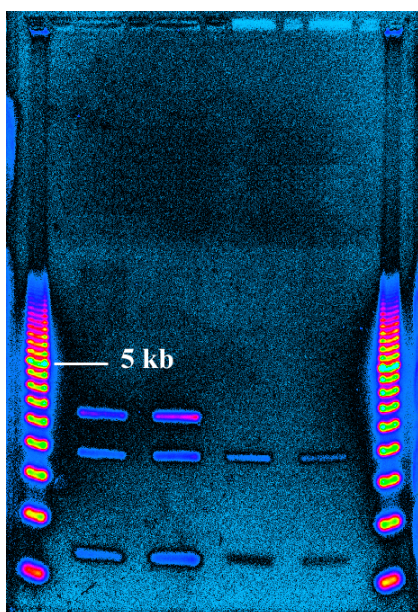


Figure 4.11. False colour image of agarose gel demonstrating the presence or absence of pREP4 and pQE9 plasmids. The false colour filter was applied due to the low concentration of DNA and therefore low staining that resulted. **Lane 1** and **6** were ladders. The 5 kb marker is indicated and all markers have a 0.5 kb spacing. **Lanes 2** and **3** were independent stocks of EC538 pREP4 pQE9 treated with SalI. **Lanes 4** and **5** were independent stocks of EC538 pREP4 treated with SalI. The bands were consistent with the expected 3.4 kb for empty pQE9, and 2.5 and 1.2 kb for the two pREP4 fragments.

4.7.2. Attempts at assembly *via* the Gibson reaction

Initial attempts at assembling WIDO, WCHIM and HCHIM into pQE9 *via* the Gibson reaction failed as did the positive control reaction provided with the Gibson reagents (which should yield a pUC19 vector with ampicillin resistance containing a 3 kb chloramphenicol resistance insert

between HindIII and AatII sites [New England Biosciences, USA, private communication]). After further extending the reaction time from 15 to 60 minutes, it was possible to obtain colonies of transformants from a Gibson reaction. However, restriction analysis showed all of these to be the empty pQE9 vector. The plasmid quantity and quality, as assessed by UV spectra, were lower than that expected based on the reported efficacy of the plasmid extraction kits in use. The plasmid isolation protocol were therefore investigated as a possible source of assembly failure, as was the transformation protocol.

4.7.3. Optimisation of plasmid isolation

Two plasmid extraction kits were compared. The GenElute Plasmid Miniprep kit from Sigma-Aldrich (USA, catalogue #PLN70) and the NucleoSpin EasyPure from Macherey-Nagel (Germany, catalogue #740727). Variables studied were the amount of cells extracted, the cell line used, the stage of cell growth and the use of plasmid copy-number amplification methods during cell growth.

Amount of cells extracted

Instructions included with the Sigma-Aldrich kits recommend growing the cells overnight in lysogeny broth (LB) and lysing 1-3 ml of culture for high copy plasmids. Alternatively, they recommend using only 1 ml of culture when using rich media such as Terrific Broth (TB). There was no recommended OD₆₀₀ for collection, but in this Ph.D. work an overnight culture of DH5α (37 °C) typically reached an OD₆₀₀ of 4 – 6, while EC538 pREP4 pQE9-HIDO typically reached an OD₆₀₀ of 6 – 8 under the same conditions. Comparatively, the Macherey-Nagel kit provides the following guidelines for an LB culture:

OD ₆₀₀	1	2	3	4	5	6
Culture volume /ml	15	8	5	4	3	2

Using the manufacturer's recommended amount of cells, the Sigma-Aldrich kit gave the results shown in Table 4.3. It was stated that up to 10 µg of plasmid DNA can be extracted with a DNA/protein absorbance ratio (UV absorbance: 260 nm/280 nm) of 1.7 – 1.9. Lower than this would indicate the presence of protein. Sigma-Aldrich do not give an expected DNA/salt ratio (260 nm/230 nm), but stated it should approach 2 for pure DNA. A ratio lower than this indicates the presence of salts. The yields obtained of 0.5 – 0.9 µg for 2 ml and 0.2 – 0.3 µg from 1 ml, were substantially below the expected 10 µg. By comparison, the Macherey-Nagel kit, using its recommended protocol, gave better results, although still below the expected mass of 15 - 30 µg stated for the kit (Table 4.3). Comparison of the Sigma-Aldrich kit and Macherey-Nagel kit (2.0 ml

vs 1.8 ml, both at an OD₆₀₀ of 6), showed a significant improvement when using the Macherey-Nagel kit of 0.7 – 0.9 vs. 1.4 – 1.8 µg.

Table 4.3. Isolation of plasmid from DH5α pQE9-HIDO at an OD₆₀₀ of 6 using the Sigma-Aldrich or Macherey-Nagel kits.

Sigma-Aldrich				Macherey-Nagel			
vol /ml	260/280 nm	260/230 nm	µg	vol /ml	260/280 nm	260/230 nm	µg
1.0	2.0 ± 0.1	1.6 ± 0.4	0.3 ± 0.1	1.8	1.7 ± 0.1	1.5 ± 0.2	1.6 ± 0.2
2.0	1.8 ± 0.1	1.8 ± 0.4	0.8 ± 0.1	3.6	1.7 ± 0.1	1.5 ± 0.1	3.3 ± 0.6
				7.2	1.6 ± 0.1	1.5 ± 0.1	1.1 ± 0.2

Results are the mean and 95% confidence interval of single replicates from 5 independent cultures of a single glycerol stock.

Effect of cell line

The above results suggest a general trend of higher yields at volumes between 2.0 and 3.6 ml of culture. Therefore, the Sigma-Aldrich kit was also tested at a higher volume of cells in addition to a comparison between EC538 and DH5α cells. The DH5α gave a significantly lower amount of DNA using the Sigma-Aldrich kit at 3.6 ml than EC538 (Table 4.4) – bearing in mind that EC538 is a dual plasmid system. There was no difference between the two kits at 3.6 ml of culture using EC538 pREP4 pQE9 cells. At 7.2 mls, the Sigma-Aldrich kit showed no difference to the Macherey-Nagel kit, remaining low, but the Macherey-Nagel kit was lower at 7.2 ml compared to 3.6 ml. There is no suggestion in this data that the cell line affects the yield.

Table 4.4. Isolation of pQE9-HIDO from DH5α and EC538 pREP4 cells at an OD₆₀₀ of 6 using the Sigma-Aldrich kits. Results represent single replicates from 5 biological replicates.

vol /ml	260/280 nm	260/230 nm	Yield /µg
DH5α pQE9-HIDO, Sigma-Aldrich			
3.6	1.8 ± 0.1	1.9 ± 0.2	1.9 ± 0.4
7.2	1.9 ± 0.1	1.4 ± 0.3	2.1 ± 0.8
EC538 pREP4 pQE9-HIDO, Sigma-Aldrich			
3.6	1.9 ± 0.1	2.0 ± 0.1	6.1 ± 2
EC538 pREP4 pQE9-HIDO, Macherey-Nagel			
1.8	1.9 ± 0.2	1.7 ± 0.1	1.6 ± 0.1
3.6	1.9 ± 0.1	1.7 ± 0.1	4.8 ± 0.6
7.2	1.7 ± 0.1	1.4 ± 0.2	1.6 ± 0.6

Results are the mean and 95% confidence interval of single replicates from 5 independent cultures of a single glycerol stock.

Effect of cell density

The effect of cell density (measured by OD₆₀₀) on the amount and purity of plasmid isolated was investigated (Table 4.5). The Macherey-Nagel kit was used to isolate DNA from 3.6 ml of culture at

an OD₆₀₀ of 1, 2 and 6, representing (roughly) the pre-exponential, mid-log and stationary phases of growth, respectively. In all cases, the isolated yield increased with increasing OD₆₀₀, as did variability. Using 7 ml of culture at an OD₆₀₀ of 3 showed no difference, suggesting that number of cells, rather than specifically the growth stage of the culture, was the more important factor. As such the amount of culture extracted in all experiments going forward was adjusted based on the relationship of the product of OD₆₀₀ and volume. For example, 3.6 ml x 6 OD₆₀₀ ≈ 7 ml x 3 OD₆₀₀ ≈ 21 OD₆₀₀.ml. Therefore a culture at an OD₆₀₀ of 4 would use 5.25 ml.

Table 4.5. Comparison of OD₆₀₀ and cell line on plasmid extraction from 3.6 ml.

OD ₆₀₀	260/280 nm	260/230 nm	µg
DH5α pQE9-HIDO			
1	1.9 ± 0.2	1.4 ± 0.3	0.3 ± 0.1
2	1.7 ± 0	1.6 ± 0.2	3.2 ± 0.7
6	1.7 ± 0.1	1.6 ± 0.1	3.6 ± 1
3 (7 ml)	1.8 ± 0.1	1.9 ± 0.2	3.2 ± 0.5
EC538 pREP4 pQE9-HIDO			
1	1.9 ± 0.2	1.6 ± 0.3	0.3 ± 0.1
2	1.8 ± 0.1	1.9 ± 0.1	1.8 ± 0.5
6	1.8 ± 0.1	1.9 ± 0.2	3.6 ± 1
3 (7 ml)	1.8 ± 0.1	1.9 ± 0.2	2.9 ± 1

Results are the mean and 95% confidence interval of single replicates from 5 independent cultures of a single glycerol stock.

Also tested was the effect of the ethanol washing step, used to desalt the DNA prior to elution from the membrane (Table 4.6). The standard procedure of the Macherey-Nagel kit calls for a single 450 µl wash. This was compared to washing twice with 225 µl or twice with 450 µl of ethanol. There was no discernible change in the quality, yield or variability in results.

Table 4.6. Effect of the ethanol wash procedure on plasmid extraction using EC538 pREP4 pQE9-HIDO, OD₆₀₀ 6 and 3.6 ml culture.

Ethanol vol /µl	260/280 nm	260/230 nm	µg
1x450	1.9 ± 0.1	1.9 ± 0.04	3.9 ± 1
2x225	1.9 ± 0.1	1.9 ± 0.1	3.5 ± 2
2x450	1.9 ± 0.1	2 ± 0.05	3.5 ± 2

Results are the mean ± SD of single technical replicates from 5 biological replicates of a single glycerol stock.

Amplification of plasmid copy number using heat or chloramphenicol

The addition of bacteriostatic chloramphenicol, or heat, during culturing of cells for plasmid extraction is known to increase copy numbers of certain vectors. Chloramphenicol can increase plasmid copy number due to preventing protein production, leading to cessation of chromosomal

DNA replication (which relies on short lived proteins) and cell division [235]. Plasmids are replicated using longer lived proteins, and therefore the plasmid copy number continues to increase while cells are unable to divide [236]. Heat (and other metabolic stresses) can affect plasmid copy number in cells through changes in both translation and transcription rates [235]. For plasmids that use relaxed control of plasmid replication (*i.e.* the plasmid replication is uncoupled from chromosomal replication) such as pUC and pQE plasmids, increased temperatures result in higher plasmid copy numbers. This is caused by a point mutation in the pre-primer RNA known as RNA II, leading to decreased interaction between RNA II and the replication repressive RNA known as RNA I [237]. Therefore, the effect of the addition of chloramphenicol or increased temperature to cultures was investigated.

Cells were grown to an OD₆₀₀ of 3, and then either treated with heat or chloramphenicol. Heat treatment involved the raising of the temperature from 37 °C to 42 °C for 14 hours. Chloramphenicol treatment involved addition of chloramphenicol to a final concentration of 0.17 mg/l, with continued incubation at 37 °C for 14 hours. The effect of delaying chloramphenicol treatment was also investigated, by growing cultures to an OD₆₀₀ of 6 prior to treatment. There were no significant differences across the treatments, with heat being just as effective as chloramphenicol, within error (Table 4.7). However, the treatments generally improved in the yields, compared to previous experiments without an amplification step. Tables 4.5 and 4.6 (above) show average yields of 4 µg, while Table 4.7 (below) show averages of 6 µg and above. The variances make it difficult to assert that the changes are statistically significant, however. Also worth noting is that the high copy number plasmid, pUC19, did not show any improvement in yields over the low copy number plasmids pQE9. Indeed, the highest results were obtained for the low copy number pET28a. Going forward, routine plasmid purification involved either growing the cultures to an OD₆₀₀ of 3, and then increasing the temperature to 42 °C for 12 – 16 hours, or growing to an OD₆₀₀ of 6 and then adding chloramphenicol to a final concentration of 0.17 mg/l and incubating for a further 12 – 16 hours.

Table 4.7. Amplification of plasmid yield through heat or chloramphenicol treatment.

Cell line	OD ₆₀₀ at time of intervention	OD ₆₀₀ at time of collection	DNA yield ^a / μ g	
			Heat	Chloramphenicol
DH5 α pUC19	3 \pm 0.2	5 \pm 0.4	9 \pm 1	
	3 \pm 0.2	3 \pm 0.2		7 \pm 3
	6 \pm 0.5	6 \pm 0.2		11 \pm 4
DH5 α pQE9-HIDO	3 \pm 0.2	5 \pm 0.2	9 \pm 6	
	3 \pm 0.2	4 \pm 0.2		6 \pm 1
	6 \pm 0.4	6 \pm 0.4		6 \pm 1
EC538 pREP4 pQE9-HIDO	3 \pm 0.4	7 \pm 0.4	13 \pm 6	
	3 \pm 0.4	6 \pm 0.4		7 \pm 1
	6 \pm 0.5	7 \pm 0.7		6 \pm 1
BL21(DE3) <i>Star</i> pET28a GUN4 ^b	6 \pm 0.5	7 \pm 0.4	13 \pm 6	15 \pm 4

Results are the mean \pm 95% CI of 5 independent cultures from a single glycerol stock.

^aYields are from a volume such that ml \times OD₆₀₀ = 21.

^bThe ~0.5 kb GUN4 gene present in the pET28a vector is unrelated to this project and was used as a BL21(DE3) *Star* pET28a example system.

4.7.4. Optimisation of transformation efficiency

Chemically competent cells were induced to uptake plasmid *via* a heat shock protocol employing rapidly heating ice-cold cells to 42 °C for 30 seconds followed by returning to ice for 2 minutes and then a 60 minute rescue in SOC media pre-warmed to 37 °C. However, use of this protocol after Gibson assembly failed to yield antibiotic-resistant colonies (colonies grew on unselective agar plates), or only yielded colonies containing empty vector. Therefore, an optimisation of the transformation efficiency was investigated as a means to increase the likelihood of obtaining assembled plasmids.

Initial experiments focused on the role of the amounts of DNA (0.1 – 10 ng) used to transform cells and the volume of SOC (0.25 – 5 ml, NEB) used to rescue cells (Table 4.8). The total number of colonies from each procedure increased both with increasing amounts of DNA and increasing volumes of rescue media. The efficiency of transformation (colony forming units/ μ g of DNA) decreased with increasing amounts of DNA. These observations were true regardless of the use of commercially obtained pUC19 (NEB) or pQE9-HIDO extracted from DH5 α cells. Cells were transformed into CCMB80 treated DH5 α cells, 50 μ l at an OD₆₀₀ of 1.

Table 4.8. Effect of plasmid amount and SOC volume on transformation results.

Plasmid ^a	DNA /ng	SOC /ml	CFU /ml of SOC	CFU /ml of SOC	CFU x10 ⁵ /ml of SOC/μg DNA
pUC19	0.1	0.20	25	12	1
			10		
			0		
	1		25	22	0.2
			35		
			5		
	10		100	45	0.05
			15		
			20		
	0.1	1	22	14	1
			13		
			7		
	1		123	82	0.8
			67		
			55		
	10		243	258	0.03
			333		
			198		
pQE9-HIDO	0.1	1	17	13	1
			15		
			7		
	1		44	67	0.7
			89		
			69		
	10		355	275	0.3
			245		
			226		
pUC19	0.1	5	424	305	30
			216		
			276		
	1		>500	>500	>5
			>500		
			>500		
	10		>500	>500	>1
			>500		
			>500		
pQE9-HIDO	0.1	5	326	246	20
			221		
			191		
	1		>500	>500	>5
			>500		
			>500		
	10		>500	>500	>1
			>500		
			>500		

^aCommercial pUC19 from NEB. pQE9-HIDO was isolated from DH5α. Results are inter-day replicates from a single batch of CCMB80 treated DH5α cells at OD₆₀₀ of 1 using aliquoted plasmid DNA stored at -80 °C in MilliQ water for < 7 days.

Next looked at was the effect of using manipulated DNA for transformation compared to the fresh unaltered plasmid used in the above tests. DNA that has been acted on by enzymes such as during restriction and ligation may be less coiled or retain scars from the enzymatic action that would not be present in freshly isolated plasmid (due to, for example, proof-reading and repair

mechanisms in the cell). Therefore, the altered plasmid would be expected to transform less efficiently. Two types of plasmids were used. The first was the positive control that comes with the Gibson reagents (New England Biosciences). This gives rise to an ampicillin resistant, pUC19-based, plasmid containing a chloramphenicol resistance insert between HindIII and AatII (3 kb in size, [NEB, private communication]). When performed according to the manual, the reaction should provide a theoretical 3.5 fmol of a 5.2 kb plasmid (12 ng) in a 20 µl reaction (0.6 ng/µl). Also used was the pQE9-HIDO plasmid (50 ng/20 µl, 2.5 ng/µl) isolated from DH5α, linearised with HindIII.

All reactions gave colonies under these conditions. This was expected of the negative control as digestion does not always go to completion, although the number of CFU should be much reduced. The HindIII digestion employed was 15 minutes at 37 °C and it is possible that fewer colonies would have resulted from a longer incubation. However, an average of 95 colonies per reaction was sufficiently different from an average of 245 colonies under equivalent conditions to still consider the negative control a success. The pQE9 reactions possessed a slightly lower transformation efficiency than the Gibson positive controls – perhaps due to a different conformation of the plasmid or due to contaminating salts/proteins (Table 4.9). It is not clear if these differences were caused by changes in the efficiency of the Gibson reaction, the cellular uptake of plasmid, or both.

Table 4.9. Transformation efficiency of Gibson treated plasmids.

Plasmid	Theoretical yield /ng	CFU /ml of SOC	Average CFU /ml of SOC	CFU x10 ⁵ /ml SOC/µg DNA
Gibson positive control	0.1	165	173	10
		235		
		120		
	0.2	125	145	7
		225		
		85		
	0.6	545	392	7
		345		
		285		
pQE9-HIDO (HindIII)	0.5	50	78	2
		65		
		120		
	0.8	85	158	2
		165		
		225		
	2.5	170	245	1
		260		
		305		
pQE9-HIDO negative control	2.5	100	93	0.1
		120		
		60		

^aAntibiotic resistant colonies.

From these results, it is clear that the Gibson reaction was capable of providing DNA that is transformable into CCMB80 treated DH5 α cells. However, transformation efficiency observed in all cases was below the $10^7 - 10^9$ cfu/ μ g quoted for commercial competent cells, even in the theoretically best case scenario of using commercially obtained pUC19. Electroporation was looked to as an alternative method, known to have increased transformation efficiency compared to heat shock methods. DH5 α cells were made electrocompetent through triple washing with ice-cold MilliQ water containing 10% glycerol (v/v). The efficiency of the cells were compared to commercially obtained NEB5 α electrocompetent cells. It was noticed that the commercial samples were of a significant higher density at around OD₆₀₀ of 20, compared to the OD₆₀₀ of 1 that had been used during heat shock experiments. It became evident that the higher cell density was beneficial in producing colonies in both electrocompetent and heat shock experiments, and all transformations were subsequently performed at this higher density.

Using the commercial pUC19 plasmid (0.1 ng) to transform into 50 μ l of either electrocompetent DH5 α cells prepared in-house, the commercial NEB α electrocompetent cells, or DH5 α cells treated in-house with CCMB80 gave transformation efficiencies of $1 \times 10^7 - 1 \times 10^8$, $2 \times 10^7 - 8 \times 10^8$, and $1 \times 10^6 - 1 \times 10^7$, respectively (initial OD₆₀₀ = 20, n = 3). This represents an approximate 10-fold increase for CCMB80 cells used at a lower density, and another 10 – 100-fold increase when using electroporation. These cells gave an average of 5×10^7 , 9×10^7 , and 2×10^7 CFU/ml/ μ g using the Gibson positive control, a modest improvement over CCMB80 cells at OD₆₀₀ of 1, indicating that the DNA coming from the Gibson reaction may still be a limiting factor. HindIII treated pQE9-HIDO plasmid after Gibson circularisation gave 4, 6 and 2×10^7 cfu/ml/ μ g respectively, indicating that there was no discernible difference between the positive control and the HindIII treated plasmid under these conditions. These results are summarised in Table 4.10.

Table 4.10. Transformation efficiency of Gibson reaction controls: electroporation versus heat shock at OD₆₀₀ of 20.

Plasmid	Cells	CFU $\times 10^3$ /ml of SOC ^a	CFU $\times 10^7$ /ml of SOC/ μ g of DNA
Gibson positive control	DH5 α electrocompetent	9	5
	NEB5 α electrocompetent	20	9
	DH5 α heat shock.	4	2
pQE9-HIDO, HindIII linearised	DH5 α electrocompetent	7	4
	NEB5 α electrocompetent	10	6
	DH5 α heat shock.	4	2

^aAntibiotic resistant colonies. Data are from single experiments.

Following these experiments, Gibson reactions were once again attempted for all IDO1, CYB5 and CPR constructs. WIDO and HIDOΔ360-370 were successfully placed into the pQE9 vector and electroporated into NEB5α cells. CYB5S failed to insert into pET28a using this method, however, did insert *via* restriction ligation into pQE9. Incompatible restriction sites prevented the use of this method for placing it into pET28a. Because the CYB5S gene was designed with its own 8xHis-tag, the construct thus contained a total of 14 His residues (6 from pQE9). Whilst such a large His-tag could be a problem for the protein's function and stability, the presence of the TEV protease site allows for it to be cleaved should the need arise, and so work proceeded with this construct.

At this stage, both the DNA fragments and the Gibson reagents were of an age that it was plausible they had degraded. In this time, the manufacturing of dsDNA by IDT had improved to the point that full length inserts could be ordered for all constructs except liposomal CPR. Therefore, for the remaining constructs excluding CPR (HCHIM, WCHIM, HIDOΔ371-380, CYB5A, and CPRS), full length inserts were ordered with internal restriction sites compatible with direct restriction-ligation into pUC19 and subsequent transference to an appropriate expression vector (either pQE9 or pET28a). CPR could not be manufactured by this process, but was ordered as a full length gene inside a proprietary sub-cloning vector based on pUC19.

4.7.5. Assembly *via* restriction-ligation

CPR arrived in a pUC19-derived plasmid, and was transformed into DH5α *via* heat-shock. The remaining genes of interest (HCHIM, WCHIM, HIDOΔ371-380, CYB5A, and CPRS) arrived as lyophilised linear dsDNA. The transformation efficiencies of inserting this DNA into a pUC19 DH5α system by heat shock is shown below in Table 4.11.

Table 4.11. Efficiencies of restriction-ligation of genes of interest into pUC19.

Gene	Transformants /ml of SOC plated ^a	Insert positive /ml of SOC plated	Insertion efficiency (%)
<i>HCHIM</i>	203	86	42
<i>WCHIM</i> (electroporation, NEB5α)	2614	1229	34
<i>HIDOΔ371-380</i>	183	151	83
<i>CYB5A</i>	417	386	93
<i>CPRS</i> (electroporation, NEB5α)	1241	119	8

^aAntibiotic resistant colonies. Data are from single experiments.

It was recognised that time constraints would prevent the complete kinetic characterisation of all proteins, thus only CPRS was carried forward into a BL21(DE3) pET28a expression host *via* a restriction-ligation method. This yielded (sequence confirmed) expressible constructs for HIDO, WIDO, HIDO Δ 360-370 and CYB5S in the EC538 pREP4 pQE9 system, and CPRS in the BL21(DE3) *Star* pET28a system.

4.8. Discussion

A major question of this thesis was to determine whether a 20 amino acid loop, unresolved in any crystal structure, played a significant role in IDO1 activity – such as through interaction with ligands or with supporting proteins (e.g. cytochrome P450:NAD[P]H reductase [CPR] or cytochrome b5 isoform A [CYB5A]). A multiple sequence alignment was performed to determine the level of conservation of the loop sequence across species. This identified that domestic ferret, walrus, and giant panda all possessed truncated sequences compared to other mammals (Figure 4.4). Assuming that these sequences are truly lost in the general population for these animals, it raises the question of whether the loop (or at least part of it) is needed for IDO1 function, or whether in these organisms its role is modified, unnecessary, or supplanted by another system. In addition to the loop, a small number of conserved residues are present around the periphery of the pocket opening, which may be useful to investigate in the future (Table 4.1).

IDO1 mutants were designed based on a multiple sequence alignment in which three animals were seen with putatively truncated loop sequences, compared to other species. This led to the design and construction of mutants of human IDO1 (HIDO) which were missing either the first or second half of the loop (HIDO Δ 360-370 and HIDO Δ 371-380, respectively). Additionally, walrus IDO1 (WIDO), which naturally contains a truncated loop sequence, was constructed. Chimeric structures of human (HCHIM) and walrus (WCHIM) IDO1 were also designed as controls against the influence of an extra-loop sequence.

Improvement of the Gibson assembly protocol for these constructs was achieved. In particular, optimising the DNA (UV) quantity and quality by first optimising amount of cells to be extracted from, was critical, and could be further improved by either heat or chloramphenicol-based plasmid amplification. The exact best method varied depending on the cell and vector being used. Only mild success was found using the Gibson reaction to construct sequences using more than one insert fragment, however, technological advancements continue in the field of synthetic DNA production, and this has become a minor issue.

Expressable constructs were generated for HIDO, WIDO, and HIDO Δ 360-370 proteins, as well as the soluble forms of the reductase (CPRS) and cytochrome b5 (CYB5S). The remaining proteins (HIDO Δ 371-380, HCHIM, WCHIM, and the liposomal forms of CPR and CYB5A) were generated in pUC19 vectors in DH5 α cells, and can be placed into expression vectors at will. Each of the IDO1 constructs was made with an uncleavable *N*-terminal 6xHis. CYB5S was originally designed to go into pET28a, but only the pQE9 construct was successful. Thus it contains both the 8xHis-tag of the designed CYB5S sequence, as well as the 6xHis-tag from the pQE9 vector. Between this 14xHis-tag and the CYB5S sequence resides a TEV recognition site, allowing for cleavage of the 14xHis-tag, if required. Finally, the BL21(DE3) *Star* pET28a-CPRS construct contains a TEV-cleavable 10xHis C-terminal tag. This subset of proteins was seen as sufficient to obtain preliminary data exploring the role of the loop during catalysis, and the role of electron donors (ascorbic acid or NAD(P)H *via* CPRS) and electron transporters (methylene blue, CYB5S).

4.9. Conclusion and future research

The identification of potentially naturally occurring truncated loops in some mammals raises interesting questions in regards to the function of IDO1. The confirmation of these loops will be a relatively trivial task in future work through mRNA sequencing and/or cDNA construction. It is also interesting in terms of the biology of the animals, and raises questions as to whether the larger sequences are appendix-like. Do they still possess important roles in today's biology, or are they left over from a previous time and simply haven't been selected against through recent evolution? A relatively simple experiment to answer these questions could take the shape of transgenic tissue or organism carrying these walrus, ferret, or panda genes, and probing both flux through the kynurenine pathway, and response of the immune system to challenges well described in the human literature, such as that presented in the first chapter.

4.10. Methods

4.10.1. Reagent sources

All water was MilliQ grade unless otherwise stated. Linear, double stranded, DNA was purchased from IDT, Singapore. Sequencing services were provided by Macrogen, South Korea. Sodium chloride (S9625), magnesium chloride (M8266), calcium chloride (223506), manganese (II) chloride (221279), magnesium sulfate (M7506), potassium acetate (P1190), EDTA disodium salt (E5134), acetic acid (A6283), α -D-glucose (G5767), and Tris (T1503), were from Sigma-Aldrich. High fidelity SalI (R3138), HindIII (R3104), NcoI (R3193) and XhoI (R0146) enzymes, NEB5 α electrocompetent cells (C2989K), pUC19 (N3041), and Gibson Assembly mix (E2611) were from New England Biolabs. T4 DNA ligase (M179A) was from Promega. FastAP (EF0654) was from Thermofisher, Australia. Agarose (1613100) was from Bio-Rad. Tryptone (211705), yeast extract

(212750), bacteriological agar (LP0011), and glycerol (GA010) were from Bacto. GelRed (41003) was from BioTium. X-gal (B1690) was from Life Technologies. IPTG (AST0487) was from Astral Scientific. Kanamycin (USP, 0405) and ampicillin (USP, 0339) were from Amresco. Chloramphenicol (6344333) was from Boehringer Mannheim. Electroporation reactions were carried out in a Gene Pulser Xcell (Bio-Rad) in 1 mm cuvettes (Bio-Rad). DNA concentrations were measured on a NanoDrop 2000 (Thermofisher) using an absorption coefficient of $50 \mu\text{g}^{-1} \text{cm}^{-1} \text{ml}$ (dsDNA).

4.10.2. Stock solutions

α -D-Glucose concentrate for SOC

A 50x concentrate of α -D-glucose for SOC formulations was made by dissolving 45 g in 250 ml of hot water that was then sterile filtered through a 0.20 μm membrane. Storage was at ambient temperatures for up to 3 months.

Antibiotics

Antibiotic stocks were made by dissolving kanamycin sulfate (100 mg/ml) or ampicillin sodium salt (50 mg/ml) in water. The stocks were then sterile filtered through a 0.20 μm membrane and aliquoted into 200 μl or 1 ml portions, before storage at -20°C for up to 6 months.

Chloramphenicol stocks consisted of chloramphenicol at 30 mg/ml in AR-grade ethanol and were stored at -20°C for up to 6 months.

CCMB80

Potassium acetate (0.98 g, 10 mmol), calcium chloride (11.8 g, 80 mmol) and magnesium chloride (2.0 g, 10 mmol) were dissolved in 100 ml of water. The pH was adjusted to 6.4 with 6 M HCl. Manganese chloride (4.0 g, 20 mmol) was then added and the solution sterile filtered through a 0.20 μm membrane. This was added to 900 ml of autoclaved water containing 10% (v/v) glycerol. The solution was stored at 4°C for up to 3 months.

Tris-Acetate EDTA

The 50x buffer consisted of Tris (24.2 g, 200 mmol), glacial acetic acid (5.71 ml, 100 mmol), and EDTA (14.6 g, 50 mmol) dissolved in 100 ml of autoclaved water, sterile filtered through a 0.20 μm membrane and stored in the fridge at 4°C for up to 12 months. 1x solutions were stored in the fridge for up to 3 months if sterile, or up to 1 week otherwise.

GelRed stain

GelRed dye (15 μl) was combined with 36 ml of water and 4 ml of a 1M solution of NaCl and stored in the dark at room temperature for up to 2 weeks. Each solution could stain up to 5 agarose gels (90 x 10 mm) without loss of sensitivity.

LB-Lennox

Tryptone (10 g), yeast extract (5 g) and NaCl (5 g) were completely suspended in a final volume of 1 litre of water and autoclaved at 121°C for 20 minutes.

Agar plates

Unless otherwise noted, agar plates used LB-Lennox media additionally containing agar powder (15 g/l). Individual plates (~15 ml in volume) were made selective by the spreading of 100 μl of desired antibiotic (kanamycin, 15 mg/ml stock, ampicillin, 7.5 mg/ml stock) across the top of

plates, and then incubating at 37 °C for 1 hour before use. Large batches of plates were made selective by adding the antibiotic to the agar solution once it had cooled to ~50 °C, prior to the pouring of plates. At the same time, plates intended for blue-white screening additionally received X-gal (20 µg/ml final concentration) and IPTG (0.1 mM final concentration) at ~50 °C, prior to pouring.

SOC

SOC broth used in the rescue of cells exposed to electroshock was obtained in conjunction with the NEB 5-alpha electrocompetent cells (Genesearch Australia, catalogue #C2989K) and used as received. All other uses of SOC was from media made in house.

SOC was made by adding tryptone (10 g), yeast extract (5 g), NaCl (5 g), KCl (2 g), MgCl₂ (1 g), and MgSO₄ (2.5 g) to 980 ml of water and autoclaving at 121 °C for 20 minutes. Upon cooling, α-D-glucose concentrate (20 ml) was added *via* a 0.2 µm syringe driven filter.

4.10.3. General protocols

General protocols for the handling of cells and DNA have been provided here. Please consult individual experiments within Chapter 4 for specified differences. Unless otherwise stated, all antibiotic selection was performed using ampicillin, 50 mg/ml (pUC19, pQE9), and kanamycin, 100 mg/ml (pET28a, pREP4).

Culturing for plasmid purification

Routine culturing for plasmid purification involved either growing a single colony in LB-Lennox media to an OD₆₀₀ of 3, followed by increasing the temperature to 42 °C for 12 – 16 hours, or growing to an OD₆₀₀ of 6 and then adding chloramphenicol to a final concentration of 0.17 mg/l and incubating for a further 12 – 16 hours.

Plasmid purification

Routine plasmid purifications used the Macherey-Nagel NucleoSpin minprep kit with modifications to volume and procedures from manufacturer's instructions. 3.5 ml of culture at an OD₆₀₀ of 6 (or 7 ml at an OD₆₀₀ of 3) was centrifuged in a 15 ml centrifuge tube at 5,000g for 10 minutes. The pellet was resuspended in 1 ml of autoclaved water, transferred to a 2 ml microcentrifuge tube and re-pelleted at 25,000g for 3 minutes. The supernatant was discarded and cells were completely resuspended in RNase-containing resuspension buffer (200 µl) by gentle pipetting. Lysis solution (400 µl) was then added and mixed with continuous, slow, inversion for 2 minutes. The sample was then neutralised with neutralisation buffer (600 µl), and mixed by gentle inversion several times until the blue colour of the solutions (an included pH indicator) turned colourless. The sample was centrifuged at 25,000g for 1 minute, and re-inspected. Any returning blue colour appeared to be due to expulsion of solution from the genomic DNA as it compressed, and could be cleared by inversion of the tube. Due to the large amount of genomic DNA, centrifugation proceeded for another 20 minutes. Prior to loading of the supernatant onto the included columns, the columns were washed with 200 µl of autoclaved water followed by 200 µl of 100% (AR-grade) ethanol. Columns were allowed to air dry for 10 – 20 minutes in a laminar flow cabinet. The supernatant was transferred to the top of column, being careful not to contaminate the pipette tip with genomic DNA, and allowed to stand for 1 minute before being centrifuged through the column at 2,000g for 2 minutes. If bubbles had formed during centrifugation, resulting in some supernatant still being on top of the column, it was spun

through the column at 5,000g for another 30 seconds. The column was then washed with 450 µl of ethanol-containing binding buffer by centrifuging at 5,000g for 30 seconds. The collected solvent was discarded and the sample was spun again at 5,000g for 30 seconds. The top of the column was loaded with 100 µl of autoclaved water and allowed to stand for 1 minute, before collecting the eluted plasmid DNA by centrifugation at 2,000g for 1 minute.

Assembly via Gibson reaction

Plasmid DNA was linearised with Sall (pQE9) or NcoI (pET28a), and the enzyme deactivated by heating at 60 or 80 °C for 10 minutes, according to the manufacturer's instructions. Linear plasmid DNA (50 ng, cooled to ambient temperature) was combined with gBlock inserts in a mole ratio of 1:3:3, plasmid:gBlock1:gBlock2. Reactions consisted of plasmid and gBlock inserts (combined volume of 5 µl in autoclaved water) and Gibson master mix (5 µl), incubated in a thermocycler at 50 °C for 30 minutes. Reactions were then diluted 1:4 with autoclaved water and 1 µl was electroporated into 50 µl of NEB5α *E. coli* cells.

Production of electrocompetent E. coli

A 200 ml culture of cells (with selection if appropriate, *e.g.* EC538 pREP4), was grown from a single colony at 25 °C with shaking to an OD₆₀₀ of 0.3 – 0.5 in SOC media. The cells were pelleted in 50 ml centrifuge tubes at 5,000g for 10 minutes at 4 °C, and the supernatant discarded. The cells were gently resuspended by pipetting in a total of 1.5 ml of ice cold 10% glycerol solution (sterile filtered through a 0.2 µm membrane), and centrifuged in a 2 ml microcentrifuge tube at 4 °C for 3 minutes. This process was repeated twice more. The cells were then gently resuspended in ice cold 10% glycerol solution to a final OD₆₀₀ of 20 (0.5 – 1 ml), and aliquoted into 50 µl portions in 0.2 ml thin walled centrifuge tubes. Tubes were flash frozen in liquid nitrogen, and stored in the bottom rear of a -80 °C freezer.

Production of chemically competent E. coli

Chemically competent cells were made in the same manner as electrocompetent cells, except exchanging ice cold CCMB80 buffer for the 10% glycerol solution.

Transformation of cells using electroporation

Electroporation cuvettes were made ice cold by submerging in ice inside its plastic packaging. To each cuvette was added 1 µl of DNA (0.5 – 1 ng). Immediately, 50 µl of electrocompetent cells (freshly removed from -80 °C and stored on ice), was added and quickly mixed by shaking. The contacts of the cell were dried of condensation with a lint-free tissue and immediately electroporated using 1.7 kV (1 mm cuvette). The cells were immediately transferred to 5 ml of SOC media, preheated to 37 °C for 1 hour. The culture was incubated at 37 °C in a 50 ml, foil-covered, centrifuge tube with shaking at 300 rpm for 60 minutes. Onto selective LB-Lennox agar plates, pre-heated to 37 °C for 1 hour, was plated 100 µl aliquots of the cells at dilutions (using SOC media at 37 °C) of 10x, 100x, 1,000x and 10,000x (2 plates per dilution). Plates were grown for 12 – 48 hours at 37 °C, until single colonies could confidently be picked. These colonies were spread by serial streaking across selective LB-Lennox agar plates. Single colonies visible after 16 hours were picked and stored as glycerol stocks.

Transformation of cells using heat shock

Chemically competent cells were removed from storage at -80 °C and immediately placed on ice to thaw (~5 minutes). To each aliquot was added 1 µl of DNA to a final concentration of 1 – 10 ng

per 50 µl of cells. The cells were mixed by pipetting and incubated on ice for 30 minutes. The cells were floated in a 42 °C water bath for 30 seconds and then immediately placed back on ice for 2 minutes. The cells were then transferred to 5 ml of SOC media, preheated to 37 °C for 1 hour. The culture was incubated at 37 °C in a 50 ml, foil-covered, centrifuge tube with shaking at 300 rpm for 60 minutes. Onto selective LB-Lennox agar plates, pre-heated to 37 °C for 1 hour, was plated 100 µl aliquots of the cells at dilutions (using SOC media at 37 °C) of 1x, 10x, 100x and 1000x (2 plates per dilution). Plates were grown for 12 – 48 hours at 37 °C, until single colonies could confidently be picked. These colonies were spread by serial streaking across selective LB-Lennox agar plates. Single colonies visible after 16 hours were picked and stored as glycerol stocks.

Bacterial glycerol stocks

Glycerol stocks were made by growing a single colony (grown on selective LB-Lennox agar plates) in 2 ml of selective LB-Lennox broth to an OD₆₀₀ of 2. The culture was diluted 1:1 with 40% (v/v) glycerol, that had been sterile filtered through a 0.2 µm membrane. Stocks were flash frozen in liquid nitrogen before being stored at -80 °C for up to 12 months. When the stocks were required for use, they were maintained on dry ice, and a scraping was taken from the top of the stock, to be spread across an agar plate by serial streaking for single colonies.

Restriction digestion of plasmid DNA

All digests using only one enzyme occurred in CutSmart buffer (New England Biosciences) with ~10 units of enzyme per µg of dsDNA, in a final volume of 50 µl, at 37 °C for 30 minutes. Digests using two enzymes, first had the enzymes diluted into CutSmart buffer, before transferring to the sample for digestion at 5 units per enzyme per µg of dsDNA. Excess enzyme resulted in band smearing on agarose gels, likely due increased glycerol concentrations allowing for less specific cleavage (star activity). The order of addition was always buffer, followed by water, then enzyme (and mixed), followed by DNA.

Agarose gels

DNA samples were analysed on a 1% agarose gel made by suspending 480 mg of agarose powder in 56 ml of autoclaved water and 4 ml of 10x TAE concentrate. The suspension was heated in a microwave oven in an uncapped Schott bottle in 1 minute increments, until 40 ml remained. Between 100 – 300 ng of DNA was loaded per lane, and stained overnight with GelRed.

Restriction-ligation – sub-cloning into DH5α pUC19

pUC19 (1 µg) in CutSmart buffer (50 µl final volume) was digested at 37 °C for 4 hours with 5 units each of HindIII and Sall, before being heat deactivated at 80 °C for 10 minutes. In a separate tube, 10 units of each enzyme was diluted into CutSmart buffer (50 µl final volume) and 5 µl of this was added to the required DNA insert (2.5 µl, 50 ng), before being incubated and heat deactivated in the same manner. Each tube was allowed to return to ambient temperature in air over the course of 20 minutes, before being placed on ice. To each insert digest (7.5 µl, 50 ng) was added digested pUC19 (2.5 µl, 50 ng), autoclaved water (7 µl), T4 DNA ligase buffer (2 µl) and, lastly, T4 DNA ligase (0.5 µl, 5-10 units). Samples were then incubated for 16 hours at 4 °C, before being heat deactivated at 65 °C for 10 minutes. Samples then transformed in DH5α cells using electroporation or heat shock. Electroporation experiments were transformed using 1 µl of a 1:10 dilution of the ligation reaction. Heat shock experiments used 1 µl of the ligation reaction directly. Selection of positive constructs occurred through blue-white screening.

Restriction-ligation into expression plasmids

The sub-cloned pUC19 constructs were digested either with Sall and HindIII (for inserts going into pQE9) or NcoI and XhoI (for pET28a) in CutSmart buffer at 37 °C for 6.5 hours using 1 µg of DNA, 3 units of each enzyme and 1 unit of FastAP. Separately, pQE9 or pET28a destination plasmid were digested under the same conditions in the absence of FastAP. All samples were heat deactivated at 80 °C for 10 minutes. Ligation occurred by the combining of digestion samples (2 µl of destination plasmid with 6 µl of pUC19 digest, ~3:1 insert-plasmid ratio), water (9 µl), ligation buffer (2 µl) and T4 DNA ligase (1 µl), and incubating at 4 °C for 16 hours, before heat deactivating at 65 °C for 10 minutes. Samples were then transformed into either EC538 pREP4 cells (pQE9 plasmids) or BL21 (DE3) *Star* (pET28a plasmid) by heat shock using directly 1 µl of the ligation reaction. Selection of colonies for pQE9-containing cells occurred on agar containing 0.06 mg/l chloramphenicol in addition to kanamycin (100 mg/l) and ampicillin (50 mg/l) to select against EC538 pREP4 pUC19 cells.

Generation of EC538 pREP4 cells from EC538 pREP4 pQE9-HIDO

A single colony was grown in 5 ml of LB-Lennox broth containing kanamycin (100 mg/l) and ampicillin (50 mg/l) overnight at 37 °C to an OD₆₀₀ of 7. The cells were pelleted and washed with fresh LB-Lennox media twice before 100 µl was diluted in 50 ml of fresh LB-Lennox broth containing kanamycin (100 mg/l) and grown at 37 °C to an OD₆₀₀ of 2. 500 µl of this was incubated at 44 °C for 45 seconds and then placed on ice for 2 minutes. The cells were rescued in SOC media at 37 °C for 30 minutes with shaking. 100 µl of 10⁴ and 10⁶ dilutions (using SOC media) were plated onto LB-Lennox agar plates containing either kanamycin (100 mg/l) or kanamycin and ampicillin (100 and 50 mg/l). The kanamycin plate yielded 24 colonies (2 x10⁶ CFU/ml), while the doubly selective plate yielded 10 colonies (1 x10⁶ CFU/ml). All 24 colonies from the kanamycin plate were stabbed onto two LB-Lennox agar plates containing either kanamycin (100 mg/l) or kanamycin and ampicillin (100 and 50 mg/l), one stab onto each plate. These plates had an externally drawn grid to match single colonies to each other across the plates. Of these 24, 22 grew on both plates. The two colonies that possessed sensitivity to ampicillin went through an identical round of selection a second time. Both colonies were confirmed to be missing the pQE9 plasmid by restriction digestion with Sall.

Appendix to Chapter 4

Multiple sequence alignment of mammalian ID01s

Human	1	MAH----	AMENSWT	TSKEYHIDE	EVGFALPN	QENLPD	FYNDWM	FI	AKHLP	DLIES	GQLR			
Gorilla	1	MAH----	AMENSWT	TSKEYHIDE	EVGFALPN	QENLPD	FYNDWM	FI	AKHLP	DLIES	GQLR			
Rhesus	1	MAH----	AMENSWT	TSKEYHIDE	EVGFALPN	QENLPD	FYNDWM	FI	AKHLP	DLIES	GQLR			
Marmoset	1	MAH----	AMENFCT	TSKEYHIDE	EVGFALPN	PLENLP	DVYNDW	MS	IAKHLP	DLIES	GQLR			
Pig	1	MALDWW	SPMDNS	WKIFEYH	IDEDVGF	ALPNLE	ELPHPY	DAWIA	IAKNLP	ELIKNG	GQLR			
Rabbit	1	-----	MGTSWET	TEEHIDK	DIGFALP	NPLEEL	PSDYD	VWFI	AKN	TELIET	GQLR			
Orca	1	MAPGKSS	PVETSW	KIFEYH	IDEDVGF	ALPNLE	ELPHPY	DAWIS	IAKNLP	ELIKNG	GQLR			
galago	1	MAEGAVS	PRDSSW	ETEEYHI	EDVGFAL	PTPLEK	LPDKYN	AWMD	IAKRLP	LIKTDQ	LR			
cow	1	MAGDMSS	PVENSW	TFKEYH	IDEDVGF	ALPYPLE	ELPHPY	DAWIS	IAKNLP	ELIKNNQ	LR			
Goat	1	MAADKSS	PVEKSW	TFKEYH	IDEDVGF	ALPLEE	ELPHPY	DAWIS	IAKNLP	ELINNNQ	LR			
Sheep	1	MAADKSS	PMEKSW	TFKEYH	IDEDVGF	ALPLEE	ELPHPY	DAWIS	IAKNLP	ELINNNQ	LR			
Pika	1	-----	MEPCWQ	ILKEH	IDEDVGF	ALPNLE	ELPSDY	DPWV	IAKN	PELIKTR	QLR			
Walrus	1	MAHNRL	IMESSP	EIFBK	YHIDE	EVGFALP	NPLEEL	PPYDE	WIC	IAKNLP	ELIEKNEL			
Dog	1	MEDDGIL	LMESPQ	RIFBK	YHIDE	EMGFALP	NPLEK	LP	PPYDE	WIS	IAKNLP	ELIKKNEL		
Shrew	1	MAHEMAPP	VESYWK	IEEYHI	DEALGF	ALPTPLE	ELPYD	AWIL	IAKNLP	ELIQNGE	LR			
Chinchilla	1	MAQNRTS	PMEISW	ETLKQY	HIDEDV	GFALPN	PLEEL	PEKYNA	WIL	IAKNLP	ELIKTGQLR			
Panda	1	MAHNRTPL	TKSSQ	EIFBK	YHIDE	EVGFALP	NPLEEL	PPYDE	WIS	IAKNLP	ELIDKNEL			
Ferret	1	MAHNATDF	MGNSQ	EIFBK	YHIDKE	IGFALPK	PLEEL	PSPYDE	WIS	IAKNLP	ELIEKNEL			
consensus	1	ma		me	sw	Ifeeyh	Idedv	GFALPn	PlEeLP	pYd	Wi	IAknlp	ELI	gqLR

Human	57	ERVEKLN	MLSIDH	LTDHKS	QRLARL	VLVGC	ITMAYV	WGK	CHGD	VRKVL	PNIAV	PYCQ	LSK		
Gorilla	57	ERVEKLN	MLSIDH	LTDHKS	QRLARL	VLVGC	ITMAYV	WGK	CHGD	VRKVL	PNIAV	PYCQ	LSK		
Rhesus	57	ERVEKLN	MLSIDH	LTDHKS	QRLAHL	VLVGC	ITMAYV	WDK	CHGD	VRKVL	PNIAV	PYCQ	LSK		
Marmoset	57	ERVEKLN	MLSIDH	LTDHKS	QRLAHL	VLVGC	ITMAYV	WDK	CGGD	VRKVL	PNIAV	PYCQ	LSK		
Pig	61	AEVEKL	ATLSID	GLQGHK	MORLAH	LVLYG	ITMAYV	WGG	ED	IRKVL	PNIA	PYCK	LSE		
Rabbit	53	MKVEKL	PILSID	KLEGH	QRLAHL	VLGYI	TMAYV	WGG	DGD	IRKVL	PNIA	PYCK	LSE		
Orca	61	AEVEKL	TTFSID	GLQGHK	LORLAH	LVLYG	ITMAYV	WGE	DGD	VRKVL	PNIAV	PYCK	LSE		
galago	61	AEVEKL	PILSID	DLQGHK	SQRLAR	LALGYI	TMAYV	VWNG	DGD	VCK	LP	NI	AVPYCE	LSE	
cow	61	VEVEKL	ATLNID	GLRGH	AQRLAHL	VLGYI	TMAYV	WGG	DGD	IRKVL	PS	NI	AVPYCK	LSE	
Goat	61	VEVEKL	ANLSID	GLRGH	KAQRLAHL	VLGYI	TMAYV	WGR	DGD	IRKVL	PS	NI	AVPYCQ	LSE	
Sheep	61	VEVEKL	AKLSID	GLRGH	KAQRLAHL	VLGYI	TMAYV	WGR	DGD	IRKVL	PS	NI	AVPYCQ	LSE	
Pika	53	EEVEKL	PILGID	QLKEH	QRLCHL	LALGYI	TMAYV	WDQ	DGD	IRKVL	PNIAV	PYCQ	LSE		
Walrus	60	KKVDQ	LKNH	SIDAL	RDHKS	QRLAHL	LALGYI	TMAYV	VWNG	DGD	VRKVL	PNIAV	PYCK	LSE	
Dog	61	KKVDQ	ELKLS	IDGLS	GHKLOR	LARLAL	GYITMAYV	VWNG	DGD	VRKVL	PNIA	PYCE	LSE		
Shrew	61	ANVEKL	PKLSID	DLQGHK	SQRLAHL	VLVGC	ITMAYV	VWNG	DGD	VRK	LP	SNIA	PYCE	LSE	
Chinchilla	61	EEVEKL	PILSID	DLKEYE	QQLCHL	LALGYI	TMAYV	VWNR	ADD	VRKVL	PS	NI	AVPYCE	LSE	
Panda	61	EKVQ	QELK	HSID	ALGHKS	QRLAHL	LALGYI	TMAYV	VWNG	DGD	VRKVL	PNIAV	PYCE	LSE	
Ferret	61	ERVQ	QELQ	HSID	GLGHKS	QRLAHL	TLGYI	TMAYV	VWNG	DGD	KDVR	EVL	PNIAV	PYCE	LSE
consensus	61	rVekl	mlsID	gLrghks	QrLahLvL	GYITMAYV	W	kgdg	Dvrkv	LPrNI	AvPYC	lSe			

Human	117	KLELPP	ILVYAD	CVLANW	KKKDPN	KPT	TYENMD	VLFS	FRD	GDCSK	GFFLV	SLLVE	IAAAS	
Gorilla	117	KLELPP	ILVYAD	CVLANW	KKKDPN	KPT	TYENMD	VLFS	FRD	GDCSK	GFFLV	SLLVE	IAAAS	
Rhesus	117	KLGLPP	ILVYAD	CVLANW	KKKDPN	KPT	TYENMD	VLFS	FRD	GDCSK	GFFLV	SLLVE	IAAAS	
Marmoset	117	KLQ	LPPI	LVYAD	CVLANW	KKKDPN	KPT	TYENMD	VLFS	FRHT	DCSK	GFFLV	SLLVE	IAAAS
Pig	121	KLGLPP	ILVYAD	CVLANW	KKKDPN	SGPMTY	KNMD	ILFS	FP	GGDCG	KGFFLV	SLLVE	IAAAS	
Rabbit	113	KLGLPP	ILVYAD	CVLANW	KKKDPN	SGPMTY	ENMD	ILF	YFPG	EDCA	KGFFLV	SLLVE	IAAAS	
Orca	121	KLGLPP	ILVYAD	CVLANW	KKKDPN	SGPMTY	ENMD	ILF	YFPG	DCG	KGFFLV	SLV	VEIAAAS	
galago	121	KLGLPP	ILVYAD	CVLANW	KKDPNG	PMTYENMD	ILFS	FP	GGDCG	KGFFLV	SLLVE	IAAAS		
cow	121	KLGLPP	ILVYAD	CVLANW	KKKDPN	SGPMTYENMD	ILFS	FP	GGDCG	KGFFLV	SLLVE	IAAAS		
Goat	121	KLGLPP	ILVYAD	CVLANW	KKKDPN	SGPMTYENMD	ILFS	FP	GGDCG	KGFFLV	SLLVE	IAAAS		
Sheep	121	KLGLPP	ILVYAD	CVLANW	KKKDPN	SGPMTYENMD	ILFS	FP	GGDCG	KGFFLV	SLLVE	IAAAS		
Pika	113	KLGLPP	ILVYAD	CVLANW	KKKDPN	SGPMTYENMD	ILF	YFPG	EDCA	KGFFLV	SLLVE	IAAAS		
Walrus	120	KLGLPP	ILVYAD	CVLANW	KKKDPN	SGPMTYENMD	ILF	YFPG	DCSK	GFFLV	SLLVE	IAAAS		
Dog	121	KLGLPP	ILVYAD	CVLANW	KKKDPN	SGPMTYENMD	ILF	YFPG	DCSK	GFFLV	SLLVE	IAAAS		
Shrew	121	KLGLPP	ILVYAD	CVLANW	KKKDPN	SGPMTYENMD	ILF	YFPG	DCSK	GFFLV	SLLVE	IAAAS		
Chinchilla	121	KLGLPP	ILVYAD	CVLANW	KKKDPN	SGPMTYENMD	ILF	YFPG	DCSK	GFFLV	SLLVE	IAAAS		
Panda	121	KLGLPP	ILVYAD	CVLANW	KKKDPN	SGPMTYENMD	ILF	YFPG	DCSK	GFFLV	SLLVE	IAAAS		
Ferret	121	KLGLPP	ILVYAD	CVLANW	KKKDPN	SGPMTYENMD	ILF	YFPG	DCSK	GFFLV	SLLVE	IAAAS		
consensus	121	KLgLPPI	LvYAD	CVLANW	KkKDPNg	PmtYe	NMDiL	Fs	Fpggd	CskGFF	LvSLl	VEiaAas		

Human	177	AIKVIPTVFRAMQMQRDTLLKALLEIASCLEKALQVFHQIHEHVNPKAFFSVLRIYLSG
Gorilla	177	AIKVIPTVFRAMQMQRDTLLKALLEIASCLEKALQVFHQIHEHVNPKAFFSVLRIYLSG
Rhesus	177	AIKEIPTVFRAMQLQERDTLLKALLEIASCLEKARQVFQIHEHVNPNAFFSVLRIYLAG
Marmoset	177	AIKEIPTVFRAMQMQLDTRKALLKIASCLEKALQVFHQIHEHVDPPQFFNVLRILYLSG
Pig	181	AIKVIPTIENATQCEDLDLQKALLDITSSSLHKALEVFHQIHEYVDPKLFNVLRILYLSG
Rabbit	173	AIKTIPTVFRSAMQHQRDTLQKALLDVSCLNKALEVFHQIHEHVDPKLFFNVLRILYLSG
Orca	181	AIKVIPTIENATQREDPTLTKALLDIASCLHKALEFHQIHEYVDPNLFNVLRILYLSG
galago	181	AIKVIPTIFRAVKCQDQDALKKGLNEIASSLKEAKTVFQIHEYVDPNLFNVLRILYLSG
cow	181	AIKVIPSIFDAVQRKSDTLQKALLEISSLHKALEVFSQIHKYVDPNLFNVLRILYLSG
Goat	181	AIKVIPNIFDAVQREDTDTLQKALLDISSSLHKAREAFSQIHEYVDPNLFNVLRILYLSG
Sheep	181	AIKVIPNIFDAVQREDTDTLQKALLDISSSLRKAKKAFSQIHEYVDPDLFFSVLRILYLSG
Pika	173	AIKTIPTVFRSAVQQQKQDSTLQKALEDITSGCLKALKVFHQIHEHVDPKLFFNVLRILYLSG
Walrus	180	AIKVIPDLFAVKNEDQDTLQKALCYIASCLRQARKEFEQINEYVDPSTFFNVLRILYLSG
Dog	181	AIKVIPNLFKAVKNQDEVTLKKALHYIASCLRHAKKEFEVHKHVDPSTFFKVLRIYLSG
Shrew	181	AIKVIPSIFKAVQEQDQNTLKNALSEIASCLHKALEVFHQIHEYVDPNLFNVLRILYLSG
Chinchilla	181	AIKVIPITVLQAVQRQDKDTLQNTLLDMANCLRNARKVFEEIHGYVDPDLFFNVLRILYLSG
Panda	181	AIKVIPDLFAVKNEDQNALQKALCYIASCLHQAHKEFEQINEYVDPSTFFNVLRILYLSG
Ferret	181	AIKVIPDLFAVKNEDQNALQKALRYIASSLRQARKEFEKMHKYVDPNTFFNVLRILYLSG
consensus	181	AiKvIPTvfKAvq qd dtLqkaLleiascLhkAl vF qiheyVdP lFfnVLRiYLSg

Human	237	WKGNPQLSDGLVYERFWDPKEFAGGSAQSSVFQCFDVLGLGIQQTAGG---GHAAQFLQ
Gorilla	237	WKGNPQLSDGLVYEGFWDPKEFAGGSAQSSVFQCFDVLGLGIQQTAGG---GHAAQFLQ
Rhesus	237	WKGNPQLSDGLVYEGFWGPKKFAGGSAQSSIFQCFDVLGLGIQQTAGG---GHAAQFLQ
Marmoset	237	WKGNPQLSEGLMYDGFWDKAKQFSGGSAQSSIFQCFDVLGLGIPORAGG---GSAAQFLQ
Pig	241	WKGNPLLSEGLLYEGVWDTPKKFAGGSAQSSIFQCFDVLGLGVOHTVGGVPSGSAAGFLQ
Rabbit	233	WKGNSQLPEGLLYEGVWDTPKKFAGGSAQSSIFQCFDVLGLGIQQKDSG---ESAEFFLQ
Orca	241	WKGNPLLSEGLLYEGVWDTPKKFAGGSAQSSIFQCFDVLGLGIQHTVGGVPSDSAAKFLQ
galago	241	WKGNPQLSEGLLYEGVWDTPKKFAGGSAQSSVFQCFDVLGLGIQHEAGK---ESAAEILR
cow	241	WKGNPLLSEGLLYEGVWDTPKKFAGGSAQSSIFQCFDVLGLGIQHSIGG---DSAAEFLQ
Goat	241	WKGNPLLSEGLLYEGVWDTPKKFAGGSAQSSIFQCFDVLGLGIQHTVGG---DSAAEFLQ
Sheep	241	WKGNPLLSEGLLYEGVWDTPKKFAGGSAQSSIFQCFDVLGLGIQHTVGGVPSDSAAEFLQ
Pika	233	WNDNSKLEPEGLLYEGVWDTPKKAGGSAQSSIFQCFDVLGLSIQSDGG---ESAAAFLO
Walrus	240	WKGNSQLPEGLKYEGFWDTPKKEFAGGSAQSSIFQCFDVLGLGIQSSGE---EFAARFLQ
Dog	241	WKGNSKLEPEGLKYEGFWNPKKEFAGGSAQSSIFQCFDVLGLGIQCCSGE---EFAAEFLQ
Shrew	241	WKGNPLLSEGLLYEGVWDTPKKFSGGSAQSSIFQCFDVLGLGIQKQDADGVQPESSGL-FLQ
Chinchilla	241	WKGNPKLPNGLLYEGVWDDPKQFAGGSAQSSIFQCLDALLGIEQTTGG---GPAAEFLK
Panda	241	WKGNSQLPEGLKYEGFWNTPKQFAGGSAQSSIFQCFDVLGLGIQSSGD---ESARFLQ
Ferret	241	WKNSSKLPKGLKYEGFSDTPREYAGGSAQSSIFQCFDVLGLGIQCKSGE---ESAARFLQ
consensus	241	Wkgnp LseGLLYegvwdtpkkfagGSAaQSSiFQCfDvLLgiqqt gg esaa flq

Human	294	DMRRTYMPPAHRNFLCSLESNPSPSVREFVLSKGDAGLREAYDACVKALVSLRSYHLQIVTKY
Gorilla	294	DMRTYMPPAHRNFLCSLESNPSPSVREFVLSKGDAGLREAYDACVKALVSLRSYHLQIVTKY
Rhesus	294	DMRTYMPPAHRNFLYSLESSPSPSVREFVLSKGDAGLREAYDACVKALVSLRSYHLQIVTKY
Marmoset	294	DMRTYMPPAHRNFLCSLESNPSPSVREFVLTSGDAGLREAYDACVKALVNLRNHYHLQIVTKY
Pig	301	EMRTYMPPAHRNFLHSLESPPSPSVREFVLSKGDALLQETYNCEVQAMVSLRNHYHLQIVTKY
Rabbit	290	DMRTYMPPAHRGFLGSLEAAPSITREFVLSKGDAGLQEAAYDKCVKALVALRSYHLQIVVAKY
Orca	301	EMRTYMPSAHQNFLRSLESPPSVRKFFVLSKGDATLQETYNCEVQAMVSLRNHYHLQIVVAKY
galago	298	EMRTYMPPAHQAFGLGSLESPPSVREFVLSQGDADLRKAMDECVAAMVNLRSYHLGIVSKY
cow	298	EMRTYMPPAHHSFLLSLKSPSVREFVLSGNATLQETIYNKCVQAMVSLRNHYHLQIVAKY
Goat	298	EMRTYMPPAHQSFLLSLKAKPSVREFVLSKGNATLQKIYNECEAMVSLRNHYHLQIVAKY
Sheep	301	EMRTYMPPAHQSFLLSLKAKPSVREFVLSKGNATLQKTYNECEAMVSLRNHYHLGIVAKY
Pika	290	EMRTYMPPAHRGFLGSLEAAPSITREFVLSKGDAGLREAYDKCVKALVDLRNHYHLQIVTKY
Walrus	297	EMRKYMPPAHQEFLLLSLESPPSVRKFFVLSKGDCLKQADYNECVKAMVSLRNHYHLQIVTKY
Dog	298	EMRNYMPPAHRDFFLLLSLESPPSVREFVLSDDVELKADYNECVKAMVSLRKHYHLKIVAKY
Shrew	300	EMRKYMPPAHQNFLLSLESPPSVRKFFVLSVDNASLQNTYNKCVRAMVSLRNHYHLNVVAKY
Chinchilla	298	EMRTYMPPAHQDFLYFLESPPSVREFVLSDDADLKEAYDKCVQALVSLRSYHLGVVTKY
Panda	298	EMRNYMPPAHQEFLLLSLESPPSVREFVLSKGDPKLRADYNECVNAMVSLRNHYHLQMVAKY
Ferret	298	EMRKYMPPAHRDFFLLLSLESPPSVREFVLSKGDTELQADYNECVKAMVSLRNHYHLIVSKY
consensus	301	eMRtYmPpAhr FL sLesgPSvReFvlskgda Lqe YneCvkAmVsLRnYHLqiVtkY

```

Human      354  ILIPASQQPKENKTSEDPSKLEAKGTGGTDLMNFLKTVRSTTEKSLLKEG
Gorilla    354  ILIPASQQPKENKTSEDPSKLEAKGTGGTDLMNFLKTVRSTTEKSLLKEG
Rhesus     354  ILIPASQQPKENKTSEDPSKLDAKGTGGTDLMEFLKTVRSTTEKYRLKEG
Marmoset   354  VLIPASQKSK-NKTSKAPSEEENKGTGGTDLMNFLKTVRTTTQNSLLKEG
Pig        361  IVIPASQQAKKKQASEEPSEEENRGTGGTNVIDFLKTVRGTTVRSLLKEG
Rabbit     350  IVIPARQKAKEKEGEEKPSALENQGTGGTDVMNFLKTVRGTTEKSLLKEG
Orca       361  IVIPASQPSKRKPTSEEPSEPKNKGTGGTDFMGFLKTVVRNTTVNSLLKED
galago     358  IMEPARQQQGPKNKSEEPS--ENKGTGGTDIMKFLTVTNTTQKFRLKDG
cow        358  IVIPARQQPQVEENLEE----ENRGTGGTNVMDFLKTVRSKTKNSLLKEE
Goat       358  IMIPASRQSKVERSSEEEASESESKGTGGTNIMDFLKTVRVKTTVNCLLKED
Sheep      361  IMIPASRQSKVERSSEEEASESESKGTGGTNIMDFLKTVRVKTTVSCLLKED
Pika       350  IVIPARQKSGKNGKAEEPSLENQGTGGTDVMNFLKTVRGTTEKSLLKEG
Walrus     357  IVIP-----SNQQESKGTGGTSVMTFLKSVRGTTENFLLRDN
Dog         358  IVIPASQQPKNNQASEESSEQKNKGTGGTNAMDFLKSVRTTETEKFLLIH
Shrew      360  IVGPARLQSKAQKTSEESAEPTNKGTGGTNIMTFLKTVRSRTEMFEVEEQ
Chinchilla 358  VLDPAKQKSREEETGSEQLEQEHRTGTGGTDFMNVLKAVRTKTTQSLLKR
Panda      358  IVIP-----SNKQENKGTGGTSVMTFLKSVRGTTENFLLRDN
Ferret     358  IVRP-----SCQQDNKGTGGTDIMTFLKSVRDTTKSFQL-EK
consensus  361  iviPasqq k tseepse enkGTGGTdlm fLktVr tTe sllke

```

Highlighted in red are the residues 360-380 (human numbering), which corresponds to the unresolved loop. Alignment performed in ClustalOmega (www.clustal.org) using default parameters. Box shading provided by the BoxShade server: (http://www.ch.embnet.org/software/BOX_form.html).

NCBI accession numbers used for alignment:

Organism	NCBI RefSeq
Homo sapiens (human)	AEF30540
Gorilla gorilla gorilla (western lowland gorilla)	XP_004046983
Macaca mulatta (Rhesus monkey)	NP_001070951
Sus scrofa (pig)	NP_001233169
Ailuropoda melanoleuca (giant panda)	XP_002918587
Odobenus rosmarus divergens (Pacific walrus)	XP_004394518
Mustela putorius furo (domestic ferret)	XP_004813156
Canis lupus familiaris (dog)	XP_532793
Callithrix jacchus (white-tufted-ear marmoset)	XP_002757028
Orcinus orca (killer whale)	XP_004286560
Ochotona princeps (American pika)	XP_004592787
Bos taurus (cattle)	XP_005226159
Otolemur garnettii (small-eared galago)	XP_003801142
Oryctolagus cuniculus (rabbit)	XP_002720846
Capra hircus (goat)	XP_005698936
Sorex araneus (European shrew)	XP_004606980
Chinchilla lanigera (long-tailed chinchilla)	XP_005410595
Ovis aries (sheep)	AGV28563

Primers

All primers were provided by Macrogen (South Korea).

Plasmid	Primer	Macrogen Product Number
pQE9-Forward	CCCGAAAAGTGCCACCTG	pQE-F
pQE9-Reverse	GTTCTGAGGTCATTACTGG	pQE-R
pET28a-Forward	TAATACGACTCACTATAGGG	T7-Promoter
pET28a-Reverse	GCTAGTTATTGCTCAGCGG	T7-Terminator
pUC19-Forward	GTTTTCCTCCAGTCACGAC	M13F-pUC
pUC19-Reverse	CAGGAAACAGCTATGAC	M13R-pUC

pQE9 H1D0 – translated sequencing results

MRGSHHHHHHGSVDMAHAMENSWTISKEYHIDEEVGFPALPNPQENLPDFYNDWMFIAKHLPLDIESGQLRERVEKLNMLSIDHLTDHKSQR
LARLVLCITMAYVWVGKHGHDVRKVLPRNIAVPYCQLSKKLELPPIVYADCVLANWKKKDPNKPLTYENMDVLFSSFRDGDSCSGFFLVSL
LVEIAAASAIKVIPTVFKAMQMQRDITLLKALLEIASCLEKALQVFHQIHDHVNPKAFFSVLRILYLSGWKGNPQLSDGLVYEGFWEDPKF
AGGSAGQSSVFCQFDVLLGIQQTAGGGHAAQFLQDMRMYMPAHRNFLCSLESNPVSREFVLSKGDAGLREAYDACVKALVSLRSYHLQIV
TKYILIPASQQPKENKTSDEPSKLEAKGTGGTDLNMFLLKTVRSTTEKSLKEG

H1D0Δ360-370_Ordered_DNA_Sequence

gBlock1

GGATCGCATCACCATCACCATCACGGATCCGTCGACATGGCGCATGCGATGGAAAACAGCTGGACCATTAGCAAAGAATATCATATTGATG
AAGAAGTGGGCTTTGCGCTGCCGAACCCGCAGGAAAACCTGCCGGATTTTATAACGATTGGATGTTTATTGCGAAACATCTGCCGGATCT
GATTGAAAGCGGCCAGCTGCGCGAACGCGTGGA AAAACTGAACATGCTGAGCATTGATCATCTGACCGATCATAAAAGCCAGCGCCTGGCG
CGCCTGGTGTCTGGGCTGCATTACCATGGCGTATGTGTGGGGCAAAGGCCATGGCGATGTGCGCAAAGTGCTGCCGCGCAACATTGCCGTGC
CGTATTGCCAGCTGAGCAAAAACCTGGAAGTCCGCCGATTCTGGTGTATGCCGATTGCGTGTGGCGAACTGGAAAAAAAAGATCCGAA
CAAACCGCTGACCTATGAAACATGGATGTGCTGTTAGCTTTCGCGATGGCGATTGCAGCAAAGGCTTTTTCTGGTGAGCCTGCTGGTG
GAAATTGCGGGCGCGAGCGGATTAAGTGATTCCGACCGTGTTTAAAGCGATGCAGATGCAGGAACGCGATACCCTGCTGAAAGCGCTGC
TGGAATTCGAGAG

gBlock2

CGCGATACCCCTGCTGAAAGCGCTGCTGGAAATTGCGAGCTGCCTGGAAAAAGCGCTGCAGGTGTTTCATCAGATTATGATCATGTGAACC
CGAAAGCGCTTTTATGCGTGTGCGCATTTATCTGAGCGGCTGGAAAGGCAACCCGAGCTGAGCGATGGCCTGGTGTATGAACGCTTTTG
GGAAGATCCGAAAGAATTTGCGGGCGCGAGCGCGGCCAGAGCAGCGTGTTTCAGTGCTTTGATGTGCTGCTGGGCATTCAGCAGACCGCG
GGCGGCGGCCATGCGGCGCAGTTTCTGAGGATATGCGCGCTATATGCCGCGCGCGCATCGCAACTTTCTGTGAGCCTGGAAAGCAACC
CGAGCGTGCGCAATTTGTGCTGAGCAAAGGCGATGCGGGCTGCGCGAAGCGTATGATGCGTGCCTGAAAGCGCTGGTGAGCCTGCGCAG
CTATCATCTGCAGATTGTGACCAAATATATTCTGATTCCGGCGAGCCGAGCAAACCTGGAAGCGAAAGGCACCGCGCGACCGATCTGATG
AACTTTCTGAAACCGTGCGCAGCACCACCGAAAAAAGCCTGCTGAAAGAAGGCTAACTGCAGCCAAGCTTAATTAGCTGAGCTTGAGCTC
CT

pQE9 H1D0Δ360-370 – translated sequencing results

MRGSHHHHHHGSVDMAHAMENSWTISKEYHIDEEVGFPALPNPQENLPDFYNDWMFIAKHLPLDIESGQLRERVEKLNMLSIDHLTDHKSQR
LARLVLCITMAYVWVGKHGHDVRKVLPRNIAVPYCQLSKKLELPPIVYADCVLANWKKKDPNKPLTYENMDVLFSSFRDGDSCSGFFLVSL
LVEIAAASAIKVIPTVFKAMQMQRDITLLKALLEIASCLEKALQVFHQIHDHVNPKAFFSVLRILYLSGWKGNPQLSDGLVYERFEDPKF
AGGSAGQSSVFCQFDVLLGIQQTAGGGHAAQFLQDMRMYMPAHRNFLCSLESNPVSREFVLSKGDAGLREAYDACVKALVSLRSYHLQIV
TKYILIPASPSKLEAKGTGGTDLNMFLLKTVRSTTEKSLKEG

H1D0Δ371-380_Ordered_DNA_Sequence

GGCGGCGTCGACCATCACCATCACCATCACATGGCTCACGCGATGGAGAACAGCTGGACGATTAGCAAGGAATATCACATTGATGAGGAGG
TAGGGTTCGCGTTACCAAATCCACAAGAGAACTTACCGGATTTTATAACGACTGGATGTTTATTGCGAAGCATCTCCCGACCTGATTGA
GAGCGGACAGCTGCGCGAACGGGTGGAAAAGCTTAATATGCTTAGTATTGATCATTTAACTGATCATAAAAGTCAGCGCTTAGCCCGCTG
GTGCTGGGTTGTATTACGATGGCATATGTATGGGGCAAAGGTCACGGCGATGTCGCAAGGTGCTCCACGTAACATCGCGGTGCCGTATT
GCCAGCTGAGTAAGAAGCTTGAGCTGCCGCCATTCTGGTCTATGCGGATTGCGTTCTGGCGAACTGGAAGAAGAAGGATCCGAACAAGCC
ACTGACATACGAGAACATGGATGTGCTGTTTCAGTTTCCGCGATGGTGACTGTAGTAAGGGCTTCTTCTAGTTTCATTACTGGTGAAATT
GCGGCTGCCAGCGCCATCAAAGTAATTCCAACCGTCTTCAAGCGATGCAAAATGCAGGAACGGGACACACTCCTGAAGCGCTGCTGGAGA
TTGCGAGCTGTCTGGAGAAGGCCCTGCAAGTGTTCACCAGATTACGACCATGTAAATCCGAAGGCTTTCTTCTCCGTGCTGCGTATTTA
CCTGTGAGGTTGGAAGGGCAACCTCAACTTAGTGACGGCTGGTATATGAACGCTTTTGGGAAGATCCGAAGGAGTTCGAGCGCGCTCT
GCAGGCCAATAGTGTGTTTCCAATGCTTCGACGTGCTGCTGCGCATCCAGCAAACGGCTGGCGGCGGTGATGCTGCTCAGTTCTTCAGG
ATATGCGTCTTATATGCTCCCGCTCACCGCAACTTCTGTGTAGCTTGGAGTCCAACCTTCAGTGCGCGAATTTGTGTTGTCGAAGGG
GGATGCGGGTTTACGTGAGGCATATGATGCATGTGTCAAGGCCCTGGTGTCTCTCCGCTCTTATCACTTACAGATTGTAACGAAGTACATT
TTGATTCCCGCAAGTCAGCAACCTAAGGAGAATAAGACGAGCGAGGATGGTACCGATTAAATGAACCTTCTGAAAACGGTCCGGAGCACTA
CTGAGAAGTCTTGTCTTAAGGAGGGCTAATAGAAGCTTGGCGCG

pUC19 H1DOΔ371-380 – translated sequencing results

MRGSHHHHHHGSVDMAHAMENSWTISKEYHIDEVGFALPNPQENLPDFYNDWMFIAKHLPLDIESGQLRERVEKLNMLSIDHLTDHKSQR
LARLVLGCITMAYVWVGKHGHDVRKVLPRNIAVPYCQLSKKLELPPIILVYADCVLANWKKKDPNKPLTYENMDVLFSDRGDCSKGFFLVSL
LVEIAAASAIKVIPTVFKAMQMQRDITLLKALLEIASCLEKALQVFHQIHDHVNPKAFFSVLRIYLSGWKGNPQLSDGLVYERFWEDPKEF
AGGSAGQSSVFQCFDVLGLGIQQTAGGGHAAQFLQDMRRYMPAHRNFLCSLESNPSVREFVLSKGDAGLREAYDACVKALVLSRSHYHLQIV
TKYILIPASQQPKENKTSDEGTDLMNFKLTVRSTTEKSLLEKG

W1DO_Ordered_DNA_Sequence

gBlock1

GGATCGCATCACCATCACCATCACGGATCCGTCGACATGGCGCATAACCGCCTGCTGATGGAAAGCAGCCCGGAAATTTTGA AAAATATC
ATATTGATGAAGAAGTGGGCTTTGCGCTGCCGAACCCGCTGGAAGAACTGCCGCCGCCGTATGATGAATGGATTGCGATTGCGAAAAACCT
GCCGGAACCTGATTGAAAAAACGAACTGCCGAAAAAAGTGGATCAGCTGAAAAACCATAGCATTGATGCGCTGCGCGATCATAAAAGCCAG
CGCCTGGCGCATCTGGCGCTGGGCTATATTACCATGGCGTATGTGTGGAACAGGGCGATGGCGATGTGCGCAAAGTCTGCCGGA AAAACA
TTGCGGTGCCGTATTGCAAACAGAGCAAAAACCTGGGCCTGCCGCCGATTCTGGTGTATGCGGATTGCGTGTGGCGAACTGGAAAAAAA
AGATCCGAACGGCCCGATGACCTATGAAACATGGATATTTCTGTTTTGGTTTTCCGGCGCGCATTTGCAGCAAAGGCTTTTTCTGGTGAGC
CTGCTGGTGGAATTGCGGGCGCGAGCGCGATTAAAGTGATTCCGGATCTGTTTAAAGCGGTGAAAAACGAAGATCAGGATACCTGCAGA
AAGCGCTGTGCTAT

gBlock2

GAAGATCAGGATACCTCGCAGAAAGCGCTGTGCTATATTGCGAGCTGCCTGCGCCAGGCGCGCAAAGAATTTGAACAGATTAACGAATATG
TGGATCCGAGCACCTTTTATAACGTGCTGCGCATTTATCTGAGCGGCTGGAAGGCAACAGCCAGCTGCCGGAAGGCTGAAATATGAAGG
CTTTTGGGATACCCCGAAAGAATTTGCGGGCGCGAGCGCGCGCAGAGCAGCATTTTTCAGTGCTTTGATGTGCTGCTGGGCATTGAGCAG
AGCAGCGCGCAAGAATTTGCGGGCGCGCTTTCTGCAGGAAATGCGCAAATATATGCCGCCGCGCATCAGGAATTTCTGCTGCTGCTGGAAA
GCGGCCCGAGCGTGCACAAATTTGTGCTGAGCAAAGGCGATGATAAAGTGCAGGCGGATTATAACGAATGCGTGAAAGCGATGGTGAGCCT
GCGCAACTATCATCTGCAGATTGTGACCAATATATTTGTGATTCCGAGCAACAGCAGGAAAGCAAAGGCACCGGCGGCACAGCGTGATG
ACCTTTCTGAAAAGCGTGCGCGGCACCAACGAAACCTTTCTGCTGCGCGATAACTAAGTGCAGCAAGCTTAATTAGCTGAGCTTGGACTC
CT

pQE9 W1DO – translated sequencing results

MRGSHHHHHHGSVDMAHNRLLMESSPEIFEKYHIDEVGFALPNPLEELPPPYDEWICIAKNLPELIEKNELRKKVDQLKNHSIDALRDHK
SQRHLALALGYITMAYVWNQDGDVVRKVLPRNIAVPYCKLSEKLGLPPIILVYADCVLANWKKKDPNGPMTYENMDILFWFPGDCSKGFFL
VSLLVEIAAASAIKVIPLDLFKAVKNEDQDTLQKALCYIASCLRQARKEFEQINEYVDPSTFYNVLR IYLSGWKGNSQLPEGLKYEGFWDTP
KEFAGGSAAQSSIFQCFDVLGLGIQQSSGEEFAARFLQEMRKYMPPAHQEFLLLLESGPSVRKFVLSKGDCLKQADYNECVKAMVSLRNYHL
QIVTKYIVIPSNQESKGTGGTSVMTFLKSVRGTTENFLLRDN

HCHIM_Ordered_DNA_Sequence

GGCGGCGTCGACCATCACCATCACCATCACATGGCTACGCTATGGAGAACAGCTGGACCATTTCGAAAGAATACCATATTGACGAAGAAG
TTGGGTTCGCTCTTCCGAACCCCAAGAGAACCTTCCCGACTTTTATAACGACTGGATGTTTATCGCCAAACACTTGCCGGATCTTATCGA
AAGCGGCCAGCTGCGCGAACGGGTAGAGAAGCTGAACATGCTTAGTATTGACCATCTGACGGATCACAAGAGTCAACGTCTCGCTCGTTTA
GTGCTCGGTTGCATCACGATGGCCTACGTGTGGGGCAAAGGCATGGTGATGTTTCGTAAAGTCTTACCCCGTAATATCGCCGTTCTTATT
GTCAGCTGAGCAAGAAGCTGGAATTACCGCGATTCTGGTTTACGAGATTGCGTTCTGGCTAATTGGAAGAAGAAGATCCAAACAAACC
TTTAACATATGAGAACATGGATGTTTTGTTAGCTTCCGTGATGGCGATTGTTCTAAGGGTTTCTTTCTTGTCAGTTTACTGGTCGAAAT
GCCGCCGATCGGCCATCAAGGTTATTCCGACCGTTTTTAAAGCCATGCAGATGCAGGAACGTGATACGCTGCTCAAAGCTCTGTTGGAAA
TCGCATCTCGCTGGAGAAAGCTCTGCAGGTCTTTCATCAGATTCTGACCATGTGAATCCGAAGGCATTCTTCTCTGTACTGCGTATCTA
TTTAAGCGGTTGGAAAGGTAACCCGAGCTCTCTGACGTTTTGGTGTACGAACGTTTTCTGGGAAGACCCGAAAGAATTGCGCGCGGTTCTG
GCGGGCCAGAGCTCGGTGTTTCAATGCTTCGACGTACTGCTTGGCATCCAGCAGACTGCCGCGGAGGACATGCGGCGCAATTCTCTGCAGG
ACATGCGTCGCTATATGCCACCTGCTCATCGCAACTTCCTGTGTAGCTGGAGTCTAATCCTAGCGTGCGTGAATTTGTTCTTTTGAAAGG
TGACGCGGGGCTTCGGGAAGCGTACGATGCGTGTGTCAAGGCTTTAGTGTCAGTGCCTTCATATCATCTCCAGATCGTAACCAATACATT
CTGATCCCGGTAGCCAGCAGGAGTCTAAAGGTACGGGAGGCACCGACCTGATGAATTTCTGAAGACCGTTCTGCTCCACCACGGAGAAGT
CCTTATTAAAGAAGGCTAATAGAAGCTTGCGGG

pUC19 HCHIM – translated sequencing results

MRGSHHHHHHGSVDMAHAMENSWTISKEYHIDEVGFALPNPQENLPDFYNDWMFIAKHLPLDIESGQLRERVEKLNMLSIDHLTDHKSQR
LARLVLGCITMAYVWVGKHGHDVRKVLPRNIAVPYCQLSKKLELPPIILVYADCVLANWKKKDPNKPLTYENMDVLFSDRGDCSKGFFLVSL
LVEIAAASAIKVIPTVFKAMQMQRDITLLKALLEIASCLEKALQVFHQIHDHVNPKAFFSVLRIYLSGWKGNPQLSDGLVYERFWEDPKEF
AGGSAGQSSVFQCFDVLGLGIQQTAGGGHAAQFLQDMRRYMPAHRNFLCSLESNPSVREFVLSKGDAGLREAYDACVKALVLSRSHYHLQIV
TKYILIPASQQESKGTGGTDLMNFKLTVRSTTEKSLLEKG

WCHIM_Ordered_DNA_Sequence

GGCGGCGTCGACCATCACCATCACCATCACATGGCGCACAATCGCTTGCTGATGGAATCTTCACCGGAGATCTTCGAGAAATACCATATTG
ACGAAGAAGTTGGATTGCGCTGCCGAACCCGCTGGAAGAACTGCCTCCGCCGTATGATGAATGGATCTGCATCGCCAAGAACCTGCCCGA
ACTGATTGAGAAGAATGAACCTGCGGAAGAAAGTGGATCAATTAAAGAACCATAGCATTGATGCACTCCGTGATCACAGTCGCAACGCTTA
GCGCATTTAGCGTTAGGGTATATTACGATGGCTTATGTTTGAACCAAGGCATGGTGATGTCCTGTAAGTGCTTCTGAGAACATCGCTG

TCCCCATTATGCAAACCTCAGTGAGAAGCTTGGCCTGCCTCCAATTCTGGTGTATGCGGACTGCGTTCTGGCGAATTGGAAGAAGAAAGATCC
GAATGCCCCGATGACGTACGAGAATATGGATATTCTGTTTTGGTTTCCGGGTGGAGATTGCTCGAAGGGGTTCTTCCCTGGTGAGCCTGCTG
GTAGAGATTGCCGCGGCTCGGCAATCAAAGTCATCCCGGATCTGTTAAAGCTGTTAAGAATGAAGATCAGGATACCTCTGCAGAAAGCAC
TGTGCTACATTGCCTCGTGTCTGCGTCAGGCCCGCAAAGAATTGCAACAGATTAACGAATATGTCGATCCGAGTACCTTCTATAACGTCTT
ACGCATTTATCTGTCTGTTGGTTGGAAAGCAATAGCCAGTTACCCTGAAGGGCTGAAATACGAAGGCTTCTGGGATACGCTTAAAGAATTTCGCT
GGAGGATCCGCTGCCAGTCTCTATTTTTCAATGTTTTGATGTTCTGCTGGGGATTGAGCAGTCTAGTGGGAAGAATTTGCGGCGCGCT
TCCTGCAGGAAATGCGCAAATATATGCCTCCGGCGCATCAAGAATTTCTGCTGTTGCTGGAGTCCGGCCCTAGCGTGCCTAAATTTGTTCT
TTCCAAGGGAGACGACAAGTTACAGGCGGATTACAATGAGTGTGTGAAAGCAATGGTCAGCCTGCGTAACTACCACCTGCAAATCGTGACC
AAGTACATTGTAATTCGTCGAACCAACAACCGAAAGAGAATAAGACCTCTGAAGATCCATCGAAATTAGAAGCGAAGGGTACGGGGGTA
CATCCGTAATGACCTTCCTGAAATCCGTTCTGTGGCACAACCGAGAACCTTTCTTCTGCGGATAACTAATAGAAGCTTGGCGGC

pUC19 WCHIM translated sequencing results

MRGSHHHHHHSVDMAHNRLLMESSPEIFEKYHIDEVGFALPNPLEELPPPYDEWICIAKNLPELIEKNELRKKVDQLKNHSIDALRDHK
SQRLAHLALGYITMAYVWNQGDGDKVRLPENIAVPYCKLSEKLGPPILVYADCVLANWKKDPNGPMTYENMDILFWFPGGDCSKGFFL
VSLLEIAAASAIKVIPDLFKAVKNEDQDTLQKALCYIASCLRQARKEFEQINEYVDPSTFYNVLRILYLSGWKNSQLPEGLKYEGFWDTP
KEFAGGSAAQSSIFQCQFDVLLGIQQSSGEEFAARFLQEMRKYMPPAHQEFLLLLLESGPSVRKFVLSKGDDKLQADYNECVKAMVSLRNYHL
QIVTKYIVIPSNQQPKENKTSKLEAKGTGGTSVMTFLKSVRGTTENFLLRDN

CYBA_Ordered_DNA_Sequence

GGCGGCGTCGACCATCACCATCACCATCACCATCAGGAGAACCTGTACTTCCAGGGCATGGCCGAACAGTCCGATGAAGCGGTGAAGTACT
ATACACTGGAAGAGATTGAGAAGCATAATCACAGTAAGTCTACGTGGCTGATCCTCCACCATAAGGTTTACGATCTGACGAAGTTCTTGGA
GGAACATCCCGCGCGGTGAAGAAGTTTTGCGGGAGCAGGCTGGGGCGGATGCTACAGAGAACCTTGAGGACGTTGGCCATTCGACTGATGCG
CGTGAGATGAGCAAGACCTTTATTATTGGCGAATTACATCCGGATGATCGTCTTAAGCTGAATAAGCCGCCGGAGACCTGATTACGACCA
TCGATTCTTCGTCTAGCTGGTGGACGAACCTGGGTATTCCCGCCATCTCGGCCGTGGCTGTTGCACTGATGTACCGCTGTACATGGCCGA
AGATTAATAGAAGCTTGGCGGC

pUC19 CYB5A

Plasmid was not sequenced. Restriction analysis showed a construct of the correct size.

CYBS_Ordered_DNA_Sequence

ATAACAATTCCTCTAGAAATAAATTTGTTTAACTTTAAGAAGGAGATATACCATGGTCGACCACCATCACCATCACCATCACCATGAGA
ACCTGTATTATTCGAAGGTCAGTCAGATGAAGCCGTCAGTATTATACTCTTGAAGAAATTCAGAAACACAACCACTCAAAAAGCACATGGCT
GATTCTGCACCACAAAGTATACGATCTTACGAAATTCCTGGAAGAACACCCGGCGGCGAGGAGGTGCTCCGTGAACAAGCCGGGGGGGAC
GCGACAGAAAACCTTTGAGGACGTGGGCCATAGTACGGATGCACGCGAAATGTCAAAAACCTTTATTATTGGAGAAGTGCATCCGGATGACC
GTCCGAAACTTAACAAACCTCCGGAGACGCTGTAATAGGGATCCAAGCTTGGATCCGAATTCGAGCTCCGTCGACAAGCTTGGCGGCCGAC
TCGA

pQE9 CYB5S – translated sequencing results

MRGSHHHHHHSVDHHHHHHHHENLYFQGSDEAVKYTTLEEIQKHNSKSTWLILHHKVYDLTKFLEEHPGGEEVLREQAGGDATENFED
VGHSTDAREMSKTFIIGELHPDDRPKLNKPPETL

CPR_Ordered_DNA_sequence

ATGGGGGATTGCGATGAAGACACGTCCGCCACCATGCCCGAAGCTGTGCGGAAGAAGTGAGTCTGTTCTCAACTACGGATATGGTGCTTT
TTAGCCTGATTGTTGGGGTCTGACGTATTGGTTATTTTCGCAAAAAAAAAAGAGGAAATTCGGAATTTAGCAAAATCCAGACCACCGC
TCCGCTGTAAAGAAAGCTCCTTTGTGGAATAAATGAAAAAACCGGCCGTAACATCATCGTATTCTACGGCTCGCAGACAGGTACTGCT
GAAGAATTTGCCAATCGTTTGTCAAAGGATGCACACCGTTACGGGATGCGCGGGATGAGCGCGATCCGGAAGAATACGATCTTGCTGATC
TTTCTTCATTACCGGAGATCGATAAGTCGTTGGTAGTGTTCATGCGCCACCTACGGGGAAGGCGACCCAACCGATAACGCGCAGGATTT
TTACGATTGGCTGCAAGAGACCGATGTCGACCTTACGGGCGTGAAAGTTGCGGTGTTTGGTCTGGGGAACAAACGTACGAACATTTCAAT
GCAATGGGCAAGTATGTGGATCAGCGCTTGAACAACCTGGGGGCGCAGCGGATCTTCGAAGTGGGCTTGGCGATGACGATGGAACCTTAG
AAGAAGACTTCATTACATGGCGCGAACAATTCGGCGGCGGTGTGCGAGTTTTTCGAGTTGAAGCGACCGGTGAAGAATCGAGTATCCG
TCAGTACGAACCTGTTGTGCACGAAGACATGGACGTCGTAAGTGTACACAGGTGAGATGGGTCGGTTGAAATCCTACGAAAATCAGAAA
CCCCCTTTGATGCCAAAAACCCATTCCTTGGCGCAGTAACAGCCAACCGTAACTGAATCAAGGTACGGAACGCCACTTAATGCATCTGG
AACTGGATATTAGCGATTCAAAAATCCGGTATGAATCAGGCGACACGTTGCGGTGTATCCTGCGAACGATAGCGCGCTTGTAAACCAAT
TGGCGAGATTCTGGGCGCAGACCTGGACGTCATTATGTCCTGAACAACCTGGACGAAGAATCAAACAAAAAGCATCCATTTCCCTGCCCCG
ACGACTTACCGACCGCACTGACCTATTATTAGACATTACAAATCCTCCACGTACGAATGTTCTTTATGAGTTGGCGCAGTACGCTAGCG
AACCATCTGAGCAAGAACACTTACATAAAATGGCATCGAGTTACGGGGAGGGGAAAGAACTCTACCTGTCTTGGGTTGTAGAAGCTCGGCG
TCATATCTTAGCCATTCTCAGGATTATCCCTCCCTGCGCCGCGCCATCGACCATCTGTGTGAAGTCTTCCGCTCTGCGAGGCCGCTAT
TATAGCATCGCGTCATCCAGCAAGAGTGCATCCCAATAGCGTCCACATCTGCGCGGTGGCGGTGCGAGTACGAGGCGAAATCAGGCGGTGCA
ATAAAGGGGTCGCGACGTCATGGCTCCGTGCGAAGGAGCGCGGCGGCGAAAAATGGTGGTCTGCCCTGGTACCGATGTTTGTGCGGAAGTC
TCAGTTTCGTCTGCCATTCAAAAGTACCACGCGGCTGATTATGGTTGGCCCGGGGACCGGTATTGCGCCGTTTATGGGCTTCATTGAGGAA
CGGGCGTGGTTACGTGAGCAAGGTAAAGAAGTGGGCGAACTTTGCTTTATTATGGCTGTCGTCGCTCCGATGAAGATTATCTGTACCGGTG
AAGAGTTGGCTCGCTTTTCATAAAGATGGTGTCTGACGCAATTAAACGTGGCTTTTAGCCGTGAACAGGCACATAAAGTGTACGTGACGCA
CCTTCTGAAGCGCGATCGTGAACATCTGTGGAAGCTGATCCATGAGGCGCGCGCCATATTTACGTCTGTGGTGACGCCCGCAACATGGCT
AAAGATGTTCAAAACACCTTCTATGATATTGTGGCAGAGTTTGGTCCGATGGAACATACGAGGCGGTGGACTATGTCAAAAACCTGATGA

CCAAAGGCCGCTATTTCGCTGGACGTTTGGAGCGAAAACCTCTACTTTCAAGGAGCGGGGGCGGCCATCACCATCATCATCATGGAGGCGG
GGGGCACCACCATCATCATCATTAATGA

pIDT CPR

Plasmid appeared to be the correct size by digestion analysis, but was not sequenced.

CPRS_Ordered_DNA_Sequence

TCATCAGTCGACCCATGGGCCAGACGACTGCTCCGCCGGTGAAGGAGAGCTCTTTCGTCGAGAAGATGAAGAAGACAGGCCGGAATATCAT
CGTGTTTTATGGCTCCCAGACCGGTACGGCCGAAGAGTTTCGCGAACCGCTCTCTAAAGATGCGCACCGCTACGGTATGCGGGGTATGTCT
GCGGATCCTGAAGAGTATGATCTGGCAGACCTGAGTTCTCTTCCGGAAATCGATAAGAGCCTCGTTGTTTTCTGCATGGCAACGTATGGGG
AAGGTGATCCAACGTGATAACGCTCAGGATTTCTACGATTGGCTGCAGGAGACCGACGTTGACTTGACCGGGGTAAATTCGCCGTTTTTCGG
TCTGGGTAACAAGACCTACGAACACTTCAATGCAATGGGTAAGTATGTCGATCAACGCCTGGAACAGCTGGGGGCACAACGCATTTTCGAA
CTCGGCCTGGGAGATGATGACGGCAACCTGGAAGAAGATTTTATTACCTGGCGCGAACAGTTCTGGCCAGCCGTTTTCGAATTCCTTTGGCG
TTGAAGCCACCGGTGAAGAATCATCCATCCGCCAGTACGAACCTGGTGTACATGAAGACATGGACGTTGCAAAGGTTTATACCGGGGAGAT
GGGACGCCTGAAGAGCTATGAGAACCAGAAGCCGCCGTTTGTATGCGAAGAACCCTTTCTGGCAGCAGTTACCGCCAATCGTAAGCTCAAC
CAAGGGACTGAACGCCATCTTATGCACCTGGAGCTTGATATTTTCGGACTCCAAGATTCGTTATGAGAGCGGTGACCACGTCCGCCGTCTATC
CGGCCAATGATTTCAGCCCTGGTGAATCAGATCGGCGAGATCCTTGGCGCCGACCTGGACGTCATTATGTCACTGAACAACCTTGGATGAAGA
ATCCAATAAGAAACATCCGTTCCCTTGTCCCAACCTATCGTACGGCACTGACCTACTATTAGATATACCAACCCCTCCGCGTACTAAT
GTATTGTACGAACCTCGCCAGTACGCGAGCGAGCCGTCCGAACAAGAACACCTGCACAAGATGGCGCTCTAGTTCGGGCGAAGGCAAAGAAT
TATACTTAAGTTGGGTCGTTGAGGCTCGCCGTCACATTTTAGCGATTCTGCAGGACTATCCGTCGCTGCGGCCACCAATCGATCATCTGTG
CGAGTTGCTGCCGCGCTGCAAGCGCGTTATTATAGCATTGCGAGTTCGTCGAAGGTGCATCCTAACTCGGTACACATTTGCGCCGTAGCG
GTAGAGTATGAAGCGAAAAGCGGCCGCGTGAATAAGGGCGTTGCTACGAGCTGGTTACGCGCTAAAGAACCGGCTGGCGAGAACGGAGGGC
GCGCCTTGGTGCCAATGTTTGTCCGCAAGAGCCAGTTTCGCCTGCCCTTCAAGAGCACGACGCCTGTATCATGTTGGTGGGCCCCGGCACGGG
TATTGCTCCCTTCATGGGTTTCATTTCAGGAACGCGCATGGCTCCGCGAACAGGGCAAAGAAGTGGGCGAGACTTTACTGTACTACGGATGC
CGCCGTTTCGGATGAGGATTACCTGTATCGCGAAGAACTGGCCCGTTTCCATAAGGACGGTGCCTGACACAGTTAAACGTCGCGTTTTTCAC
GTGAGCAAGCGCATAAGGTTTATGTTTCAGCATTTGCTGAAACGTGATCGTGAACATCTGTGGAAACTCATCCACGAAGGTGGAGCACACAT
CTACGTGTGCGGTGATGCCCCGAATATGGCTAAAGATGTCCAAAACACGTTCTATGACATTGTAGCCGAATTCGGGCCGATGGAACATACC
CAGGCCGTTGACTATGTCAAGAAGTTGATGACCAAAGGCCGCTATTTCGCTGGATGTGTGGAGCGAGAACCTGTACTTCCAGGGCCATCACC
ATCACCATCAGCGCGCGCGGCCATCACCATCACCATCACTAACGAGAAGCTT

pET28a CPRS_Confirmed_Protein_Sequence

MGQTTAPPVKESSFVEKMKKTGRNIIVFYGSQTGTAEFANRLSKDAHRYGMRGMSADPEEYDLADLSSLPEIDKSLVVFCMATYGECDPT
DNAQDFYDWLQETDVLDTGVKFAVFGNGKTYEHFNAMKGYVDQRLEQLGAQRIFELGLGDDDNLEEDFITWREQFWPAVCEFFGVEATG
EESSIRQYELVVHEDMDVAKVYTGEMGRRLKSYENQKPPFDKPNFLAAVTANRKLNQGTERHLMHLELDISDSKIRYESGDHVAVYPANDS
ALVNQIGEILGADLDVIMSLNLDDESNKKHPFPCPTTYRTALTYLDITNPRTNVLYELAQYASEPSEQEHLHKMASSSGEGKELYLSW
VVEARRHILAILQDYPSLRPPIDHLCCELLPRLQARYYSIASSSKVHPNSVHICAVAVEYEAKSGRVNKGVATSWLRAKEPAGENGGRALVP
MFVRKSQFRLPFKSTTPVIMVPGTGIAPFMGFIQERAWLREQKEVGETLLYYGCRRSDEDYLYREELARFHKDALTQLNVAFSREQAH
KVYVQHLLKRDREHLWKLIEGGAHIYVCGDARNMAKDQNTFYDIVAEFGPMEHTQAVDYVKKLMTKGYSLDVWSENLYFQGHHHHHHG
GGGHHHHHH

Chapter 5

Protein Expression and Purification

This chapter describes the expression and purification of the IDO1s and of soluble forms of cytochrome b5 (CYB5S) and cytochrome NAD(P)H:P450 reductase (CPR). It explores the proteins in terms of dispersity by size exclusion chromatography, heme incorporation, and absorption spectroscopy and how these were affected by culturing conditions.

5.1. Introduction

Expression and purification of IDOs

All IDO1 proteins and CYB5S were expressed from *E. coli* strain EC538 (J.E.G. McCarthy) and the pREP4/pQE9 plasmid pair (Qiagen). CPRS was expressed from *E. coli* BL21 (DE3) *Star* from a modified pET28a plasmid (Merck Millipore). Expression of human IDO1 (HIDO) has been a routine procedure in this lab and the literature (*e.g.* [222, 223, 238-242]). Literature IDO1 expression and purification using the EC538 system has typically involved the growing of single colonies on agar plates, followed by production of an overnight seed culture. The seed cultures were then diluted with fresh media to a known OD₆₀₀ so that they could be predictably grown at the desired temperature (4 – 37 °C). During mid-exponential growth (*e.g.* an OD₆₀₀ of 0.5), the heme biological precursor 5-aminolevulinic acid (ALA), and the allolactose mimic Isopropyl β-D-1-thiogalactopyranoside (IPTG), were added to induce heme production and HIDO expression, respectively. The serine protease inhibitor, phenylmethylsulfonylfluoride (PMSF), was also added to reduce protease activity during growth. Cell culturing was continued for a desired time, usually 6 – 12 hours post induction, with cells being lysed and purified by immobilised metal affinity chromatography (IMAC, *e.g.* nickel nitrilotriacetic acid [Ni-NTA]). Lewis bases, especially the nitrogens of imidazole compounds such as His, have a high affinity for these ions. As such, the His-tag of the proteins have a much stronger affinity for the nickel than other species present in the lysate, allowing for semi-selective binding of the desired protein to the Ni-NTA column. Elution of bound protein from the IMAC column was then achieved with a gradient of imidazole-containing buffer, which competes with proteins for nickel binding. A final round of purification was then achieved through the use of size exclusion chromatography (SEC), which separates the proteins based on size. This has the effect of removing holo enzyme from other species lacking heme. Protein and heme content of the eluent was monitored by the absorbance at 280 and 404 nm, respectively. Figure 5.1 outlines these general procedures. Protocols employed in this Ph.D. work generally followed these procedures for heme-containing IDO1 and CYB5S proteins, with specific modifications as listed below. CPRS was grown in a likewise manner, but without ALA addition as heme is not a cofactor.

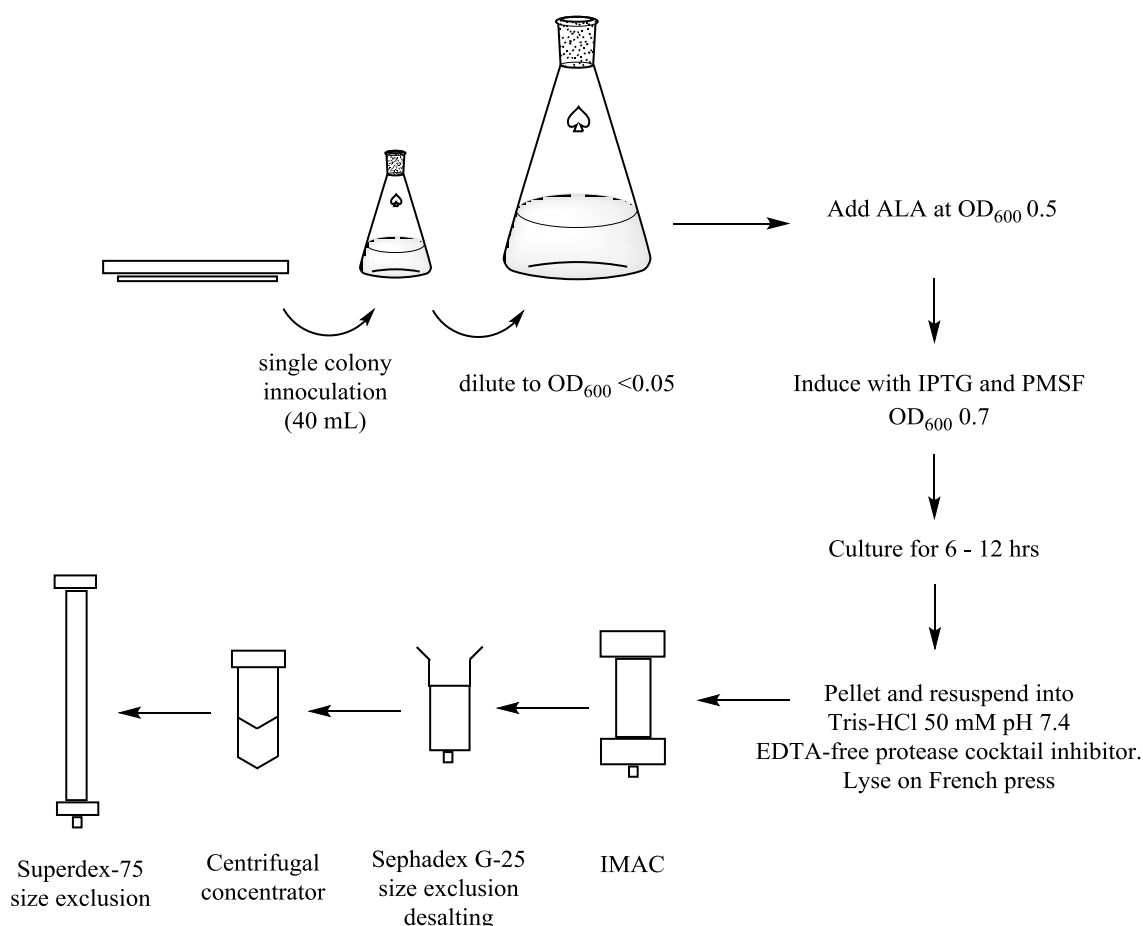


Figure 5.1. Schematic flow chart of general protein growth and purification procedures. **ALA:** 5-aminolevulinic acid. **IPTG:** Isopropyl β -D-1-thiogalactopyranoside. **PMSF:** phenylmethylsulfonylfluoride. **EDTA:** Ethylenediaminetetraacetic acid. **IMAC:** immobilised metal affinity chromatography.

5.2. Results

5.2.1. Expression of IDO1 proteins

Initial HIDO and WIDO expression

Initial protein growth and purification was conducted on the HIDO and WIDO EC538 constructs using the general procedure outlined in Figure 5.1, above. However, for both proteins, the yield, purity, and heme/protein ratio was below that expected from previous experiences in obtaining HIDO under the same conditions (Figure 5.2). Upon loading either lysates on to an IMAC column, the blue of the nickel-containing media was still clearly visible, indicating a low amount of protein produced by the cultures and/or very poor affinity between the nickel and the proteins. In fact, whilst a HIDO band was at least visible on the column, a WIDO band was not. Additionally, WIDO was bound much more weakly to the column, showing signs of elution at just 40 mM imidazole; comparable to the slight elution observed for HIDO at 80 mM (as visually judged by the intensity of red in the eluent). SDS-PAGE analysis pointed to poor retention of the IDO1 proteins by the

nickel affinity column – with substantial amounts of IDO1 being present in the wash steps, in addition to other contaminating proteins being present. Figure 5.3 compares an SDS-PAGE gel for the HIDO expression during this work and during previous studies, and WIDO is shown in Figure 5.4. Of note with the WIDO sample is that the intensity of staining for the contaminating proteins rivals that of WIDO itself, in contrast to the staining levels of the HIDO gels. In all cases, the various imidazole fractions shown on the gels were concentrated on a 30 kDa centrifugal device, but still showed bands as low as 15 kDa. Possibly, these proteins had affinity for other proteins or for the centrifugal device itself, and were not passing through the filter. In total, the 40 – 160 mM IMAC fractions gave ~3.8 mg/l of culture during the HIDO expression, and ~1.5 mg/l of culture for WIDO.

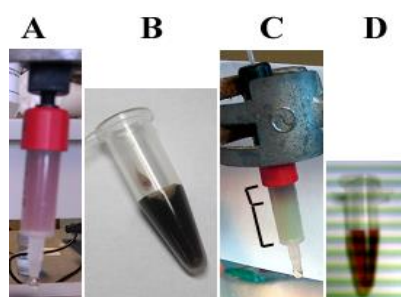


Figure 5.2. **A)** Previous example of HIDO from 1 litre of EC538 culture bound to a GE nickel affinity column [242]. The blue nickel colour was hidden by the red HIDO. **B)** The same sample after SEC and concentration showing an opaque red-black sample. **C)** Initial HIDO expression in this work. Only a small band of red was visible at the top of the column, with the rest of the column remaining blue (black lines). **D)** The 40, 80 and 160 mM imidazole fraction from sample **C**, SEC purified and concentrated, showing a translucent red due to a substantially lower concentration, roughly 35 mg/ml vs 15 mg/ml for **B** vs **D** based on a Bradford assay (Bio-Rad).

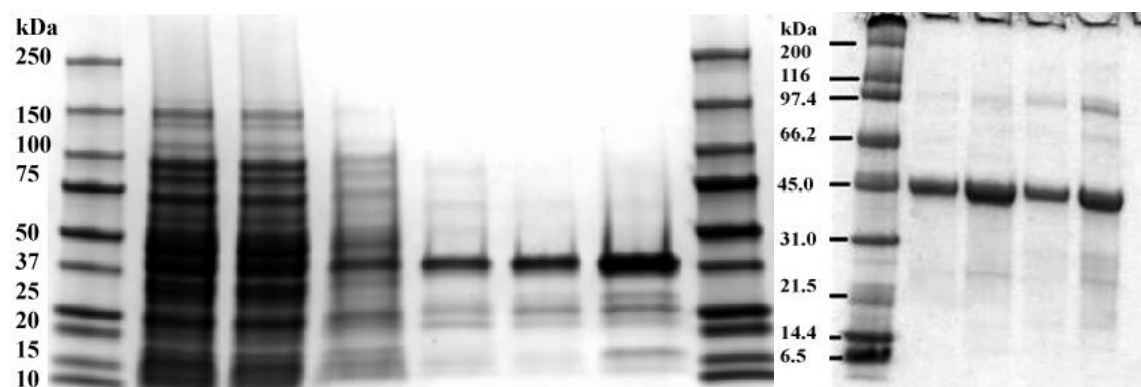


Figure 5.3. SDS-PAGE of HIDO IMAC fractions. **Left:** SDS-PAGE from initial HIDO expression attempts in this work. **1st** and **8th** lanes were ladder standards with indicated sizes. **Lane 2)** Cell lysate. **Lane 3)** Unbound fraction from IMAC. **Lane 4)** 20 mM imidazole fraction. **Lane 5)** 40 mM wash. **Lane 6)** 80 mM wash. **Lane 7)** 160 mM elution pre-SEC. **Right:** SDS-PAGE of HIDO expression from a previous study [242]. **Lane 1)** Ladder standards with indicated sizes. **Lanes 2 and 3)** SEC purified HIDO. **Lanes 4 and 5)** the same samples prior to SEC.

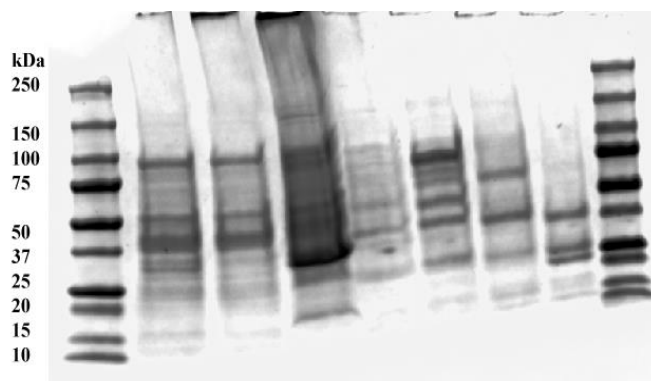


Figure 5.4. SDS-PAGE from initial WIDO expression attempt. 1st and 9th lanes are ladder with indicated sizes. **Lane 2)** Cell lysate. **Lane 3)** IMAC unbound fraction. **Lane 4)** SDS-solubilised pellet from lysate. **Lane 5)** 20 mM imidazole wash. **Lane 6)** 40 mM imidazole wash. **Lane 7)** 80 mM imidazole wash. **Lane 8)** 160 mM elution.

Size exclusion chromatography of initial samples

Each IMAC fraction was concentrated on a 30 kDa centrifugal device before being applied to a Superdex-75 10/300 SEC column (10 mm \varnothing x 300 mm) (Figure 5.5). Elution from the column (Tris 50 mM, pH 7.4) was followed at 215, 280 and 404 nm. 215 nm is a generic and sensitive wavelength for carbonyl groups such as the amides of proteins. 280 nm is absorption by aromatic residues, especially tryptophan, and 404 nm is the Soret peak of HIDO. The overall shape of the SEC trace was consistent with previous work, with a major heme-containing peak eluting at 10 – 11 ml and preceded by 2-4 distinct protein containing peaks associated with variable, but significantly smaller, 404 nm peaks [241, 242]. However, what was evident, was the significantly lower 404/280 nm ratio, indicating poor heme incorporation/retention to the protein. Previously, the pre-SEC treated HIDO protein had been observed with a 404/280 nm ratio of >1.5, whilst these samples gave a ratio of <1.0 [242]. The inset table (Figure 5.5) shows the 404/280 nm ratio (heme/protein ratio) of the collected HIDO fractions. The ratio was improved in later IMAC fractions, and also with later SEC fractions within each IMAC fraction. However, as Figure 5.6 also shows, these SEC fractions retained contaminating bands identical to those present prior to SEC. Therefore, whilst SEC was enriching the heme/protein ratio, probably by separating out unfolded or misfolded HIDO based on the correlated 280 and 404 nm absorptions, it was not producing homogenous protein.

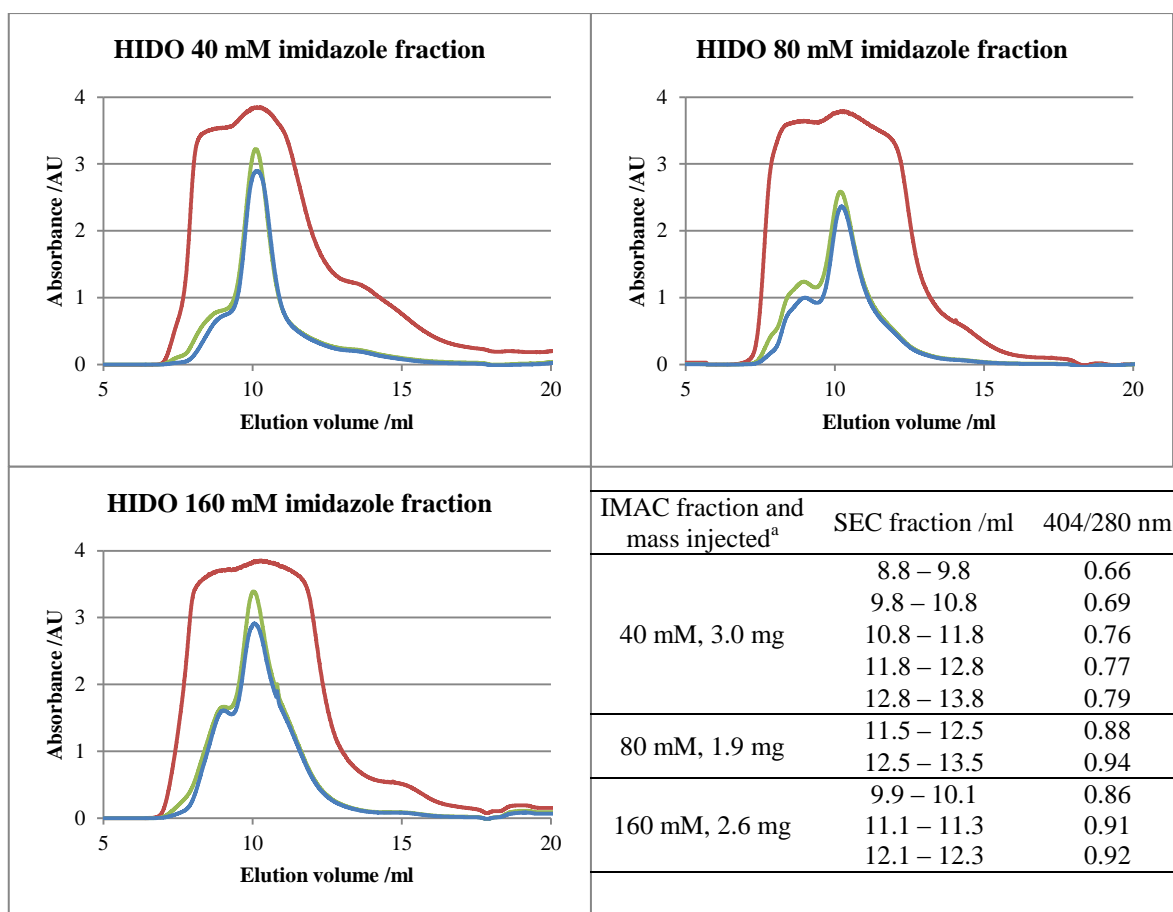


Figure 5.5. SEC (Superdex-75 10/300) fractionation of 40, 80 and 160 mM imidazole fractions of initial HIDO sample monitored at 215 nm (red), 280 nm (green), and 404 nm (blue). **Inset:** Table showing 404/280 nm ratios of fractions collected from SEC. ^aAssuming a typical protein mixture gives a percent solution extinction coefficient ($\epsilon_{280\text{ nm}}^{0.1\%}$) of $1.0\text{ mg}^{-1}\cdot\text{ml}\cdot\text{cm}^{-1}$.

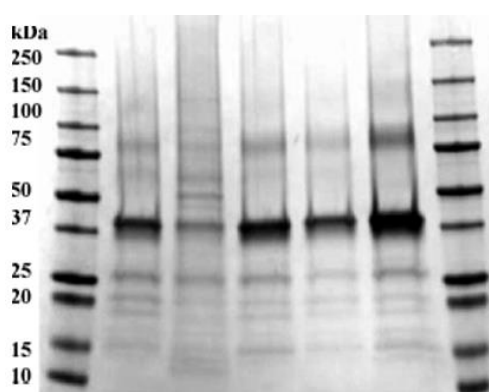


Figure 5.6. Comparison between pre- and post-SEC purification of this initial HIDO experiment. **Lane 1)** Ladder. **Lane 2)** Pre-SEC 80 mM imidazole fraction. **Lane 3)** post-SEC 80 mM imidazole, 7.5 – 8.5 ml fraction. **Lane 4)** 80 mM imidazole, 11.5 – 12.5 ml fraction. **Lane 5)** Pre-SEC 160 mM imidazole fraction, **Lane 6)** 160 mM imidazole 10.9 – 11.1 ml fraction. **Lane 7)** Ladder.

The 160 mM IMAC fraction of WIDO was analysed by analytical SEC (Superdex-75 3.2/30, Figure 5.7). The UV-vis absorption spectrum of the fraction with the highest 404/280 nm ratio is also presented in Figure 5.7, and compared to the 12.1 – 12.3 ml fraction collected from the HIDO 160 mM imidazole fraction. The HIDO sample had the expected Soret peak at 404 nm, although the Soret/protein ratio was very low at less than 1 (1.6 – 2.0 was expected based on previous work and the literature [213, 223]). Unexpectedly, the WIDO sample displayed a double Soret peak at ~408 and 419 nm. The UV-vis results of these proteins are explored in more detail in Section 5.2.3. However, based on the poor heme incorporation for both HIDO and WIDO, the contaminating proteins by SDS-PAGE in both samples, and the unusual double Soret peak for WIDO, work was focused on obtaining higher quality and purity IDO1 proteins for use in subsequent functional experiments. In particular, investigations looked at the modification of culture conditions as a means of improving yields and heme incorporation at a biosynthetic level.

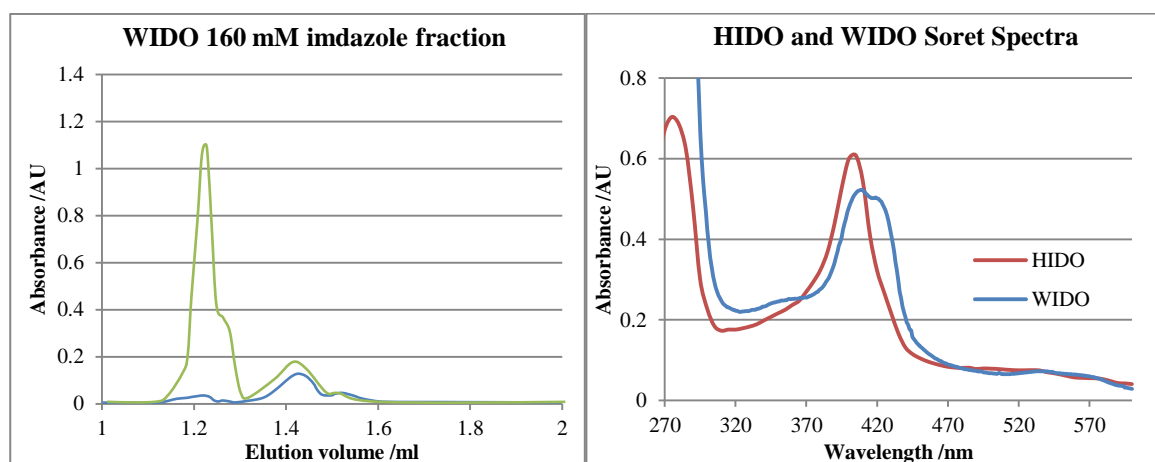


Figure 5.7. Left: SEC (Superdex-75 3.2/30) trace of initial WIDO sample monitored at 280 nm (green) and 404 nm (blue). Right: Comparison of HIDO and WIDO Soret region (Tris 25 mM, pH 7.4, 25 °C) after SEC purification. Note the double Soret peak for WIDO. The 404/280 nm ratio for HIDO was 0.86, and the 409/280 nm ratio for WIDO was 0.4.

5.2.2. Efforts to improve isolated IDO1 proteins

Bacterial growth at different temperatures

Bacteria in this work were grown under shake-flask conditions. This entails an inoculation of the bacteria into a vessel (*e.g.* conical flask) containing a fixed volume of media with shaking sufficient to provide a source of oxygen and provide a homogenous mixture. Under these conditions, the bacteria cannot create a biofilm layer, but instead exist suspended in the media. There is no exchange of media such as that occurring within a bio-reactor. Therefore, over time, the nutrient concentrations decrease and the metabolic waste concentrations increase. When cell density (*e.g.* measured by colony counting [CFU] or optical density [OD₆₀₀]) is plotted against time, this leads to the prototypical growth curve shown in Figure 5.8. After inoculating cells into the media, there is an expected lag phase. During this time, the cell numbers do not increase, but are instead

acclimatising to their new environment. The length of this lag time varies heavily with the amount of difference between the cells' former environment and new environments – as they take this time to build the machinery required for nutrient import, vitamin and protein biosynthesis, or resistance against stresses such as toxins or temperature shock [243]. Cells enter the exponential phase after building the metabolic machinery required to take advantage of the high nutrient levels present – with the cells dividing as rapidly as possible. As nutrient levels decline and toxic waste products increase, the cells begin to enter the stationary phase where cell division slows and the rate of cell death increases, eventually becoming equal. Whether this is stochastic in nature or the result of programmed cell death is not understood, but cell death is accompanied by cell lysis, releasing some of the previously stored nutrients to the surviving cells and allowing for the prolonged declining (death) phase [243].

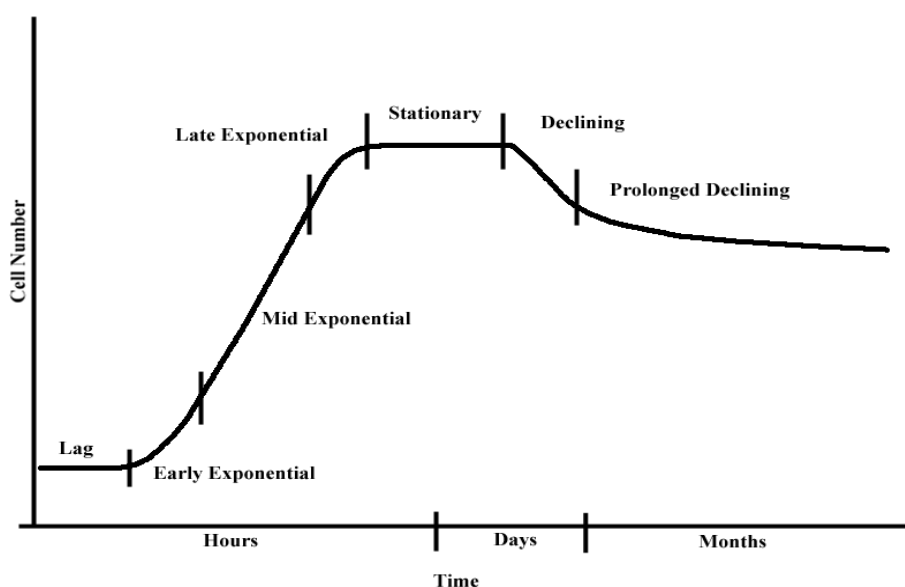


Figure 5.8. Simplification of a typical bacterial growth curve under shake-flask conditions. The exponential phase has been divided into 3 sections based on the curve shape. Adapted from [243].

Growth curves of EC538 pREP4 pQE9-HIDO cultures are shown below (Figure 5.9). The lag phase was not present here as the cells were already metabolically acclimatised by diluting a 1.0 OD₆₀₀ culture back to 0.05 in fresh media. Each culture received ALA at ~0.5 OD₆₀₀ and IPTG and PMSF at ~0.6 OD₆₀₀. These growth curves were performed to more easily understand the metabolic context of later investigations into the effects of induction time and growth temperature on purified protein quality. Such curves served as a basis for comparison of the growth of other cell lines, and to identify OD₆₀₀ points relative to metabolic activity.

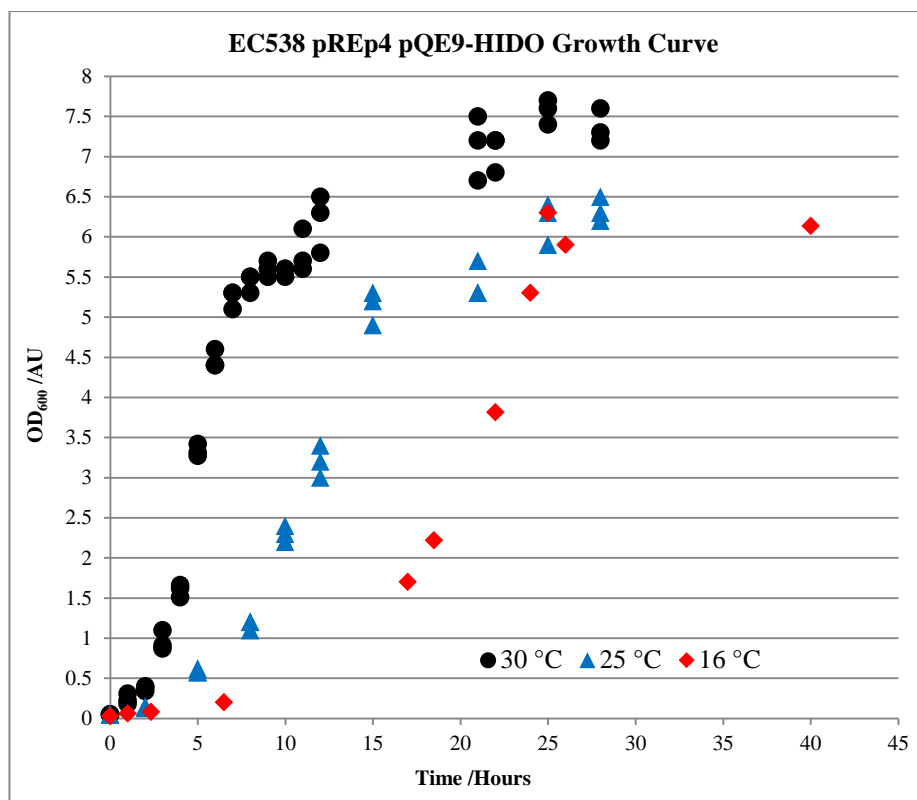


Figure 5.9. Growth curves of *E. coli* strain EC538 pREP4 pQE9-HIDO at various temperatures. Data are the mean of two OD₆₀₀ readings from three shake flasks originating from the same seed culture. The exception to this was 16 °C, which was two OD₆₀₀ readings from a single flask.

Growing WIDO at different temperatures

The WIDO protein displayed weaker IMAC affinity compared to other the proteins, and as such could not be washed as stringently. This lack of washing was assumed to be the main source of contaminating proteins on the SDS-PAGE gel (Figure 5.4). The WIDO and HIDO proteins share 70% identity, and are therefore expected to possess similar native folds. However, if WIDO possessed a significantly different native fold, or a susceptibility to misfold or unfold, then this may be one reason for a lowering of the IMAC affinity if it led to steric occlusion of His-tag residues.

Misfolding or unfolding could similarly explain the poor heme incorporation if either the protein was aggregating prior to receiving heme, or was losing heme after loss of the native IDO1 fold. A lowering of the 404/280 nm ratio has been observed in HIDO when stored at temperatures above -80 °C (data not shown), and heme loss is followed by protein unfolding in nitric oxide-induced IDO1 degradation *in vivo* [244, 245]. In *E. coli*, improperly folded WIDO would be expected to lead to protein aggregates and inclusion bodies, as has been observed for HIDO expression [223]. Such aggregates and inclusion bodies are generally stressful at low concentrations, and toxic at high concentrations, including in *E. coli* [246]. Growing HIDO at reduced temperatures has previously shown an increase in the quality of HIDO isolated and a reduction in inclusion body formation [223]. As such, WIDO culturing at a reduced temperature was compared to HIDO and to CYB5S.

WIDO cultures were grown at 25 °C or 12 °C, as well as one of CYB5S at 12 °C. The 25 °C culture was induced with IPTG at OD₆₀₀ 0.6 for 6 hours, whilst both 12 °C cultures were induced at 0.8 OD₆₀₀ and harvested 41 hours post induction. Both WIDO growths gave similar amounts of final protein per litre of culture. The 25 °C culture was seen to grow slightly slower than the previous HIDO culture at the same temperature (Figure 5.10). WIDO cells (25 °C, no IPTG) took 6 hours to reach 0.6 OD₆₀₀, compared to 5 hours for HIDO. After induction, the WIDO sample then took a further 6 hours to reach an OD₆₀₀ of 2 (the point of collection), compared to less than 5 hours for HIDO. This reduced growth repeats itself in comparing the WIDO and CYB5S cells at 12 °C. For the first 31 hours of non-induced growth, both cultures grew at equivalent rates – 0.13 vs 0.15 OD₆₀₀ after 6 hours and 0.82 vs 1.1 after 31 hours for WIDO and CYB5S, respectively. However, a separation between the WIDO and HIDO or CYB5S curves was observed post-induction (red circle, Figure 5.10). Both WIDO cultures and the CYB5S culture were performed at the same time using the same master mixes of media and additives. Therefore, any contaminants in, for example, the media or the IPTG, should manifest itself in all cultures. Both WIDO cultures again had weak IMAC binding compared to HIDO and gave poor purity by SDS-PAGE as a result (Figure 5.11). Both WIDO cultures continued to produce a double Soret peak. Further details of CYB5S production can be found in Section 5.2.4, and further UV-vis analysis can be found in Section 5.2.3.

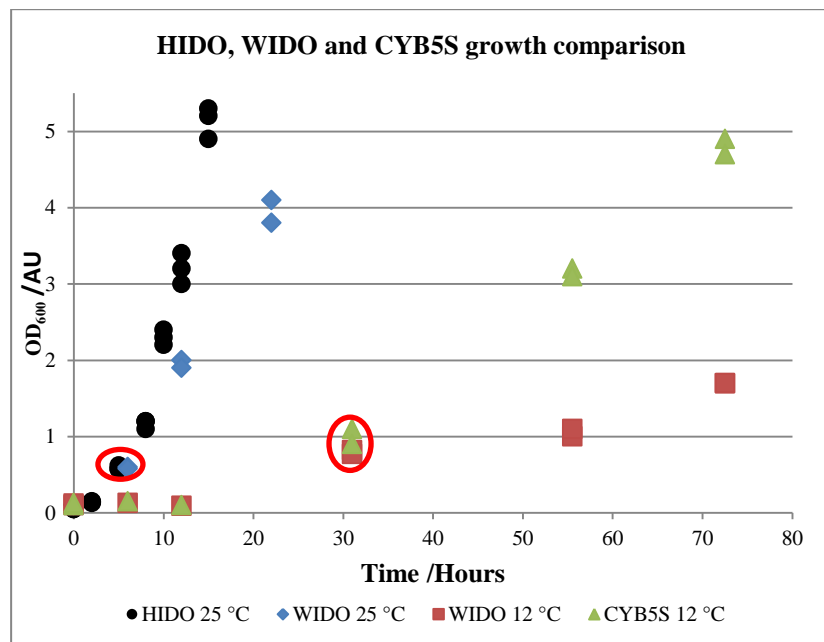


Figure 5.10. HIDO data taken from Figure 5.9 for comparison. Circled are the points of induction. WIDO and CYB5S data are three OD₆₀₀ readings from a single biological replicate.

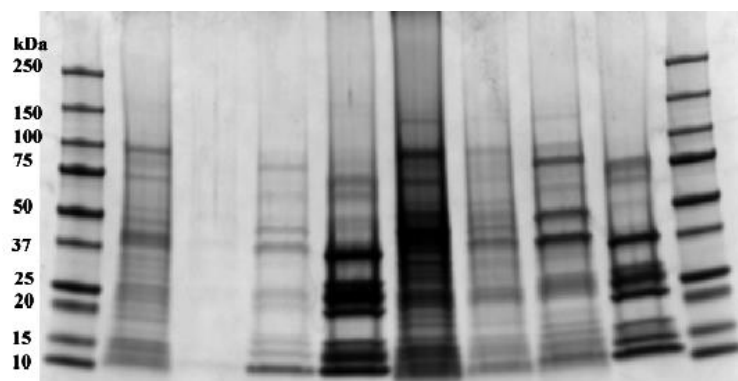


Figure 5.11. WIDO growths. Lanes 2-5 were grown at 25 °C with 6 hrs of IPTG induction starting at 0.6 OD₆₀₀. Lanes 6-9 were grown at 12 °C with 41 hours of IPTG induction. **Lanes 1 and 10)** Ladder. **Lane 2)** unbound IMAC fraction. **Lane 3)** Empty. **Lane 4)** 20 mM imidazole fraction. **Lane 5)** 160 mM imidazole fraction. **Lane 6)** unbound IMAC fraction. **Lane 7)** 10 mM imidazole fraction. **Lane 8)** 20 mM imidazole fraction. **Lane 9)** 160 mM imidazole fraction.

These data indicate that culture temperature does not affect the IMAC retention of WIDO, the SDS-PAGE purity, or the heme spectrum. The formation of inclusion bodies or aggregates was not investigated for these cultures. The growth curves also suggest that induction of WIDO may be stressful to the cells relative to HIDO or CYB5S induced under similar conditions. As all cultures were from EC538 pREP4 pQE9 systems, and the two WIDO and one CYB5S cultures were performed at the same time using the same master mix of media and additives, the differences observed post induction were unlikely to be due to contaminants or media differences. The source of the apparent toxicity was not investigated further, but would be consistent with the formation of aggregates or inclusion bodies upon induction of WIDO [246]. Additionally, improperly folded WIDO could lead to increased toxicity through increased cellular heme concentrations due to reduced heme utilisation (if initially misfolding prior to heme incorporation), or through heme loss (if unfolding after heme incorporation). It also cannot be excluded that the different heme environment of WIDO observed by UV-vis could be leading to a new catalytic consequence (*e.g.* reactive oxygen species production), with detrimental consequences for growth. Not looked at yet is whether repression of WIDO induction rescues the growth rate, nor whether induction of HIDO or CYB5S might be causing an increase in growth rate in those cells, relative to cells with an empty plasmid. As such, the causative nature of WIDO expression cannot be confirmed from this data.

Effect of induction procedures

Typical HIDO production involves the IPTG induction of protein overexpression during the early exponential phase, generally around OD₆₀₀ 0.5. At this time the cells are rapidly dividing and consequently have higher levels of protein production and reduced proteolytic activity [247]. Conversely, during stationary phase, proteins related to proteolysis, chaperone and carbon metabolism functions are upregulated, and protein synthesis becomes a lower priority – as the

cells grapple with the pressures of reduced nutrient availability, increased waste concentration and a decreasing extracellular pH (in unbuffered media) [247]. Heme biosynthesis is also expected to play a factor in IDO1 expression systems. Whilst heme biosynthesis is very tightly regulated under normal conditions, overexpression of a hemoprotein such as IDO1 may upset that balance and cause competition for heme with other cellular hemoproteins. This can be addressed through the addition of ALA as, biosynthetically, ALA production is the committed step of heme biosynthesis [248]. IDO1 quality would, therefore, be dependent on the balance between peptide production, heme production, and heme uptake by apo peptide. Peptide production would be expected to be dependent on the availability of peptide synthesis machinery, proteolytic pathways and chaperone pathways, as well as the inherent half-life of the apo IDO1 peptide as it awaits heme incorporation. Meanwhile, heme over production, a known producer of oxidative stress, must be avoided through the balanced addition of ALA. To determine if manipulation of these variables could impact on the quality of protein produced, experiments were conducted looking at the timing and length of IPTG induction, and the comparison between IPTG induction and lactose-based auto-induction.

Length of IPTG induction

The effect of the length of time between induction and harvesting was investigated in HIDO. A single culture was grown at 25 °C at a 2 litre scale and treated as per the general scheme illustrated in Figure 5.1. After induction with IPTG at 0.6 OD₆₀₀, one third of the cells were harvested at growth phases corresponding to mid-exponential (2 OD₆₀₀), late exponential (5 OD₆₀₀) and early/mid-stationary (~15 hours after 5 OD₆₀₀ was reached). These roughly equated to 5, 12 and 27 hours of induction time. Table 5.1 shows the results of these cultures. The 5 hour induction length resulted in the lowest amount of protein and heme incorporation, whilst proportionally little benefit was seen in extending induction to 27 hours compared to 12 hours. SEC (Superdex-75 10/300) was performed on the 12 hour and 27 hour induction growths, with no significant differences in the shape or relative peak intensities between the pair. The SEC trace shows that at least four heme-associated protein peaks elute closely together, presumably all different structures of HIDO (Figure 5.12). The much lower association of the heme peak (405 nm¹⁰) with protein peaks (280 nm), suggests that these were HIDO peaks with drastically reduced amounts of heme incorporation. They are not expected to be *E. coli* proteins associating with HIDO based on relative staining in SDS-PAGE analysis (Figure 5.6, above, presents a HIDO SDS-PAGE gel typical in this study), however, that does not prevent them from being *E. coli*

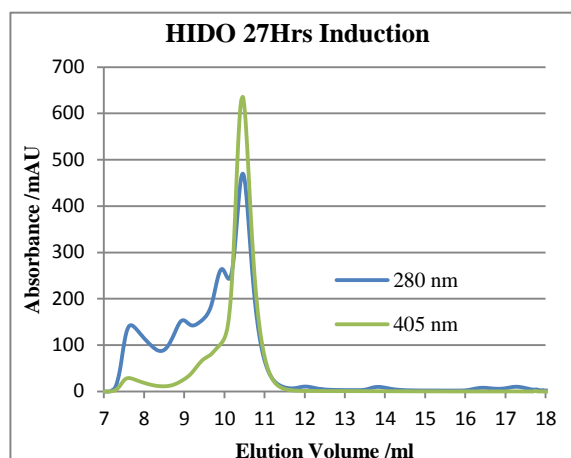
¹⁰ In this work, both 404 nm and 405 nm were used to measure the Soret peak of HIDO, depending on which wavelength had the higher absorbance on the specific instrument being used.

proteins of the same size as HIDO. The shape of the SEC trace is consistent with HIDO expression carried out previously [241, 242, 249].

Table 5.1. Comparison of collection time, yield and heme incorporation.

Induction /hr	OD ₆₀₀	Protein /mg/ml	Yield /mg/l	405/280 nm
5	2	10	2	1.3
12	5	30	5	1.5
27	7	40	8	1.5

Figure 5.12. SEC (Superdex-75 10/300) of HIDO collected from cells induced for either 12 or 27 hours with IPTG at 25 °C.



Auto-induction with lactose

The *lac* operon being used to control expression of the recombinant proteins in this project is the same as that used to control the expression of proteins required for the use of lactose as an energy source, and is controlled by the concentration of lactose (or the isomer, allolactose) and glucose. Glucose prevents expression by indirectly inhibiting transcription, while lactose enhances transcription by removing the machinery responsible for this inhibition [250]. IPTG is a non-metabolised analogue of allolactose capable of performing the same function. Under conditions where both glucose and lactose are present, glucose is preferentially metabolised. As the glucose level falls, the competition between glucose and lactose becomes less inhibitory and expression increases. A number of bacterial media recipes have been reported by Studier in relation to recombinant protein expression in *E. coli* BL21(DE3) [250]. These include glycerol/glucose/lactose mixtures designed for the exponential growth on glucose followed by lactose induction of the protein of interest (glycerol serves as an additional carbon source which does not inhibit lactose-dependent induction). Use of this auto-induction media was of interest as a means to provide a less stressful culturing condition through the presence of increased amounts of energy/carbon sources, and the gradual induction of IDO1 instead of the instant induction caused by IPTG addition. Cultures grown using this auto-induction method are referred to herein as ZYP5052 growths, referring to the final concentrations of glycerol, glucose, and lactose of 0.5%, 0.05% and 0.2% (w/v), respectively.

Initial HIDOΔ360-370, WIDO and HIDO growths (ZYP5052 media, 25 °C) were performed. Single colonies were used to create 40 ml of seed culture grown in media identical to the ZYP5052 culture, without glycerol or lactose. Seed cultures were grown to an OD₆₀₀ of 6 – 8 before being diluted into ZYP5052 culture to a calculated OD₆₀₀ of 0.05. The HIDO culture was collected 14 hours after seed culture inoculation, and gave <1 mg of protein per litre of culture in the final

IMAC fraction. Due to the low yield and low heme incorporation of the HIDO sample, HIDO Δ 360-370 and WIDO cultures were collected 36 hours after initial seed inoculation and gave ~3 mg of protein per litre of culture. SEC traces are shown in Figure 5.12. The main heme peak can be seen at 1.38 ml (Superdex-75 3.2/30) or 10.4 ml (Superdex-75 10/300) for each protein, but the majority of protein eluted prior to this and contained very poor heme content. Also shown, is an analytical SEC trace (Superdex-75 3.2/30) of the WIDO collected peak at 10.5 ml, illustrating that the protein remained a single peak after storage overnight at -80 °C.

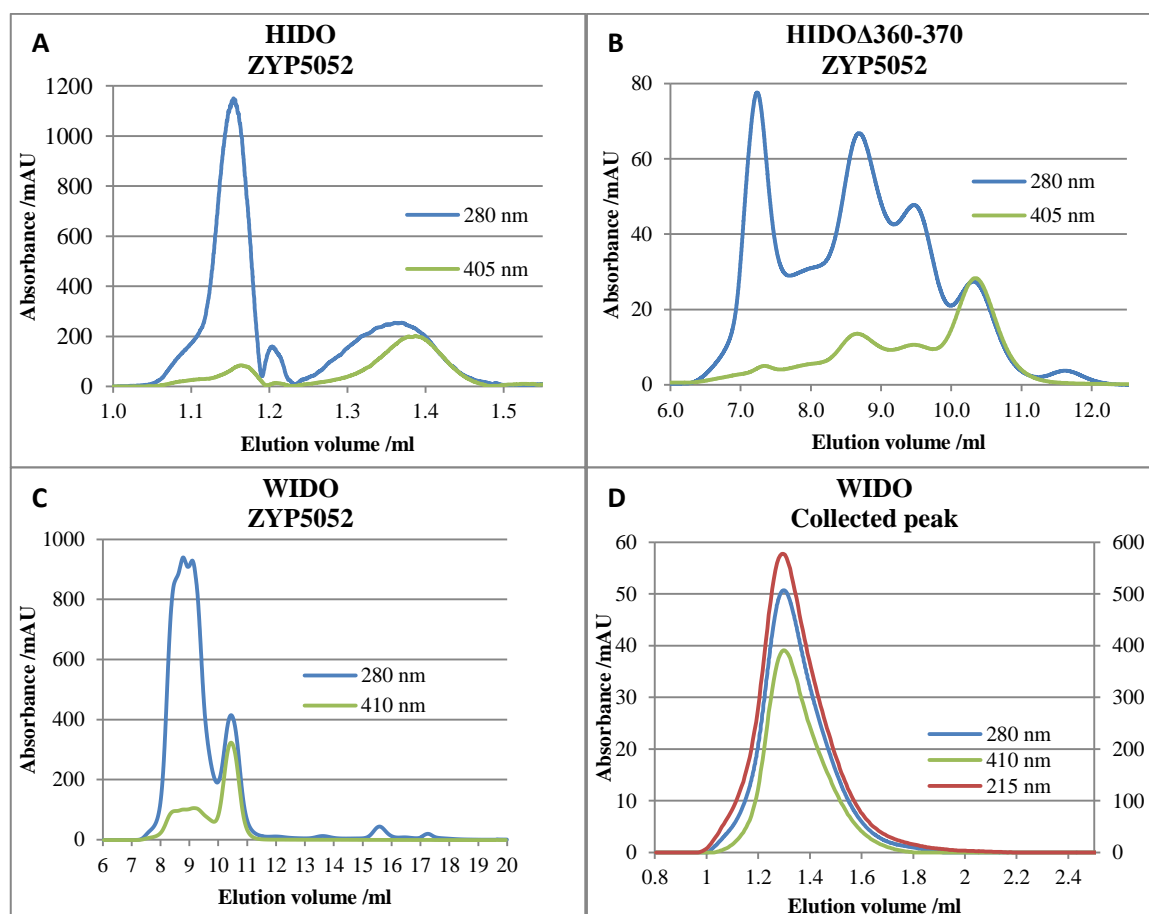


Figure 5.13. SEC analysis of IDO1 proteins from auto-inducing ZYP5052 media. **A)** HIDO from IMAC, collected 14 hours post inoculation. **B)** HIDO Δ 360-370 from IMAC, collected 36 hours post inoculation. **C)** WIDO from IMAC, collected 36 hours post inoculation. **D)** Highest quality fraction from **C**, stored overnight at -80 °C (Tris 25 mM, pH 7.4, 40% glycerol).

By comparison, another HIDO Δ 360-370 culture was performed using the IPTG method, without the addition of glycerol, glucose or lactose. The SEC (Superdex-75 10/300) again displayed the multi-peak profile, but had the major heme-associated peak as the dominant protein peak. Analytical SEC of this heme peak (after storage overnight at -80 °C) showed two merged peaks. In this case, the 280 nm and 405 nm traces were not identical, indicating that there was not a constant heme/protein ratio present within the sample. This was possibly due to batch-to-batch variation in the collection of the sample from the SEC column in the first instance, and not

necessarily evidence of sample degradation during storage. In a biological replicate of IPTG-based HIDO Δ 360-370 production, a single peak was observed after overnight storage at -80 °C, supporting this (Figure 5.13). This later sample gave a 405/280 nm ratio of 1.4 in its final quality.

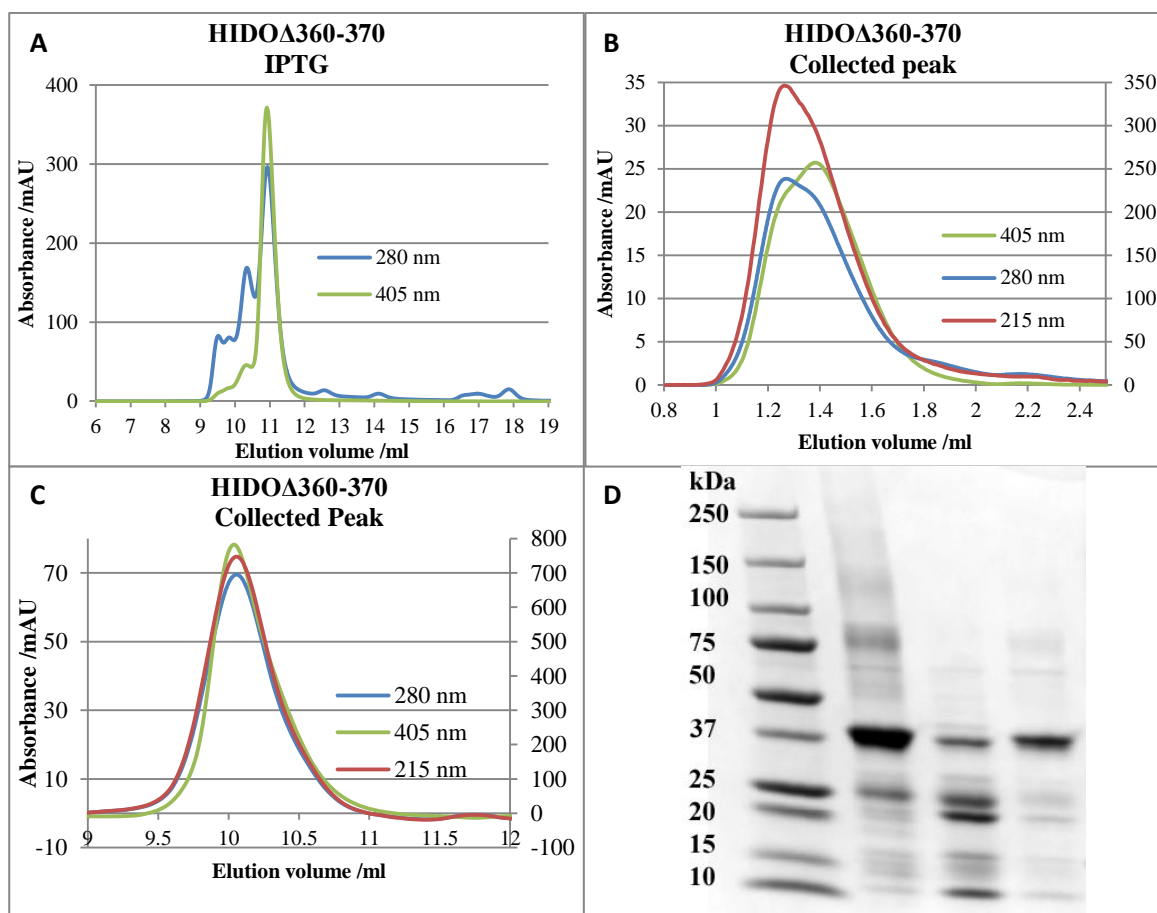


Figure 5.13. **A)** Representative SEC trace of HIDO Δ 360-370 produced by IPTG induction during early log-phase. **B)** Re-testing of the collected peak from **A** demonstrated heterogeneous heme-protein traces after storage at -80 °C overnight. **C)** Re-testing of a separate IPTG-induced HIDO Δ 360-370 demonstrated homogenous heme and protein traces. **D)** SDS-PAGE analysis of the HIDO (lane 2), WIDO (lane 3), and HIDO Δ 360-370 (lane 4) obtained from the above IPTG cultures.

The auto-induction method tried here gave substantially lower quality of HIDO and HIDO Δ 360-370 compared to IPTG-induced cultures. Both IPTG and auto-induction media gave poor quality WIDO, with significant amounts of the SEC trace showing no or little heme association. SDS-PAGE analysis demonstrated contaminating protein bands in all samples, mostly smaller than IDO1, but this was particularly obvious in the WIDO samples.

Late phase induction of WIDO under semi-anaerobic conditions

The final set of conditions explored involved inducing *via* IPTG much later in the growth curve, as well as reducing the metabolic burden of WIDO cells through weaker induction with IPTG (20 μ M instead of 100 μ M), in response to the possibly detrimental nature of WIDO expression on cell viability (Figure 5.10). A less oxidative environment was also sought through the lowering of the

agitation rate from 250 to 100 rpm. The culture was grown with aeration at 25 °C to an OD₆₀₀ of 5 using glucose as a repressor of WIDO expression. The culture was then exchanged into fresh media absent of glucose, acclimatised to the semi-anaerobic conditions (100 rpm) and sequentially treated with ALA, PMSF, and IPTG, 30 minutes apart. After 18 hours of induction, the resultant cell pellet was substantially darker than was customary for a WIDO growth. Where previously, resuspended pellets of WIDO culture generally gave an off-white colour, this cell suspension appeared more beige to brown, and the lysate demonstrated a distinct brown (Figure 5.14).

SEC analysis showed a monodispersed trace with consistent protein and heme absorption profiles (Figure 5.15). SDS-PAGE of post-SEC protein showed a substantially improved purity with respect to other proteins, as judged by the relative coomassie staining of the WIDO band to contaminating bands (Figure 5.14). The absorption spectrum of the protein, once again displayed a double peak, consistent with previous samples (Figure 5.17). Typical heme/protein absorption ratios for previous WIDO growths were in the range of 0.2 – 0.4, compared to the 0.56 obtained in this growth. The isolated protein yield, after SEC, for this 1 litre culture was 3.8 mg by Bradford assay, compared to 7 – 15 mg/l for HIDO growths.

These data from a single experiment indicate that weaker late-phase induction and/or low oxygen content substantially changes the fate of WIDO in the cell, with moderate increases to the yield and heme incorporation, but substantial changes to the SEC trace and SDS-PAGE purity. No previous record could be found detailing the expression of monodispersed IDO1 protein [241, 242, 249].

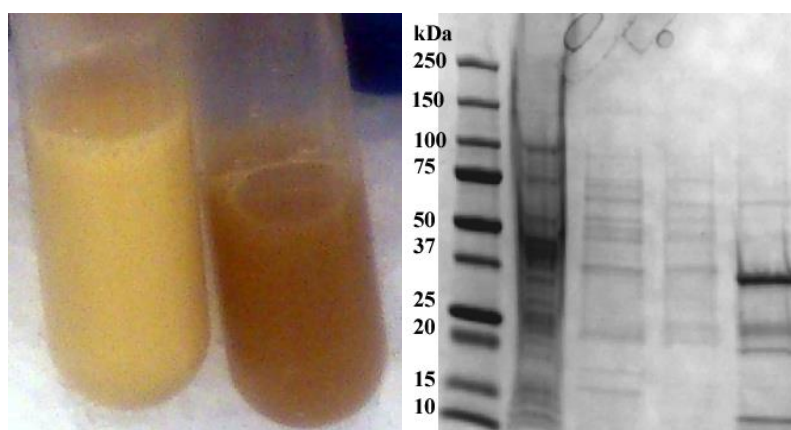


Figure 5.14. Left: Resuspended WIDO cells induced in stationary phase before (left tube) and after (right tube) lysis. Right: SDS-PAGE of WIDO from late-phase induction. **Lanes 1)** ladder. **Lane 2)** unbound fraction. **Lane 3)** 5 mM imidazole fraction. **Lane 4)** 20 mM imidazole fraction. **Lane 5)** 160 mM elution fraction.

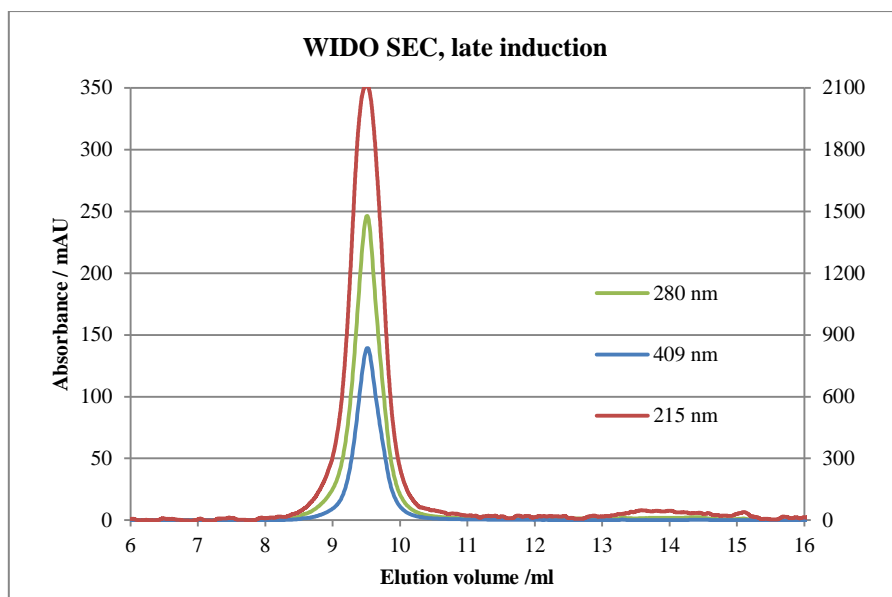


Figure 5.15. SEC analysis (Superdex-75 10/300) of WIDO eluted from the IMAC column. A nearly monodispersed peak was observed, with only some slight asymmetry. Data for 280 and 409 nm are plotted on the left y-axis, while 215 nm is on the right.

5.2.3. Heme spectra of IDOs

The visible absorption spectra of heme contains distinct features that provide information on its electronic structure, which in turn is determined by the conformation of the heme, the nature of the surrounding protein matrix, the oxidation state, and the nature of bound ligands [251]. The major peak, the Soret peak (sometimes referred to as the gamma [γ] peak), generally occurs in the 400 – 450 nm range. Additional, weaker, peaks also appear above 500 nm, consisting of Q-bands (sometimes referred to as α and β peaks) and charge-transfer bands [252, 253].

Due to IDO1's propensity for auto-oxidation, the native state of the heme is ferric. Ferric heme can be converted to ferrous through the addition of sodium dithionite, which also depletes dissolved oxygen, whilst oxidation of a reduced heme can be achieved through the use of ferricyanide. The absorption spectra of the IDO1s were obtained as a rapid and simple means of identifying changes in the heme environment across the mutants.

For all spectroscopy experiments, native enzyme refers to samples isolated from SEC without ferricyanide or dithionite intervention. Ferric samples were treated with potassium ferricyanide and ferrous samples were treated with sodium dithionite in unsealed cuvettes. Data were collected in Tris (25 mM, pH 7.4) at ambient temperature.

Soret peaks

Native HIDO possessed a Soret peak at 404 nm, which was blue shifted to 424 nm with a lower extinction coefficient upon dithionite treatment (Figure 5.16) and is consistent with previous reports [222, 253, 254]. Native HIDO Δ 360-370 displayed equivalent characteristics (404 nm

shifted to 422 nm). Comparatively, native WIDO was consistently isolated with two Soret peaks at 409 and 425 nm. These peaks could be consistent with the presence of both oxidised and reduced forms of the enzyme. They could also be consistent with the binding of a novel sixth ligand. For example, cyanides and thiols have induced a blue shift with a lowering of the extinction coefficient for rabbit intestinal IDO1 [253]. The active site in the HIDO crystal structures contain Cys129 and Tyr126 as being the closest nucleophiles to heme's sixth ligation position, and these residues are present in WIDO. Considerable structural re-arrangement would be required for these residues to occupy the heme's sixth axial position, however [119, 216]. The relative intensity of the Soret peaks in each WIDO experiment also varied (Figure 5.16). Also note that the δ -peak (~350-355 nm) can be observed in WIDO but not in HIDO or HIDO Δ 360-370. Sono previously reported this absorbance for rabbit intestinal IDO1 (354 nm), but only in the presence of a ligands (*e.g.* L-Trp, cyanide, and others) [253].

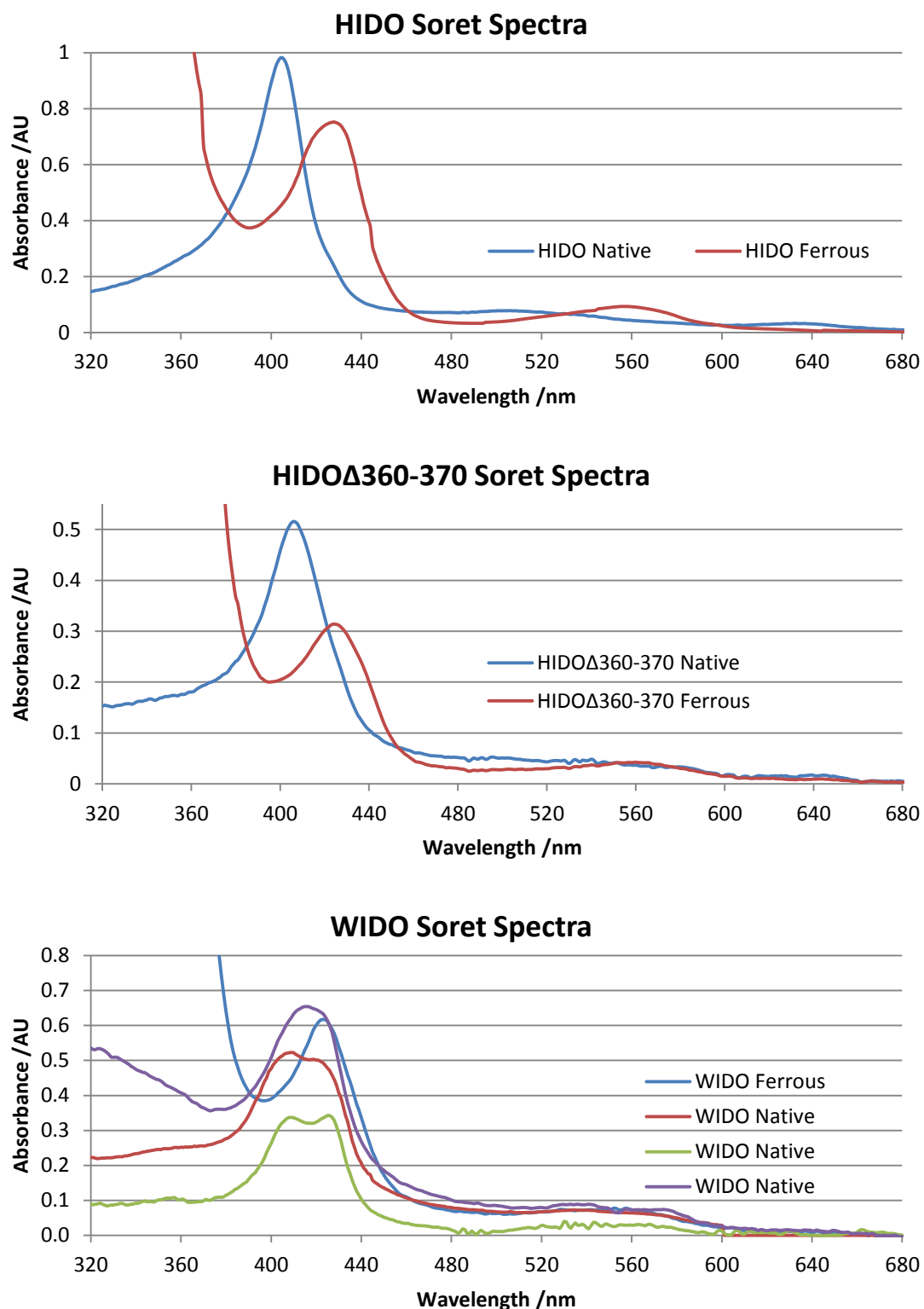


Figure 5.16. Representative UV-Vis absorption spectra of HIDO (top), HIDOΔ360-370 (middle), and WIDO (bottom). HIDO and HIDOΔ360-370 gave equivalent Soret spectra with an oxidised peak blue shifting with a lower extinction coefficient (404 and 405 nm shifting to 424 and 425 nm, respectively). WIDO gave two peaks in each independent protein batch, with varying relative intensities. **Purple:** Primarily oxidised with a much broader peak width than expected, suggesting a second underlying peak at 425 nm. **Blue:** The purple sample reduced with dithionite to yield a single Soret peak at 425 nm. **Red and Green:** Two independent samples with different 409/425 ratios. Increased absorbance in ferrous samples below 400 nm was due to unsubtracted dithionite absorbance.

Q-bands and charge-transfer bands

Above 500 nm, native HIDO possessed peaks at 540, 575, ~638 nm (weak, Figure 5.17 **A**). These were assigned as β , α , and charge-transfer bands (respectively) based on previous assignments for rabbit intestinal IDO1 [253]. Upon treatment of native HIDO with potassium ferricyanide, the α and β peaks effectively disappear, and the charge transfer band increases in absorbance. After treatment of either ferric or native enzyme with sodium dithionite, only a single peak at 557 nm was apparent. In HIDO Δ 360-370, the Q-band region behaves similarly to that of HIDO (Figure 5.17 **B**), with (effectively) the same absorption bands.

WIDO, however, displayed some differences in the Q-band region compared to HIDO. With overall identical peak positions (although the 638 nm absorption was quite weak), their behaviour with respect to ferricyanide and dithionite treatments were not consistent either with HIDO, or each other among different batches of WIDO. Shown in Figure 5.17 are the spectra of three different WIDO batches, one each from: standard IPTG induction at OD₆₀₀ 0.5, lactose auto-induction, and stationary phase induction with IPTG. In the first sample, native WIDO gave a negligible response to ferricyanide treatment, whilst treatment with dithionite produced the expected peak at 557 nm. An almost imperceptible shoulder at 540 nm may also still exist (Figure 5.17 **C**). The next sample examined (Figure 5.17 **D**), gave a dose-dependent response to ferricyanide addition, decreasing the 540 and 575 nm peaks and increasing the 638 nm peak. Treatment of this native enzyme with dithionite again gave a peak at 557 nm with a residual small absorbance apparent at ~530 nm. The final sample, gave the usual native peaks, in addition to a new peak at 670 nm, which remained after dithionite treatment but not after ferricyanide addition (Figure 5.17 **E**). Again, a residual peak at ~530 nm was apparent after treatment of native enzyme with dithionite.

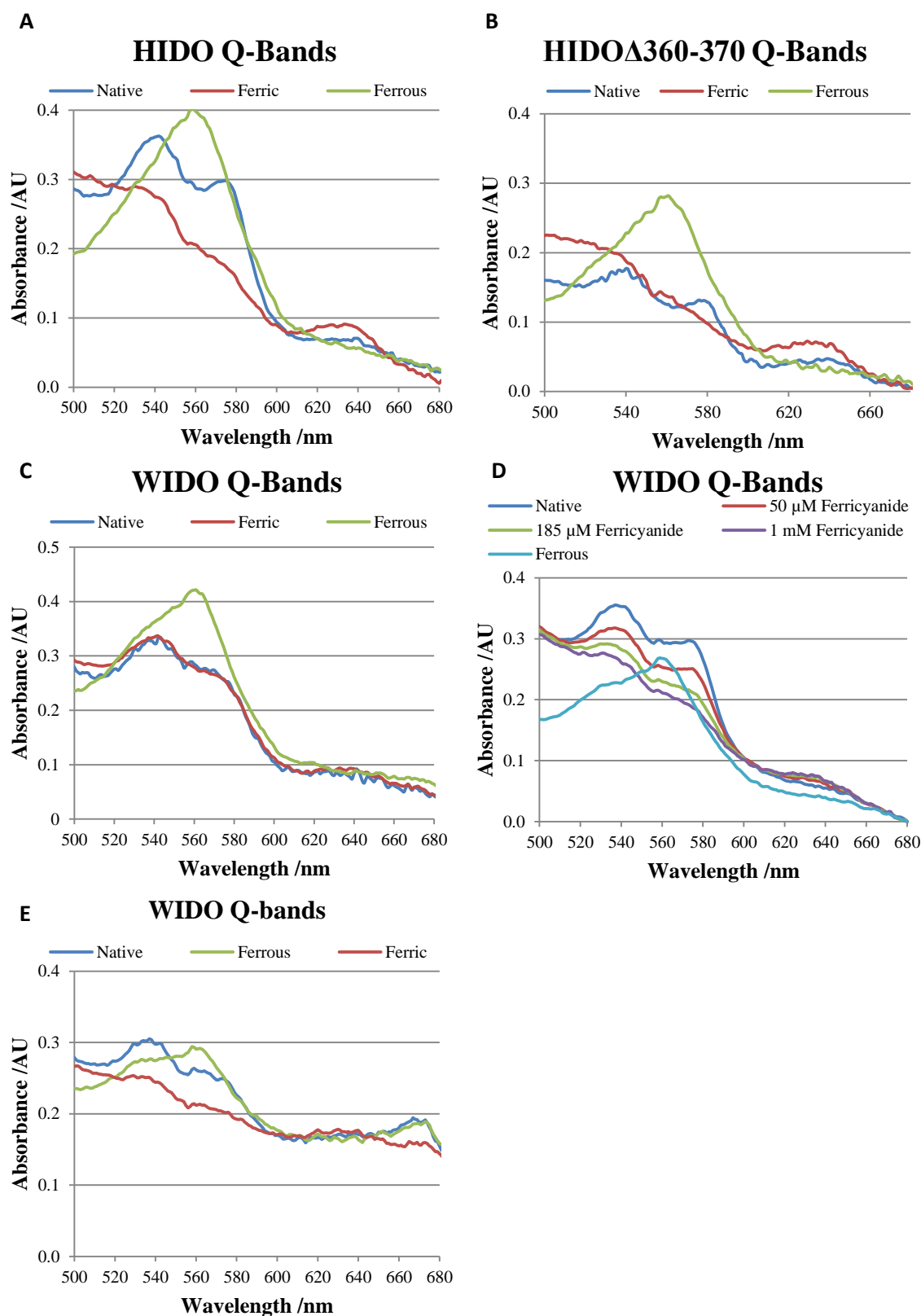


Figure 5.17. Q-band spectra of IDO1 proteins in the presence of either potassium ferricyanide (ferric), sodium dithionite (ferrous), or nothing (native). Spectra are in Tris buffer (50 mM, pH 7.4) at 20 °C in a 1 cm quartz cuvette. Ferricyanide had a final concentration of 2 mM unless otherwise stated. Dithionite was added as a single small crystal. HIDO and HIDO Δ 360-370 spectra are representative of all batches. Three separate batches are shown for WIDO, demonstrating batch-to-batch variation. See the main text above for peak assignments.

Taken together, the heme environments of HIDO and HIDO Δ 360-370 appear to show little difference by this technique, with equivalent Soret and Q-band behaviour. This was different to the case of WIDO, where two Soret peaks were found in all batches produced. Additionally, the Q-band region behaved in a batch specific manner with regards to responses to ferricyanide or dithionite. With regards to the Q-band region of the IDO1 proteins, differences between the native and ferricyanide-produced spectra is not expected to be due to a mixture of oxidations (all proteins were catalytically inactive without an additional reducing system); but is instead assumed to be due to electronic fine structure, such as different high and low spin populations between native and ferricyanide-treated protein.

No easy explanation for the behaviour of the WIDO mutant is apparent from this data. If the observed double Soret peak were the result of both oxidised and reduced heme, this would not explain the batch-to-batch variation observed in the Q-band region. Further, the presence of ferrous WIDO would be expected to be catalytically competent. In one instance, the Q-band spectra did not respond to ferricyanide treatment, while in other instances, a residual 540 nm peak was observed after dithionite treatment. The observations imply that the variances are not due to inherent chemical properties of the protein, but rather are due to batch-to-batch variation in the isolated protein – perhaps caused by protein misfolding and/or instability.

5.2.4. Expression of CYB5S

An initial 100 ml growth of EC538 pREP4 pQE9-CYB5S was performed at 37 °C to determine parameters for CYB5S production. This produced a rose-pink cellular pellet upon centrifugation. The His-tag present in the IDO1 constructs are 6 residues long, while for CYB5A and CYB5S they are 14 residues long. As such, it was expected that CYB5S would bind much more tightly to the IMAC column. The lysate was loaded in 20 mM imidazole (instead of 10 mM used for IDO1 proteins) and washed with 5 column volumes each of 20, 40 and 80 mM Tris-buffered imidazole. Elution was attempted with 160 mM imidazole, which was successful at moving the heavily coloured protein down the column, but relatively slowly. Therefore, the buffer was switched to 300 mM imidazole, which eluted the protein with the solvent front. These 160 and 300 mM fractions were collected together. They were analysed by SDS-PAGE, as shown in Figure 5.18. The protein was estimated to be $\geq 90\%$ pure by coomassie staining.

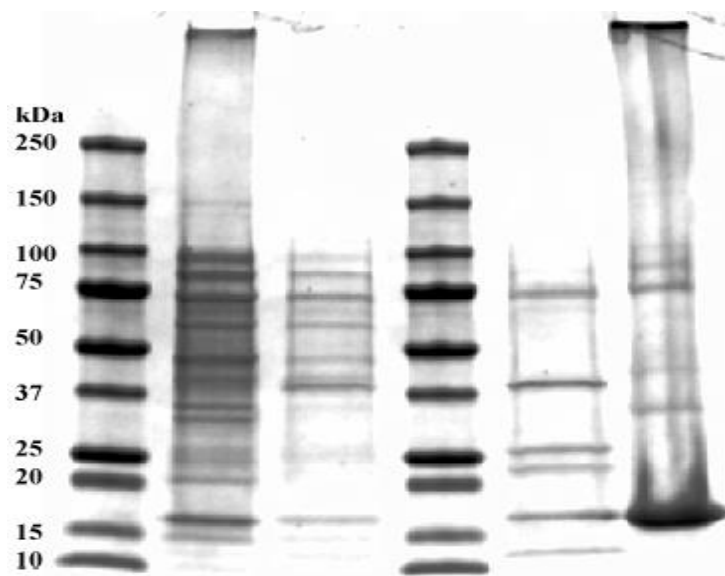


Figure 5.18. CYB5s IMAC purification analysis by SDS-PAGE. **Lane 1 and 4)** Ladder. **Lane 2)** IMAC unbound fraction. **Lane 3)** 40 mM wash. **Lane 5)** 80 mM wash. **Lane 6)** 160/300 mM elution fraction.

CYB5S oligomerises and was not protected by 1 mM EDTA and 1 mM DTT

SEC analysis of IMAC-purified CYB5S demonstrated two distinct peaks (Figure 5.19). Repeated injection every 30 minutes of aliquots from this sample, stored on ice between injections, demonstrated that the later eluting peak (smaller species, presumed monomer, referred to herein as α -form) was decreasing in absorbance and the earlier eluting peak (larger species, referred to herein as β -form) was increasing, and that the α/β ratio was also decreasing (Figure 5.19 and 5.20). A subsequent batch of CYB5S was made, and EDTA and DTT (1 mM final concentrations, each) was added to the protein immediately after IMAC elution. Again, SEC analysis (also containing EDTA and DTT in the FPLC mobile phase) demonstrated a shift from the α -form into the β -form (Figure 5.19 and 5.20). As the addition of EDTA and DTT did not prevent the change in CYB5S, all future work proceeded without the additives so as to avoid any artefacts introduced by their presence in IDO1 experiments. All α -form CYB5S going forward was immediately concentrated, diluted 1:1 with 80% glycerol, and flash frozen in liquid nitrogen and placed at -80 °C. During experiments, the protein was immediately placed onto dry ice after removal from storage, and only thawed at the time of dispensing.

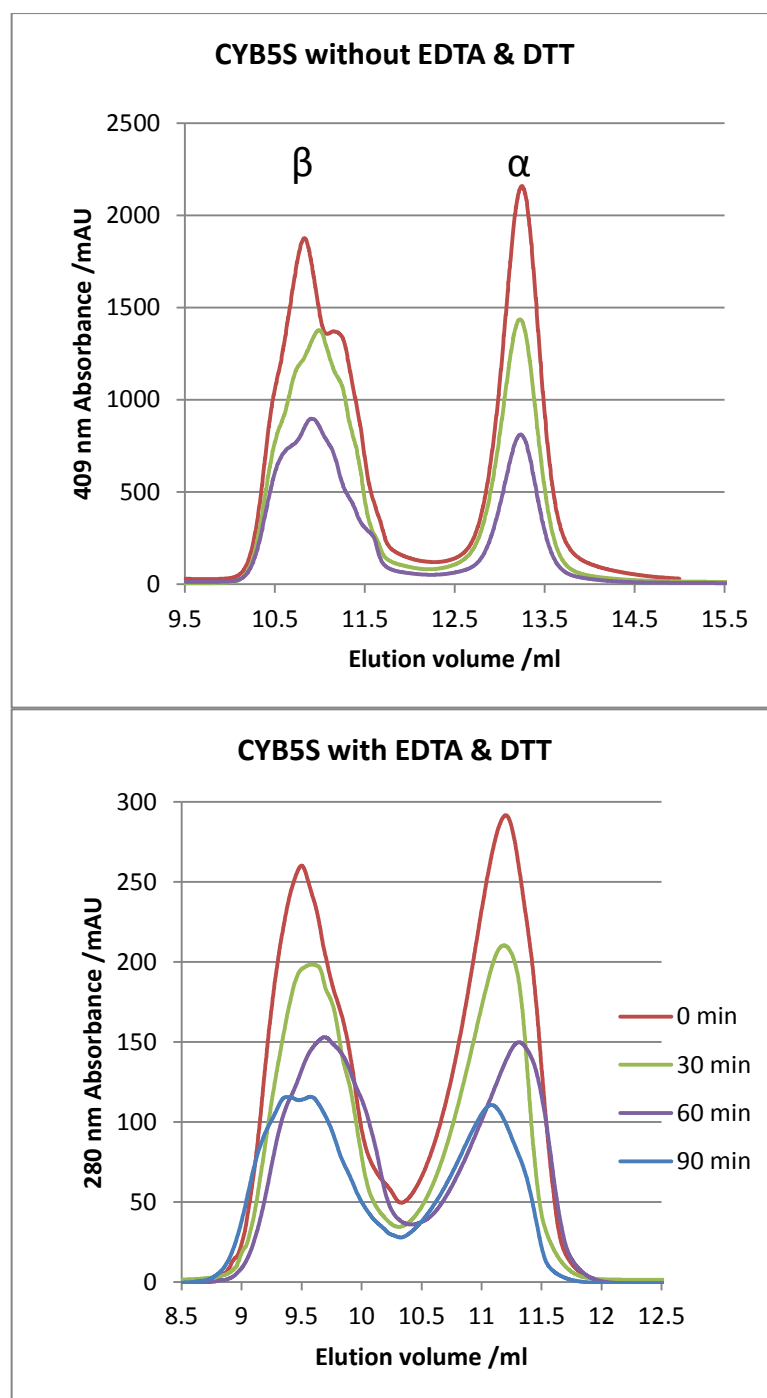


Figure 5.19. SEC of IMAC-eluted CYB5S with (bottom) or without (top) EDTA and DTT. **Top:** α - and β -peaks eluting from an ENrich SEC-70, 10/300 column (Bio-Rad) on a Bio-Rad NGC purification system monitored at 409 nm. **Bottom:** An independent growth of CYB5S purified on a GE Lifesciences Akta Pure with a Superdex-75 10/300 column (GE Lifesciences) monitored at 280 nm. Both samples were eluted with Tris buffer (50 mM, pH 7.4, 25 °C). The second sample was run with 1 mM of EDTA and DTT in both sample and buffer. Only one wavelength from each experiment is shown to aid visualisation. Note that the β -peak consistently has shoulders indicating a heterogeneous mixture.

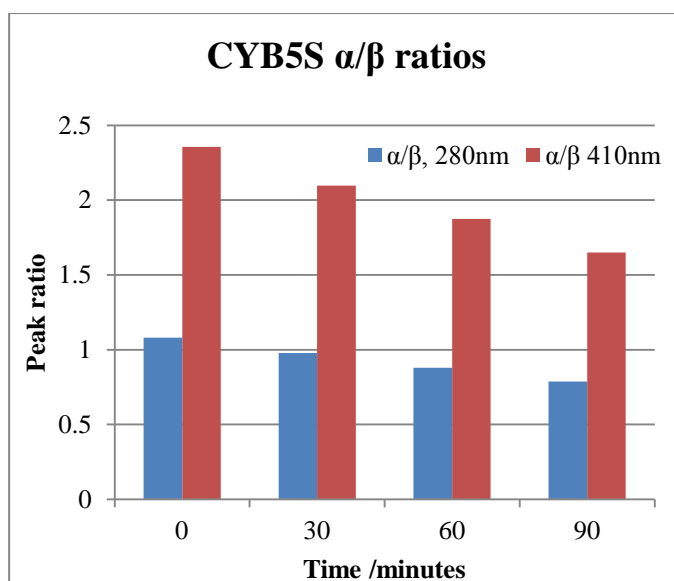


Figure 5.20. Area under the curve ratios for the α - and β -form in the CYB5S/EDTA/DTT sample (Figure 5.19, bottom) with respect to time. Despite the presence of EDTA and DTT, a clear trend towards the β -form is apparent at both wavelengths.

5.2.5. Expression of CPRS

A trial growth of CPRS from BL21(DE3) *Star* cells was conducted. The culture (100 ml, 25 °C) was induced overnight after 0.8 OD₆₀₀, and cells collected at 5 OD₆₀₀. A typical purification was carried out in the same manner as that of HIDO. After IMAC elution (160 mM) and concentration, the protein sample yielded a yellow/green tinge and a UV-vis spectrum with local maxima at 365 and 455 nm, consistent with the presence of FAD and/or FMN (Figure 5.21) [130]. Both FAD and FMN have peaks at these wavelengths, and it was not possible from this data alone to confirm that both co-factors were present. SEC purification (Superdex-75 3.2/30) described an almost homogenous sample (Figure 5.22). SDS-PAGE of SEC-purified CPRS (main peak) gave a single band consistent with the expected 74 kDa. Some small bands were present below this, and could either have been contaminating protein or ghosting due to overloading the lane (Figure 5.22).

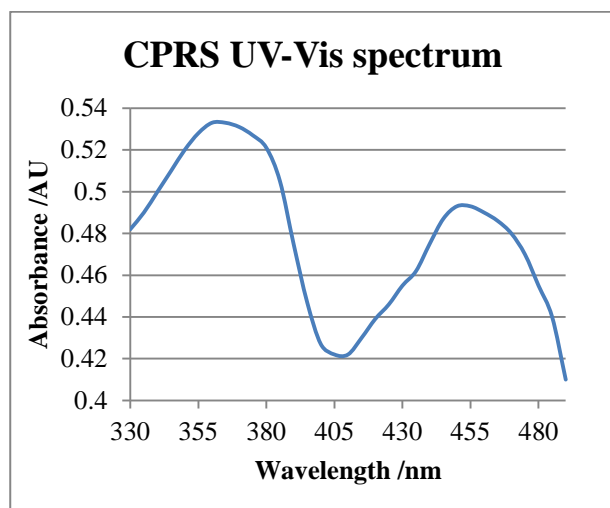


Figure 5.21. UV-Vis spectrum of the FAD/FMN region of CPRS taken at 5 nm resolution. The sample gave maxima at approximately 365 and 455 nm, consistent with the presence of FAD and/or FMN.

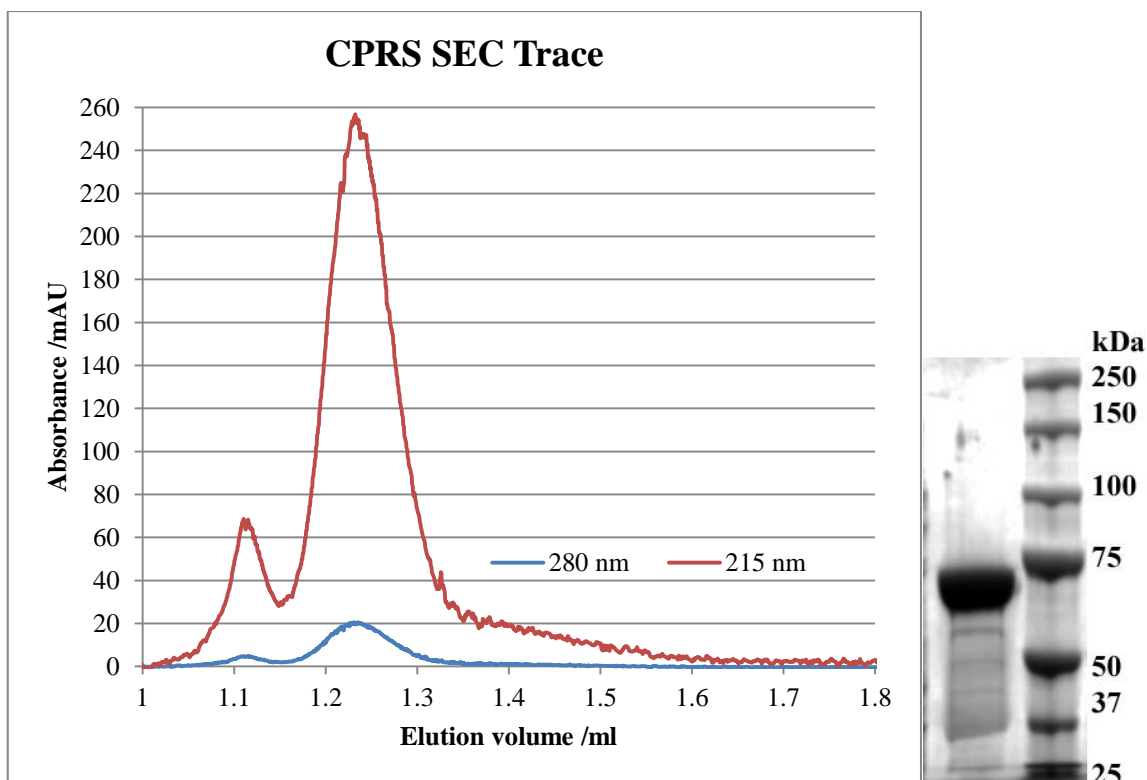


Figure 5.22. Left: SEC trace of CPRS on a Superdex-75 3.2/30 column using Tris buffer (50 mM, pH 7.4) at 25 °C. On this small scale, the protein produced was nearly homogenous after just IMAC purification. The major peak was collected for investigation. The minor peak was not investigated. **Right:** SDS-PAGE of recombinant CPRS after SEC purification.

CPRS contains both co-factors

The ability for CPRS to reduce potassium ferricyanide was monitored by ferricyanide's absorbance at 420 nm (measured extinction coefficient $\epsilon_{420} = 1.0 \pm 0.2$ (mean \pm standard deviation, $n=4$), manufacturer (Sigma-Aldrich) quoted value $1.04 \text{ mM}^{-1} \text{ cm}^{-1}$). CPRS (2 μg , 90 μl final volume, $\sim 300 \text{ nM}$) was assayed with 1 mM of ferricyanide and 1 mM of NADPH in potassium phosphate buffer (50 mM, pH 7.9) at 25 °C, and the absorbance recorded at 6 second intervals alongside a negative control that contained no CPRS (Figure 5.23). Reactions, started by the addition of NADPH, gave a rate of $75 \mu\text{M min}^{-1}$ for the negative control, whilst control-subtracted CPRS reactions gave a rate of $81 \mu\text{M min}^{-1} \mu\text{g}^{-1}$, when measured over the first minute (linear regression, R^2 0.990 and 0.999, respectively). This reaction confirmed the presence of FAD, from which ferricyanide receives its electron in CPR [255].

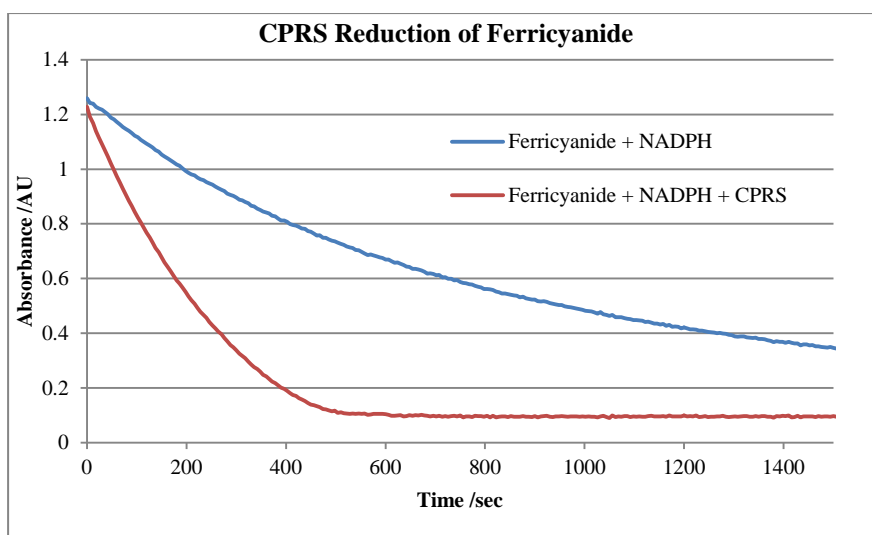


Figure 5.23. Reaction of CPRS reducing potassium ferricyanide *via* NADPH at 25 °C. Each assay contained, in a 90 µl volume, ferricyanide (1 mM), NADPH (1 mM), potassium phosphate (50 mM, pH 7.9) with the CPRS reaction additionally containing 2 µg of CPRS. Reactions were started by the addition of 9 µl of 10 mM NADPH.

The reduction of horse heart cytochrome c and CYB5S was visually investigated through the addition of 2 µg of CPRS protein to a cytochrome diluted into Tris buffer (25 mM pH 7.4), alongside negative controls missing either CPRS or NADPH. The strong purple colour indicative of the reduction of these cytochromes presented itself almost immediately when both CPRS and NADPH were present, whilst all negative controls maintained their red colour for at least 30 seconds. When 300 nM of CPRS was placed into a reaction containing 1 mM NADPH, 30 nM HIDO and 100 µM of L-tryptophan, approximately half of the tryptophan was converted after 10 minutes at 37 °C, whilst a control reaction containing no CPRS gave <5% conversion. The ability of CPRS to reduce these proteins allows for the inference that both FAD and FMN are present, as the FMN is required for electron transfer [256].

5.3. Discussion

Initial expressions of HIDO and WIDO proteins gave lower than expected yields per litre of culture and, especially in the case of WIDO, decreased purity as visualised by coomassie staining. These samples also possessed lower than expected heme incorporation. Cultures at 25 °C were compared to those at 12 °C, however, no obvious impact on these properties was observed. IPTG induction was also compared to auto-induction *via* lactose. For both HIDO and HIDOΔ360-370, auto-induction resulted in lower quality samples, as depicted by SEC traces. No substantial change was seen for WIDO, being poor in both cases. Lactose auto-induction was not optimised in this study, and therefore it is plausible that further optimisation could improve these data, especially in regards to balancing lactose-induced protein expression and ALA-induced heme synthesis.

Lower IPTG, combined with lower oxygen and a later phase of IPTG induction showed promising results. WIDO from these conditions contained an improved heme incorporation, yield, and purity by coomassie staining than with any other batch isolated – including the production of a single peak by SEC. It was not investigated whether all of these parameters contributed to the change, nor were any of them optimised beyond the single biological replicate produced here.

The IDO1 proteins and CYB5S were also characterised by absorption spectroscopy. HIDO and HIDO Δ 360-370 displayed effectively the same absorption spectra. WIDO gave a perplexing double Soret peak across all biological samples collected. Contrastingly, the peaks of the WIDO Q-band region were the same as those observed for HIDO and HIDO Δ 360-370, albeit with highly variable reactions to ferricyanide or dithionite treatment. The current hypothesis from this work regarding WIDO's absorption properties is that it was caused by mis- or unfolding of the protein, and led to a modified heme environment in some of the molecules. This has not yet been confirmed by structural characterisation such as circular dichroism or melting point analysis. It is possible that changes to the expression system may help to answer these questions, such as the use of a different affinity tag or expression from a non-bacterial expression system.

CYB5S was also purified. Some instability was observed by repeated SEC analysis in terms of both protein and heme absorbance. The hypothesis for this was that nickel may be leaching from the IMAC column. The addition of 1 mM of EDTA and DTT did not alleviate the observed instability. However, the hemochromagen analysis of CYB5S samples indicated a concentration of 1 – 3 mM of heme across different batches, and it is possible at these concentrations that CYB5S effectively competes for nickel *via* its His-tag. Increased concentrations of EDTA and DTT may help to alleviate this, as would cleavage of the His-tag *via* its TEV site. Storage of CYB5S at -80 °C after SEC appeared to prevent any further degradation, and was therefore sufficient for this work.

CPRS was also isolated and shown to be correct by SDS-PAGE sizing, easily separable from a minor peak seen in SEC, nearly pure by coomassie staining, and to be active against the expected substrates. Further characterisation was not undertaken at this time, however, optimisation of the expression protocol might be needed in the future given *E. coli*'s inability to import the biosynthetic precursor of FAD and FMN [257]. The co-expression of import machinery has been described [258].

Due to questions surrounding the purity and quality of IDO1 proteins produced, it was decided that the primary means of investigating whether the different IDO1 sequence led to different interactions with substrate tryptophan or electron carriers methylene blue and CYB5S, would be enzyme kinetics. This was rationalised as being a method that might be less susceptible to the

influence of differently folded proteins compared to other techniques such as circular dichroism or isothermal calorimetry. In particular, the presence of apo IDO1 molecules would not contribute to the catalytic turnover of tryptophan, whereas it or other proteins might still have some interaction with CYB5S and so produce noise in circular dichroism or isothermal calorimetry experiments.

5.4. Conclusion and future research

HIDO, WIDO, and HIDO Δ 360-370 proteins were produced and characterised, in addition to CYB5S and CPRS. A large amount of effort was put into determining how modulation of *E. coli* growth conditions could be used to improve the quality and the yield of the IDO1 proteins. In a final attempt, the use of low oxygen and low induction levels using IPTG produced the first example of a monodispersed IDO1 protein on size-exclusion chromatography. Replication of this work, and potentially identification of the biochemistry behind it, is of interest in future work. The easy production of high quality, monodispersed, apo-enzyme is not just of interest as a protein engineering project, but could also lead to easier crystallisation in the future. Such crystal structures are of major interest to the fields of structural biology and medicinal chemistry in better understanding how IDO1 functions in vivo, and in aiding the design of potential new drugs.

5.5. Methods

General procedures have been provided here. Please consult individual experiments within Chapter 5 for specified differences.

5.5.1. Reagents and stock solutions

Myoglobin (M1882), hemin (51280), DMSO (D8418), pyridine (360570), sodium hydroxide (S5881), Sodium chloride (S9625), sodium dithionite (85%, 157953), ammonium sulfate (A4418), potassium dihydrogen phosphate (795488), disodium hydrogen phosphate heptahydrate (S9390), coomassie Brilliant G-250 (B0770), glycine (V900144), phenylmethylsulfonylfluoride (P7626), magnesium chloride (M8266), EDTA disodium salt (E5134), α -D-glucose (G5767), and Tris (T1503), were from Sigma-Aldrich. Potassium ferricyanide (104971) was from Merck.

Kanamycin (USP, 0405) and ampicillin (USP, 0339) were from Amresco, Australia. DNase I (10104159001), cOmplete Ultra EDTA-free protease inhibitor cocktail (05892953001) were from Roche. HisTrap-HP IMAC columns (17-5248-05), and Sephadex G25 (PD-10, 17-0851-01) were from GE Lifesciences. Tryptone (211705), yeast extract (212750), bacteriological agar (LP0011), and glycerol (GA010), and lactose (LL031) were from Bacto, Australia. Centrifugal devices with 30 kDa were Amicon Ultra devices (UFC803024) from Merck-Millipore, and 10kDa were Microsep Advance (MCP010C41) from Pall Corporation.

ZYP5052 carbon sources

A 50x concentrate of carbon sources for ZYP5052 autoinducing media was made by dissolving α -D-glucose (6.25 g), α -lactose (25 g), and glycerol (62.5 g) into a final volume of 250 ml of hot water that was then sterile filtered through a 0.20 μ m membrane. Storage was at ambient temperature for up to 3 months.

NPS

A 20x concentrate of NPS was made by mixing $(\text{NH}_4)_2\text{SO}_4$ (6.6 g), KH_2PO_4 (13.6 g) and Na_2HPO_4 (14.2 g) into a final volume of 100 ml of hot water that was then sterile filtered through a 0.20 μ m membrane. Storage was at ambient temperatures for up to 3 months.

Antibiotic stocks

Antibiotic stocks were made by dissolving kanamycin sulfate (100 mg/ml) or ampicillin sodium salt (50 mg/ml). Stocks were then sterile filtered through a 0.20 μ m membrane, aliquoted into 200 μ l or 1 ml portions, before storage at -20 °C for up to 6 months.

Imidazole

Imidazole (17.02 g, 250 mmol) recrystallised from boiling ethanol (AR-grade, 100%) was dissolved in water (250 ml) and adjusted to pH 7.4 with 6 M HCl and stored in the fridge for up to 12 months.

Tris

Tris (60.72 g, 500 mmol) was dissolved in 1 litre of water and adjusted to pH 7.4 with 6 M HCl. The stock was sterile filtered through a 0.20 μ m membrane, and stored in the fridge for the shorter of 12 months or until particulates formed. Diluted solutions (<250 mM) were stored in the fridge for up to 3 months if sterile, or up to 1 week otherwise.

Tris-Gly-SDS

The 10x stock consisted of Tris (30.3 g, 250 mmol), glycine (144.1 g, 1.92 mol) and SDS (10 g, 35 mmol) dissolved in 1 litre of water, and stored in the fridge at 4 °C for up to 12 months. 1x solutions were stored in the fridge until particulates were observed (<1 month).

Coomassie stain

Ammonium sulfate (10 g) was dissolved in water (40 ml) followed by methanol (40 ml). Coomassie G-250 was then added (120 mg) and stirred for 20 minutes. Orthophosphoric acid (85% w/v, 12 ml) was then added while stirring. The stain was resuspended by shaking briefly before use.

LB-Lennox

Tryptone (10 g), yeast extract (5 g) and NaCl (5 g) were completely suspended in a final volume of 1 litre of water and autoclaved at 121 °C for 20 minutes.

Agar plates

Unless otherwise noted, agar plates used LB-Lennox media additionally containing bacteriological agar powder (15 g/l). Individual plates (~15 ml in volume) were made selective by the spreading of 100 μ l of desired antibiotic (kanamycin, 15 mg/ml stock; ampicillin, 7.5 mg/ml stock) across the top of plates, and then incubating at 37 °C for 1 hour before use.

ZYP5052

Tryptone (10 g), yeast extract (5 g), and MgCl_2 (95 mg, 1 mmol), was added to 930 ml of water and autoclaved at 121 °C for 20 minutes. Upon cooling NPS (50 ml) and ZYP5052 carbon sources (20 ml) were added *via* a 0.20 μm syringe driven filter.

5.5.2. Culturing for protein expression

Cultures of HIDO, HIDO Δ 360-370, WIDO and CYB5S with IPTG induction

The relevant glycerol stock was kept frozen on dry ice. A scraping was taken under sterile conditions and serially streaked for single colonies. A single colony was inoculated into 40 ml of LB-Lennox media with kanamycin (100 mg/l) and ampicillin (50 mg/l) and grown overnight at 25 – 37 °C with shaking to an OD_{600} of 5 – 8. Cells were diluted into 1 litre of antibiotic-containing LB-Lennox media to a final OD_{600} of 0.05 in a 5 l conical flask and shaken at 250 rpm, 25 °C. At an OD_{600} of 0.6, 5-aminolevulinic acid (ALA hydrochloride, 84 mg/l, 0.5 mM) was added by dissolving in 1 ml of water and adding *via* a 0.2 μm syringe driven filter. After 30 minutes, Isopropyl β -D-1-thiogalactopyranoside (IPTG, 24 mg/l, 0.1 mM) was added *via* the same means. After another 30 minutes, phenylmethylsulfonylfluoride (PMSF, 174 mg/l, 1 mM final concentration) was added by dissolving in 1 ml of DMSO and adding directly to the culture. Induction occurred for a total of 12 – 16 hours (OD_{600} 6 – 8).

Cultures of HIDO, HIDO Δ 360-370, WIDO and CYB5S autoinduced in ZYP5052

A single colony was inoculated into 40 ml of LB-Lennox media with kanamycin (100 mg/l) and ampicillin (50 mg/l), and grown overnight with shaking (500 ml conical, 200 rpm, 25 °C). The culture (OD_{600} 6 – 8) was diluted into 1 litre of ZYP5052 media (containing kanamycin [100 mg/l] and ampicillin [50 mg/l]) to a final OD_{600} of 0.05, and cultured in a 5 litre conical flask (250 rpm, 25 °C). At an OD_{600} of ~4 (roughly 12 hours), 5-aminolevulinic acid (ALA hydrochloride, 84 mg/l, 0.5 mM) was added by dissolving in 1 ml of water and adding *via* a 0.2 μm syringe driven filter. 30 minutes later, phenylmethylsulfonylfluoride (PMSF, 174 mg/l, 1 mM) was added by dissolving in 1 ml of DMSO and adding directly to the culture. Culturing in ZYP5052 continued for a total of 36 hours.

Culture of WIDO with late phase IPTG induction

A single colony was inoculated into LB-Lennox media (1 litre) containing ampicillin and kanamycin (50 and 100 mg/l, respectively), 1 mM magnesium sulfate, and 0.3% (w/v) glucose and grown overnight (25 °C, 180 rpm) to an OD_{600} of 5. The cells were collected by centrifugation (17, 000g, 4 °C, 10 minutes) before being resuspended in 1 l of LB-Lennox with additives as above, except without glucose. The culture was shaken at 100 rpm at 25 °C for 90 minutes before ALA hydrochloride (84 mg/l, 0.5 mM), IPTG (5 mg/l, 0.02 mM) and PMSF (174 mg/l) were added at 30 minute intervals. Induction proceeded for a total of 18 hours.

Cultures of CPRS with IPTG induction

Expression of CPRS was conducted under essentially identical conditions to the IDO1 proteins, except only a 100 ml culture was performed. Expression was induced *via* IPTG at OD_{600} 0.8, with PMSF being added 30 minutes later. Induced cells were collected at an OD_{600} of 5.

5.5.3. Protein purification

Cells were pelleted in 500 ml Beckmann bottles at 17,000g, 20 minutes, 4 °C, to yield 7 – 10 g of wet pellet per litre of culture when collected between OD₆₀₀ 5 – 6. To each bottle was added 20 ml of lysis buffer containing NaCl (300 mM), Tris (50 mM, pH 7.4), DNase (<1 mg), EDTA-free protease inhibitor cocktail, and imidazole as listed in Table 5.2. Bottles were then secured in a single orbital shaker and spun at 350 rpm for 15 – 20 minutes until the pellet completely resuspended. Cells were lysed on a French press at >20,000 psi (two passes), centrifuged (25,000g, 15 minutes, 4 °C), and filtered through a 0.45 µm membrane before being applied to a 1 ml Ni-NTA column (2x 1 ml columns in series for CYB5S) using a peristaltic pump. The column was washed with 10-column volumes of binding buffer (the same buffer as lysis buffer, without DNase or protease inhibitor), and then washed further with wash solutions as listed in Table 5.2. Proteins were eluted with imidazole (160 mM) in Tris (50 mM, pH 7.4), except CYB5S which used 300 mM imidazole instead. Eluted material was desalted on a Sephadex G-25 column and eluted with Tris (50 mM, pH 7.4) before being concentrated on a 30 kDa centrifugal device and further purified by FPLC (AKTA Pure, GE Lifesciences) on a Superdex-75 column using Tris (50 mM, pH 7.4, 1 ml/min). Fractions with high heme-protein ratios were combined, diluted 1:1 with 80% (v/v) glycerol in water, and concentrated on a 30 kDa centrifugal device. Protein was aliquoted into 5 µl portions, flash frozen in liquid nitrogen, and stored at -80 °C.

Table 5.2. Imidazole concentration in lysis buffers.

Protein	Lysis and binding	Imidazole amounts	
		Wash 1	Wash 2
HIDO, HIDOΔ360-370, CPRS	10 mM	20 mM x10 column volumes	40 mM x10 column volumes
WIDO	5 mM	10 mM x20 column volumes	40 mM x5 column volumes
CYB5S	20 mM	40 mM x20 column volumes	80 mM x10 column volumes

5.5.4. Protein characterisation

Bradford assay

BSA was prepared as a stock solution (10.0 mg/ml) in Tris buffer (25 mM, pH 7.4, glycerol 40% [v/v]) and stored at -20 °C for up to 6 months. Temporary stocks of BSA 100 – 580 µg/ml, in 100 µg/ml increments, were made by diluting into Tris (25 mM, pH 7.4). This diluted BSA (10 µl) was then added into wells of a 96-well plate. A master mix of Bradford dye reagent (Bio-Rad) was made by diluting 1 part dye with 4 parts water and mixing thoroughly. Dye (200 µl) was then distributed into each BSA containing well. Negative controls used Tris buffer (10 µl, 25 mM, pH 7.4). Using the same dye master mix, protein samples (10 µl) were made in the same fashion. Absorbance measurements were conducted on a Pherastar FS (BMG) at 595 nm, using raw data points between 0.2 and 0.7 AU.

SDS-PAGE

SDS-PAGE was performed using mini-Protean TGX 4-20% gels (Bio-Rad, Australia). Each lane contained a total of 2 – 10 µg of protein as measured by Bradford assay or by absorbance at 280 nm using $\epsilon_{280\text{nm}} = 1.0 \text{ mg}^{-1} \cdot \text{ml} \cdot \text{cm}^{-1}$. Gels were run in Tris-Gly-SDS buffer at 150 V for 60 minutes.

Better band shape was observed when the outer buffer volume was filled to the bottom of each loading well, and the tank was submerged in an ice-water mixture to the same level. After running, the gel was washed of SDS by fixing in ethanol:water:acetic acid (4:5:1) mix for 2 hours. The best sensitivity and contrast was achieved when staining for 16 hours followed by destaining in acetonitrile:water (4:6, 2x 20 minutes) followed by 6 hours in a 2:8 mixture. Alternatively, intense bands could be stained in 20 minutes without fixation or destaining steps. Imaging was performed on a Gel DOC EZ system (Bio-Rad, Australia).

Absorption spectra

Absorption spectra of heme proteins was collected in Tris buffer (25 mM, pH 7.4) at ambient temperature. Ferric and ferrous comparison were created by diluting into Tris buffer and collecting the native spectrum, before splitting the sample. To one was added a stock solution of potassium ferricyanide (100 mM) to a final concentration of 1 mM (unless otherwise stated). To the other was added the same volume of water and a single crystal of sodium dithionite. Except in the case of fresh sodium dithionite, the use of stock solutions created high turbidity due to decomposition. Ferricyanide and dithionite spectra were obtained immediately, and then again at 30 second intervals for 2 minutes, to ensure a stable spectrum.

Pyridine-heme chromagen

Hemin standard was dissolved in DMSO at 2 mM, aliquoted into 50 µl portions, and stored at – 80 °C, and thawed only once. Myoglobin (10 mg/ml) was stored in Tris (25 mM, pH 7.4, 40% glycerol) at – 20 °C for up to 7 days. Absorption spectra (500 – 800 nm) were obtained in a 10 mm quartz cuvette at ambient temperature. Dilutions of hemin and protein were performed using DMSO or Tris (25 mM, pH 7.4), respectively. Hemin concentrations were calculated from their mass on a 5 decimal place balance using a density of 1.1 g/ml.

Samples (10 – 20 µl) were diluted into 100 µl of a solution of pyridine (20% v/v) in sodium hydroxide (20 mM). The sample was then split in half. To one was added a stock solution of potassium ferricyanide (100 mM) to a final concentration of 1 mM (unless otherwise stated). To the other was added the same volume of water and a single crystal of sodium dithionite. Except in the case of fresh sodium dithionite, the use of stock dithionite solutions created high turbidity due to decomposition. Ferricyanide and dithionite spectra were obtained immediately, and then again at 30 second intervals for 2 minutes, to ensure a stable spectrum.

Chapter 6

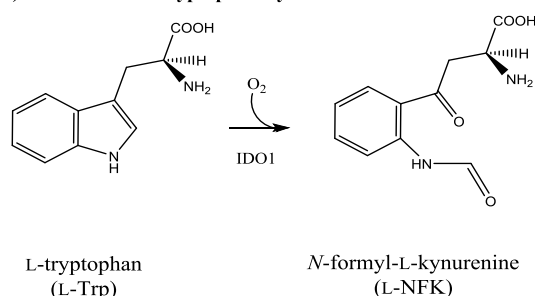
Kinetics of IDO1 Proteins

This chapter presents background on the molecular mechanism of IDO1, followed by background on the theory of enzyme kinetics. It then combines these two in order to define the physical bounds in which the kinetics of the enzyme can be interpreted. It then presents the kinetics of human IDO1 (HIDO), walrus IDO1 (WIDO) and the first of the human deletion mutants, $\text{HIDO}\Delta 360\text{-}370$, when supported either by an ascorbic acid/methylene blue, or ascorbic acid/soluble cytochrome b5 (CYB5S) reducing system. These kinetics were analysed from the perspective of the role of the reducing system, and the role of the loop, on IDO1 kinetics.

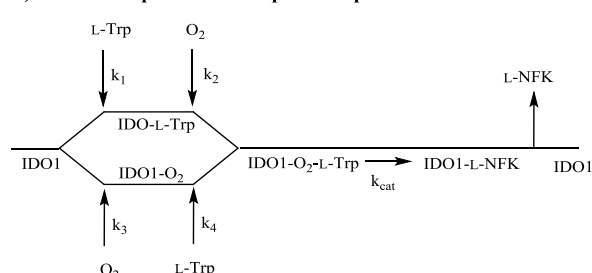
6.1. IDO1 as a multi-substrate enzyme

The conversion of D- or L-tryptophan (D- or L-Trp) to the equivalent *N*-formyl kynurenine (D- or L-NFK) requires oxygen, in addition to a ferrous IDO1 enzyme. Under experimental conditions, ferrous IDO1 is auto-oxidised to the inactive ferric form (the electron is not consumed by the oxidation of substrate [210]). Thus, an electron could be considered a third substrate under equilibrium conditions. Multi-substrate enzymes fall into a number of categories with respect to the sequence of substrate and product binding and leaving events. Two of these are the random-sequential and the ordered-sequential models. In random-sequential cases, the order in which the substrates bind is not relevant, whilst under ordered-sequential conditions, the substrates have a defined binding order (the term ‘sequential’ refers to the requirement for all substrates to bind prior to any product leaving – a superfluous concept for IDO1). These scenarios are shown in Figure 6.1 using Cleland notation [259], for the bi-uni molecular case (two substrates, one product) of IDO1. The scheme shown only considers ferrous IDO1.

A) Oxidation of L-tryptophan by IDO1



B) Random-sequential: two equivalent paths



C) Ordered-sequential: Two alternative paths

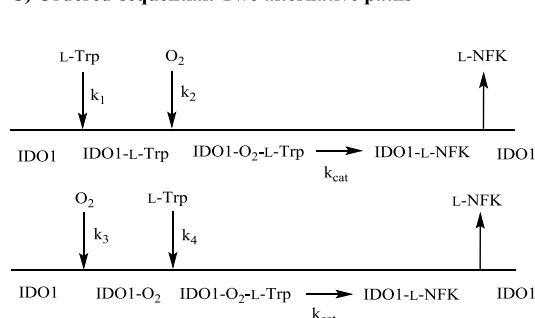


Figure 6.1. **A)** Oxidation of L-tryptophan carried out by IDO1. **B)** and **C)** Cleland notation describing the bi-uni molecular model of ferrous IDO1 as either a random-sequential (**B**) or an ordered-sequential (**C**) enzyme. The notation is read from left to right with the horizontal line representing reaction progression. An arrows moving toward the horizontal line indicates the binding of, while an arrow moving away indicates the leaving of product. Only binding events in the forward direction (*i.e.* leading to reaction) are considered in this example.

In a completely random mechanism, the reaction path taken has no impact on the kinetics observed. Assuming that k_{cat} is constant regardless of the path taken, then in a completely random mechanism, the rates of either pathway are identical: $V_{(k1,k2)} = V_{(k3,k4)}$. For a completely ordered mechanism, the path taken has a large impact, as $V_{(k1,k2)} \ll V_{(k3,k4)}$, to the point that one of the rates approaches zero for practical conditions. An intermediary path may also exist, where $V_{(k1,k2)} \approx V_{(k3,k4)}$. That is, the rates are unequal, but similar enough in magnitude that both contribute appreciably to the observable rate. For IDO1 under *in vitro* conditions, it has been identified that the path defined by $V_{(k3,k4)}$ predominates, whilst the path defined by $V_{(k1,k2)}$ is slower [219, 224]. However, as the concentration of L-Trp increases, it begins to competitively inhibit oxygen from binding to ferrous heme, and thus substrate inhibition becomes apparent. This substrate inhibition is not observed for D-Trp within experimentally accessible concentrations (low mM). In this case, k_1 is likely so small relative to k_3 , that the k_1k_2 path is not observed, and the kinetics assume a standard Michaelis-Menten (hyperbolic) shape. The K_M of D-Trp is ~200-fold higher than that of L-Trp, supporting this [260].

6.2. Auto-oxidation of IDO1

A complication of the IDO1 case is the oxidation state of the heme. IDO1 is only functional in the ferrous form, and the reaction does not consume the electron – ferrous IDO1 remains after the release of product [210, 261]. The electronic state of the binary complex (IDO1- O_2) is best described as ferric-superoxide in nature, where the electron primarily resides on the dioxygen ($Fe^{3+}-O_2^-$) [211, 212]. This superoxide can be replaced by water to yield the ferric enzyme and superoxide [212, 213]. It is known that using a superoxide generating system such as xanthine oxidase, potassium superoxide, or superoxide produced by non-enzymatic reactions of NAD(P)H, can support the oxidation of tryptophan *via* IDO1 [210, 214]. A more comprehensive representation of the IDO1 reaction cycle is shown in Figure 6.2.

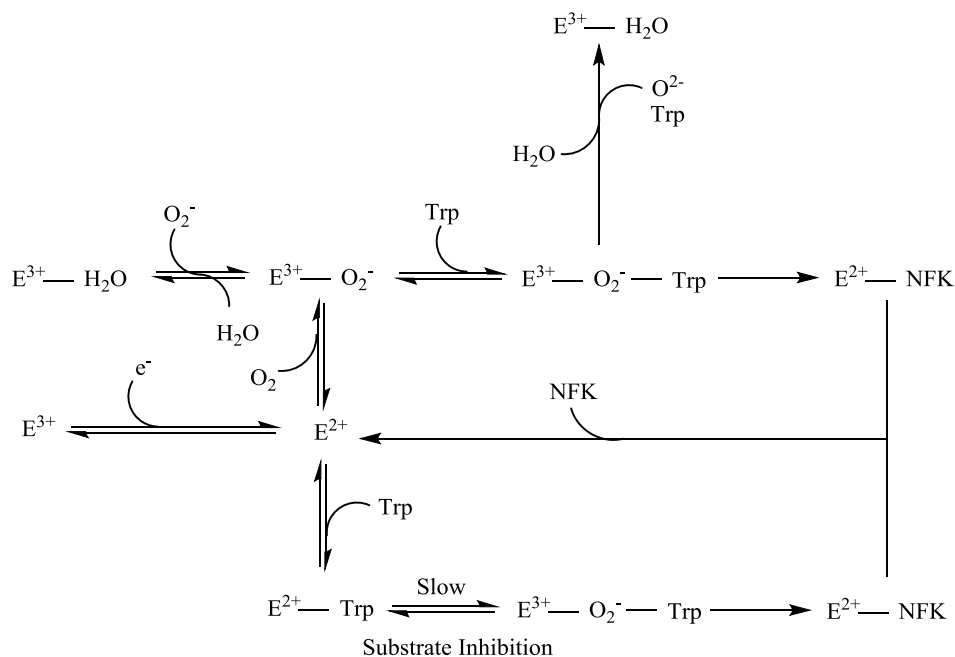


Figure 6.2. Reaction scheme of substrate oxidation by IDO1, where E^{3+} and E^{2+} are the ferric and ferrous enzymes, respectively. There is some evidence to suggest that L-Trp may accelerate the rate of auto-oxidation [210, 212, 262], but here it is assumed to also occur in the absence of substrate. No allostery is considered here (see Section 6.4.2 Analysis of multi-substrate reactions).

6.3. Methods of IDO1 reduction

Historically, *in vitro* experiments on IDO1 have most commonly been carried out using ascorbic acid as an electron source and methylene blue (MB) as an electron delivery system. The major route of electron transfer is the reduction of MB by an undetermined number of electrons (one or two) and the subsequent transfer from reduced MB to IDO1 [214]. At high MB concentrations ($>100 \mu\text{M}$), superoxide generation also participates in observed product formation [214]. Use of superoxide dismutase (SOD) demonstrated that this was not the major route of electron transfer, however [214]. Additionally, the reaction between ascorbic acid and MB can create hydrogen peroxide, which has been shown to deactivate IDO1 through protein residue oxidation [240]. For this reason, catalase has been included in the reaction, although SOD has generally not been.

An alternative method has been to use a cytochrome redox cycling system. Pearson *et al.* provide kinetics of IDO1 reactions *via* nicotinamide adenine dinucleotide phosphate (NADPH) using cytochrome P450:NAD(P)H reductase (CPR), or CPR and cytochrome b5 (CYB5) in a liposomal system [122]. In this liposomal system, IDO1 reactions supported by CPR and NADPH gave variously Michaelis-Menten, substrate inhibition, or allosteric sigmoidal kinetics, depending on the concentration of CYB5 and MB present. Traditionally, the allosteric sigmoidal kinetic shape has been interpreted as representing the presence of at least two non-equivalent active sites, where the binding of substrate to one site improves the reaction rate at another site. For IDO1,

therefore, this may represent the first evidence of a heteromeric complex between two IDO1 molecules and these other proteins [122]. The necessity of two active sites is not obligatory, though. Rather, it means only that two (or more) non-equivalent reaction rates were present and their relative predominance was affected by the concentration of L-Trp. For example, it is possible under liposomal conditions, that the relative sizes of k_1 , k_2 , k_3 and k_4 (Figure 6.1) were substantially different to that of a non-liposomal system, and this could have led to a differently shaped kinetic graph. Whilst there is no doubt that both CYB5 and CPR interact with and reduce IDO1, it should be noted that a system with both of these proteins, as well as NADPH in the absence of catalase and superoxide dismutase, can reduce IDO1 *via* multiple pathways (Figure 6.3), and this leads to difficulty in assigning molecular mechanisms to kinetic observations [210]. Thus far, there has been no follow up investigations as to the molecular-level source of the different kinetic shapes described by Pearson *et al.* [122].

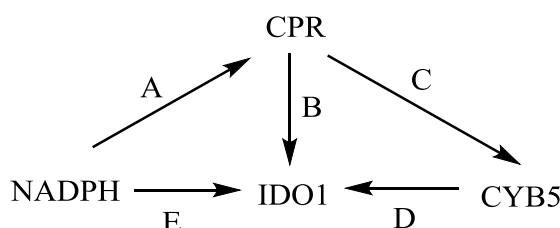
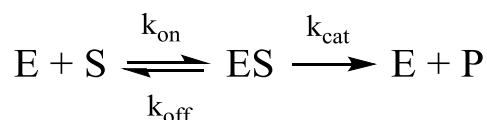


Figure 6.3. Possible pathways of electron movement during the experiments of Pearson *et al.* reporting variously Michaelis-Menten, substrate inhibition and allosteric sigmoidal kinetics, and in the absence of either catalase or superoxide dismutase [122]. NADPH reduction of CPR (path A), which can then pass the electron to IDO1 (B) or to CYB5 (C) (and then to IDO1 [D]). Reduction of IDO1 *via* Compound I and Compound II formation, initiated by hydrogen peroxide and/or superoxide derived from NADH, has been reported [210], and is represented here as (E) due to the similar chemical properties of NADPH.

6.4. Models for kinetic analysis

6.4.1. Michaelis-Menten and Briggs-Haldane kinetics

The Michaelis-Menten equation describes a simple model of an enzyme reaction where a single substrate molecule (S) binds reversibly to an enzyme (E), and where some portion of that enzyme-substrate complex (ES) irreversibly reacts to form a product (P) that instantly dissociates, leaving behind the active enzyme (Scheme 6.1).



Scheme 6.1. A simple model for a single substrate enzyme acting irreversibly.

Michaelis and Menten assumed that the rate-limiting step was product formation, with substrate and product binding/unbinding events being very much faster ($k_{\text{cat}} \ll k_{\text{off}}$), known as the rapid equilibrium approximation [263]. Using this, they could define the concentration of all species as differential rate equations with respect to time, and come to the instantaneous Michaelis-Menten equation shown in Equation 6.1 and plotted in Figure 6.4 [264, 265]. Here, v is the instantaneous velocity of the reaction at a substrate concentration of S , V_{max} is the theoretical maximum velocity at infinite substrate concentration (for a specified concentration of active sites) and K_M is the concentration of S required to obtain a velocity of half V_{max} .

$$v = \frac{V_{\text{max}}[S]}{K_M + [S]}$$

Equation 6.1. The Michaelis-Menten equation used to analyse enzyme reactions.

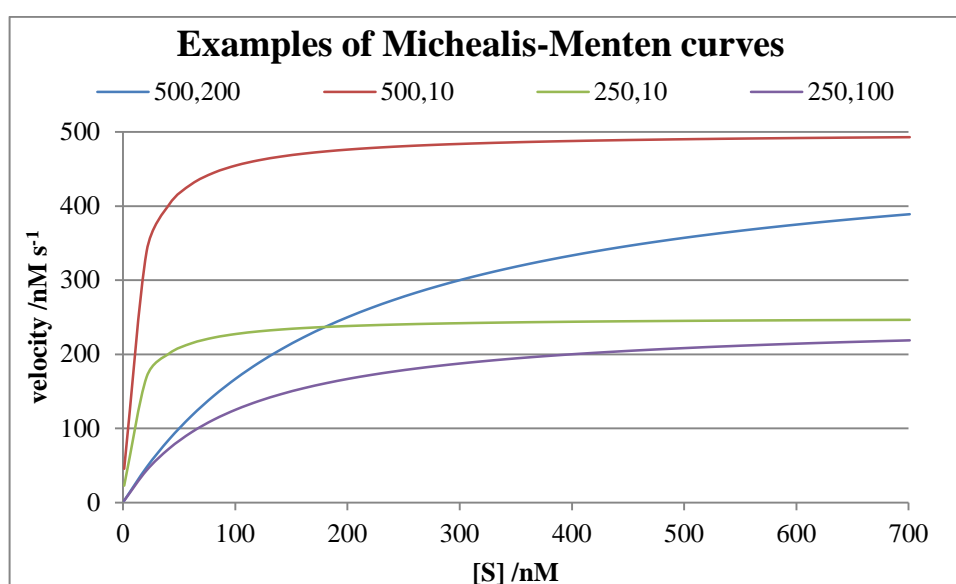


Figure 6.4. Michaelis-Menten kinetics give a hyperbolic shape. The legend gives the values of V_{max} and K_M used for each curve, respectively.

Later, Briggs and Haldane derived the same instantaneous equation using the steady-state assumption and free-ligand approximation *in lieu* of the rapid equilibrium equation [266]. The steady-state approximation states that the concentration of ES does not change over time and thus the rate equation is: $d[\text{ES}]/dt = 0$. The free-ligand approximation states that the concentration of substrate at a sufficiently early time t , $[S]_t$, is much higher than the concentration of $[\text{ES}]$, and therefore approximately equals the starting substrate concentration $[S]_0$. This is true when the K_M is much higher than the total enzyme concentration, which is the case in IDO1 experiments where the enzyme concentration is nanomolar and L-Trp is micromolar to millimolar. Thus, the applicability of the Michaelis-Menten equation is broadened by no longer only describing reactions where $k_{\text{cat}} \ll k_{\text{off}}$ holds true. This also changes the analytical definition of K_M .

Under Michaelis-Menten assumptions: $K_M = k_{\text{off}}/k_{\text{on}} = K_d$, the substrate dissociation constant. Whilst under Briggs-Haldane conditions: $K_M = (k_{\text{off}} + k_{\text{cat}})/k_{\text{on}} \neq K_d = k_{\text{off}}/k_{\text{on}}$. Whilst the equation is referred to as the Michaelis-Menten equation, the analysis used here (and generally in the literature) is based on the Briggs-Haldane assumptions.

6.4.2. Analysis of multi-substrate reactions – assumptions made for IDO1 analysis

IDO1 is a multi-substrate enzyme, thus a realistic analysis should include terms for both tryptophan and oxygen binding to both ferric and ferrous forms of the enzyme. The transitions between oxidised and reduced enzyme should also be given their own equations, as these reactions are not part of a simple equilibrium. The addition of multiple substrate terms, and therefore multiple binding events, make such equations large and unwieldy. Instead, multi-substrate reactions are generally performed under pseudo-first order conditions, where all substrates except the one under consideration are at a constant and saturating concentration. As such, the observed velocity and kinetic constants should be related only to the variable substrate.

Oxidation state

Remembering that the enzyme concentration at a given time t , $[E]_t$ is equal to $[E^{2+}] + [E^{3+}]$, this work still assumes that the steady-state approximation holds, such that: $d[E^{2+}]/dt = d[E^{3+}]/dt = d[ES]/dt = 0$. It has not been accounted for at this time the changes in $[E^{2+}]/[E^{3+}]$ across different experiments, but it has been assumed to only be dependent on the concentrations of MB (or CYB5S as another electron carrier) and ascorbic acid. This has not been experimentally verified, and the mechanism of auto-oxidation requires the binding of oxygen, and may be increased by the binding of L-Trp [210, 212, 262]. Thus the ratio $[E^{2+}]/[E^{3+}]$ may be dependent on the concentration of all the species (ascorbic acid, MB/CYB5S, O_2 , and L-Trp). This would only be relevant if the rate of IDO1 activation and deactivation are of a similar magnitude under the experimental conditions. The half-life of the ferric-superoxide binary complex has been reported as 36 sec at pH 8.0 in the absence of substrate [267]. Given that there has never been any reports of a lag phase of IDO1 activation in steady-state experiments, it is likely that reduction occurs at a much greater rate than oxidation under these conditions. Further, reports of 10-50 turnover cycles in flash photolysis experiments before samples became deactivated has been reported [219]. In this work, it was assumed that $[E]_0 \approx [E^{2+}]$, and thus: $V_{\text{max}} = k_{\text{cat}}[E^{2+}] \approx k_{\text{cat}}[E]_0$.

Affinity between the ferric enzyme and either oxygen or tryptophan was ignored during analysis. The K_d of L-Trp for the ferric enzyme has been reported as 0.6 – 0.9 mM [254, 268], with a ferrous K_d expected to be roughly half that value [268]. Under the above assumption, that the reduction rate is much faster than the oxidation rate, this also means that the ratio ($[E^{2+}]/[E^{3+}]$) lies much

closer to the ferrous than ferric side. Thus, despite the relatively similar K_d values, the concentrations of any ferric bound species is likely to be much lower than ferrous, and contribute a proportionally low amount to the kinetics. Measurement of the ratio $[E^{2+}]/[E^{3+}]$ is non-trivial and was not performed in this work.

Oxygen binding

For IDO1, a ferrous K_d for oxygen has been reported as 13 μM at pH 8.0 in the absence of other substrates [267], with an apparent K_M of 42 μM (36 μM L-Trp, pH 7.4 [260]). Solubility of oxygen in pure water in air at 25 and 35 $^{\circ}\text{C}$ is 258 and 218 μM , falling to 206 and 176 μM in seawater (defined as 35 ‰ dissolved ions) [269]. Literature studies of IDO1 activity have generally used buffers of <10 ‰. Thus, ~258 μM of oxygen equates to $\sim 258/(\sim 258+13) \approx 95\%$ occupancy at pH 8.0 – effectively a pseudo-first order reaction with respect to oxygen. Binding constants for pH 6.5, the pH used in this study, could not be found. Under pseudo-first order conditions, the ferrous IDO1 reaction can be simplified as in Scheme 6.2, which is equivalent to Scheme 6.1, above.



Scheme 6.2. The simple model for a single substrate enzyme acting irreversibly (Scheme 6.1) as applied to ferrous IDO1.

Substrate inhibition kinetics

Given these caveats, experiments displaying substrate inhibition were analysed using the canonical Equation 6.2 (examples of this equation have been plotted in Figure 6.5) [270]. In this equation V_{max} is the maximum velocity that would be achieved if substrate inhibition did not exist, and K_M is the Michaelis-Menten constant in a system without substrate inhibition. K_{si} has been traditionally defined as the dissociation constant for binding in a system where both substrate molecules can bind to the target simultaneously. This latter definition makes sense for the canonical substrate inhibition scenario of two binding sites on a single enzyme or complex. Although this has been a popular theory in the past for IDO1, invoking a hydrophobic pocket near the heme as a potential allosteric site, current data lends its support to the formation of a low-productivity complex in a single binding site arising from changes in the order of binding [224, 271] (See Figure 6.2, above). This does not preclude the possibility that an allosteric site does indeed exist within IDO1, and may contribute some additional effect which may not be differentiable by steady-state data. In the absence of an allosteric site or contribution from ferric IDO1, the K_{si} is instead a function of the dissociation constants of tryptophan binding to the ferrous and ferrous-oxy forms (and therefore also a function of oxidation and reduction rates of

heme). Although this equation was derived for cases of substrate inhibition caused by allosteric binding, and not the case of IDO1 where it is caused tryptophan binding to different forms of the enzyme, the equation has regressed quite successfully in the literature for IDO1 (*e.g.* [219, 224, 272]). For this work, the analytical definition and accuracy of the kinetic constants (V_{\max} , K_M , K_{si}) is only of secondary importance; as the shape of the kinetics, and the magnitude of change in the kinetic constants, were to be the true indicators as to whether the loop of IDO1 plays a significant role in its interaction with other molecules.

$$v = \frac{V_{\max}[S]}{K_M + [S] \left(\frac{1 + [S]}{K_{si}} \right)}$$

Equation 6.2. The substrate inhibition equation used to analyse IDO1 reactions.

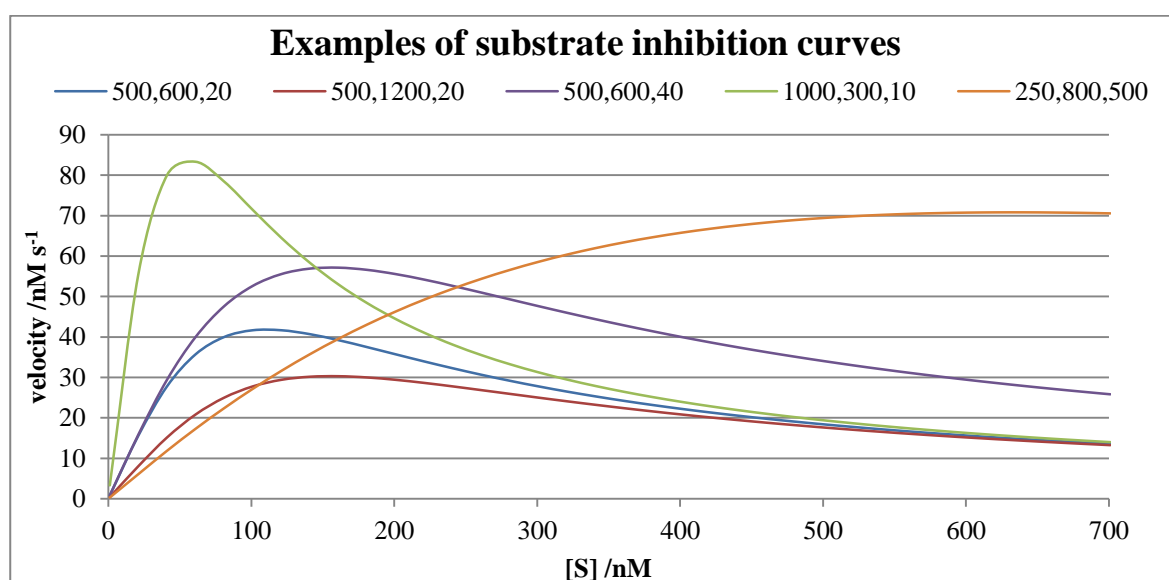


Figure 6.5. Substrate inhibition kinetics give an initial increase followed by a decrease in velocity with increasing substrate concentration. The legend gives the values of V_{\max} , K_M and K_{si} used for each case, respectively. Note that if data points beyond the maximum observable velocity are not obtained, the data may appear Michaelis-Menten in nature.

6.4.3. Experimental design of IDO1-based reactions

From an experimental point of view, collecting kinetics from a superoxide generating system was not ideal, as the superoxide could oxidise any of the organic substrates, products, or the protein matrix. Superoxide can also dismutate to hydrogen peroxide, which has been shown to oxidise and deactivate the protein [240]. Meanwhile use of the cytochrome b5/P450 reductase system is a much more laborious and expensive endeavour – mostly due to the presence of liposomes. Hence, the ascorbic acid/MB system has been the preferred set of conditions in the literature, although some more recent studies have begun to employ cytochrome b5 reductase in a non-liposomal environment, in place of CPR in a liposomal one [219]. Cytochrome b5 reductase was

not included in this work as it has not been reported to be able to directly reduce IDO1, unlike CPR [122]. The reducing conditions for this work consisted of either ascorbic acid and MB due to its prevalence, or ascorbic acid and CYB5S due to its ease. Other systems will be of interest to investigate at a later time.

6.5. Results

For all experiments, reactions were initiated through the addition of ascorbic acid, unless otherwise noted. Data on IDO1 activity was collected by two methods: absorbance at 321 nm, monitoring the formation of L-NFK, or HPLC analysis of kynurenine after L-NFK hydrolysis with acid. All IDO1 and CYB5S concentrations have been expressed as hemin equivalents, as measured from pyridine-heme chromagen analysis [273]. Some regression curves, particularly those using the substrate inhibition model, are presented with concentration of a \log_2 scale for better visualisation, however, all regression analysis was performed on data on a linear scale.

Absorbance at 321 nm

The formation of L-NFK was monitored in real time by the increasing absorbance at 321 nm at 25 °C. The extinction coefficient, ϵ_{321} , was measured through the addition of a known amount of L-Trp (20 – 100 μM) to an excess ($\sim 1 \mu\text{M}$) of HIDO supported by MB and ascorbic acid (10 μM and 20 mM, respectively) in potassium phosphate buffer (50 mM, pH 6.5). The reaction was monitored for 10 minutes, but was complete before reading could commence (~ 2 minutes), with the absorbance unchanging over this 10 minute interval. ϵ_{321} was calculated to be $3.7 \pm 0.06 \text{ mM}^{-1} \text{ cm}^{-1}$ (mean \pm standard error of four curves with $n = 6$), agreeing with the reported value of $3.75 \text{ mM}^{-1} \text{ cm}^{-1}$ [274]. A value of $3.7 \text{ mM}^{-1} \text{ cm}^{-1}$ was used in this work.

HPLC quantitation

The standard curve for kynurenine formation was similarly created. HIDO (1 μM) was used to convert L-Trp (0.05 – 100 μM) under the same conditions. After 10 minutes of incubation, HCl (0.5M, containing 132 μM of 5-nitro-L-tryptophan) was used to quench the reaction and hydrolyse the product. 5-Nitro-L-tryptophan was used as a standard for injection errors and plate evaporation. Quantification of kynurenine was performed by absorbance at 360 nm. Each experiment series contained its own 8-point (single concentration, with excess HIDO) calibration (between 0.05 and 100 μM).

6.5.1. HIDO kinetics

Initial experiments focused on ensuring that human IDO1 (HIDO) was reproducing known kinetic results. Namely, substrate inhibition by L-Trp and the non-dependence of kinetics on superoxide. Although experimental concentrations vary from study to study in the literature, the most

common concentrations used have been 20 mM ascorbic acid, 10 μ M MB, and L-Trp between 50 – 400 μ M, in a 50 mM phosphate buffer at pH 6.5 [118, 120, 275-288]. The following kinetics, expressed in terms of L-NFK production, were measured by the absorbance increase at 321 nm.

HIDO showed the expected substrate inhibition with respect to L-Trp (Figure 6.6 **A**). Additionally tested was the effect of MB concentration on activity. This also gave substrate inhibition with increasing MB concentrations, independent on the addition of superoxide dismutase (SOD, 0.5 mg/ml), to within error (Figure 6.6 **B**). Conversely, increasing concentrations of CYB5S displayed Michaelis-Menten kinetics within the accessible concentrations (Figure 6.6 **C**). Higher concentrations of CYB5S were not possible due to increasing background at 321 nm with increasing CYB5S amounts. This indicated that different processes were occurring with regards to IDO1 and MB compared to CYB5S. This was only a single biological replicate with respect to the CYB5S, however, and the experiment was performed before the realisation that CYB5S was changing between between α - and β - forms when stored on ice (Section 5.2.4). As the protein was thawed and stored on ice for ~30 minutes prior to use, it must be assumed that both α - and β - forms of the enzyme were present, and this may have had an effect on the observed kinetics. Further data is required. The kinetic parameters from non-linear regression are given in Table 6.1.

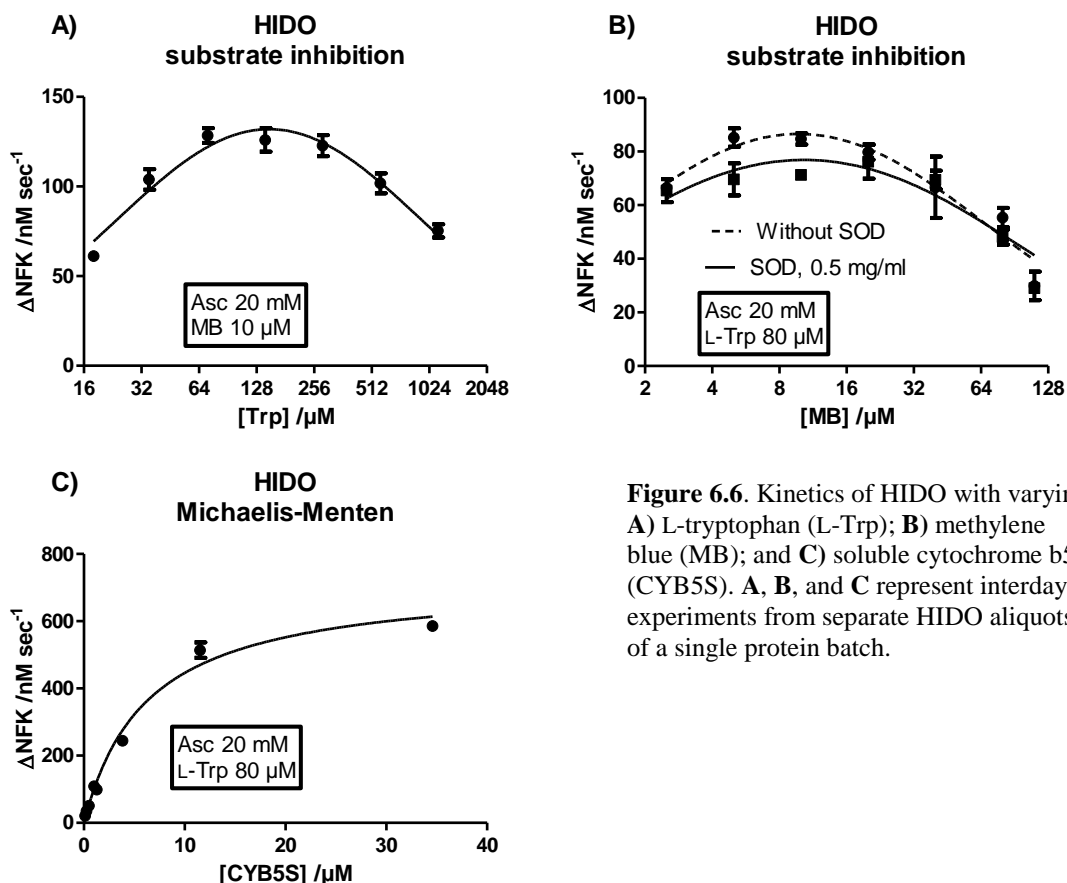


Figure 6.6. Kinetics of HIDO with varying: **A)** L-tryptophan (L-Trp); **B)** methylene blue (MB); and **C)** soluble cytochrome b5 (CYB5S). **A**, **B**, and **C** represent interday experiments from separate HIDO aliquots of a single protein batch.

Table 6.1. Effect of varying L-Trp, MB and CYB5S concentrations on HIDO kinetics.

Variable species	k_{cat} / s^{-1}	$K_M / \mu M$	$k_{cat}/K_M / \mu M^{-1} s^{-1}$	$K_{si} / \mu M$	Notes
L-Trp	6 ± 1	29 ± 11	0.21	760 ± 296	10 μM MB, 20 mM ascorbic acid, 25 °C
MB	5 ± 0.5^a	1.2 ± 0.4^c	4.2	66 ± 22	80 μM L-Trp, 20 mM ascorbic acid. pH 6.5, 25 °C
	4 ± 0.8^b	1.1 ± 0.8^c	3.6	140 ± 111	
	4 ± 0.8^a	1.6 ± 1	2.5	58 ± 29	
	3 ± 0.7^b	1.2 ± 1^c	2.5	86 ± 60	
CYB5S	12 ± 0.8	6.2 ± 1.0	1.9	-	80 μM L-Trp, 20 mM ascorbic acid. pH 6.5, 37 °C

All values are \pm 95% confidence interval. ^aNo SOD. ^b0.5 mg/ml SOD. ^cThis was below the lowest concentration actually tested. Listed K_M and K_{si} are of the variable species.

Previous reports of MB inhibition could not be found, however, the literature-typical concentration of 10 μM coincided with the maximum observable rate in this data. Due to the effect of MB on activity, the effect of increasing ascorbic acid concentration was also tested. Each curve represents a technical triplicate on individual days. High interday variability was seen from these experiments, and a conclusion could not be deduced from this data (Figure 6.7, Table 6.2).

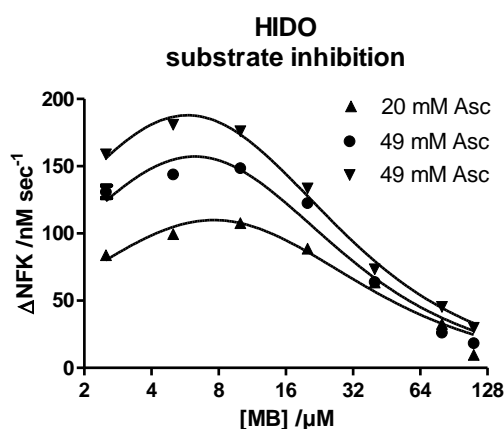


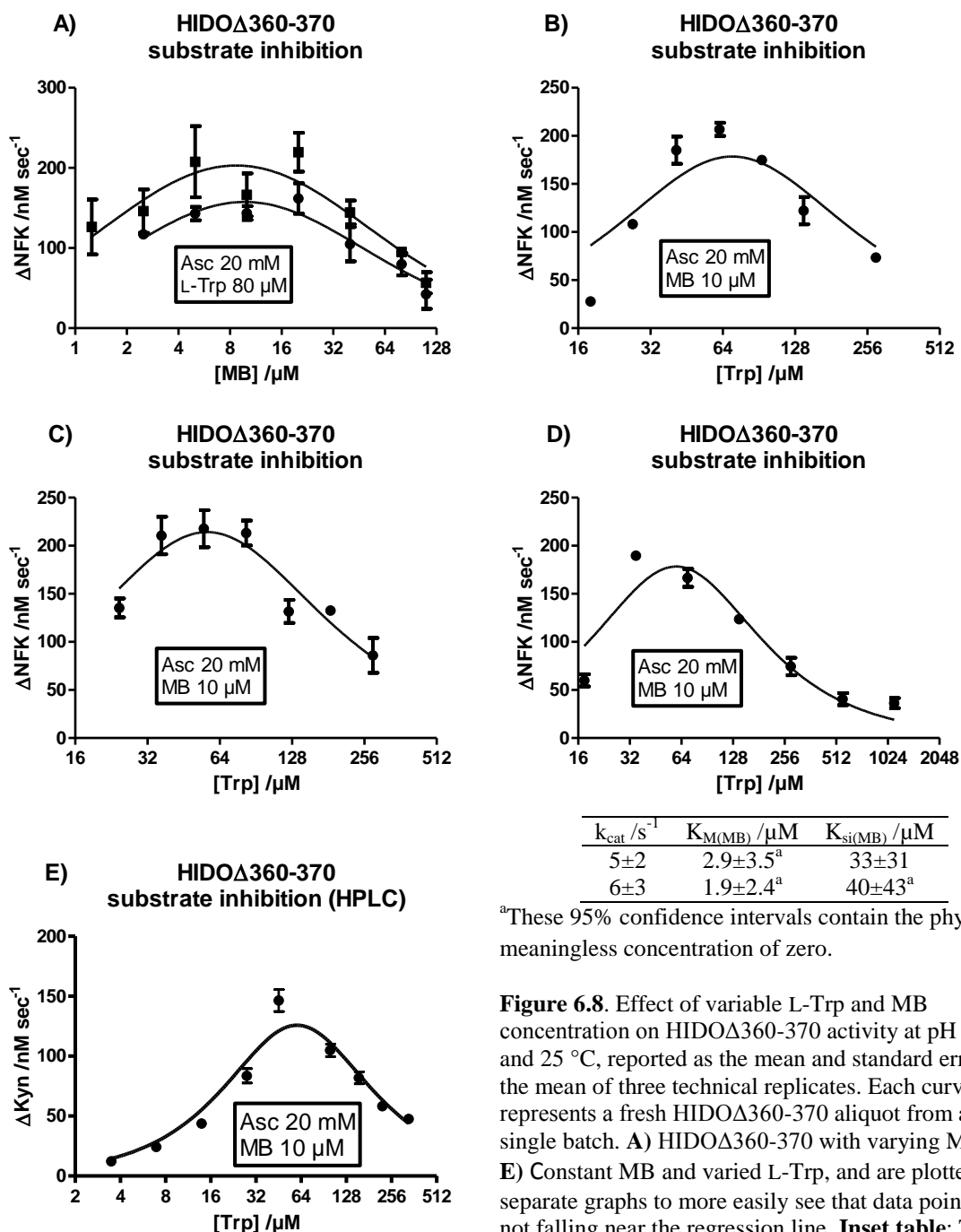
Table 6.2. Effect of varying MB and ascorbic acid concentrations on HIDO kinetics.

k_{cat} / s^{-1}	$K_{M(MB)}$ / μM	$K_{si(MB)}$ / μM	Notes
8 ± 4	4.5 ± 4.2	13 ± 9.9	20 mM ascorbic acid, 80 μM L-Trp. pH 6.5, 25 °C.
14 ± 3 13 ± 6	3.4 ± 1.6 4.5 ± 3.8	9.8 ± 3.6 8.6 ± 5.9	49 mM ascorbic acid, 80 μM L-Trp. pH 6.5, 25 °C.

Figure 6.7. Effect of increased ascorbic acid (Asc) concentration on HIDO activity. Error bars are one standard error to the mean. Kinetic parameters in the adjoining table are shown with a 95% confidence interval. Each curve represents a fresh HIDO protein aliquot from a single batch.

6.5.2. Comparison to HIDOΔ360-370

The human deletion mutant, HIDOΔ360-370, likewise gave substrate inhibition kinetics with respect to L-Trp and MB, although it displayed large confidence intervals due to noise in the data. Surprisingly, the curve with respect to varying levels of L-Trp was ambiguous by the regression software (GraphPad Prism 5.01). Ideally, when moving any combination of these parameters away from the best value, the sum-of-squares should always increase, and thus each regression should have only a single combination of values leading to the lowest sum-of-squares. This ambiguous label effectively means that more than one combination of parameters (V_{max} , K_M , K_{si}) gives equally well fitting curves (low sum-of-squares), and therefore the ‘correct’ combination of kinetic constants cannot be confidently deduced. Removal of the apparent outlying data point did not alleviate this, indicating it was a systemic problem with the data. Independent replicates, using a new HIDOΔ360-370 aliquot from the same protein batch and freshly made solutions, and analysed by either UV absorbance or by HPLC quantitation, continued to give ambiguous regressions. Therefore, it was unlikely that the results were a consequence of the measurement technique or the reaction solutions, but must have come either from the experimental design or the protein sample. It was unlikely to have been the experimental design as the same procedure was used in the above HIDO experiments. Therefore, the results likely arose from the protein sample itself. These results are presented in Figure 6.8 and the inset table.



^aThese 95% confidence intervals contain the physically meaningless concentration of zero.

Figure 6.8. Effect of variable L-Trp and MB concentration on HIDO Δ 360-370 activity at pH 6.5 and 25 °C, reported as the mean and standard error to the mean of three technical replicates. Each curve represents a fresh HIDO Δ 360-370 aliquot from a single batch. **A)** HIDO Δ 360-370 with varying MB. **B – E)** Constant MB and varied L-Trp, and are plotted on separate graphs to more easily see that data points are not falling near the regression line. **Inset table:** The table depicts the kinetic constants extracted from the MB reactions in (A), showing 95% confidence intervals.

Subsequently, a new batch of HIDO Δ 360-370 was purified and assayed under similar conditions using HPLC quantitation of the hydrolysed product, L-Kyn (hence, the graphs display Δ Kyn, rather than Δ NFK). This later batch was analysed for its L-Trp substrate inhibition with regards to constant MB and varying ascorbic acid (Figure 6.9). These experiments regressed to the substrate inhibition model, and it was concluded that the previous ambiguous kinetic shape was due to a batch-specific issue. HPLC quantitation of HIDO Δ 360-370 and HIDO reactions gave consistently

lower variance in the data points and a larger dynamic range over which the experiments could be performed. Therefore, all data going forward was collected from HPLC experiments.

The increased number of ascorbic acid reactions allowed for a more thorough assessment of the role of ascorbic acid on the kinetics. It showed that the maximum observable rate occurs with ascorbic acid concentrations between ~ 10 and 20 mM, with higher concentrations reducing k_{cat} 18-fold at 80 mM, while increasing $K_{\text{M}(\text{Trp})}$ 1.8-fold and $K_{\text{si}(\text{Trp})}$ 4.5-fold (Figure 6.9). A series of HIDO experiments under similar conditions were also performed for comparison (Figure 6.10). These results mimicked those of HIDO Δ 360-370: a decreasing k_{cat} (17-fold between 20 and 80 mM), and increasing $K_{\text{M}(\text{Trp})}$ and $K_{\text{si}(\text{Trp})}$, with increasing ascorbic acid concentration (1.6-fold and 5.6-fold between 10 and 80 mM, respectively). Both proteins gave a decrease in $k_{\text{cat}}/K_{\text{M}}$ with increasing ascorbic acid concentrations.

An inhibitory effect of increasing ascorbic acid concentrations may be due to its consumption of dissolved oxygen, as measured on a Clark-type oxygen electrode. Three experiments at 37 °C saw ascorbic acid (23 mM) in potassium phosphate buffer (42 mM, pH 6.5) consume 0.6 ± 0.2 (mean \pm SD, $n = 3$) $\mu\text{M}/\text{min}$ of oxygen, increasing to 2 ± 0.5 $\mu\text{M}/\text{min}$ (mean \pm SD, $n = 2$) upon addition of 10 μM MB in the absence of catalase. The subsequent injection of catalase to the reaction reduced the oxygen consumption to 0.5 ± 0.4 (mean \pm SD, $n = 2$). It was expected that this oxygen consumption should result in a decrease in $K_{\text{si}(\text{Trp})}$, due to tryptophan more successfully competing with oxygen for binding to ferrous heme. One possible explanation for this would be a non-specific, detrimental interaction between HIDO and ascorbic acid under these high concentrations. Alternatively, the increased concentration may have overpowered the catalase present in terms of peroxide production, causing oxidative damage to the IDO1 protein [240]. The role of increased ascorbic acid concentration was not looked at further.

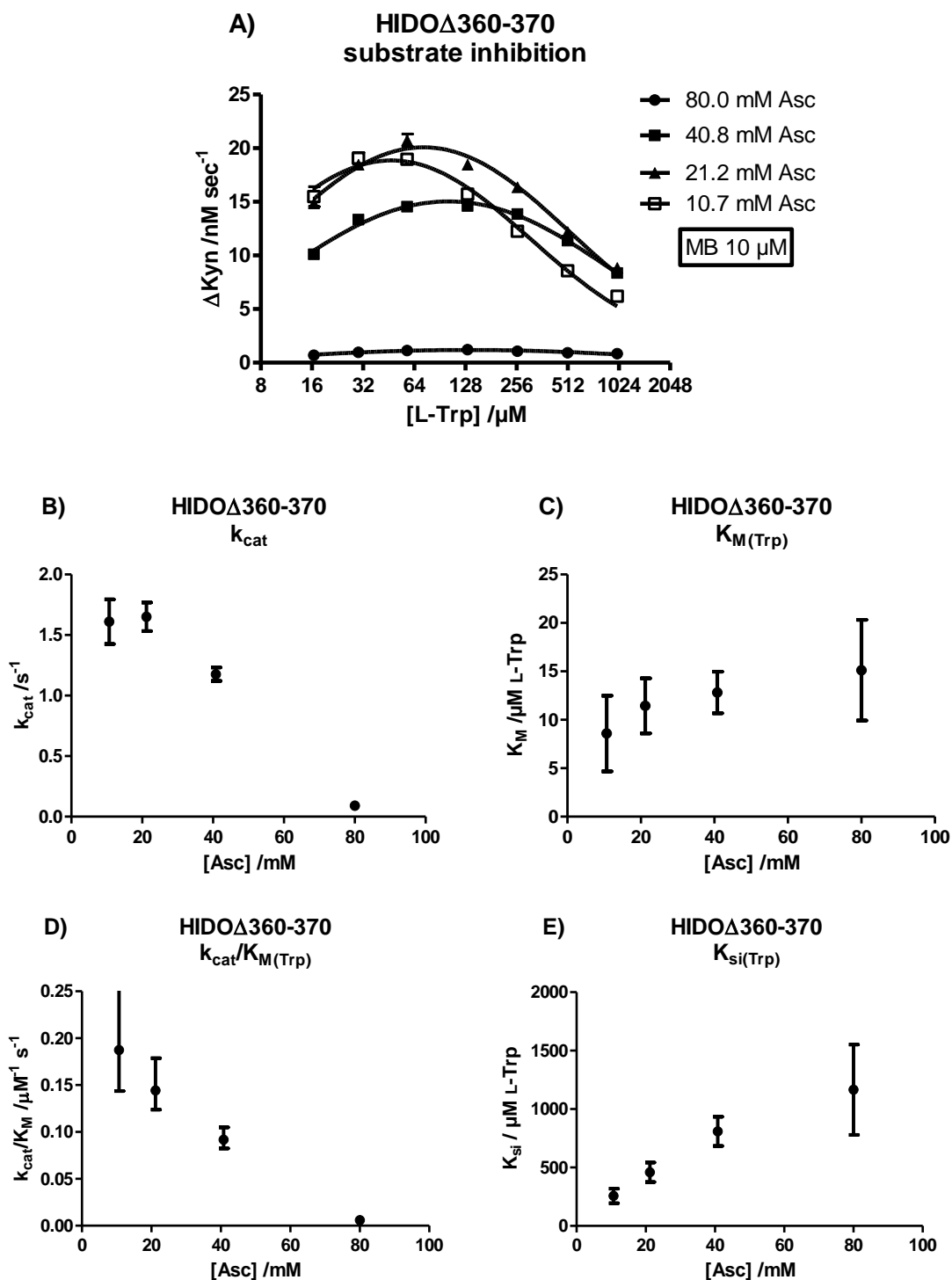


Figure 6.9. HIDO Δ 360-370 kinetics with varying L-Trp and ascorbic acid (Asc) using 10 μ M MB, 20 $^{\circ}$ C, pH 6.5. Error bars for (A) are the standard error to the mean, and 95% confidence intervals for kinetic constants extracted from each regression curve (B – E). Data are technical triplicates from a single batch of protein.

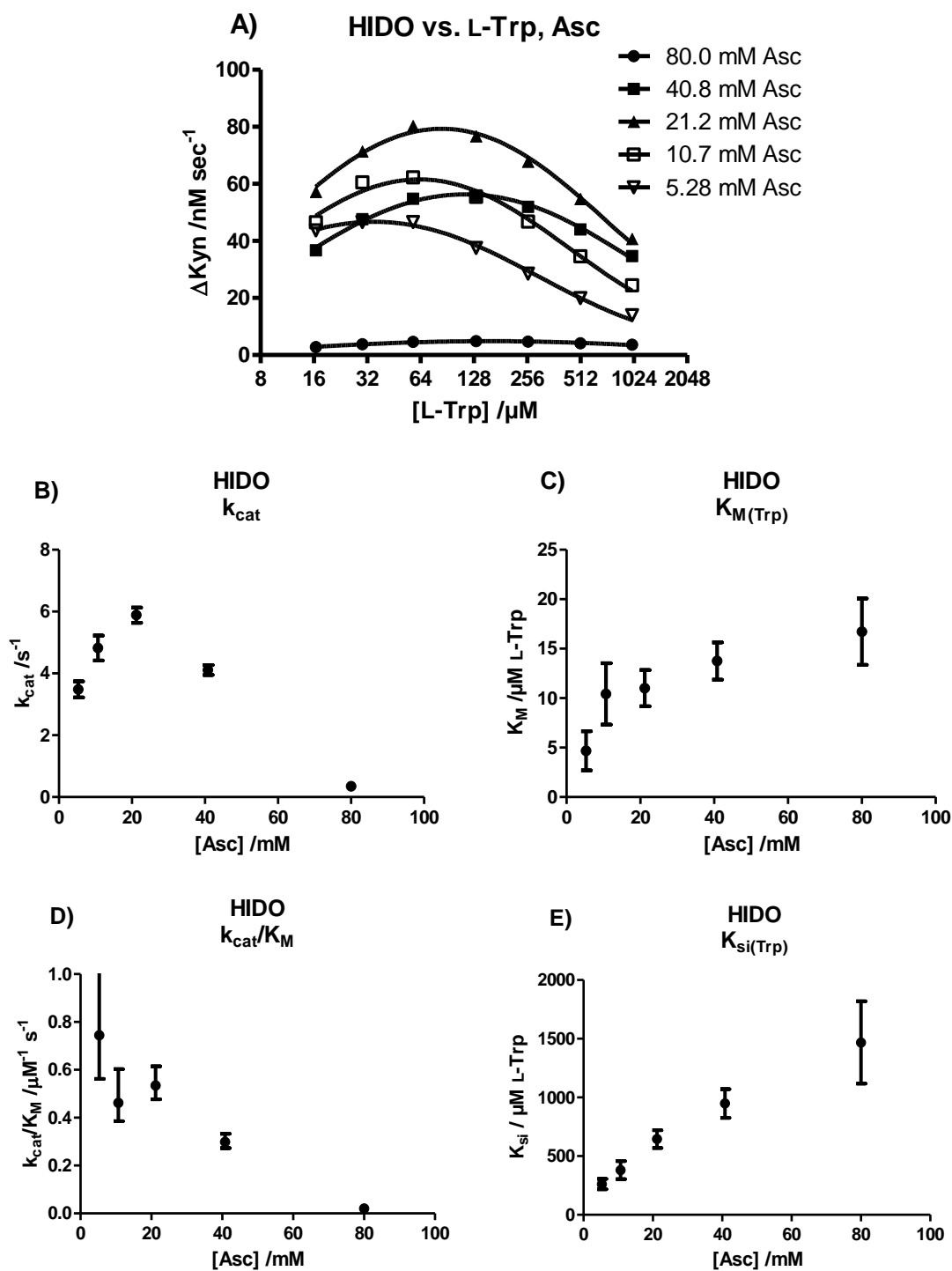


Figure 6.10. HIDO kinetics with varying L-Trp and ascorbic acid using 10 μM MB, 20 $^{\circ}C$, pH 6.5. Error bars for (A) are the standard error to the mean, and 95% confidence intervals for kinetic constants extracted from each regression curve (B – E). Data are technical triplicates from a single batch of protein.

6.5.3. HIDO and WIDO Comparisons

HIDO and WIDO were compared for their kinetics in regards to varying L-Trp and MB concentrations. HIDO Δ 360-370 had already shown substrate inhibition with regards to increasing MB concentration and constant L-Trp, and HIDO and WIDO also displayed these characteristics (Figures 6.11 and 6.12). In HIDO, both k_{cat} and K_M displayed a substrate inhibition shape, whilst K_{si} dropped and appeared to plateau at $\sim 260 \mu\text{M}$ of L-Trp with $40 \mu\text{M}$ MB. WIDO gave similar results, with a general increase in k_{cat} and $K_{M(\text{Trp})}$ with increasing MB, and a decrease in K_{si} . In this instance, the extracted kinetic constants, particularly at high MB concentrations, had much larger confidence intervals, making conclusions difficult. Whilst, it does appear that K_{si} increased again beyond $16 \mu\text{M}$ MB, this was almost within error of the $10 \mu\text{M}$ data point, and could be a noisy plateau. In WIDO, increasing MB showed a k_{cat}/K_M that initially declined and then increased; possibly indicating competing mechanisms at low and high MB concentrations. This is in contrast to the data observed for HIDO and HIDO Δ 360-370 with increasing ascorbic acid (Figures 6.9 and 6.10), which saw k_{cat}/K_M . The fact that these observations are different further highlights the likelihood that these two molecules are participating in some mechanism beyond only transferring an electron from ascorbic acid to ferric heme.

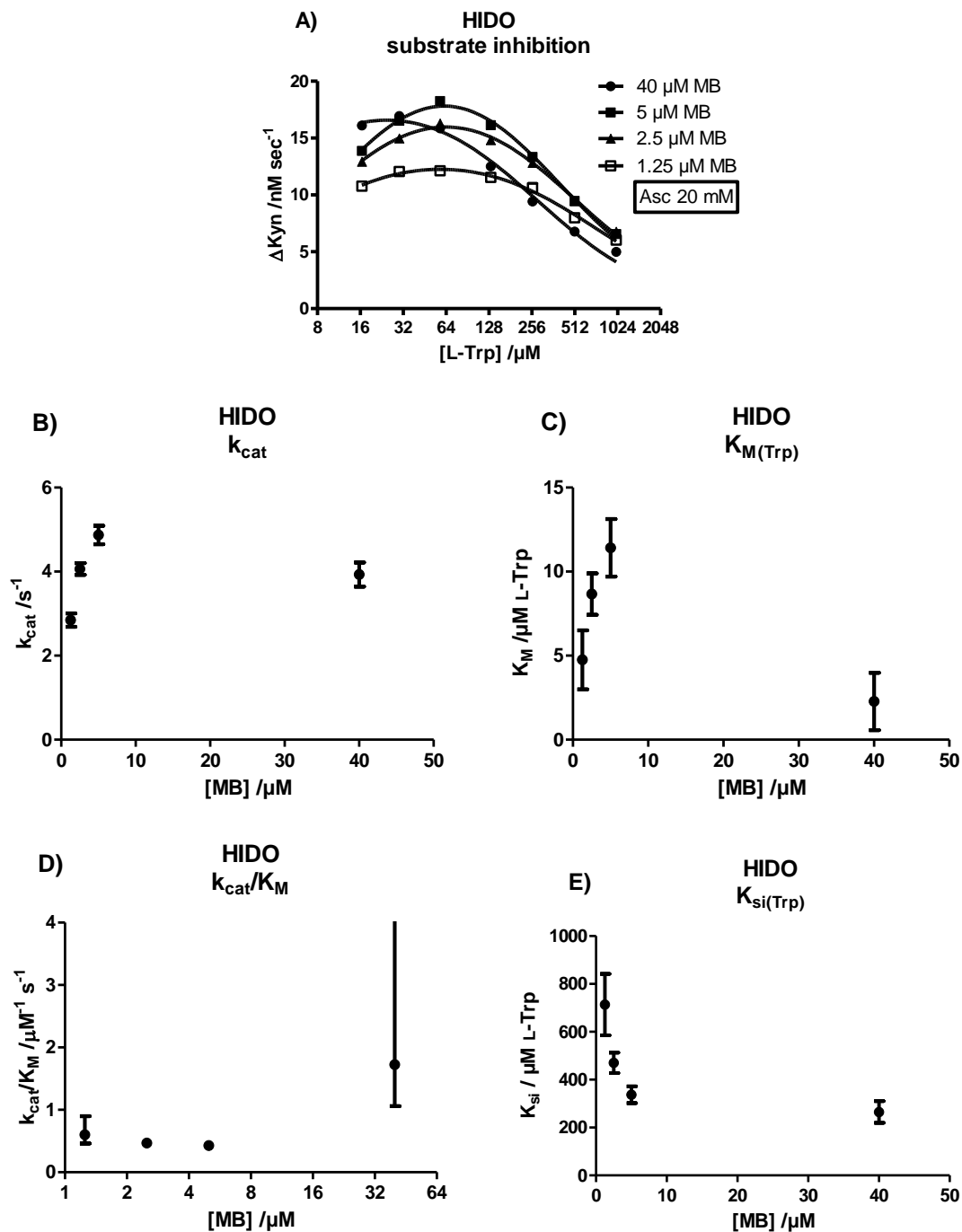


Figure 6.11. HIDO kinetics with varying L-Trp and MB using 20 mM ascorbic acid (Asc), 20 °C, pH 6.5. Error bars for A) are the standard error to the mean, and 95% confidence intervals for kinetic constants extracted from each regression curve (B – E). Data are technical triplicates from a single batch of protein.

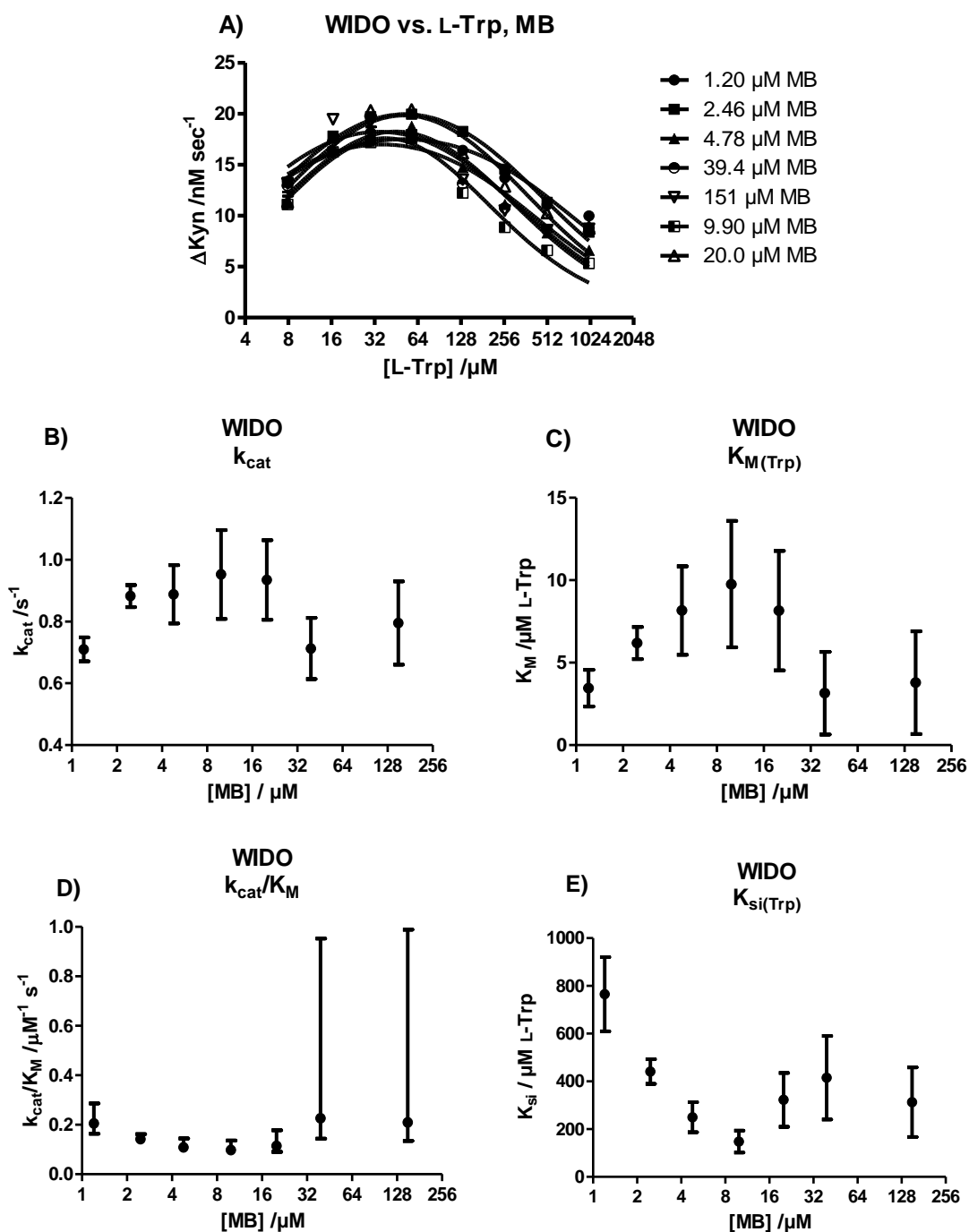


Figure 6.12. WIDO kinetics of L-Trp conversion supported by MB/ascorbic acid (Asc) reactions. Error bars for A) are the standard error to the mean, and 95% confidence intervals for kinetic constants extracted from each regression curve (B – E). Data are technical triplicates from a single batch of protein.

6.5.4. Conversion of D-tryptophan

The three proteins were looked at in terms of their ability to oxidise D-tryptophan using ascorbic acid (20 mM) and MB (10 μM), as shown in Figure 6.13. HIDO and HIDO Δ 360-370 possessed $K_{\text{M(D-Trp)}}$ values in agreement with literature values of 2 – 5 mM [260, 289, 290]. The k_{cat} values obtained here were collected at 25 $^{\circ}\text{C}$, and so cannot be compared to the literature values of 2 – 12 s^{-1} at 37 $^{\circ}\text{C}$ [260, 289, 290]). It is interesting to note that WIDO was substantially easier to saturate, with a $K_{\text{M(D-Trp)}}$ value a magnitude lower than the human-derived proteins. This places the $K_{\text{M(D-Trp)}}$ just one order of magnitude above WIDO's $K_{\text{M(L-Trp)}}$ of ~ 10 μM , while the human

derived proteins displays two orders of magnitude difference between the two isomers. Only small differences in $k_{\text{cat}}/K_{\text{M(D-Trp)}}$ were observed, all within a single order of magnitude.

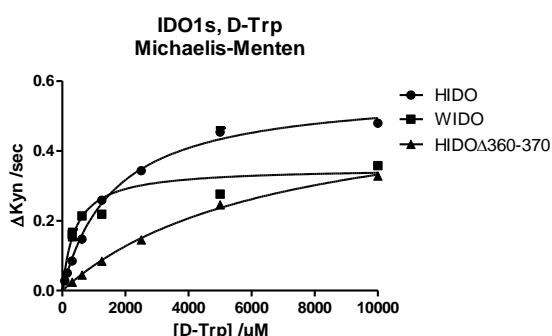


Figure 6.13. Conversion of D-tryptophan by IDO1 proteins. Error bars on the graph are the standard error to the mean of triplicates from a single protein aliquot. Reaction velocity was normalised by heme content for each protein. The inset table gives the kinetic constants (\pm 95% confidence intervals) from each regression curve.

6.5.5. CYB5S supported reactions

The next series of reactions examined whether there were differences between reactions supported by soluble cytochrome b5 (CYB5S) and ascorbic acid, compared to those of MB and ascorbic acid. HIDO reactions supported by CYB5S continued to display substrate inhibition kinetics with respect to L-Trp (Figure 6.14, **A**). The addition of high MB to these HIDO CYB5S-supported reactions slightly decreased k_{cat} , slightly increased K_{M} (for an overall decrease in $k_{\text{cat}}/K_{\text{M}}$), and increased $K_{\text{si(Trp)}}$. This in contrast to HIDO supported by ascorbic acid and MB, where k_{cat} and $K_{\text{M(Trp)}}$ initially rose (displaying inhibition at high MB concentrations), $k_{\text{cat}}/K_{\text{M}}$ rose slightly, and where $K_{\text{si(Trp)}}$ dropped (Figure 6.11). In the CYB5S supported reactions, k_{cat} appeared to fall with increasing concentrations of MB. The size of the change is quite small, however, and the biological relevance of such a small change is questionable (Figure 6.14). The addition of MB did not change the kinetic shape from substrate inhibition, unlike the liposomal system of Pearson *et al.* [122]. Pearson *et al.* reported three different kinetic shapes depending on the use of CPR, CYB5A, and NADPH (Section 6.3).

Conversely, WIDO demonstrated hyperbolic kinetics with respect to L-Trp in the CYB5S/ascorbic acid system. No substrate inhibition was observed up to a concentration of 1 mM of L-Trp. Addition of 2.5 μM MB minimally increased V_{max} ($0.44 - 0.60$ vs. $0.76 - 0.89 \text{ nM s}^{-1}$, 95% confidence intervals), but did not change K_{M} ($4.8 - 31$ vs. $9.5 - 22 \mu\text{M}$). It should be noted that this was only a single biological replicate with regards to WIDO, and batch-to-batch variation has already been highlighted for WIDO absorption spectra (Section 5.2.3), and for HIDOΔ360-370 kinetics. It is also possible that inhibition may be seen above concentrations of 1 mM. However, this change in kinetic shape makes WIDO an even more interesting protein for further study.

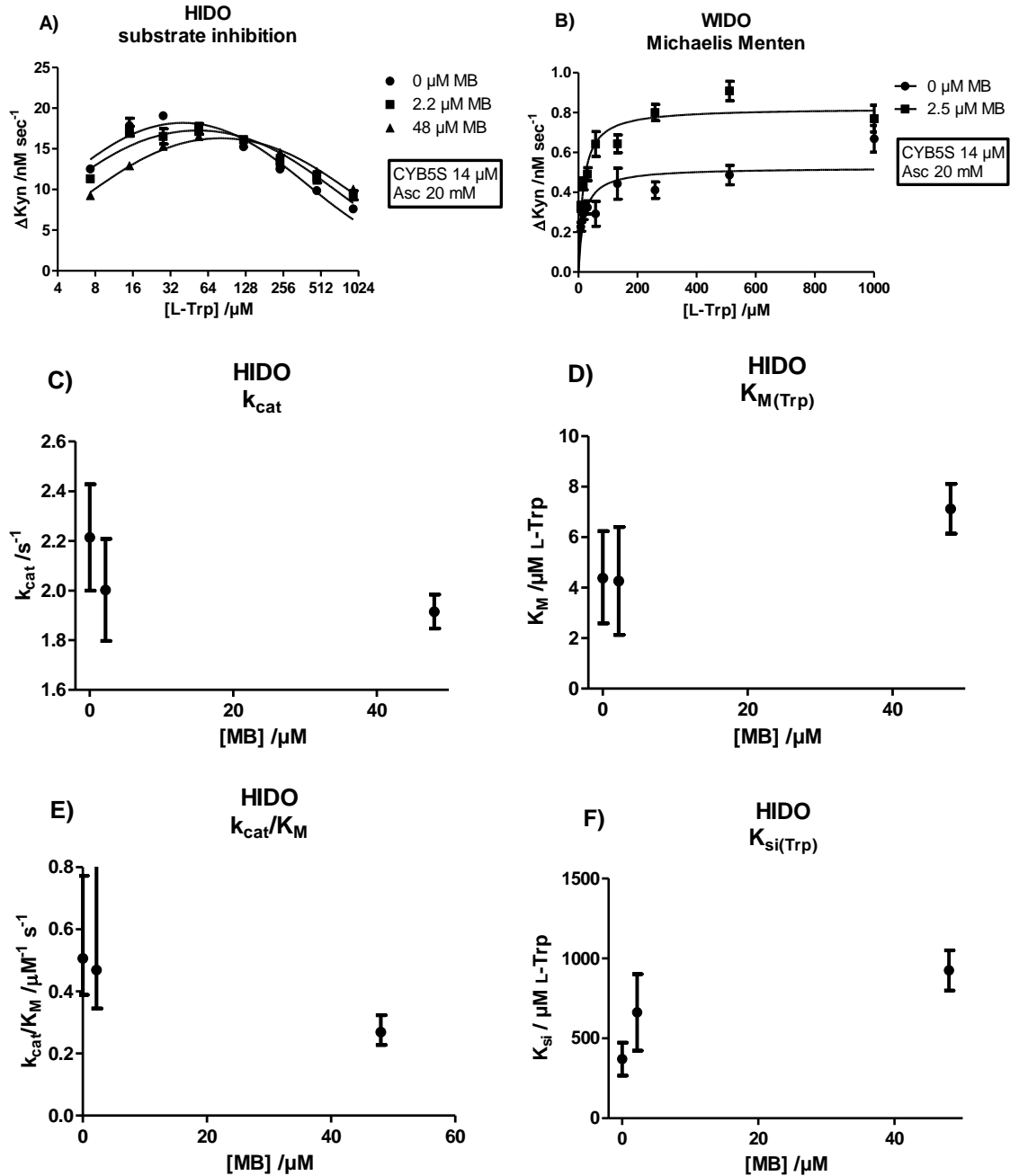


Figure 6.14. **A)** HIDO supported by CYB5S (14 μM) and ascorbic acid (Asc, 20 mM) with indicated concentrations of MB. **B)** WIDO supported by CYB5S (14 μM) and ascorbic acid (20 mM) with indicated concentrations of MB. Error bars for **A)** are the standard error to the mean, and 95% confidence intervals for kinetic constants extracted from each regression curve (**C** – **F**). Data are technical triplicates from a single batch of protein.

6.6. Discussion

Ascorbic acid/methylene blue assays

All three IDO1 proteins showed the same general trends with regards to their kinetic parameters and the effect of different concentrations of L-Trp, ascorbic acid and MB – with all three substrates displaying substrate inhibition. They had maximum observable velocities at

concentrations of 50-100 μM L-Trp, $\sim 10\ \mu\text{M}$ MB and $\sim 20\ \text{mM}$ ascorbic acid. Of interest from these assays was the observation that MB caused a substrate inhibition profile as its concentration varied, compared to CYB5S, which displayed a Michaelis-Menten shape. This is clear evidence that the two electron carriers have differences in their chemistry as they interact with IDO1. Varying the concentration of MB showed a clear influence on the k_{cat} , $K_{\text{M}}(\text{Trp})$ and $K_{\text{si}}(\text{Trp})$ of HIDO and WIDO (the errors in $k_{\text{cat}}/K_{\text{M}}(\text{Trp})$ were too large to assess the true significance). There was insufficient time to repeat these experiments to the same degree against HIDO360 Δ 370, but showed the same effects at single concentration of L-Trp (Figures 6.88, 6.11, 6.12). These changes, whilst small, are reproducible. As such, their biological relevance is likely to be minor, but their cause is clearly attributable to the properties of MB. In some respects, their biological relevance is a mute point, as MB is not present naturally in the body. The mechanistic source of this MB inhibition can not be determined from this data alone. It could be caused by a low affinity binding site of MB's, whose influence would only be seen at higher concentrations. It may also be a result of some solution-phase chemistry, independent of interaction with IDO1. It must also be remembered that changing the concentrations of species' involved in the reducing system may also be influencing the concentration of ferrous and ferrous-oxy protein, and this will have an impact on how easily L-Trp can form an inhibitory complex.

Ascorbic acid/CYB5S assays

HIDO reactions supported by CYB5S continued to display substrate inhibition induced by increasing concentrations of L-Trp. However, WIDO employed under the same conditions, demonstrated a hyperbolic kinetic shape, with no inhibition observable up to 1 mM of L-Trp. Addition of MB to CYB5S supported reactions of HIDO, displayed MB-induced inhibition (lowering k_{cat} , Figure 6.14) and made it harder for L-Trp to induce inhibition (increased $K_{\text{si}}(\text{Trp})$, Figure 6.14). It is not possible to tell from this steady-state data the mechanistic cause of this – whether it is from MB slowing down the rate of reduction of either HIDO or CYB5S, or whether it caused by an affinity between MB and one of the proteins. Although changes were reproducible, they are relative small and likely reaching the limits of what steady-state experiments such as these can tell us. It is important to note that the inclusion of MB to these CYB5S reactions did not induce a change in the kinetic shape, as was observed by Pearson et al. for their reactions supported by for reaction containing HIDO and liposomal version of CYB5S and the reductase, CPR [122].

Implications for the role of the unresolved loop

Deletion of the first half of the loop from wild-type HIDO, to yield HIDO360 Δ 370, gave no substantial differences in the observed kinetics with either L- or D-Trp as substrates.

HIDO360 Δ 370 was competent when supported by CYB5S, and there was no indication that this

portion of the loop is specifically needed for interaction with the cytochrome. The WIDO protein, by contrast, showed a substrate inhibition shape with respect to L-Trp when supported by MB, and a Michaelis-Menten shape when supported by CYB5S. This does not yet have any direct insight into the role of the loop in the human system, however, as the chimeric structures, HCHIM and WCHIM (Section 4.6.1) could not be tested as controls. These differences could easily be attributable to a batch specific problem with the protein, or to artefacts induced by poor expression, and further characterisation is required.

6.7. Conclusion and future research

The kinetics of the three IDO1 proteins were investigated in regards to the effect of the two electron transporting agents: methylene blue and CYB5S. All IDO1 proteins displayed substrate inhibition, with both L-tryptophan and methylene blue being inhibitory at elevated concentrations. This was the case even in the presence of catalase and superoxide dismutase, arguing against the formation of reactive oxygen species being the main culprit for the inhibition. The substrate inhibition constant of L-tryptophan, $K_{si(Trp)}$, decreased with increasing concentrations of methylene blue for all proteins. It cannot be ruled out that this may be due to an increased level of superoxide production, however, may also indicate an ability for methylene blue binding to affect the binding of L-tryptophan beyond just the reduction of the heme.

Intriguingly, when either HIDO or HIDO Δ 360-370 were supported by CYB5S, they retained a substrate inhibition profile, however, WIDO displayed Michaelis-Menten kinetics. This must be taken with caution at this early stage, however, as batch-specific artefacts were observed for an early HIDO Δ 360-370 sample, and the same cannot be ruled out here. However, if correct, then WIDO represents an important protein for the study of the structure-function relationship of heme dioxygenases of tryptophan.

On the question of if the loop interacts with small molecules or proteins, Álvarez *et al.* has since shown that Thr379 is required for binding in human IDO1 [220]. Determined here is that deleting the first half of the loop (360-370) yields protein with effectively identical spectroscopic and kinetic properties, using either a methylene blue/ascorbic acid, or a cytochrome b5/ascorbic acid reducing system. With HIDO Δ 360-370 possessing similar kinetic properties to wild-type, this sequence is a good candidate for crystallography work, as the smaller loop might allow the full structure to be visualised. This could present an opportunity to obtain the first IDO1 crystal structures with bound substrate or substrate analogues. Further reproductions of the kinetic work contained here, and orthogonal investigations (e.g. using UV-Vis, circular dichroism, and/or isothermal calorimetry) are required to confirm any differences that might be apparent,

particularly with regards to the WIDO protein. The physical requirement for Thr379 lies in the hydroxyl group interacting with substrate L-Trp [220]. Although Thr379 is missing from the HIDOΔ371-380 construct, it may still be worthwhile determining its catalytic competence if only to see how specific this interaction is, or whether other hydrogen-bond acceptors in the vicinity can substitute.

6.8. Methods

Kinetic data were analysed in GraphPad Prims 5.01 (GraphPad Software, San Diego, USA). Tris (T1503), potassium dihydrogen phosphate (795488), ascorbic acid (A7506), methylene blue (M9140), sodium hydroxide (S5881), L-tryptophan (T0254), D-tryptophan (T9753), catalase (C9322), and superoxide dismutase (S7571) were purchased from Sigma-Aldrich. 5-Nitro-L-tryptophan was previously synthesised by the candidate according to literature procedures [242].

6.8.1. Stock solutions

Potassium phosphate buffer

Free flowing KH_2PO_4 (136.1 g/mol, 17.01 g, 125 mmol) was placed into a 250 ml volumetric flask with approximately 230 ml of MilliQ water and shaken at room temperature until dissolved. The pH was adjusted using 6M HCl. The final volume was made to 250 ml (500 mM), thoroughly mixed, and portioned in 45 ml aliquots in 50 ml polypropylene centrifuge tubes, filtered through a 0.2 μm membrane, and stored at 4 °C for up to 1 month.

Ascorbic acid

Ascorbic acid (176.1 g/mol, 1.76 g, 10 mmol) was placed into 40 ml of water and dissolved at room temperature. The pH was adjusted dropwise with 3M NaOH, whilst being stirred to prevent hydroxide-mediated oxidation, to a pH of 6.5 – 7.5. The final volume was made up to 50.00 g (200 mM final concentration assuming a density of 1.0 g/ml) aliquoted into 10 ml portions in 15 ml polypropylene centrifuge tubes, and stored at 4 °C, -20 °C or -80 °C for 2 days, 2 months or indefinitely. Samples were discarded if they displayed a visual yellowing.

Methylene blue

Methylene blue (319.85 g/mol, 16 mg, 0.05 mmol) was dissolved in 50.00 g of water (500 μM assuming a density of 1.0 g/ml) and stored in a polypropylene centrifuge tube at 4 °C for 6 months.

L- and D-tryptophan

L- or D-tryptophan (204.2 g/mol, 102.1 mg, 0.5 mmol) was dissolved in 50.00 g of water (10 mM assuming a density of 1.0 g/ml), portioned into 10 ml aliquots in 15 ml polypropylene centrifuge tubes, and stored at 4 °C for 1 month or -20 °C indefinitely.

NADPH

Free flowing $\text{Na}_4\text{.NADPH.xH}_2\text{O}$ (833.35 g/mol [anhydrous], 20.8 mg, 0.05 mmol) was dissolved into 2.5 ml of TAPS buffer (15 mM, pH 10 using NaOH) to yield a theoretical concentration of 10 mM and stored at -80 °C for up to 2 months in 1 ml aliquots. At the beginning of each day of use,

NADPH concentration was calculated based on its absorbance at 340 nm using $\epsilon_{340} = 6.22 \text{ mM}^{-1} \text{ cm}^{-1}$, as specified in the product manual.

Catalase

Catalase (5 mg) was dissolved into 1.0 ml of Tris buffer (25 mM, pH 7.4, 40% glycerol v/v) by vortexing for 1 minute. The sample was aliquoted into 50 μl portions and stored at -80°C indefinitely.

Superoxide dismutase

Superoxide dismutase was dissolved and stored under the same conditions as catalase at a final concentration of 9 mg/ml.

HCl quenching solution

5-Nitro-L-tryptophan (249.23 g/mol, 16.5 mg, 66 μmol) was dissolved in 500 ml of 0.5 M HCl and stored at 4°C .

6.8.2. Reactions monitored by absorbance

Experiments were performed in UV-transparent 384-well plates (black polystyrene non-binding, Greiner BioOne Cat# 781096). *N*-formyl-L-kynurenine formation was followed by an increase in absorbance at 321 nm on a Pherastar FS instrument with internal fluid handling (BMG Labtech) at 25°C .

Standard curve

L-Tryptophan (20 – 100 μM final concentration) was converted using HIDO (1 μM) supported by MB (10 μM) and ascorbic acid (20 mM) in potassium phosphate buffer (50 mM, pH 6.5). The reaction was monitored for 10 minutes not including ~2 minutes after initiation of the reaction.

Reactions

Reactions were followed for two minutes with a data rate of 2 Hz and 100 flashes per data point in well mode (reaction 1 was completed before initiation and monitoring of reaction 2). The variable species under investigation (*e.g.* L-tryptophan, methylene blue, CYB5S, *etc.*) was added to each well in a 10 μl volume. A master mix (pre-incubated to 25°C) containing all species except the variable species and ascorbic acid, in a volume of 80 μl , was added to each well. The reaction was initiated through the addition of ascorbic acid (10 μl) followed by shaking (single orbital) at 500 rpm for 1 sec. Signal increase was linear over the measurement time, although the first 30 seconds often contained high noise and was discarded from analysis. This noise was usually in the form of either a flat or decreasing signal, and was presumed to be due to bubble formation during shaking. The final reactions contained: IDO1 (*e.g.* 30 nM), potassium phosphate (50 mM, pH 6.5), catalase (0.1 mg/ml), and D- or L-tryptophan, methylene blue, CYB5S, and ascorbic acid at indicated concentrations. Each plate contained two negative control reactions. The first replacing the variable species with water, the second replacing ascorbic acid with water.

6.8.3. Reactions monitored by HPLC

Reactions were performed in U-bottom 96-well plates (clear polystyrene non-binding, Greiner BioOne Cat# 650101). In these reactions, two variable species were investigated per well, one of them always being D- or L-tryptophan. Negative controls consisted of a sample using boiled IDO1 with all other species at the highest concentration used on the plate.

Standard curves

The standard curve for kynurenine was made using HIDO (1 μ M), catalase (0.1 mg/ml), methylene blue (10 μ M), ascorbic acid (20 mM) and L-tryptophan at concentrations between 0.05 – 100 μ M. The reaction was incubated for 10 minutes at \sim 20 $^{\circ}$ C and then quenched with HCl (0.5M) containing 5-nitro-L-tryptophan (132 μ M) using 20 μ l/100 μ l of reaction. The plates were incubated at \sim 20 $^{\circ}$ C for 16 hours in the fridge before being equilibrated back to ambient temperature for 5 hours. 10 μ l was used per injection.

Variable methylene blue (MB)

Tryptophan and methylene blue were added to each well in a volume of 10 μ l each. A master mix was created such that final concentrations were: IDO1 (30 – 100 nM), sodium phosphate (50 mM, pH 6.5), and catalase (0.1 mg/ml). This was added to each well in a volume of 70 μ l. Reactions were started with the addition of ascorbic acid (200 mM, 10 μ l).

Variable ascorbic acid

Tryptophan and ascorbic acid were added to each well in a volume of 10 μ l each. A master mix was created such that final concentrations were: IDO1 (10 – 30 nM), sodium phosphate (50 mM, pH 6.5), catalase (0.1 mg/ml), and methylene blue (10 μ M). Reactions were initiated by the addition of master mix (80 μ l) to each well.

All reactions ran for 7 minutes, and were quenched through the addition of HCl quenching solution (132 μ M 5-nitro-L-tryptophan in 0.5 M HCl, 20 μ l). Here, the yellow 5-nitro-L-tryptophan acted as an internal standard to control for injection errors and plate evaporation. Plates were then sealed with an adhesive layer (Excel Scientific, Cat# 100-SEAL-PLT) and stored at 4 $^{\circ}$ C overnight. Plates were equilibrated to ambient temperature for 4 – 6 hours prior to analysis by HPLC. The choice of acid was important here, as HCl gave no indication of precipitating protein or causing blockages on the C18 columns. Organic acids (formic, acetic, trichloroacetic or trifluoroacetic) precipitated proteins, and centrifugation of samples caused increases in column backpressure within 50 injections.

HPLC analysis of IDO1 reactions

After equilibration of the plates to ambient temperature, the seal above each well was perforated in a cross-wise fashion with a scalpel. Failure to do so resulted in instrument blockages approximately every 50 – 100 injections. Removal of the seal entirely resulted in a much noisier standard curve for both tryptophan and kynurenine, and excessive evaporation towards the end of each injection sequence.

Reactions were monitored on an Agilent 1260 HPLC system using a G1311B quaternary pump, a G1367E autosampler, a G1316A column heater, a G4212B diode array detector, and a 6130 electrospray ionisation quadrupole mass spectrometer. Samples were run using a Kinetex C18 column (2.6 μ m, 75x3.00 mm, 100 \AA . Phenomenex) at 1 ml/min. Mobile phases were 0.1% formic acid in water (solvent A), and acetonitrile (solvent B). Elution was 100% solvent A for 2 minutes, followed by a change to 40% A, 60% B, over 4 minutes. The column was then washed with 10% A and 90% B for 1 minute, before being washed with 100% solvent A for 4 minutes, ready for the next injection. One-hundred percent aqueous phase was required to obtain acceptable baseline separation between salts and other highly polar species, and kynurenine. UV absorbance of the eluent were monitored at 215.0 nm (salts), 276.0 nm (tryptophan), 333.0 nm (5-nitrotryptophan),

and 360.0 nm (kynurenine), all with a 2 nm bandwidth. A reference wavelength of 500 nm, with a 25 nm bandwidth, was used, and a data rate of 20 Hz. Single ion mass spectrometry (SIM) was conducted using atmospheric pressure electrospray ionisation (AP-ESI) in positive mode. Gain was set to 15 (arbitrary units) with a dwell time of 195 msec/ion and a peak width of 0.1 minutes. A nitrogen drying gas was used at 10.0 l/min, 60 PSIG, and 350 °C. The capillary voltage was 4 kV, and the fragmentor voltage was 90 V. Ions followed were (m/z , M+H): 205.0 (tryptophan) and 209.1 (kynurenine).

This page left intentionally blank

Chapter 7

Other Contributions

This chapter provides details of contributions to related collaborative research projects involving the kynurenine pathway. In particular, exploring the use of carborane cages in inhibitors of human IDO1, and possible structural insights into the mechanism of transport of quinolinic acid across neuronal cellular membranes.

7.1. Modification of known IDO1 inhibitors with carborane cages and their effect on IDO1 inhibition

Work from this section appears in: *The first indoleamine-2, 3-dioxygenase-1 (IDO1) inhibitors containing carborane*. Dalton Transactions, 43(28) 10719-10724, 2014. Christopher J. D. Austin¹¹, Jan Kahlert¹¹, Fatiah Issa¹¹, John H. Reed¹¹, Jason R. Smith¹², Joseph A. Ioppolo¹¹, Jennifer A. Ong¹³, Joanne F. Jamie¹², David Hibbs¹³, and Louis M. Rendina¹¹.

and:

Carborane-containing hydroxyamidine scaffolds as novel inhibitors of indoleamine 2,3-dioxygenase 1 (IDO 1). Australian Journal of Chemistry, 68(12) 1866-1870, 2015. Christopher J. D. Austin¹¹, Michael Moir¹¹, Jan Kahlert¹¹, Jason R. Smith¹², Joanne F. Jamie¹², Michael Kassiou¹¹, and Louis M. Rendina¹¹.

Austin and Rendina have a long standing interest in both the inhibition of IDO1 for drug purposes, and the expansion of the medicinal chemistry space through the use of boron. In this instance, the interest was in the replacement of phenyl rings with non-aromatic, lipophilic carborane cages in known IDO1 inhibitors based on naphthoquinone and hydroxyamidine scaffolds (Figure 7.1) [118, 286]. The molecules were synthesised in the Rendina lab and tested in the Jamie lab by Austin, using protein and protocols provided by the candidate. Low-mode molecular dynamics (LMMD) were performed by the candidate in order to look at the effect that replacing a phenyl ring with a carborane ring in the 3*S*,4*S*-naphthoquinone inhibitor would have on IDO1 binding. During these simulations, an adamantyl ring was used in place of the carborane cage, as the force fields available were not able to reproduce the carborane structure observed from X-ray diffraction experiments on naphthoquinone **6** (Figure 7.2) [195]. The adamantyl cage was used as an analogue with similar lipophilic properties and is of a similar volume.

The naphthoquinones were docked into the active site of human IDO1 (PDB: 2D0T [119]) using a docking methodology previously developed for the docking of inhibitors to this structure [117]. This methodology employs an energy potential restraint between heme iron and specified ligand atoms to ensure that poses are representative of those expected when a co-ordinate covalent

¹¹ School of Chemistry, The University of Sydney, NSW, Australia.

¹² Department of Chemistry and Biomolecular Sciences, Macquarie University, NSW, Australia.

¹³ Faculty of Pharmacy, The University of Sydney, NSW, Australia.

bond is present between ligand and heme [291]. The naphthoquinone was docked such that poses were generated for ligation between both carbonyl oxygens. These are referred to as 5-oxo (for ligation through the carbonyl at the 5 position, next to the amino group), and 10-oxo structures. LMMD simulations were then run on the pose containing the smallest internal strain energy in the ligand (Figure 7.2). This type of simulation is especially suited to the identification of varied conformations of a complex system, but where trajectory information between each conformation is not important. By only following the trajectories of low frequency motions, such as bond rotation and angle bends, the computational time is substantially reduced, while still producing conformations that are based on atomic motions realistically expected to be able to occur at physiological temperatures [194]. The process occurs by running a series of 1 picosecond molecular dynamics simulations, with an energy minimisation step in between, and each new simulation starting with random trajectory information for each atom [196]. Assessment of the results was performed by visually following the motions of the ligand and the residues from one structure to another. Figure 7.3 shows a composite overlay of the structures created *via* LMMD.

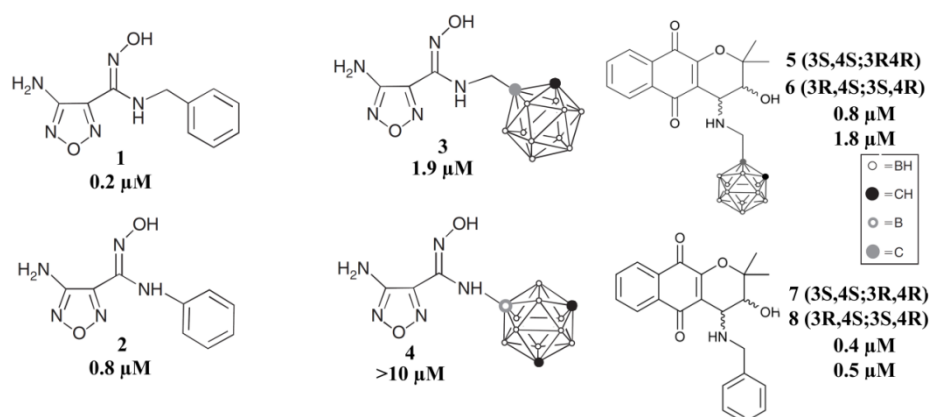


Figure 7.1. A series of phenyl- and carborane-containing IDO1 inhibitors were synthesised and tested by Austin [195, 292]. Compounds **5** – **8** were isolated and tested as the indicated racemates. IC_{50} concentrations are shown (10 μ M methylene blue, 10 mM ascorbic acid, 100 μ M tryptophan).

A total of 700 attempts at finding poses for each ligand were performed, with duplicate poses being discarded (RMSD <0.25 Å across flexible heavy atoms). The 5-oxo form of 3S,4S-**7** gave 51 structures – almost double that of the next highest (23 for the 10-oxo version of 3S,4S-**7**). Fifty-one non-duplicate structures from 700 attempts suggested that the sampling was sufficient. In Figure 7.3 **A**, which shows the starting structure of 5-oxo-3S,4S-**7** using a ball-and-stick structure, Arg231 starts in an open position, moves to a partially closed position, and then a fully closed position. Concurrently, the phenyl ring moves from the right of heme's propanoate arm, to being above propanoate. In the case of the 10-oxo-3S,4S-**7** (Figure 7.3 **B**), the same desire for a closed Arg231 conformation and a phenyl ring above propanoate was observed, with only 2 structures showing a phenyl ring in another position. In Figure 7.3 **C**, the carborane cage displays no trend to

move towards another position, nor does the Arg231 move to a closed position. In Figure 7.3 **D**, the carborane cage started and remained above the propanoate arm, but this time Arg231 was seen to move towards a closed position, in order to interact with the hydroxyl group not available for interaction in Figure 7.3 **C**. It must be cautioned that these were single simulations from single starting structures using implicit solvent, but the results coincided well with expected behaviour: The tendency for Arg231 to take a closed position when an available attractive force from the ligand was present (*i.e.* a hydroxyl group or pi system) would be consistent with an Arg231 gating function, posited by the literature [119, 123, 220]. Such a loss of gating function, along with loss of the favourable pi-cation interaction, likely explain the drop in inhibitory power of the carboranes, compared to the benzyl compounds (Figure 7.1). The small drop in activity, 10-fold for the hydroxyamidines **1 – 4**, and 4-fold for the naphthoquinones **5 – 8**, paint these disruptions as minor under the assay conditions.

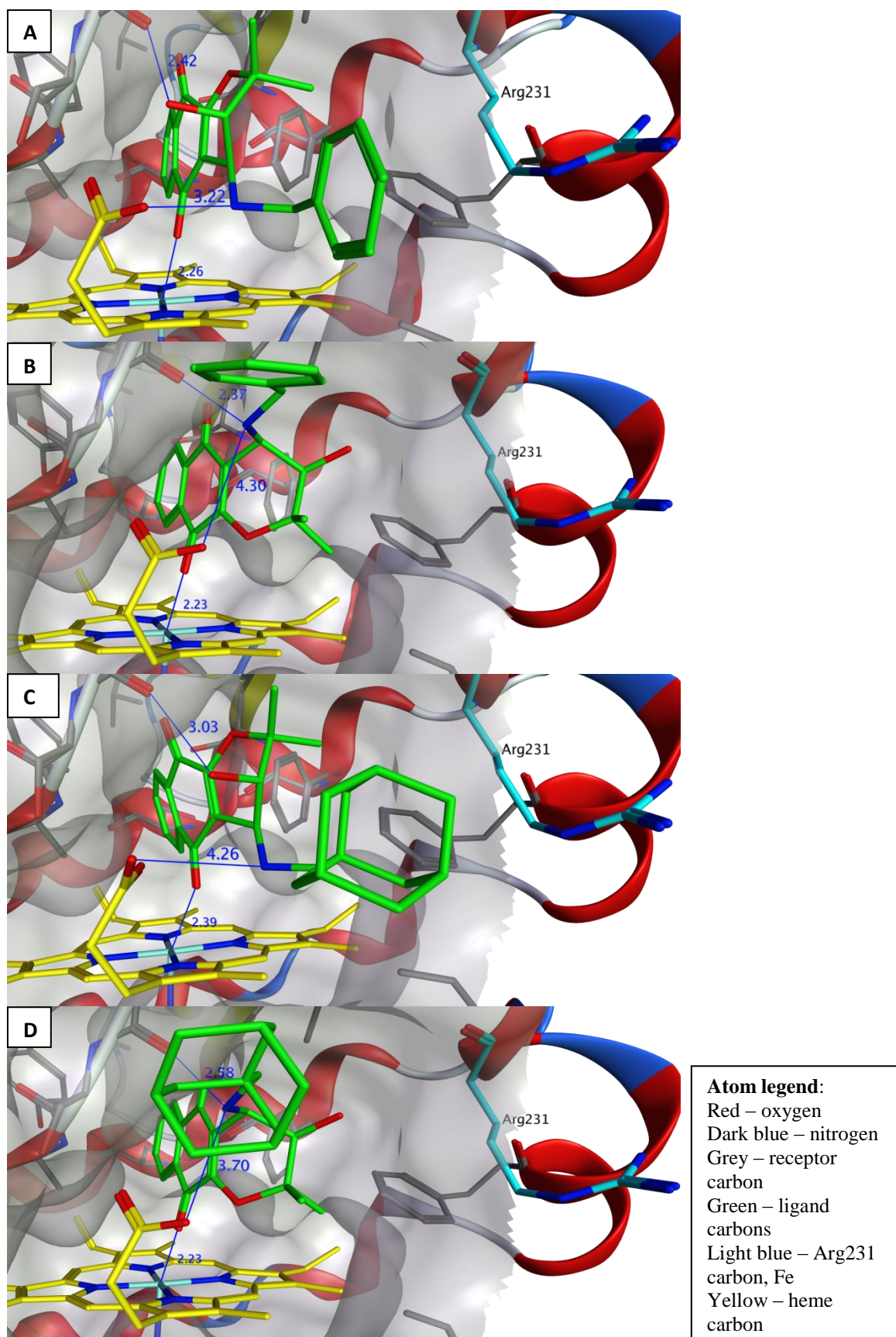
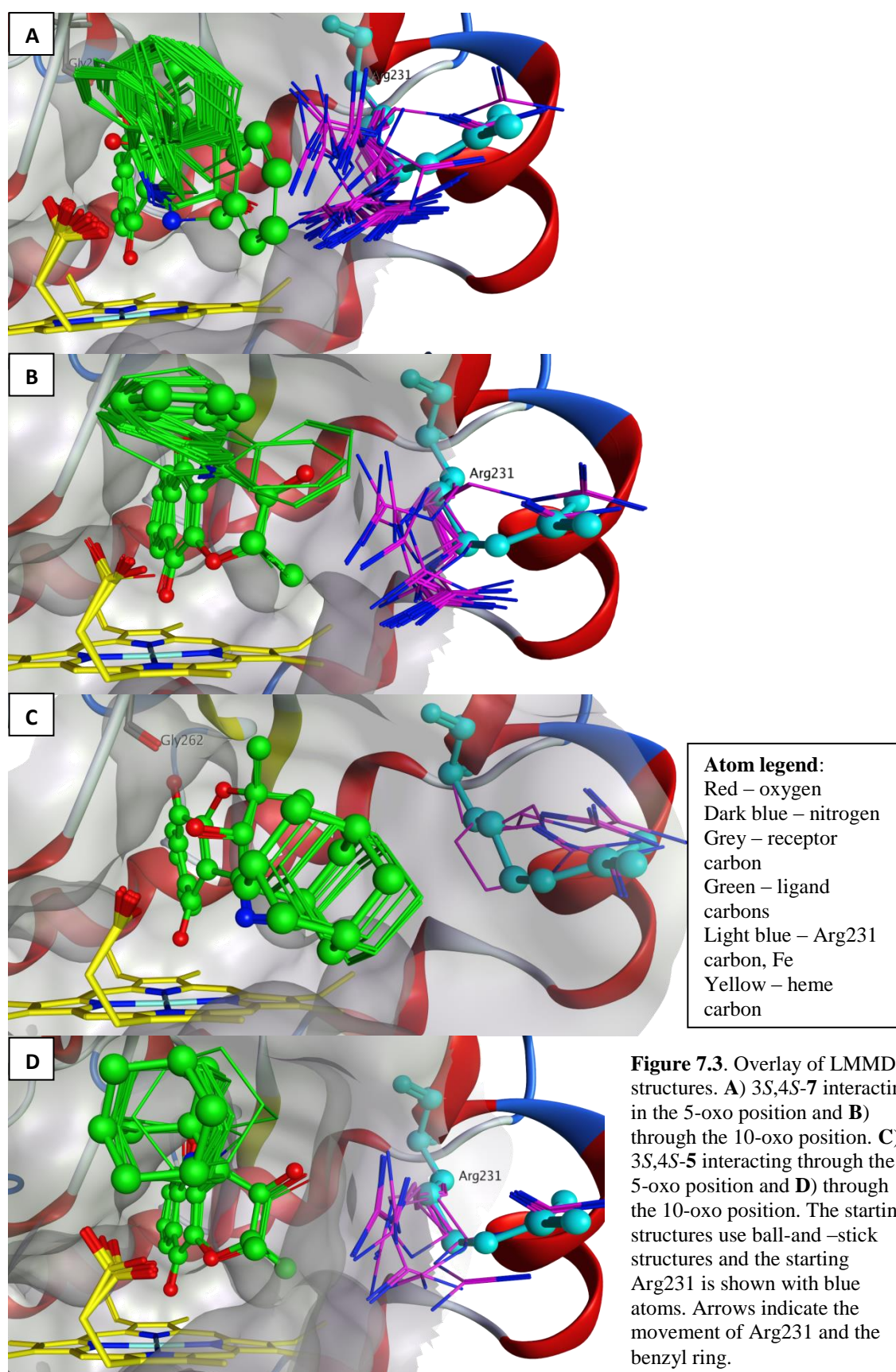


Figure 7.2. Starting structures from which LMMD simulations were run. **A)** 3*S*,4*S*-naphthoquinone **7** interacting in the 5-oxo position and **B)** through the 10-oxo position. **C)** 3*S*,4*S*-naphthoquinone **5** interacting through the 5-oxo position and **D)** through the 10-oxo position.



7.2. Mechanism of cellular uptake of the excitotoxin quinolinic acid in primary human neurons

Quinolinic acid is an excitatory amino acid in the human brain, present in low nanomolar concentrations [293]. It plays a variety of roles including the initiation of lipid peroxidation [294], activation and inhibition of cellular release and uptake of the excitatory amino acid glutamic acid [295], over-excitation of NMDA receptors leading to neurotoxicity [17, 18], and hyperphosphorylation of the *tau* protein under neurodegenerative conditions [40]. The neuropathological roles of quinolinic acid are of great interest both for the better understanding of neurological disease mechanisms, and for the better development of drugs targeting neurodegenerative conditions (See [2] and references therein). One avenue of investigation has been the links between quinolinic acid and glutamic acid in terms of their concentrations and importation mechanism in human neurons. The excitatory amino acid transport 3 (EAAT3) is one such possible site of this link, as EAAT3 is a pathophysiologically relevant transporter of glutamic acid that has shown correlations with neuropathological conditions [296], and interferon-gamma has been shown to downregulate the uptake of glutamic acid [297] and upregulate the kynurenine pathway that leads to quinolinic acid production [298]. Based on unpublished data being accrued in the Braidy¹⁴ and Guillemín¹⁵ labs at the time, a request was made by the Guillemín lab to investigate, using available structural information, whether a direct relationship between EAAT3, and glutamic and quinolinic acids, was plausible.

Structural insights into the binding between quinolinic acid, glutamic acid, and EAAT3 were investigated by the candidate by docking using Molecular Operating Environment (MOE, Chemical Computing Group, Montreal, Canada) software package. A human structure of EAAT3 was not available in the RCSB protein databank. The closest ancestor available was the glutamate symport protein Glt_{ph} from the archaea *Pyrococcus horikoshii*. Heinzelmán *et al.* used the *P. horikoshii* crystal structures to generate human homology models, validated through molecular dynamics to reproduce empirically observed properties [299]. The structure used for this thesis was provided upon request by Heinzelmán *et al.* The bound glutamic acid molecule was compared to docking poses obtained for quinolinic acid in the same binding site.

One hundred energy minimised poses for quinolinic acid binding to EAAT3 were generated and manually clustered based on their three dimensional orientation within the binding site. 40% of structures were found in the first cluster and this cluster had the lowest energy and the smallest spread of energies (Figure 7.4). The residues in contact with either substrate were largely the

¹⁴ Centre for Healthy Brain Ageing, School of Psychiatry, University of New South Wales, NSW, Australia.

¹⁵ MND and Neurodegenerative diseases Research Centre, Macquarie University, NSW, Australia

same. Glutamic acid's carboxyl groups were in contact with Arg447, Thr370, Asn451 and Ser333 (Figure 7.5). The nitrogen was in contact with Asp444, Thr448 and Val411. Val411, which is part of a loop locking glutamic acid in place prior to translocation [299], was not in direct contact with quinolinic acid, and may have implications for loop behaviour during the binding of quinolinic vs. glutamic acids. These poses suggest that quinolinic acid has the potential to interact with EAAT3, and that such interaction could lead to competitive inhibition with glutamic acid for transport. The structure of EAAT3 used was of the protein immediately prior to translocation of substrate, however, quinolinic acid would first need to bind to an open structure of the transporter to perform this function. This has not yet been investigated. Further work is required to determine more on the relationship between glutamic acid and quinolinic acid in EAAT3 expressing cells.

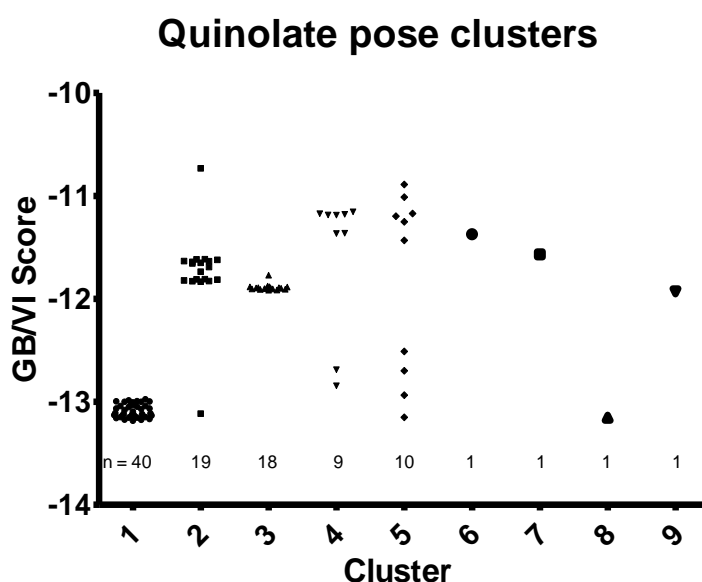


Figure 7.4. Clustering of the quinolinic acid poses within the glutamic acid binding site EAAT3. Each cluster represents a specific orientation of the quinolinic acid molecule along the x, y, and z axes.

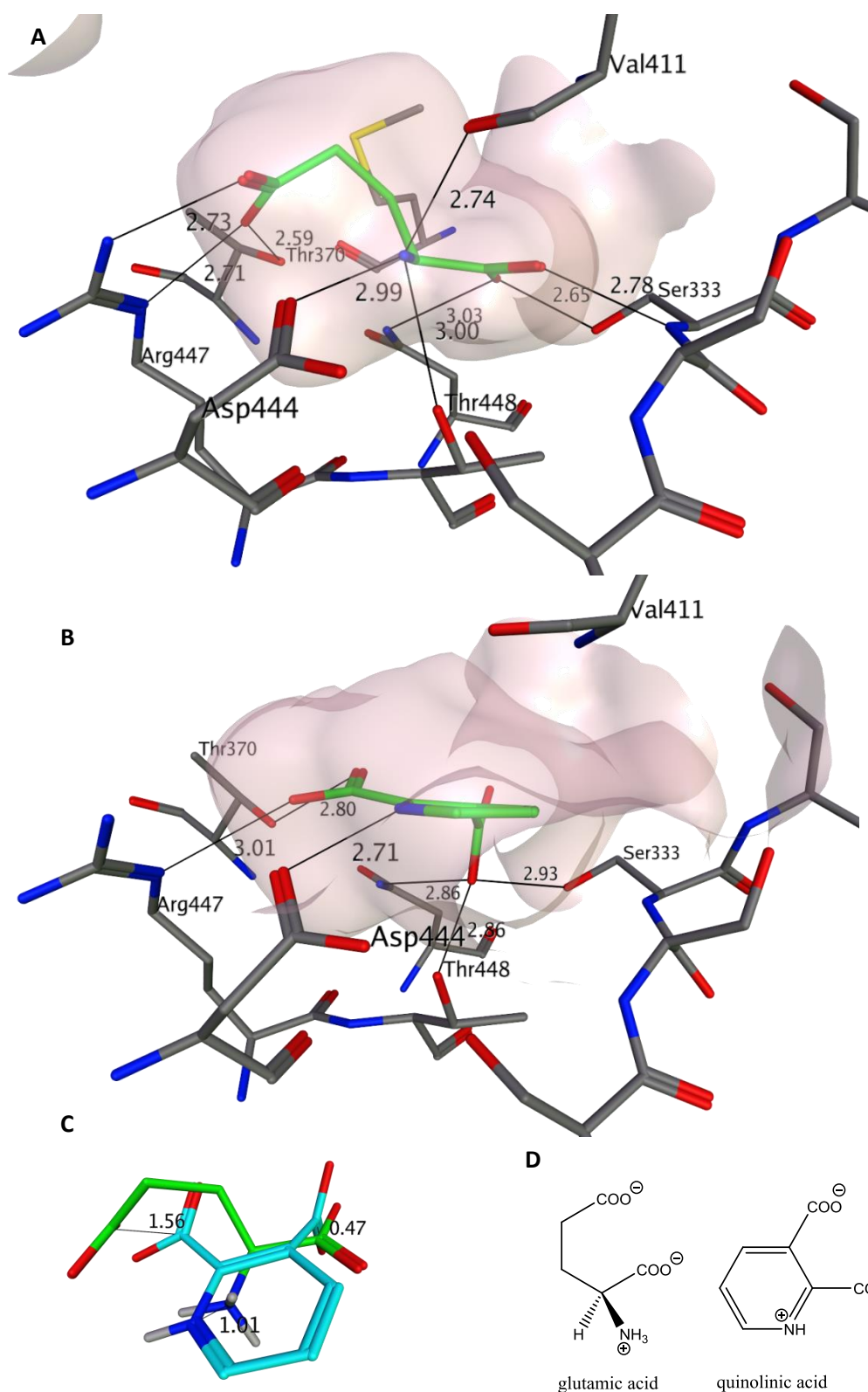


Figure 7.5. **A)** Glutamic acid and **B)** quinolinic acid bound to EAAT3 prior to translocation. Green numbers represent distances in angstroms between substrate and transporter. Nitrogens are blue, oxygens are red, hydrogens are white. Carbons of the protein are grey while carbons of the substrates are green. **C)** Bound forms of glutamic acid (green carbons) and quinolinic acid (light blue carbons) showing similar overlap of features in space. Distances between carboxyl carbons and nitrogens are given in angstroms. **D)** structures of glutamic and quinolinic acids.

7.3. Methods

7.3.1. Modification of known IDO1 inhibitors with carborane cages and their effect on IDO1 inhibition

All calculations were performed in MOE 2011.10 (Chemical Computing Group, Montreal, Canada) using the CHARMM22 force field and a Generalised-Born solvation model with dielectric constants of 4 and 80. RMSG for energy minimisation was 0.005.

Docking

The two naphthoquinones, in the 3S,4S configuration, were docked into the 2D0T crystal structure using MOE's "Dock" function with refinement set to "force field" and a rigid receptor. All other values were default. A pharmacophore restraint was used so that only poses with an oxygen in proximity to the iron of heme would be considered. The structures were then refined using the cubic potential previously described [117]. For each molecule, and each carbonyl oxygen orientation, the poses with the smallest internal strain energy was selected for low mode molecular dynamics (4 structures in total).

Low mode molecular dynamics

The low mode molecular dynamics (LMMD) methodology was employed using MOE's Conformational Search protocol. Default parameters were used except the iteration limit for finding new conformations was 700. The RMSD for defining two poses as equivalent was 0.25 Å and fixed atoms were excluded from this measurement. Flexible species were the ligand, the propanoate arm of heme, and the IDO1 amino acid residues: T126, C129, V130, F163, F164, S167, F226, L230, R231, L234, S235, A260, S263, A264, F291, H346, I354 and L384. All backbone atoms of the protein were held fixed.

7.3.2. Mechanism of cellular uptake of the excitotoxin quinolinic acid in primary human neurons

All calculations were performed in MOE 2014.0901 (Chemical Computing Group, Montreal, Canada) using the CHARMM27 force field and a Generalised-Born solvation model with dielectric constants of 4 and 80.

Structure preparation:

The starting EAAT3 structure (representing the structure immediately prior to translocation) contained glutamic acid and all three required sodium ions, but was devoid of solvating water or lipids. As the starting structure came directly from a molecular dynamics simulation, energy minimisation was performed to obtain a local minimum structure. The backbone was held fixed and the remainder of the system energy minimised with heavy atoms tethers. Over four consecutive energy minimisation steps, these tethers had weighting constants of 100, 10, 1 and 0 kcal/mol, respectively, in order to gently lower the protein into the nearest local energy minima.

All remaining work was performed on this minimised structure.

Docking of quinolinic acid

It was assumed that both substrates were formally in the -1 protonation state. The glutamate substrate was removed from the structure and replaced with quinolate in such a manner as to maximise overlap between their amino acid groups. The protein was held rigid whilst quinolate was energy minimised. This yielded a quinolate molecule experiencing some small ring strain due to a slightly too small binding pocket. Therefore, surrounding residues in contact with quinolate, or present in loops that control glutamate binding [299], were allowed to move freely to accommodate quinolate more fully (residues S132-A141, S331-S334, M367, T370, A408-M419, D444, R447, T448, N451). This structure was then used to perform docking of quinolate into EAAT3. During docking, all backbone atoms were held fixed. 9999 unique, non-minimised, poses between quinolate and EAAT3 were randomly generated by placing different conformations of quinolate into the binding pocket. These were scored with MOE's LondonDG function and the best 100 non-duplicate poses were kept for energy minimisation. These minimised structures were scored using MOE's GB/VI function and manually clustered based on the orientation of quinolate within the binding site. RMSG for energy minimisation was 0.005.

Chapter 8

Conclusions and Future Directions

This chapter summarises briefly the results obtained in this project, and provides suggestions for future work of interest based on these observations.

8.1. KMO and drug design

Work was conducted here in finding new lead compounds as KMO inhibitors. The current knowledge surrounding KMO structure, kinetics and mechanism, and inhibition structure-activity relationship (SAR) was reviewed in detail (Section 2.1 – 2.4). From this, models were generated to gain a better understanding of the interactions between KMO and small molecule inhibitors. These models consisted of a pharmacophore generated from the common feature alignment of active KMO inhibitors (Section 3.2), which gave excellent geometric consistency with the active site of yeast KMO crystal structure, and was able to moderately describe the relationship between the structure of KMO inhibitors and inhibitory potency (R^2 0.64, n = 39, using \log_{10} IC_{50} values). Further insight was gained through the use of docking experiments between yeast KMO and inhibitor structures (Section 3.2.5). These models were then used to screen through a commercial library, of which 41 hit compounds were purchased for testing (Section 3.2.6). *In vitro* testing demonstrated that six of these compounds had IC_{50} s below 100 μ M. *In vivo* testing in human cells (over-expressing human KMO) was still on-going, but demonstrated at least one compound with an EC_{50} <20 μ M. Toxicity testing in these same cells indicated that some of the compounds were either metabolically unstable, or unable to penetrate the cells.

Structure-activity investigations of identified hit molecules is the next logical step, in order to find specific compounds with improved potency, toxicity, and pharmacokinetic profiles. During docking work of known KMO inhibitors, the natural product ianthellamide was identified as potentially possessing a novel binding mechanism, due to the absence of any poses using an FAD-benzene interaction. This molecule also represents an interesting lead point for future SAR projects. A number of other compounds were identified as being of interest by the computational techniques, but were not available for purchase at the time, including one bearing a resemblance to the newly reported GSK180 (Figure 3.13 F). The acquisition of these compounds would be of interest in future work.

The docking experiments and literature review also highlight that a number of dynamic processes might be present in the KMO protein and of relevance to the binding of ligands. The crystal structure depicts a helix that makes up a small portion of the active site roof, and is pushed out of

the way upon the binding of the co-crystallised inhibitor (Section 2.3). Additionally, spectroscopic data suggests that chloride ions lock KMO into a static structure, leading to inhibition. The docking also identified that a number of molecules possessed an extra aromatic group, that not only likely increased the potency of those molecules towards KMO, but also extended outside of the active site defined in the crystal structure (Section 3.2.5). Nearby to this active site entrance resides a small loop with a partially conserved sequence. Therefore, future studies could be directed towards better understanding the role of these protein sequences and chloride binding site.

8.2. IDO1 and its mutants

Nine crystal structures of IDO1 are currently available in the RCSB protein databank, and all of these or missing most of a 20 amino acid loop (Section 4.2). Early simulations suggested the hypothesis that the loop may interact with substrate L-tryptophan upon binding, as such, it seems plausible that some inhibitors might be able to take advantage of such an interaction as well. It was reported that cytochrome P450:NAD(P)H reductase (CPR) and cytochrome b5, isoform A (CYB5A) could be used to support IDO1 reactions. A natural hypothesis formed as part of this work was that this too might involve interactions with the loop. Therefore, work began on the construction on a series of protein expression systems that could be used to investigate the role of the unresolved loop of IDO1 in the binding of substrates, inhibitors, and the proteins CPR and CYB5A. In addition to wild-type human IDO1 (HIDO), this set of proteins were comprised of two deletion mutants of human IDO1 (HIDO Δ 360-370 and HIDO Δ 371-380), walrus wild-type (WIDO), and human and walrus chimeras (HCHIM and WCHIM). Liposomal and truncated versions of CPR (CPR and CPRS) and CYB5A (CYB5A and CYB5S) constructs were also made (Sections 4.7.2 and 4.7.5).

A selection of these constructs were then expressed and characterised. HIDO, HIDO Δ 360-370, and WIDO were expressed and purified as His-tagged proteins. HIDO and HIDO Δ 360-370 gave nearly identical absorption spectra, although WIDO gave a unique double peak in the Soret region (Section 5.2.3). This double peak was consistently present across multiple protein batches. Although the Q-band region of the three proteins was consistent in their peak positions, here again WIDO was unique in its reaction with ferricyanide and dithionite – with batch-to-batch variation in the extent to which the peaks would change. In those samples that did react to the addition of the ferricyanide and/or dithionite, those reactions were consistent with the human-derived proteins. This led to the hypothesis that the unique spectral results are artefacts created by batch-to-batch variation in the quality of WIDO protein, rather than any inherent physical property of the system. Various parameters surrounding the induction of these IDO1 proteins

were also explored (Section 5.2.2). Substantial changes were observed when comparing IPTG induction to that of lactose-based autoinduction, as the lactose system gave poor yields and poor heme-protein ratios across all proteins. This may be the result of needing to balance protein production and heme production, and no optimisation of the lactose-based method was undertaken here. Instead, a significant change was noted when growing cells with lower oxygen levels, lower IPTG concentration, and inducing expression lower in the growth phase. Previous to this, the expression of the three IDO1 proteins and analysis by size exclusion chromatography had always yielded multiple peaks, only one of which coincided with substantial amounts of heme. This change, which has thus far only been tested on the WIDO protein, yielded a single peak. These results clearly demonstrate room for improvement. Whilst WIDO was able to be expressed as a single peak by size exclusion chromatography, the protein still possessed a double Soret peak and a Q-band region that did not completely react to the presence of dithionite as indicated by the presence of a residual peak, absent from the other IDO1 proteins.

8.3. Kinetics of the IDO1 proteins

The kinetics of the three IDO1 proteins were investigated in regards to the effect of the two electron transporting agents: methylene blue and CYB5S. All IDO1 proteins displayed substrate inhibition, with both L-tryptophan and methylene blue being inhibitory at elevated concentrations. This was the case even in the presence of catalase and superoxide dismutase, arguing against the formation of reactive oxygen species being the main culprit for the inhibition. The substrate inhibition constant of L-tryptophan, $K_{si(Trp)}$, decreased with increasing concentrations of methylene blue for all proteins. It cannot be ruled out that this may be due to an increased level of superoxide production, however, may also indicate an ability for methylene blue binding to affect the binding of L-tryptophan beyond just the reduction of the heme.

When HIDO was supported by CYB5S instead of methylene blue, substrate inhibition with respect to L-tryptophan was also seen. This is in contrast to reports of liposomal CYB5A, in the presence of liposomal CPR, giving allosteric sigmoidal kinetics instead. When methylene blue was added to the HIDO and non-liposomal CYB5S reactions, a reduction in k_{cat} was observed, supporting an inhibitory nature of methylene blue, however the $K_{si(Trp)}$ constant showed an increase with increasing methylene blue, suggesting a difference between the inhibition imposed by methylene blue in the presence and absence of CYB5S. Most intriguing of all, however, was the observation that WIDO, when supported by CYB5S, showed a hyperbolic shape, both with and without methylene blue. If this is due to an inherent difference in the WIDO protein, rather than being an artefact in the same manner as the unique heme spectra, then this points to an important system for studying the structure-function relationship of heme dioxygenases of tryptophan.

The loop and small molecules

At the outset of this work, these proteins were designed so as to be able to answer questions surrounding the role of the unresolved loop in IDO1 function. On the question of if the loop interacts with small molecules, it can now be said that the loop interacts with Thr379, due to the report by Álvarez *et al.* [220]. It can also be said that the first half of the loop is not obligatory to binding, as HIDOΔ360-370 was competent for both L- and D-tryptophan (Section 6.5). It is tempting to analyse whether the missing sequence of HIDOΔ360-370 led to kinetics that could be attributed to a less optimal ability for Thr379 to do its job as a result of the smaller loop, however, such a question would be difficult to answer using the kinetic data here, and would be better addressed through non-steady-state means, such as the spectroscopic investigation of the binding of L- and D-tryptophan to ferric-cyanide or ferrous-carbon monoxide protein samples, which are catalytically inactive. Circular dichroism of the heme and isothermal calorimetry could also be used, such as for the binding of tryptophan to ferric forms of the enzyme.

The loop and other proteins

On the question on whether CPRS or CYB5 proteins interact directly with loop. CPRS was not tested in these set of experiments, but is available for such testing. CYB5S was used to successfully support reactions of HIDOΔ360-370, and therefore, here again it can be said that the first half of the loop does not play a substantial role in binding IDO1 function, or that those roles can be easily supplanted by the residues remaining within the loop. Further work should focus on the activity of CPRS-supported reactions, and the reactions supported by both CPRS and CYB5S. In particular, attempting to reproduce the allosteric and Michaelis-Menten nature of these kinetics when differing amounts of methylene blue, CPRS and CYB5S are present, and ensuring that these results are consistent regardless of the construct used. HIDOΔ371-380 cannot be used for kinetic evaluation in the same manner, due to missing the required Thr379 (although there is always the possibility that another residue could occupy its place), however it can still be assessed for its ability to reduce the IDO1 proteins *via* spectroscopic experiments. Alternatively, a HIDOΔ371-378 construct could be used. With HIDOΔ360-370 possessing similar kinetic properties to wild-type, this sequence is a good candidate for crystallography work, as the smaller loop might allow the full structure to be visualised. This could present an opportunity to obtain the first IDO1 crystal structures with bound substrate or substrate analogues.

References

1. Takikawa, O., *Biochemical and medical aspects of the indoleamine 2,3-dioxygenase-initiated L-tryptophan metabolism*. Biochemical and Biophysical Research Communications, 2005. **338**(1): p. 12-19.
2. *Targeting the broadly pathogenic kynurenine pathway*. 1st ed, ed. S. Mittal. 2015, Switzerland: Springer International Publishing.
3. Griffiths, H.R., Lunec, J., and Blake, D.R., *Oxygen radical induced fluorescence in proteins; identification of the fluorescent tryptophan metabolite, N-formyl kynurenine, as a biological index of radical damage*. Amino Acids, 1992. **3**(2): p. 183-194.
4. Dreaden, T.M., Chen, J., Rexroth, S., and Barry, B.A., *N-Formylkynurenine as a Marker of High Light Stress in Photosynthesis*. The Journal of Biological Chemistry, 2011. **286**(25): p. 22632-22641.
5. Parker, N.R., Jamie, J.F., Davies, M.J., and Truscott, R.J.W., *Protein-bound kynurenine is a photosensitizer of oxidative damage*. Free Radical Biology and Medicine, 2004. **37**(9): p. 1479-1489.
6. Linetsky, M., Raghavan, C.T., Johar, K., Fan, X., Monnier, V.M., Vasavada, A.R., and Nagaraj, R.H., *UVA Light-excited Kynurenines Oxidize Ascorbate and Modify Lens Proteins through the Formation of Advanced Glycation End Products: implications for human lens aging and cataract formation*. Journal of Biological Chemistry, 2014. **289**(24): p. 17111-17123.
7. Opitz, C.A., Litzenburger, U.M., Sahm, F., Ott, M., Tritschler, I., Trump, S., Schumacher, T., Jestaedt, L., Schrenk, D., Weller, M., Jugold, M., Guillemin, G.J., Miller, C.L., Lutz, C., Radlwimmer, B., Lehmann, I., Deimling, A.v., Wick, W., and Platten, M., *An endogenous tumour-promoting ligand of the human aryl hydrocarbon receptor*. Nature, 2011. **478**: p. 197-203.
8. Noakes, R., *The Aryl Hydrocarbon Receptor: A Review of Its Role in the Physiology and Pathology of the Integument and Its Relationship to the Tryptophan Metabolism*. International Journal of Tryptophan Research, 2015. **8**: p. 7-18.
9. Schwarcz, R., Bruno, J.P., Muchowski, P.J., and Wu, H.-Q., *Kynurenines in the mammalian brain: when physiology meets pathology*. Nature Reviews Neuroscience, 2012. **13**(7): p. 465-477.
10. Goldstein, L.E., Leopold, M.C., Huang, X., Atwood, C.S., Saunders, A.J., Hartshorn, M., Lim, J.T., Faget, K.Y., Muffat, J.A., Scarpa, R.C., Chylack, L.T., Bowden, E.F., Tanzi, R.E., and Bush, A.I., *3-Hydroxykynurenine and 3-Hydroxyanthranilic Acid Generate Hydrogen Peroxide and Promote α -Crystallin Cross-Linking by Metal Ion Reduction*. Biochemistry, 2000. **39**(24): p. 7266-7275.
11. Perkins, M.N. and Stone, T.W., *An iontophoretic investigation of the actions of convulsant kynurenines and their interaction with the endogenous excitant quinolinic acid*. Brain Research, 1982. **247**(1): p. 184-187.
12. Parsons, C.G., Danysz, W., Quack, G., Hartmann, S., Lorenz, B., Wollenburg, C., Baran, L., Przegalinski, E., Kostowski, W., Krzascik, P., Chizh, B., and Max. Headley, P., *Novel systemically active antagonists of the glycine site of the N-methyl-D-aspartate receptor: electrophysiological, biochemical and behavioral Characterization*. Journal of Pharmacology and Experimental Therapeutics, 1997. **283**(3): p. 1264-1275.
13. Hilmas, C., Pereira, E.F.R., Alkondon, M., Rassoulpour, A., Schwarcz, R., and Albuquerque, E.X., *The brain metabolite kynurenic acid inhibits $\alpha 7$ nicotinic receptor activity and increases non- $\alpha 7$ nicotinic receptor expression: physiopathological implications*. The Journal of Neuroscience, 2001. **21**(19): p. 7463-7473.
14. Wang, J., Simonavicius, N., Wu, X., Swaminath, G., Reagan, J., Tian, H., and Ling, L., *Kynurenic acid as a ligand for orphan G protein-coupled receptor GPR35*. Journal of Biological Chemistry, 2006. **281**(31): p. 22021-22028.

15. DiNatale, B.C., Murray, I.A., Schroeder, J.C., Flaveny, C.A., Lahoti, T.S., Laurenzana, E.M., Omiecinski, C.J., and Perdew, G.H., *Kynurenic acid is a potent endogenous aryl hydrocarbon receptor ligand that synergistically induces interleukin-6 in the presence of inflammatory signaling*. Toxicological Sciences, 2010. **115**(1): p. 89-97.
16. Lugo-Huitrón, R., Blanco-Ayala, T., Ugalde-Muñiz, P., Carrillo-Mora, P., Pedraza-Chaverri, J., Silva-Adaya, D., Maldonado, P.D., Torres, I., Pinzón, E., Ortiz-Islas, E., López, T., García, E., Pineda, B., Torres-Ramos, M., Santamaría, A., and La Cruz, V.P.-D., *On the antioxidant properties of kynurenic acid: Free radical scavenging activity and inhibition of oxidative stress*. Neurotoxicology and Teratology, 2011. **33**(5): p. 538-547.
17. Stone, T.W. and Perkins, M.N., *Quinolinic acid: a potent endogenous excitant at amino acid receptors in CNS*. European Journal of Pharmacology, 1981. **72**: p. 411-412.
18. Guillemín, G.J., *Quinolinic acid, the inescapable neurotoxin*. FEBS Journal, 2012. **279**(8): p. 1356-1365.
19. Ríos, C. and Santamaría, A., *Quinolinic acid is a potent lipid peroxidant in rat brain homogenates*. Neurochemical Research, 1991. **16**: p. 1139-1143.
20. Štípek, S., Štátný, F.e., Pláteník, J., Crkovská, J.i., and Zima, T., *The effect of quinolinate on rat brain lipid peroxidation is dependent on iron*. Neurochemistry International, 1997. **30**(2): p. 233-237.
21. Pláteník, J., Stopka, P., Vejrazka, M., and Štípek, S., *Quinolinic acid–iron (II) complexes: slow autoxidation, but enhanced hydroxyl radical production in the fenton reaction*. Free Radical Research, 2001. **34**: p. 445-459.
22. Campesan, S., Green, Edward W., Breda, C., Sathyaikumar, Korrapati V., Muchowski, Paul J., Schwarcz, R., Kyriacou, Charalambos P., and Giorgini, F., *The kynurenine pathway modulates neurodegeneration in a drosophila model of Huntington's disease*. Current Biology, 2011. **21**(11): p. 961-966.
23. Ross, C.A. and Tabrizi, S.J., *Huntington's disease: from molecular pathogenesis to clinical treatment*. The Lancet Neurology, 2011. **10**(1): p. 83-98.
24. Giorgini, F., Guidetti, P., Nguyen, Q., Bennett, S.C., and Muchowski, P.J., *A genomic screen in yeast implicates kynurenine 3-monooxygenase as a therapeutic target for Huntington's disease*. Nature Genetics, 2005. **37**(5): p. 526-531.
25. Okamoto, H., Yamamoto, S., Nozaki, M., and Hayaishi, O., *On the submitochondrial localization of L-kynurenine-3-hydroxylase*. Biochemical and Biophysical Research Communications, 1967. **26**(3): p. 309-314.
26. Orr, A.L., Li, S., Wang, C.-E., Li, H., Wang, J., Rong, J., Xu, X., Mastroberardino, P.G., Greenamyre, J.T., and Li, X.-J., *N-terminal mutant huntingtin associates with mitochondria and impairs mitochondrial trafficking*. The Journal of Neuroscience, 2008. **28**(11): p. 2783-2792.
27. Stone, T.W. and Darlington, L.G., *Endogenous kynurenines as targets for drug discovery and development*. Nature Reviews Drug Discovery, 2002. **1**(8): p. 609-620.
28. Guidetti, P., Luthi-Carter, R.E., Augood, S.J., and Schwarcz, R., *Neostriatal and cortical quinolinate levels are increased in early grade Huntington's disease*. Neurobiology of Disease, 2004. **17**(3): p. 455-461.
29. Guidetti, P., Bates, G.P., Graham, R.K., Hayden, M.R., Leavitt, B.R., MacDonald, M.E., Slow, E.J., Wheeler, V.C., Woodman, B., and Schwarcz, R., *Elevated brain 3-hydroxykynurenine and quinolinate levels in Huntington disease mice*. Neurobiology of Disease, 2006. **23**(1): p. 190-197.
30. Giorgini, F., *Targeting the Kynurenine Pathway in Huntington's Disease*. Advances in Clinical Neuroscience and Rehabilitation, 2012. **12**(1): p. 7-8.
31. Sathyaikumar, K.V., Stachowski, E.K., Amori, L., Guidetti, P., Muchowski, P.J., and Schwarcz, R., *Dysfunctional kynurenine pathway metabolism in the R6/2 mouse model of Huntington's disease*. Journal of Neurochemistry, 2010. **113**(6): p. 1416-1425.

32. Jauch, D., Urbańska, E.M., Guidetti, P., Bird, E.D., Vonsattel, J.P.G., Whetsell Jr, W.O., and Schwarcz, R., *Dysfunction of brain kynurenic acid metabolism in Huntington's disease: focus on kynurenine aminotransferases*. Journal of the Neurological Sciences, 1995. **130**(1): p. 39-47.
33. Stoy, N., Mackay, G.M., Forrest, C.M., Christofides, J., Egerton, M., Stone, T.W., and Darlington, L.G., *Tryptophan metabolism and oxidative stress in patients with Huntington's disease*. Journal of Neurochemistry, 2005. **93**(3): p. 611-623.
34. Mazarei, G., Neal, S.J., Becanovic, K., Luthi-Carter, R., Simpson, E.M., and Leavitt, B.R., *Expression analysis of novel striatal-enriched genes in Huntington disease*. Human Molecular Genetics, 2010. **19**(4): p. 609-622.
35. Amori, L., Guidetti, P., Pellicciari, R., Kajii, Y., and Schwarcz, R., *On the relationship between the two branches of the kynurenine pathway in the rat brain in vivo*. Journal of Neurochemistry, 2009. **109**(2): p. 316-325.
36. Behan, W.M.H. and Stone, T.W., *Role of kynurenines in the neurotoxic actions of kainic acid*. British Journal of Pharmacology, 2000. **129**(8): p. 1764-1770.
37. Moroni, F., Cozzi, A., Carpendo, R., Cipriani, G., Veneroni, O., and Izzo, E., *Kynurenine 3-mono-oxygenase inhibitors reduce glutamate concentration in the extracellular spaces of the basal ganglia but not in those of the cortex or hippocampus*. Neuropharmacology, 2005. **48**(6): p. 788-795.
38. Moroni, F., Carpenedo, R., Cozzi, A., Meli, E., Chiarugi, A., and Pellegrini-Giampietro, D., *Studies on the Neuroprotective Action of Kynurenine Mono-Oxygenase Inhibitors in Post-Ischemic Brain Damage*, in *Developments in Tryptophan and Serotonin Metabolism*, G. Allegri, et al., Editors. 2003, Springer US. p. 127-136.
39. Citron, M., *Alzheimer's disease: strategies for disease modification*. Nature Reviews Drug Discovery, 2010. **9**(5): p. 387-398.
40. Rahman, A., Ting, K., Cullen, K.M., Braid, N., Brew, B.J., and Guillemin, G.J., *The excitotoxin quinolinic acid induces tau phosphorylation in human neurons*. PLoS ONE, 2009. **4**(7): p. e6344.
41. Bonda, D.J., Mailankot, M., Stone, J.G., Garrett, M.R., Stanisiewska, M., Castellani, R.J., Siedlak, S.L., Xiongwei, Z., Hyoung-gon, L., Perry, G., Nagaraj, R.H., and Smith, M.A., *Indoleamine 2,3-dioxygenase and 3-hydroxykynurenine modifications are found in the neuropathology of Alzheimer's disease*. Redox Report, 2010. **15**(4): p. 161-168.
42. Guillemin, G.J., Brew, B.J., Noonan, C., Knight, T.G., and Cullen, K., *Mass spectrometric detection of quinolinic acid in microdissected Alzheimer disease plaques*. International Congress Series, 2007. **1304**: p. 404-408.
43. Guillemin, G.J., Brew, B.J., Noonan, C., Takikawa, O., and Cullen, K., *Indoleamine 2,3 dioxygenase and quinolinic acid immunoreactivity in Alzheimer's disease hippocampus*. Neuropathology and Applied Neurobiology, 2005. **31**: p. 395-404.
44. Guillemin, G.J., Smythe, G.A., Veas, L.A., Takikawa, O., and Brew, B.J., *Aβ1-42 induces production of quinolinic acid by human macrophages and microglia*. NeuroReport, 2003. **14**(18): p. 2311-2315.
45. Zwillig, D., Huang, S.-Y., Sathyaikumar, Korrapati V., Notarangelo, Francesca M., Guidetti, P., Wu, H.-Q., Lee, J., Truong, J., Andrews-Zwillig, Y., Hsieh, Eric W., Louie, Jamie Y., Wu, T., Scarce-Levie, K., Patrick, C., Adame, A., Giorgini, F., Moussaoui, S., Laue, G., Rassoulpour, A., Flik, G., Huang, Y., Muchowski, Joseph M., Masliah, E., Schwarcz, R., and Muchowski, Paul J., *Kynurenine 3-Monooxygenase Inhibition in Blood Ameliorates Neurodegeneration*. Cell, 2011. **145**(6): p. 863-874.
46. Rover, S., Cesura, A.M., Huguenin, P., Kettler, R., and Sente, A., *Synthesis and biochemical evaluation of N-(4-phenylthiazol-2-yl)benzenesulfonamides as high-affinity inhibitors of kynurenine 3-hydroxylase*. Journal of Medicinal Chemistry, 1997. **40**(26): p. 4378-4385.

47. Muchowski, P.J., Muchowski, J.M., Schwarz, R., and Guidetti, P., *Gladstone Institute and University of Maryland. Small molecule inhibitors of kynurenine-3-monooxygenase. International Patent Application Number WO2008/022286*. 2008.
48. Benatti, L., Fariello, R., Salvati, P., Pellicciari, R., and Caccia, C., *Newron Pharmaceuticals. glycoside derivatives of 2-(3,4-dichlorobenzoyl)-cyclopropane-1-carboxylic acid [sic]. European patent Publication Number EP1475385A1*. 2004.
49. Toledo-Sherman, L.M., Prime, M.E., Mrzljak, L., Beconi, M.G., Beresford, A., Brookfield, F.A., Brown, C.J., Cardaun, I., Courtney, S.M., Dijkman, U., Hamelin-Flegg, E., Johnson, P.D., Kempf, V., Lyons, K., Matthews, K., Mitchell, W.L., O'Connell, C., Pena, P., Powell, K., Rassoulpour, A., Reed, L., Reindl, W., Selvaratnam, S., Friley, W.W., Weddell, D.A., Went, N.E., Wheelan, P., Winkler, C., Winkler, D., Wityak, J., Yarnold, C.J., Yates, D., Munoz-Sanjuan, I., and Dominguez, C., *Development of a Series of Aryl Pyrimidine Kynurenine Monooxygenase Inhibitors as Potential Therapeutic Agents for the Treatment of Huntington's Disease*. Journal of Medicinal Chemistry, 2015. **58**(3): p. 1159-1183.
50. Hwang, O., *Role of Oxidative Stress in Parkinson's Disease*. Experimental Neurobiology, 2013. **22**(1): p. 11-17.
51. Winklhofer, K.F. and Haass, C., *Mitochondrial dysfunction in Parkinson's disease*. Biochimica et Biophysica Acta (BBA) - Molecular Basis of Disease, 2010. **1802**(1): p. 29-44.
52. Olanow, C.W. and Brundin, P., *Parkinson's disease and alpha synuclein: is parkinson's disease a prion-like disorder?* Movement Disorders, 2013. **28**(1): p. 31-40.
53. Dong, X.-x., Wang, Y., and Qin, Z.-h., *Molecular mechanisms of excitotoxicity and their relevance to pathogenesis of neurodegenerative diseases*. Acta Pharmacologica Sinica, 2009. **30**(4): p. 379-387.
54. Reale, M., Iarlori, C., Thomas, A., Gambi, D., Perfetti, B., Di Nicola, M., and Onofri, M., *Peripheral cytokines profile in Parkinson's disease*. Brain, Behavior, and Immunity, 2009. **23**(1): p. 55-63.
55. Widner, B., Leblhuber, F., and Fuchs, D., *Increased neopterin production and tryptophan degradation in advanced Parkinson's disease*. Journal of Neural Transmission, 2002. **109**(2): p. 181-189.
56. Ogawa, T., Matson, W.R., Beal, M.F., Myers, R.H., Bird, E.D., Milbury, P., and Saso, S., *Kynurenine pathway abnormalities in Parkinson's disease*. Neurology, 1992. **42**(9): p. 1702.
57. Hartai, Z., Klivenyi, P., Janaky, T., Penke, B., Dux, L., and Vecsei, L., *Kynurenine metabolism in plasma and in red blood cells in Parkinson's disease*. Journal of the Neurological Sciences, 2005. **239**(1): p. 31-35.
58. Gulaj, E., Pawlak, K., Bien, B., and Pawlak, D., *Kynurenine and its metabolites in Alzheimer's disease patients*. Advances in Medical Sciences, 2010. **55**(2): p. 204-211.
59. Lee, D.Y., Lee, K.-S., Lee, H.J., Noh, Y.H., Kim, D.H., Lee, J.Y., Cho, S.H., Yoon, O.J., Lee, W.B., Kim, K.Y., Chung, Y.H., and Kim, S.S., *Kynurenic acid attenuates MPP+-induced dopaminergic neuronal cell death via a Bax-mediated mitochondrial pathway*. European Journal of Cell Biology, 2008. **87**(6): p. 389-397.
60. Silva-Adaya, D., Pérez-De La Cruz, V., Villeda-Hernández, J., Carrillo-Mora, P., González-Herrera, I.G., García, E., Colín-Barenque, L., Pedraza-Chaverri, J., and Santamaría, A., *Protective effect of L-kynurenine and probenecid on 6-hydroxydopamine-induced striatal toxicity in rats: Implications of modulating kynurenate as a protective strategy*. Neurotoxicology and Teratology, 2011. **33**(2): p. 303-312.
61. Miranda, A.F., Boegman, R.J., Beninger, R.J., and Jhamandas, K., *Protection against quinolinic acid-mediated excitotoxicity in nigrostriatal dopaminergic neurons by endogenous kynurenic acid*. Neuroscience, 1997. **78**(4): p. 967-975.
62. Beers, D.R., Zhao, W., Liao, B., Kano, O., Wang, J., Huang, A., Appel, S.H., and Henkel, J.S., *Neuroinflammation modulates distinct regional and temporal clinical responses in ALS mice*. Brain Behavior and Immunity, 2011. **25**(5): p. 1025-35.

63. McGeer, P.L. and McGeer, E.G., *Inflammatory processes in amyotrophic lateral sclerosis*. Muscle Nerve, 2002. **26**(4): p. 459-70.
64. Chen, Y. and Guillemin, G.J., *Kynurenine pathway metabolites in humans: disease and healthy States*. International Journal of Tryptophan Research, 2009. **2**: p. 1-19.
65. Chen, Y., Meininger, V., and Guillemin, G.J., *Recent advances in the treatment of amyotrophic lateral sclerosis. Emphasis on kynurenine pathway inhibitors*. Central Nervous System Agents in Medicinal Chemistry, 2009. **9**(1): p. 32-9.
66. Guillemin, G.J., Meininger, V., and Brew, B.J., *Implications for the kynurenine pathway and quinolinic acid in amyotrophic lateral sclerosis (Review)*. Neurodegenerative Diseases, 2006. **2**: p. 166-176.
67. Fukui, S., Schwarcz, R., Rapoport, S.I., Takada, Y., and Smith, Q.R., *Blood-brain barrier transport of kynurenines: implications for brain synthesis and metabolism*. Journal of Neurochemistry, 1991. **56**(6): p. 2007-2017.
68. Erickson, J.B., Flanagan, E.M., Russo, S., and Reinhard Jr, J.F., *A radiometric assay for kynurenine 3-hydroxylase based on the release of 3H₂O during hydroxylation of l-[3,5-³H]kynurenine*. Analytical Biochemistry, 1992. **205**(2): p. 257-262.
69. Guillemin, G.J., Kerr, S.J., Smythe, G.A., Smith, D.G., Kapoor, V., Armati, P.J., Croitoru, J., and Brew, B.J., *Kynurenine pathway metabolism in human astrocytes: a paradox for neuronal protection*. Journal of Neurochemistry, 2001. **78**(4): p. 842-853.
70. Guillemin, G., Smith, D., Smythe, G., Armati, P., and Brew, G., *Expression of the kynurenine pathway enzymes in human microglia and macrophages*, in *Developments in Tryptophan and Serotonin Metabolism*, G. Allegri, et al., Editors. 2003, Springer US. p. 105-112.
71. Heyes, M., Chen, C., Major, E., and Saito, K., *Different kynurenine pathway enzymes limit quinolinic acid formation by various human cell types*. Biochemical Journal, 1997. **326**: p. 351-356.
72. Rzeski, W., Kocki, T., Dybel, A., Wejksza, K., Zdzisińska, B., Kandefer-Szerszeń, M., Turski, W.A., Okuno, E., and Albrecht, J., *Demonstration of kynurenine aminotransferases I and II and characterization of kynurenine acid synthesis in cultured cerebral cortical neurons*. Journal of Neuroscience Research, 2005. **80**(5): p. 677-682.
73. Guillemin, G.J., Cullen, K.M., Lim, C.K., Smythe, G.A., Garner, B., Kapoor, V., Takikawa, O., and Brew, B.J., *Characterization of the kynurenine pathway in human neurons*. The Journal of Neuroscience, 2007. **27**(47): p. 12884-12892.
74. Hirata, F. and Hayaishi, O., *New degradative routes of 5-hydroxytryptophan and serotonin by intestinal tryptophan 2,3-dioxygenase*. Biochemical and Biophysical Research Communications, 1972. **47**(5): p. 1112-1119.
75. Munn, D.H., Zhou, M., Attwood, J.T., Bondarev, I., Conway, S.J., Marshall, B., Brown, C., and A.L. Mellor, *Prevention of allogeneic fetal rejection by tryptophan catabolism*. Science, 1998. **281**: p. 1191-1193.
76. Muller, A.J., DuHadaway, J.B., Donover, P.S., Sutanto-Ward, E., and Prendergast, G.C., *Inhibition of indoleamine 2,3-dioxygenase, an immunoregulatory target of the cancer suppression gene Bin1, potentiates cancer chemotherapy*. Nature Medicine, 2005. **11**(3): p. 312-319.
77. Haber, R., Bessette, D., Hulihan-Giblin, B., Durcan, M.J., and Goldman, D., *Identification of Tryptophan 2,3-Dioxygenase RNA in Rodent Brain*. Journal of Neurochemistry, 1993. **60**(3): p. 1159-1162.
78. Miller, C.L., Llenos, I.C., Dulay, J.R., Barillo, M.M., Yolken, R.H., and Weis, S., *Expression of the kynurenine pathway enzyme tryptophan 2,3-dioxygenase is increased in the frontal cortex of individuals with schizophrenia*. Neurobiology of Disease, 2004. **15**(3): p. 618-629.
79. Manuelpillai, U., Wallace, E., Nicholls, T., Guillemin, G., Phillips, D., and Walker, D., *Increased mRNA Expression of Kynurenine Pathway Enzymes in Human Placentae Exposed To Bacterial Endotoxin*, in *Developments in Tryptophan and Serotonin Metabolism*, G. Allegri, et al., Editors. 2003, Springer US. p. 85-89.

80. Urata, Y., Koga, K., Hirota, Y., Akiyama, I., Izumi, G., Takamura, M., Nagai, M., Harada, M., Hirata, T., Yoshino, O., Kawana, K., Fujii, T., and Osuga, Y., *IL-18 Increases Expression of Tryptophan 2,3-dioxygenase and Stimulates Tryptophan Catabolism in Endometrioma Stromal Cells*. American Journal of Reproductive Immunology, 2014. **72**(5): p. 496-503.
81. Knox, W.E., *Two Mechanisms which Increase in vivo the Liver Tryptophan Peroxidase Activity: Specific Enzyme Adaptation and Stimulation of the Pituitary-Adrenal System*. British Journal of Experimental Pathology, 1951. **32**(5): p. 462-469.
82. Knox, W.E. and Auerbach, V.H., *The hormonal control of tryptophan peroxidase in the rat*. Journal of Biological Chemistry, 1955. **214**(1): p. 307-313.
83. Bessedé, A., Gargaro, M., Pallotta, M.T., Martino, D., Servillo, G., Brunacci, C., Bicciato, S., Mazza, E.M.C., Macchiarulo, A., Vacca, C., Iannitti, R., Tissi, L., Volpi, C., Belladonna, M.L., Orabona, C., Bianchi, R., Lanz, T.V., Platten, M., Della Fazio, M.A., Piobbico, D., Zelante, T., Funakoshi, H., Nakamura, T., Gilot, D., Denison, M.S., Guillemin, G.J., DuHadaway, J.B., Prendergast, G.C., Metz, R., Geffard, M., Boon, L., Pirro, M., Iorio, A., Veyret, B., Romani, L., Grohmann, U., Fallarino, F., and Puccetti, P., *Aryl hydrocarbon receptor control of a disease tolerance defence pathway*. Nature, 2014. **511**(7508): p. 184-190.
84. Pilotte, L., Larrieu, P., Stroobant, V., Colau, D., Dolušić, E., Frédérick, R., De Plaen, E., Uyttenhove, C., Wouters, J., Masereel, B., and Van den Eynde, B.J., *Reversal of tumoral immune resistance by inhibition of tryptophan 2,3-dioxygenase*. Proceedings of the National Academy of Sciences, 2012. **109**(7): p. 2497-2502.
85. Nguyen, N.T., Nakahama, T., Le, D.H., Le, S.V., Chu, H.H., and Kishimoto, T., *Aryl hydrocarbon receptor and kynurenine: recent advances in autoimmune disease research*. Frontiers in Immunology, 2014. **5**.
86. Julliard, W., Fechner, J.H., and Mezrich, J.D., *The Aryl Hydrocarbon Receptor Meets Immunology: Friend or Foe? A Little of Both*. Frontiers in Immunology, 2014. **5**: p. 458.
87. Noonepalle, S.K.R., Lee, E.J., Ouzounova, M., Kim, J., Choi, J.-H., Shull, A., Pei, L., Kolhe, R., Hsu, P.-Y., Putluri, N., Huang, T.H.-M., Sreekumar, A., Korkaya, H., Munn, D., and Shi, H., *Abstract 4060: Promoter methylation regulates interferon- γ induced indoleamine 2,3-dioxygenase expression in breast cancer*. Cancer Research, 2015. **75**(15 Supplement): p. 4060.
88. D'Angelo, J.A., Mattox, M.L., Fiebiger, E., and Dickinson, B.L., *The Cystine/Glutamate Antiporter Regulates the Functional Expression of Indoleamine 2,3-Dioxygenase in Human Dendritic Cells*. Scandinavian Journal of Immunology, 2012. **76**(4): p. 448-449.
89. Mattox, M.L., D'Angelo, J.A., and Dickinson, B.L., *Redox Control of Indoleamine 2,3-Dioxygenase Expression and Activity in Human Monocyte-Derived Dendritic Cells is Independent of Changes in Oxygen Tension*. Scandinavian Journal of Immunology, 2014. **79**(5): p. 325-332.
90. Ball, H.J., Sanchez-Perez, A., Weiser, S., Austin, C.J.D., Astelbauer, F., Miu, J., McQuillan, J.A., Stocker, R., Jermini, L.S., and Hunt, N.H., *Characterization of an indoleamine 2,3-dioxygenase-like protein found in humans and mice*. Gene, 2007. **396**(1): p. 203-213.
91. Metz, R., DuHadaway, J.B., Kamasani, U., Laury-Kleintop, L., Muller, A.J., and Prendergast, G.C., *Novel Tryptophan Catabolic Enzyme IDO2 Is the Preferred Biochemical Target of the Antitumor Indoleamine 2,3-Dioxygenase Inhibitory Compound D-1-Methyl-Tryptophan*. Cancer Research, 2007. **67**(15): p. 7082-7087.
92. Prendergast, G., Metz, R., Muller, A.J., Merlo, L.M.F., and Mandik-Nayak, L., *IDO2 in immunomodulation and autoimmunity*. Frontiers in Immunology, 2014. **5**(DOI: 10.3389/fimmu.2014.00585).
93. Metz, R., Smith, C., DuHadaway, J.B., Chandler, P., Baban, B., Merlo, L.M.F., Pigott, E., Keough, M.P., Rust, S., Mellor, A.L., Mandik-Nayak, L., Muller, A.J., and Prendergast, G.C., *IDO2 is critical for IDO1-mediated T-cell regulation and exerts a non-redundant function in inflammation*. International Immunology, 2014. **26**(7): p. 357-367.

94. Löb, S., Königsrainer, A., Zieker, D., Brücher, B., Rammensee, H.-G., Opelz, G., and Terness, P., *IDO1 and IDO2 are expressed in human tumors: levo- but not dextro-1-methyl tryptophan inhibits tryptophan catabolism*. *Cancer Immunology, Immunotherapy*, 2009. **58**(1): p. 153-157.
95. Sørensen, R.B., Kølsgaard, T., Andersen, R.S., van den Berg, J.H., Svane, I.M., Straten, P.t., and Andersen, M.H., *Spontaneous Cytotoxic T-Cell Reactivity against Indoleamine 2,3-Dioxygenase-2*. *Cancer Research*, 2011. **71**(6): p. 2038-2044.
96. Witkiewicz, A.K., Costantino, C.L., Metz, R., Muller, A.J., Prendergast, G.C., Yeo, C.J., and Brody, J.R., *Genotyping and Expression Analysis of IDO2 in Human Pancreatic Cancer: A Novel, Active Target*. *Journal of the American College of Surgeons*, 2009. **208**(5): p. 781-787.
97. Lo, B.K.K., Jalili, R.B., Zloty, D., Ghahary, A., Cowan, B., Dutz, J.P., Carr, N., Shapiro, J., and McElwee, K.J., *CXCR3 ligands promote expression of functional indoleamine 2,3-dioxygenase in basal cell carcinoma keratinocytes*. *British Journal of Dermatology*, 2011. **165**(5): p. 1030-1036.
98. Trabanelli, S., Očadlíková, D., Ciciarello, M., Salvestrini, V., Lecciso, M., Jandus, C., Metz, R., Evangelisti, C., Laury-Kleintop, L., Romero, P., Prendergast, G.C., Curti, A., and Lemoli, R.M., *The SOCS3-Independent Expression of IDO2 Supports the Homeostatic Generation of T Regulatory Cells by Human Dendritic Cells*. *The Journal of Immunology*, 2014. **192**(3): p. 1231-1240.
99. Ball, H.J., Jusof, F.F., Bakmiwewa, S.M., Hunt, N.H., and Yuasa, H., *Tryptophan catabolizing enzymes – party of three*. *Frontiers in Immunology*, 2014. **5**(DOI: 10.3389/fimmu.2014.00485).
100. Fukunaga, M., Yamamoto, Y., Kawasoe, M., Arioka, Y., Murakami, Y., Hoshi, M., and Saito, K., *Studies on Tissue and Cellular Distribution of Indoleamine 2,3-Dioxygenase 2: The Absence of IDO1 Upregulates IDO2 Expression in the Epididymis*. *Journal of Histochemistry and Cytochemistry*, 2012. **60**(11): p. 854-860.
101. Hahn, M.E., *Aryl hydrocarbon receptors: diversity and evolution*. *Chemico-Biological Interactions*, 2002. **141**(1–2): p. 131-160.
102. Manchester, D.K., Gordon, S.K., Golas, C.L., Roberts, E.A., and Okey, A.B., *Ah Receptor in Human Placenta: Stabilization by Molybdate and Characterization of Binding of 2,3,7,8-Tetrachlorodibenzo-p-dioxin, 3-Methylcholanthrene, and Benzo(a)pyrene*. *Cancer Research*, 1987. **47**(18): p. 4861-4868.
103. Dolwick, K.M., Schmidt, J.V., Carver, L.A., Swanson, H.I., and Bradfield, C.A., *Cloning and expression of a human Ah receptor cDNA*. *Molecular Pharmacology*, 1993. **44**(5): p. 911-917.
104. Jiang, Y.-z., Wang, K., Fang, R., and Zheng, J., *Expression of Aryl Hydrocarbon Receptor in Human Placentas and Fetal Tissues*. *Journal of Histochemistry & Cytochemistry*, 2010. **58**(8): p. 679-685.
105. Cox, M.B. and Miller, C.A., *Cooperation of heat shock protein 90 and p23 in aryl hydrocarbon receptor signaling*. *Cell Stress & Chaperones*, 2004. **9**(1): p. 4-20.
106. Ikuta, T., Kobayashi, Y., and Kawajiri, K., *Phosphorylation of nuclear localization signal inhibits the ligand-dependent nuclear import of aryl hydrocarbon receptor*. *Biochemical and Biophysical Research Communications*, 2004. **317**(2): p. 545-550.
107. Quintana, F.J. and Sherr, D.H., *Aryl Hydrocarbon Receptor Control of Adaptive Immunity*. *Pharmacological Reviews*, 2013. **65**(4): p. 1148-1161.
108. Fukunaga, B.N., Probst, M.R., Reisz-Porszasz, S., and Hankinson, O., *Identification of Functional Domains of the Aryl Hydrocarbon Receptor*. *Journal of Biological Chemistry*, 1995. **270**(49): p. 29270-29278.
109. Ohtake, F., Fujii-Kuriyama, Y., and Kato, S., *AhR acts as an E3 ubiquitin ligase to modulate steroid receptor functions*. *Biochemical Pharmacology*, 2009. **77**(4): p. 474-484.

110. Ohtake, F., Baba, A., Takada, I., Okada, M., Iwasaki, K., Miki, H., Takahashi, S., Kouzmenko, A., Nohara, K., Chiba, T., Fujii-Kuriyama, Y., and Kato, S., *Dioxin receptor is a ligand-dependent E3 ubiquitin ligase*. *Nature*, 2007. **446**(7135): p. 562-566.
111. Davarinos, N.A. and Pollenz, R.S., *Aryl Hydrocarbon Receptor Imported into the Nucleus following Ligand Binding Is Rapidly Degraded via the Cytosolic Proteasome following Nuclear Export*. *Journal of Biological Chemistry*, 1999. **274**(40): p. 28708-28715.
112. Pollenz, R.S. and Barbour, E.R., *Analysis of the Complex Relationship between Nuclear Export and Aryl Hydrocarbon Receptor-Mediated Gene Regulation*. *Molecular and Cellular Biology*, 2000. **20**(16): p. 6095-6104.
113. Ma, Q. and Baldwin, K.T., *2,3,7,8-Tetrachlorodibenzo-p-dioxin-induced Degradation of Aryl Hydrocarbon Receptor (AhR) by the Ubiquitin-Proteasome Pathway: role of the transcription activation and DNA binding of AhR*. *Journal of Biological Chemistry*, 2000. **275**(12): p. 8432-8438.
114. Murray, I.A., Morales, J.L., Flaveny, C.A., DiNatale, B.C., Chiaro, C., Gowdahalli, K., Amin, S., and Perdew, G.H., *Evidence for Ligand-Mediated Selective Modulation of Aryl Hydrocarbon Receptor Activity*. *Molecular Pharmacology*, 2010. **77**(2): p. 247-254.
115. Vogel, C.F.A., Goth, S.R., Dong, B., Pessah, I.N., and Matsumura, F., *Aryl hydrocarbon receptor signaling mediates expression of indoleamine 2,3-dioxygenase*. *Biochemical and Biophysical Research Communications*, 2008. **375**(3): p. 331-335.
116. Litzenburger, U.M., Opitz, C.A., Sahm, F., Rauschenbach, K.J., Trump, S., Winter, M., Ott, M., Ochs, K., Lutz, C., Liu, X., Anastasov, N., Lehmann, I., Höfer, T., von Deimling, A., Wick, W., and Platten, M., *Constitutive IDO expression in human cancer is sustained by an autocrine signaling loop involving IL-6, STAT3 and the AHR*. *Oncotarget*, 2014. **5**(4): p. 1038-1051.
117. Smith, J.R., Evans, K.J., Wright, A., Willows, R.D., Jamie, J.F., and Griffith, R., *Novel indoleamine 2,3-dioxygenase-1 inhibitors from a multistep in silico screen*. *Bioorganic & Medicinal Chemistry*, 2012. **20**(3): p. 1354-1363.
118. Kumar, S., Malachowski, W.P., DuHadaway, J.B., LaLonde, J.M., Carroll, P.J., Jaller, D., Metz, R., Prendergast, G.C., and Muller, A.J., *Indoleamine 2,3-Dioxygenase Is the Anticancer Target for a Novel Series of Potent Naphthoquinone-Based Inhibitors*. *Journal of Medicinal Chemistry*, 2008. **51**(6): p. 1706-1718.
119. Sugimoto, H., Oda, S.-i., Otsuki, T., Hino, T., Yoshida, T., and Shiro, Y., *Crystal structure of human indoleamine 2,3-dioxygenase: Catalytic mechanism of O₂ incorporation by a heme-containing dioxygenase*. *Proceedings of the National Academy of Sciences*, 2006. **103**(8): p. 2611-2616.
120. Dolusic, E., Larrieu, P., Blanc, S., Sapunaric, F., Norberg, B., Moineaux, L., Colette, D., Stroobant, V., Pilotte, L., Colau, D., Ferain, T., Fraser, G., Galeni, M., Frere, J.-M., Masereel, B., Van den Eynde, B., Wouters, J., and Frederick, R., *Indol-2-yl ethanones as novel indoleamine 2,3-dioxygenase (IDO) inhibitors*. *Bioorganic & Medicinal Chemistry*, 2010. **19**(4): p. 1550-1561.
121. Meininger, D., Zalameda, L., Liu, Y., Stepan, L.P., Borges, L., McCarter, J.D., and Sutherland, C.L., *Purification and kinetic characterization of human indoleamine 2,3-dioxygenases 1 and 2 (IDO1 and IDO2) and discovery of selective IDO1 inhibitors*. *Biochimica et Biophysica Acta (BBA) - Proteins and Proteomics*, 2011. **1814**(12): p. 1947-1954.
122. Pearson, J.T., Siu, S., Meininger, D.P., Wienkers, L.C., and Rock, D.A., *In Vitro Modulation of Cytochrome P450 Reductase Supported Indoleamine 2,3-Dioxygenase Activity by Allosteric Effectors Cytochrome b5 and Methylene Blue*. *Biochemistry*, 2010. **49**(12): p. 2647-2656.
123. Macchiarulo, A., Nuti, R., Bellocchi, D., Camaioni, E., and Pellicciari, R., *Molecular modelling and spatial graining simulations as tools to investigate substrate recognition*,

- enhancer binding and conformational transitions in indoleamine-2,3-dioxygenase (IDO)*. Biochimica et Biophysica Acta, 2007. **1774**: p. 1058-1068.
124. van Berkel, W.J.H., Kamerbeek, N.M., and Fraaije, M.W., *Flavoprotein monooxygenases, a diverse class of oxidative biocatalysts*. J Biotechnol, 2006. **124**(4): p. 670-689.
 125. Breton, J., Avanzi, N., Magagnin, S., Covini, N., Magistrelli, G., Cozzi, L., and Isacchi, A., *Functional characterization and mechanism of action of recombinant human kynurenine 3-hydroxylase*. European Journal of Biochemistry, 2000. **267**(4): p. 1092-1099.
 126. Amaral, M., Levy, C., Heyes, D.J., Lafite, P., Outeiro, T.F., Giorgini, F., Leys, D., and Scrutton, N.S., *Structural basis of kynurenine 3-monooxygenase inhibition*. Nature, 2013. **496**(7445): p. 382-385.
 127. Marielle J. H. Moonen, Marco W. Fraaije, Ivonne M. C. M. Rietjens, Colja Laane, and Berkela, W.J.H.v., *Flavoenzyme-catalyzed oxygenations and oxidations of phenolic compounds*. Advanced Synthesis and Catalysis, 2008. **344**(10): p. 1023-1035.
 128. Crozier-Reabe, K.R., Phillips, R.S., and Moran, G.R., *Kynurenine 3-monooxygenase from Pseudomonas fluorescens: substrate-like inhibitors both stimulate flavin reduction and stabilize the flavin-peroxo intermediate yet result in the production of hydrogen peroxide*. Biochemistry, 2008. **47**(47): p. 12420-12433.
 129. Crozier, K.R. and Moran, G.R., *Heterologous expression and purification of kynurenine-3-monooxygenase from Pseudomonas fluorescens strain 17400*. Protein Expression and Purification, 2007. **51**(2): p. 324-333.
 130. Stephen K. Chapman and Reid, G.A., eds. *Flavoprotein protocols*. Vol. 131. 1999, Humana Press: Totowa, New Jersey, USA.
 131. Montersino, S., Tischler, D., Gassner, G.T., and van Berkel, W.J.H., *Catalytic and structural features of flavoprotein hydroxylases and epoxidases*. Advanced Synthesis & Catalysis, 2011. **353**(13): p. 2301-2319.
 132. Gatti, D., Palfey, B., Lah, M., Entsch, B., Massey, V., Ballou, D., and Ludwig, M., *The mobile flavin of 4-OH benzoate hydroxylase*. Science, 1994. **266**(5182): p. 110-114.
 133. Wilson, K., Mole, D.J., Binnie, M., Homer, N.Z.M., Zheng, X., Yard, B.A., Iredale, J.P., Auer, M., and Webster, S.P., *Bacterial expression of human kynurenine 3-monooxygenase: Solubility, activity, purification*. Protein Expression and Purification, 2014. **95**(0): p. 96-103.
 134. Hirai, K., Kuroyanagi, H., Tatebayashi, Y., Hayashi, Y., Hirabayashi-Takahashi, K., Saito, K., Haga, S., Uemura, T., and Izumi, S., *Dual role of the carboxyl-terminal region of pig liver l-kynurenine 3-monooxygenase: mitochondrial-targeting signal and enzymatic activity*. Journal of Biochemistry, 2010. **148**(6): p. 639-650.
 135. Wonodi, I., McMahon, R.P., Krishna, N., Mitchell, B.D., Liu, J., Glassman, M., Elliot Hong, L., and Gold, J.M., *Influence of kynurenine 3-monooxygenase (KMO) gene polymorphism on cognitive function in schizophrenia*. Schizophrenia Research, 2014. **160**(1-3): p. 80-87.
 136. Lavebratt C, O.S., Backlund L, Frisén L, Sellgren C, Priebe L, Nikamo P, Träskman-Bendz L, Cichon S, Vawter MP, Osby U, Engberg G, Landén M, Erhardt S, Schalling M., *The KMO allele encoding Arg452 is associated with psychotic features in bipolar disorder type 1, and with increased CSF KYNA level and reduced KMO expression*. Molecular psychiatry, 2014. **19**(3): p. 334-341.
 137. Natalini, B., Mattoli, L., Pellicciari, R., Carpenedo, R., Chiarugi, A., and Moroni, F., *Synthesis and activity of enantiopure (S) (m-nitrobenzoyl) alanine, potent kynurenine-3-hydroxylase inhibitor*. Bioorganic & Medicinal Chemistry Letters, 1995. **5**(14): p. 1451-1454.
 138. Carpenedo, R., Chiarugi, A., Russi, P., Lombardi, G., Carl  , V., Pellicciari, R., Mattoli, L., and Moroni, F., *Inhibitors of kynurenine hydroxylase and kynureninase increase cerebral formation of kynurenate and have sedative and anticonvulsant activities*. Neuroscience, 1994. **61**(2): p. 237-244.
 139. Giordani, A., Pevarello, P., Cini, M., Bormetti, R., Greco, F., Toma, S., Speciale, C., and Varasi, M., *4-Phenyl-4-oxo-butanoic acid derivatives inhibitors of kynurenine 3-hydroxylase*. Bioorganic & Medicinal Chemistry Letters, 1998. **8**(20): p. 2907-2912.

140. Varasi, M., Giordani, A., Varello, P., Pellicciari, R., and Speciale, C., *Pharmcia and Upjohn. 2-substituted benzoyl-cycloalkyl-1-carboxylic acid derivatives. International patent Publication Number WO 98/40344.* 1998.
141. Wityak, J., Toledo-Sherman, L., Dominguez, C., Courtney, S., Martin, Yarnold, C., John, Deaguier Pena, P., Scheel, A., and Winkler, D., *CHDI Inc. Certain kynurenine-3-monooxygenase inhibitors, pharmaceutical compositions, and methods of use thereof. International Patent Application Number WO2010/017132.* 2010.
142. Autier, V., Arbellot de Vacqueur, A., Moinet, G., Marais, D., Kargar, C., and Kergot, M., *Merck GMBH. Kynurenine 3-hydroxylase inhibitors for the treatment of diabetes. International patent Publication Number WO2004/060369.* 2004.
143. Autier, V., Fabregue, R., and Miossec, P., *Merck GMBH. Use of 4-oxobutanoic acid derivatives in the treatment of pathologies associated with immunological disorders. International patent Publication Number WO2009/071161.* 2009.
144. Benatti, L., Fariello, R., Salvati, P., Pellicciari, R., and Caccia, C., *Newron Pharmaceuticals. Halothenoil-cyclopropane-1-carboxylic acid derivatives. European Patent Application Number 1 424 333.* 2004.
145. Muchowski, P.J., Muchowski, J.M., schwarcz, R., and Guidetti, P., *Gladstone Institute and University of Maryland. Small molecule inhibitors of kynurenine-3-monooxygenase. Internal patent Publicaton Number WO2008/022281.* 2008.
146. Milne, G., *Inhibition studies of kynurenine 3-monooxygenase* 2013, University of St Andrews, PhD Thesis.
147. Wilkinson, M., *Structural dynamics and ligand binding in kynurenine-3-monooxygenase.* 2013, The University of Edinburgh, PhD Thesis.
148. Heidempergher, F., Pevarello, P., Pillan, A., Pinciroli, V., Della Torre, A., Speciale, C., Marconi, M., Cini, M., Toma, S., Greco, F., and Varasi, M., *Pyrrolo[3,2-c]quinoline derivatives: a new class of kynurenine-3-hydroxylase inhibitors.* *Il Farmaco*, 1999. **54**(3): p. 152-160.
149. Pevarello, P., Varasi, M., Amici, R., Toma, S., and Speciale, C., *Pharmcia and Upjohn. Tricyclic 3-oxo-propanitrile compounds. International patent Publication number WO99/16753.* 1999.
150. Feng, Y., Bowden, B.F., and Kapoor, V., *lanthellamide A, a selective kynurenine-3-hydroxylase inhibitor from the Australian marine sponge lanthella quadrangulata.* *Bioorganic & Medicinal Chemistry Letters*, 2012. **22**(10): p. 3398-3401.
151. Giordani, A., Corti, L., Cini, M., Bormetti, R., Marconi, M., Veneroni, O., Speciale, C., and Varasi, M., eds. *Enantionspecific synthesis and in vitro activity of selective inhibitors of rat brain kynureninase and kynurenine-3-hydroxylase.* 8th ed. Recent advances in tryptophan research, ed. G.A. Filippini. Vol. 398. 1995, Plenum Press: New York. 531-534.
152. Farha, M.A. and Brown, E.D., *Unconventional screening approaches for antibiotic discovery.* *Annals of the New York Academy of Sciences*, 2015. **1354**(1): p. 54-66.
153. Emanuele, A.A., Adams, N.E., Chen, Y.-C., Maurelli, A.T., and Garcia, G.A., *Potential Novel Antibiotics from HTS Targeting the Virulence-regulating Transcription Factor, VirF, from Shigella flexneri.* *The Journal of Antibiotics*, 2014. **67**(5): p. 379-386.
154. Lewis, K., *Platforms for antibiotic discovery.* *Nat Rev Drug Discov*, 2013. **12**(5): p. 371-387.
155. Mishra, A., Dobritsa, S.V., Crouch, M.-L., Rabenstein, J., Lee, J.X.Y., and Dhakshinamoorthy, S., *Establishment and validation of a 384-well antibacterial assay amenable for high-throughput screening and combination testing.* *Journal of Microbiological Methods*, 2015. **118**: p. 173-175.
156. Foloppe, N., Fisher, L.M., Howes, R., Potter, A., Robertson, A.G.S., and Surgenor, A.E., *Identification of chemically diverse Chk1 inhibitors by receptor-based virtual screening.* *Bioorganic & Medicinal Chemistry*, 2006. **14**(14): p. 4792-4802.
157. Shoichet, B.K., McGovern, S.L., Wei, B., and Irwin, J.J., *Lead discovery using molecular docking.* *Current Opinion in Chemical Biology*, 2002. **6**(4): p. 439-446.

158. Pouliot, M. and Jeanmart, S., *Pan Assay Interference Compounds (PAINS) and Other Promiscuous Compounds in Antifungal Research*. Journal of Medicinal Chemistry, 2016. **59**(2): p. 497-503.
159. Feng, B.Y., Shelat, A., Doman, T.N., Guy, R.K., and Shoichet, B.K., *High-throughput assays for promiscuous inhibitors*. Nature Chemical Biology, 2005. **1**(3): p. 146-148.
160. Feng, B.Y. and Shoichet, B.K., *A detergent-based assay for the detection of promiscuous inhibitors*. Nat. Protocols, 2006. **1**(2): p. 550-553.
161. Davies, J.W., Glick, M., and Jenkins, J.L., *Streamlining lead discovery by aligning in silico and high-throughput screening*. Current Opinion in Chemical Biology, 2006. **10**(4): p. 343-351.
162. Sheridan, R.P., Miller, M.D., Underwood, D.J., and Kearsley, S.K., *Chemical Similarity Using Geometric Atom Pair Descriptors*. Journal of Chemical Information and Computer Sciences, 1996. **36**(1): p. 128-136.
163. Stoddart, E.S., Senadheera, S., MacDougall, I.J.A., Griffith, R., and Finch, A.M., *A Novel Structural Framework for α 1A/D Adrenoceptor Selective Antagonists Identified Using Subtype Selective Pharmacophores*. PLoS ONE, 2011. **6**(5): p. e19695.
164. Drwal, M.N., Agama, K., Wakelin, L.P.G., Pommier, Y., and Griffith, R., *Exploring DNA Topoisomerase I Ligand Space in Search of Novel Anticancer Agents*. PLoS ONE, 2011. **6**(9): p. e25150.
165. Durant, J.L., Leland, B.A., Henry, D.R., and Nourse, J.G., *Reoptimization of MDL Keys for Use in Drug Discovery*. Journal of Chemical Information and Computer Sciences, 2002. **42**(6): p. 1273-1280.
166. Friedrich, L., Rodrigues, T., Neuhaus, C.S., Schneider, P., and Schneider, G., *From Complex Natural Products to Simple Synthetic Mimetics by Computational De Novo Design*. Angewandte Chemie International Edition, 2016. **55**(23): p. 6789-6792.
167. Kalinski, C., Umkehrer, M., Weber, L., Kolb, J., Burdack, C., and Ross, G., *On the industrial applications of MCRs: molecular diversity in drug discovery and generic drug synthesis*. Molecular Diversity, 2010. **14**(3): p. 513-522.
168. Schneider, P., Rothlisberger, M., Reker, D., and Schneider, G., *Spotting and designing promiscuous ligands for drug discovery*. Chemical Communications, 2016. **52**(6): p. 1135-1138.
169. Awale, M. and Reymond, J.-L., *Atom Pair 2D-Fingerprints Perceive 3D-Molecular Shape and Pharmacophores for Very Fast Virtual Screening of ZINC and GDB-17*. Journal of Chemical Information and Modeling, 2014. **54**(7): p. 1892-1907.
170. Xiao, Z., Varma, S., Xiao, Y.-D., and Tropsha, A., *Modeling of p38 mitogen-activated protein kinase inhibitors using the Catalyst™ HypoGen and k-nearest neighbor QSAR methods*. Journal of Molecular Graphics and Modelling, 2004. **23**(2): p. 129-138.
171. Debnath, A.K., *Generation of Predictive Pharmacophore Models for CCR5 Antagonists: Study with Piperidine- and Piperazine-Based Compounds as a New Class of HIV-1 Entry Inhibitors*. Journal of Medicinal Chemistry, 2003. **46**(21): p. 4501-4515.
172. John, S., Thangapandian, S., Arooj, M., Hong, J.C., Kim, K.D., and Lee, K.W., *Development, evaluation and application of 3D QSAR Pharmacophore model in the discovery of potential human renin inhibitors*. BMC Bioinformatics, 2011. **12**(14): p. S4.
173. Halgren, T.A. and Damm, W., *Polarizable force fields*. Current Opinion in Structural Biology, 2001. **11**(2): p. 236-242.
174. Bjerrum, E.J., *Machine learning optimization of cross docking accuracy*. Computational Biology and Chemistry, 2016. **62**: p. 133-144.
175. Guha, R. and Van Drie, J.H., *Structure-Activity Landscape Index: Identifying and Quantifying Activity Cliffs*. Journal of Chemical Information and Modeling, 2008. **48**(3): p. 646-658.

176. Kokh, D.B., Wade, R.C., and Wenzel, W., *Receptor flexibility in small-molecule docking calculations*. Wiley Interdisciplinary Reviews: Computational Molecular Science, 2011. **1**(2): p. 298-314.
177. Best, R.B., Lindorff-Larsen, K., DePristo, M.A., and Vendruscolo, M., *Relation between native ensembles and experimental structures of proteins*. Proceedings of the National Academy of Sciences, 2006. **103**(29): p. 10901-10906.
178. Verkhivker, G.M., Bouzida, D., Gehlhaar, D.K., Rejto, P.A., Freer, S.T., and Rose, P.W., *Complexity and simplicity of ligand-macromolecule interactions: the energy landscape perspective*. Current Opinion in Structural Biology, 2002. **12**(2): p. 197-203.
179. Hammes, G.G., Chang, Y.-C., and Oas, T.G., *Conformational selection or induced fit: A flux description of reaction mechanism*. Proceedings of the National Academy of Sciences, 2009. **106**(33): p. 13737-13741.
180. Boehr, D.D., Nussinov, R., and Wright, P.E., *The role of dynamic conformational ensembles in biomolecular recognition*. Nature Chemical Biology, 2009. **5**(11): p. 789-796.
181. Henzler-Wildman, K.A., Thai, V., Lei, M., Ott, M., Wolf-Watz, M., Fenn, T., Pozharski, E., Wilson, M.A., Petsko, G.A., Karplus, M., Hubner, C.G., and Kern, D., *Intrinsic motions along an enzymatic reaction trajectory*. Nature, 2007. **450**(7171): p. 838-844.
182. Zhang, Q., Stelzer, A.C., Fisher, C.K., and Al-Hashimi, H.M., *Visualizing spatially correlated dynamics that directs RNA conformational transitions*. Nature, 2007. **450**(7173): p. 1263-1267.
183. Schotte, F., Lim, M., Jackson, T.A., Smirnov, A.V., Soman, J., Olson, J.S., Phillips, G.N., Wulff, M., and Anfinrud, P.A., *Watching a Protein as it Functions with 150-ps Time-Resolved X-ray Crystallography*. Science, 2003. **300**(5627): p. 1944.
184. Csermely, P., Palotai, R., and Nussinov, R., *Induced fit, conformational selection and independent dynamic segments: an extended view of binding events*. Trends in Biochemical Sciences, 2010. **35**(10): p. 539-546.
185. James, L.C. and Tawfik, D.S., *Structure and kinetics of a transient antibody binding intermediate reveal a kinetic discrimination mechanism in antigen recognition*. Proceedings of the National Academy of Sciences of the United States of America, 2005. **102**(36): p. 12730-12735.
186. Boehr, D.D., McElheny, D., Dyson, H.J., and Wright, P.E., *Millisecond timescale fluctuations in dihydrofolate reductase are exquisitely sensitive to the bound ligands*. Proceedings of the National Academy of Sciences, 2010. **107**(4): p. 1373-1378.
187. Weikl, T.R. and von Deuster, C., *Selected-fit versus induced-fit protein binding: Kinetic differences and mutational analysis*. Proteins: Structure, Function, and Bioinformatics, 2009. **75**(1): p. 104-110.
188. Claußen, H., Buning, C., Rarey, M., and Lengauer, T., *FlexE: efficient molecular docking considering protein structure variations1*. Journal of Molecular Biology, 2001. **308**(2): p. 377-395.
189. Polgár, T. and Keserü, G.M., *Ensemble Docking into Flexible Active Sites. Critical Evaluation of FlexE against JNK-3 and β -Secretase*. Journal of Chemical Information and Modeling, 2006. **46**(4): p. 1795-1805.
190. Houston, D.R. and Walkinshaw, M.D., *Consensus Docking: Improving the Reliability of Docking in a Virtual Screening Context*. Journal of Chemical Information and Modeling, 2013. **53**(2): p. 384-390.
191. Hartmann, C., Antes, I., and Lengauer, T., *Docking and scoring with alternative side-chain conformations*. Proteins: Structure, Function, and Bioinformatics, 2009. **74**(3): p. 712-726.
192. Whalen, K.L., Chang, K.M., and Spies, M.A., *Hybrid Steered Molecular Dynamics-Docking: An Efficient Solution to the Problem of Ranking Inhibitor Affinities Against a Flexible Drug Target*. Molecular informatics, 2011. **30**(5): p. 459-471.

193. Tatsumi, R., Fukunishi, Y., and Nakamura, H., *A hybrid method of molecular dynamics and harmonic dynamics for docking of flexible ligand to flexible receptor*. Journal of Computational Chemistry, 2004. **25**(16): p. 1995-2005.
194. Labute, P., *LowModeMD—Implicit Low-Mode Velocity Filtering Applied to Conformational Search of Macrocycles and Protein Loops*. Journal of Chemical Information and Modeling, 2010. **50**(5): p. 792-800.
195. Austin, C.J.D., Kahlert, J., Issa, F., Reed, J.H., Smith, J.R., Ioppolo, J.A., Ong, J.A., Jamie, J.F., Hibbs, D., and Rendina, L.M., *The first indoleamine-2,3-dioxygenase-1 (IDO1) inhibitors containing carborane*. Dalton Transactions, 2014. **43**(28): p. 10719-10724.
196. *MOE technical documentation (v2014.0901)*, Chemical Computing Group. 2014.
197. Collingridge, D.S., *A Primer on Quantitized Data Analysis and Permutation Testing*. Journal of Mixed Methods Research, 2013. **7**(1): p. 81-97.
198. Rueda, M. and Abagyan, R., *Best Practices in Docking and Activity Prediction*. bioRxiv, 2016. 10.1101/039446.
199. McGann, M., Nicholls, A., and Enyedy, I., *The statistics of virtual screening and lead optimization*. Journal of Computer-Aided Molecular Design, 2015. **29**(10): p. 923-936.
200. http://www.daylight.com/dayhtml_tutorials/languages/smarts/index.html#INTRO. Last accessed 24/11/2011; Available from: <http://www.daylight.com/dayhtml/doc/theory/theory.smarts.html>.
201. Mole, D.J., Webster, S.P., Uings, I., Zheng, X., Binnie, M., Wilson, K., Hutchinson, J.P., Mirguet, O., Walker, A., Beaufils, B., Ancellin, N., Trottet, L., Beneton, V., Mowat, C.G., Wilkinson, M., Rowland, P., Haslam, C., McBride, A., Homer, N.Z.M., Baily, J.E., Sharp, M.G.F., Garden, O.J., Hughes, J., Howie, S.E.M., Holmes, D.S., Liddle, J., and Iredale, J.P., *Kynurenine-3-monooxygenase inhibition prevents multiple organ failure in rodent models of acute pancreatitis*. Nature Medicine, 2016. **22**(2): p. 202-209.
202. Tidten-Luksch, N., Grimaldi, R., Torrie, L.S., Frearson, J.A., Hunter, W.N., and Brenk, R., *IspE Inhibitors Identified by a Combination of In Silico and In Vitro High-Throughput Screening*. PLoS ONE, 2012. **7**(4): p. e35792.
203. Chen, D., Ranganathan, A., Ijzerman, A.P., Siegal, G., and Carlsson, J., *Complementarity between in Silico and Biophysical Screening Approaches in Fragment-Based Lead Discovery against the A2A Adenosine Receptor*. Journal of Chemical Information and Modeling, 2013. **53**(10): p. 2701-2714.
204. Mitra, I., Saha, A., and Roy, K., *Predictive Modeling of Antioxidant Coumarin Derivatives Using Multiple Approaches: Descriptor-Based QSAR, 3D-Pharmacophore Mapping, and HQSAR*. Scientia Pharmaceutica, 2013. **81**(1): p. 57-80.
205. Ekins, S., Bravi, G., Ring, B.J., Gillespie, T.A., Gillespie, J.S., Vandenbranden, M., Wrighton, S.A., and Wikel, J.H., *Three-Dimensional Quantitative Structure Activity Relationship Analyses of Substrates for CYP2B6*. Journal of Pharmacology and Experimental Therapeutics, 1999. **288**(1): p. 21-29.
206. Rao, S., Aoyama, R., Schrag, M., Trager, W.F., Rettie, A., and Jones, J.P., *A Refined 3-Dimensional QSAR of Cytochrome P450 2C9: Computational Predictions of Drug Interactions*. Journal of Medicinal Chemistry, 2000. **43**(15): p. 2789-2796.
207. Da, C., Mooberry, S.L., Gupton, J.T., and Kellogg, G.E., *How to Deal with Low-Resolution Target Structures: Using SAR, Ensemble Docking, Hydropathic Analysis, and 3D-QSAR to Definitively Map the α -Tubulin Colchicine Site*. Journal of Medicinal Chemistry, 2013. **56**(18): p. 7382-7395.
208. Sun, X.-q., Chen, L., Li, Y.-z., Li, W.-h., Liu, G.-x., Tu, Y.-q., and Tang, Y., *Structure-based ensemble-QSAR model: a novel approach to the study of the EGFR tyrosine kinase and its inhibitors*. Acta Pharmacol Sin, 2014. **35**(2): p. 301-310.
209. Ahmed, N.S., Ali, A.H., El-Nashar, S.M., Gary, B.D., Fajardo, A.M., Tinsley, H.N., Piazza, G.A., Negri, M., and Abadi, A.H., *Exploring the PDE5 H-pocket by ensemble docking and*

- structure-based design and synthesis of novel β -carboline derivatives*. *European Journal of Medicinal Chemistry*, 2012. **57**: p. 329-343.
210. Rosell, F.I., Kuo, H.H., and Mauk, A.G., *NADH Oxidase Activity of Indoleamine 2,3-Dioxygenase*. *Journal of Biological Chemistry*, 2011. **286**(33): p. 29273-29283.
 211. Capece, L., Lewis-Ballester, A., Yeh, S.-R., Estrin, D.A., and Marti, M.A., *Complete Reaction Mechanism of Indoleamine 2,3-Dioxygenase as Revealed by QM/MM Simulations*. *The Journal of Physical Chemistry B*, 2011. **116**(4): p. 1401-1413.
 212. Lewis-Ballester, A., Batabyal, D., Egawa, T., Lu, C., Lin, Y., Marti, M.A., Capece, L., Estrin, D.A., and Yeh, S.R., *Evidence for a ferryl intermediate in a heme-based dioxygenase*. *Proceedings of the National Academy of Sciences*, 2009. **106**(41): p. 17371-17376.
 213. Sono, M., Taniguchi, T., Watanabe, Y., and Hayaishi, O., *Indoleamine 2,3-dioxygenase. Equilibrium studies of the tryptophan binding to the ferric, ferrous, and CO-bound enzymes*. *Journal of Biological Chemistry*, 1980. **255**(4): p. 1339-45.
 214. Sono, M., *The roles of superoxide anion and methylene blue in the reductive activation of indoleamine 2,3-dioxygenase by ascorbic acid or by xanthine oxidase-hypoxanthine*. *Journal of Biological Chemistry*, 1989. **264**(3): p. 1616-1622.
 215. Vottero, E., Mitchell, D.A., Page, M.J., MacGillivray, R.T.A., Sadowski, I.J., Roberge, M., and Mauk, A.G., *Cytochrome b5 is a major reductant in vivo of human indoleamine 2,3-dioxygenase expressed in yeast*. *FEBS Letters*, 2006. **580**(9): p. 2265-2268.
 216. Tojo, S., Kohno, T., Tanaka, T., Kamioka, S., Ota, Y., Ishii, T., Kamimoto, K., Asano, S., and Isobe, Y., *Crystal Structures and Structure–Activity Relationships of Imidazothiazole Derivatives as IDO1 Inhibitors*. *ACS Medicinal Chemistry Letters*, 2014. **5**(10): p. 1119-1123.
 217. Peng, Y.-H., Ueng, S.-H., Tseng, C.-T., Hung, M.-S., Song, J.-S., Wu, J.-S., Liao, F.-Y., Fan, Y.-S., Wu, M.-H., Hsiao, W.-C., Hsueh, C.-C., Lin, S.-Y., Cheng, C.-Y., Tu, C.-H., Lee, L.-C., Cheng, M.-F., Shia, K.-S., Shih, C., and Wu, S.-Y., *Important Hydrogen Bond Networks in Indoleamine 2,3-Dioxygenase 1 (IDO1) Inhibitor Design Revealed by Crystal Structures of Imidazoleisindole Derivatives with IDO1*. *Journal of Medicinal Chemistry*, 2016. **59**(1): p. 282-293.
 218. Horitani, M., Kometani, E., Vottero, E., Otsuki, T., Shiro, Y., and Sugimoto, H., *Conformation and Mobility of Active Site Loop is Critical for Substrate Binding and Inhibition in Human Indoleamine 2,3-Dioxygenase* (Unpublished results) DOI:10.2210/pdb4u72/pdb, 2014.
 219. Kolawole, A.O., Hixon, B.P., Dameron, L.S., Chrisman, I.M., and Smirnov, V.V., *Catalytic activity of human indoleamine 2,3-dioxygenase (hIDO1) at low oxygen*. *Archives of Biochemistry and Biophysics*, 2015. **570**: p. 47-57.
 220. Álvarez, L., Lewis-Ballester, A., Roitberg, A., Estrin, D.A., Yeh, S.-R., Marti, M.A., and Capece, L., *Structural Study of a Flexible Active Site Loop in Human Indoleamine 2,3-Dioxygenase and Its Functional Implications*. *Biochemistry*, 2016. **55**(19): p. 2785-2793.
 221. Camp, J.V., Svensson, T.L., McBrayer, A., Jonsson, C.B., Liljeström, P., and Bruder, C.E., *De-Novo Transcriptome Sequencing of a Normalized cDNA Pool from Influenza Infected Ferrets*. *PLoS ONE*, 2012. **7**(5): p. e37104.
 222. Littlejohn, T.K., Takikawa, O., Skylas, D., Jamie, J.F., Walker, M.J., and Truscott, R.J.W., *Expression and Purification of Recombinant Human Indoleamine 2,3-Dioxygenase*. *Protein Expression and Purification*, 2000. **19**(1): p. 22-29.
 223. Austin, C.J.D., Mizdrak, J., Matin, A., Sirijovski, N., Kosim-Satyaputra, P., Willows, R.D., Roberts, T.H., Truscott, R.J.W., Polekhina, G., Parker, M.W., and Jamie, J.F., *Optimised expression and purification of recombinant human indoleamine 2,3-dioxygenase*. *Protein Expression and Purification*, 2004. **37**(2): p. 392-398.
 224. Efimov, I., Basran, J., Sun, X., Chauhan, N., Chapman, S.K., Mowat, C.G., and Raven, E.L., *The Mechanism of Substrate Inhibition in Human Indoleamine 2,3-Dioxygenase*. *Journal of the American Chemical Society*, 2012. **134**(6): p. 3034-3041.

225. Gibson, D.G., Young, L., Chuang, R.-Y., Venter, J.C., Hutchison, C.A., and Smith, H.O., *Enzymatic assembly of DNA molecules up to several hundred kilobases*. Nature Methods, 2009. **6**: p. 343-345.
226. Hayashi, S., Omata, Y., Sakamoto, H., Hara, T., and Noguchi, M., *Purification and characterization of a soluble form of rat liver NADPH-cytochrome P-450 reductase highly expressed in Escherichia coli*. Protein Expression and Purification, 2003. **29**(1): p. 1-7.
227. Beck von Bodman, S., Schuler, M., Jollie, D., and Sligar, S.G., *synthesis, bacterial expression and mutagenesis of the gene coding for mammalian cytochrome b5*. Proceedings of the National Academy of Sciences, 1986. **83**(24): p. 9443-9447.
228. Goldman, B.S., Gabbert, K.K., and Kranz, R.G., *Use of heme reporters for studies of cytochrome biosynthesis and heme transport*. Journal of Bacteriology, 1996. **178**(21): p. 6338-47.
229. Mizrahi, D., Chen, Y., Liu, J., Peng, H.-M., Ke, A., Pollack, L., Turner, R.J., Auchus, R.J., and DeLisa, M.P., *Making water-soluble integral membrane proteins in vivo using an amphipathic protein fusion strategy*. Nature Communications, 2015. **6**.
230. Pandey, A.V. and Flück, C.E., *NADPH P450 oxidoreductase: Structure, function, and pathology of diseases*. Pharmacology & Therapeutics, 2013. **138**(2): p. 229-254.
231. Honsho, M., Mitoma, J.-y., and Ito, A., *Retention of Cytochrome b 5 in the Endoplasmic Reticulum Is Transmembrane and Luminal Domain-dependent*. Journal of Biological Chemistry, 1998. **273**(33): p. 20860-20866.
232. ITO, A., *Cytochrome b5-like Hemoprotein of Outer Mitochondrial Membrane; OM Cytochrome b II. Contribution of OM Cytochrome b to Rotenone-Insensitive NADH-cytochrome c Reductase Activity*. Journal of Biochemistry, 1980. **87**(1): p. 73-80.
233. Haniu, M., McManus, M.E., Birkett, D.J., Lee, T.D., and Shively, J.E., *Structural and functional analysis of NADPH-cytochrome P-450 reductase from human liver: complete sequence of human enzyme and NADPH-binding sites*. Biochemistry, 1989. **28**(21): p. 8639-8645.
234. Hill, W.E. and Carlisle, C.L., *Loss of plasmids during enrichment for Escherichia coli*. Applied and Environmental Microbiology, 1981. **41**(4): p. 1046-1048.
235. Camps, M., *Modulation of ColE1-like Plasmid Replication for Recombinant Gene Expression*. Recent patents on DNA & gene sequences, 2010. **4**(1): p. 58-73.
236. Million-Weaver, S., Alexander, D.L., Allen, J.M., and Camps, M., *Methods for quantifying plasmid copy number to investigate plasmid dosage effects associated with directed protein evolution*. Methods in molecular biology (Clifton, N.J.), 2012. **834**: p. 33-48.
237. Lin-Chao, S., Chen, W.-T., and Wong, T.-T., *High copy number of the pUC plasmid results from a Rom/Rop-suppressible point mutation in RNA II*. Molecular Microbiology, 1992. **6**(22): p. 3385-3393.
238. Austin, C.J.D., Kosim-Satyaputra, P., Smith, J.R., Willows, R.D., and Jamie, J.F., *Mutation of cysteine residues alters the heme-binding pocket of indoleamine 2,3-dioxygenase-1*. Biochemical and Biophysical Research Communications, 2013. **436**(4): p. 595-600.
239. Austin, C., Astelbauer, F., Kosim-Satyaputra, P., Ball, H., Willows, R., Jamie, J., and Hunt, N., *Mouse and human indoleamine 2,3-dioxygenase display some distinct biochemical and structural properties*. Amino Acids, 2009. **36**(1): p. 99-106.
240. Poljak, A., Grant, R., Austin, C.J.D., Jamie, J.F., Willows, R.D., Takikawa, O., Littlejohn, T.K., Truscott, R.J.W., Walker, M.J., Sachdev, P., and Smythe, G.A., *Inhibition of indoleamine 2,3 dioxygenase activity by H2O2*. Archives of Biochemistry and Biophysics, 2006. **450**(1): p. 9-19.
241. Kosim-Satyaputra, P., *Recombinant human indoleamine 2,3-dioxygenase*. 2009, Macquarie University, PhD Thesis.
242. Smith, J.R., *Indoleamine 2,3-dioxygenase 1: mapping the active site and discovery of novel inhibitors*. 2012, Macquarie University, MPhil Thesis.

243. Navarro Llorens, J.M., Tormo, A., and Martínez-García, E., *Stationary phase in gram-negative bacteria*. FEMS Microbiology Reviews, 2010. **34**(4): p. 476-495.
244. Samelson-Jones, B.J. and Yeh, S.-R., *Interactions between Nitric Oxide and Indoleamine 2,3-Dioxygenase*. Biochemistry, 2006. **45**(28): p. 8527-8538.
245. Hucke, C., MacKenzie, C.R., Adjogble, K.D.Z., Takikawa, O., and Däubener, W., *Nitric Oxide-Mediated Regulation of Gamma Interferon-Induced Bacteriostasis: Inhibition and Degradation of Human Indoleamine 2,3-Dioxygenase*. Infection and Immunity, 2004. **72**(5): p. 2723-2730.
246. Bednarska, N.G., Schymkowitz, J., Rousseau, F., and Van Eldere, J., *Protein aggregation in bacteria: the thin boundary between functionality and toxicity*. Microbiology, 2013. **159**(9): p. 1795-1806.
247. Sowell, S.M., Norbeck, A.D., Lipton, M.S., Nicora, C.D., Callister, S.J., Smith, R.D., Barofsky, D.F., and Giovannoni, S.J., *Proteomic Analysis of Stationary Phase in the Marine Bacterium "Candidatus Pelagibacter ubique"*. Applied and Environmental Microbiology, 2008. **74**(13): p. 4091-4100.
248. Woodard, S.I. and Dailey, H.A., *Regulation of Heme Biosynthesis in Escherichia coli*. Archives of Biochemistry and Biophysics, 1995. **316**(1): p. 110-115.
249. Austin, C., *Structure and ligand based investigations of indoleamine 2,3-dioxygenase*. 2005, Macquarie University, PhD Thesis.
250. Studier, F.W., *Protein production by auto-induction in high-density shaking cultures*. Protein Expression and Purification, 2005. **41**(1): p. 207-234.
251. Nienhaus, K. and Nienhaus, G.U., *Probing heme protein-ligand interactions by UV/visible absorption spectroscopy*, in *Protein-ligand interactions*, G.U. Nienhaus, Editor. 2005, Humana Press: Totowa, NJ, USA. p. 215-241.
252. Giovannetti, R., *The use of spectrophotometry UV-Vis for the study of porphyrins*, in *Macro to nano spectroscopy*, J. Uddin, Editor. 2012, InTech: Rijeka, Croatia. p. 87-108.
253. Sono, M., *Spectroscopic and equilibrium studies of ligand and organic substrate binding to indoleamine 2,3-dioxygenase*. Biochemistry, 1990. **29**(6): p. 1451-1460.
254. Papadopoulou, N.D., Mewies, M., McLean, K.J., Seward, H.E., Svistunenko, D.A., Munro, A.W., and Raven, E.L., *Redox and Spectroscopic Properties of Human Indoleamine 2,3-Dioxygenase and a His303Ala Variant: Implications for Catalysis*. Biochemistry, 2005. **44**(43): p. 14318-14328.
255. Vermilion, J.L. and Coon, M.J., *Identification of the high and low potential flavins of liver microsomal NADPH-cytochrome P-450 reductase*. Journal of Biological Chemistry, 1978. **253**(24): p. 8812-8819.
256. Wang, M., Roberts, D.L., Paschke, R., Shea, T.M., Masters, B.S.S., and Kim, J.-J.P., *Three-dimensional structure of NADPH-cytochrome P450 reductase: Prototype for FMN- and FAD-containing enzymes*. Proceedings of the National Academy of Sciences of the United States of America, 1997. **94**(16): p. 8411-8416.
257. Bacher, A., Eberhardt, S., Fischer, M., Kis, K., and Richter, G., *Biosynthesis of vitamin B12 (riboflavin)*. Annual Review of Nutrition, 2000. **20**(1): p. 153-167.
258. Mathes, T., Vogl, C., Stolz, J., and Hegemann, P., *In Vivo Generation of Flavoproteins with Modified Cofactors*. Journal of Molecular Biology, 2009. **385**(5): p. 1511-1518.
259. Cleland, W.W., *The kinetics of enzyme-catalyzed reactions with two or more substrates or products*. Biochimica et Biophysica Acta (BBA) - Specialized Section on Enzymological Subjects, 1963. **67**: p. 104-137.
260. Lu, C., Lin, Y., and Yeh, S.-R., *Inhibitory Substrate Binding Site of Human Indoleamine 2,3-Dioxygenase*. Journal of the American Chemical Society, 2009. **131**(36): p. 12866-12867.
261. Nickel, E., Nienhaus, K., Lu, C., Yeh, S.-R., and Nienhaus, G.U., *Ligand and Substrate Migration in Human Indoleamine 2,3-Dioxygenase*. Journal of Biological Chemistry, 2009. **284**(46): p. 31548-31554.

262. Davydov, R.M., Chauhan, N., Thackray, S.J., Anderson, J.L.R., Papadopoulou, N.D., Mowat, C.G., Chapman, S.K., Raven, E.L., and Hoffman, B.M., *Probing the Ternary Complexes of Indoleamine and Tryptophan 2,3-Dioxygenases by Cryoreduction EPR and ENDOR Spectroscopy*. Journal of the American Chemical Society, 2010. **132**(15): p. 5494-5500.
263. Cleland, W.W., *Enzyme Kinetics*. Annual Review of Biochemistry, 1967. **36**(1): p. 77-112.
264. Michaelis, L. and Menten, M., *Die kinetik der invertinwirkung*. Biochemistry Zeitung, 1913. **49**: p. 333-369.
265. Johnson, K.A. and Goody, R.S., *The Original Michaelis Constant: Translation of the 1913 Michaelis–Menten Paper*. Biochemistry, 2011. **50**(39): p. 8264-8269.
266. Briggs, G.E. and Haldane, J.B.S., *A Note on the Kinetics of Enzyme Action*. Biochemical Journal, 1925. **19**(2): p. 338-339.
267. Chauhan, N., Basran, J., Efimov, I., Svistunenko, D.A., Seward, H.E., Moody, P.C.E., and Raven, E.L., *The Role of Serine 167 in Human Indoleamine 2,3-Dioxygenase: A Comparison with Tryptophan 2,3-Dioxygenase*. Biochemistry, 2008. **47**(16): p. 4761-4769.
268. Lu, C., Lin, Y., and Yeh, S.-R., *Spectroscopic Studies of Ligand and Substrate Binding to Human Indoleamine 2,3-Dioxygenase*. Biochemistry, 2010. **49**(24): p. 5028-5034.
269. Ed. Battino, R., *NIST solubility data series: Oxygen and ozone*. <http://srdata.nist.gov/solubility/IUPAC/SDS-7/SDS-7.pdf>, 1981. **7**: p. 2.
270. Copeland, R.A., *Enzymes*. 2nd Ed. ed. 2000, New York, N.Y.: Wiley.
271. Yanagisawa, S., Horitani, M., Sugimoto, H., Shiro, Y., Okada, N., and Ogura, T., *Resonance Raman study on the oxygenated and the ferryl-oxo species of indoleamine 2,3-dioxygenase during catalytic turnover*. Faraday Discussions, 2011. **148**(0): p. 239-247.
272. Weber, B., Nickel, E., Horn, M., Nienhaus, K., and Nienhaus, G.U., *Substrate Inhibition in Human Indoleamine 2,3-Dioxygenase*. The Journal of Physical Chemistry Letters, 2014. **5**(4): p. 756-761.
273. Berry, E.A. and Trumpower, B.L., *Simultaneous determination of hemes a, b, and c from pyridine hemochrome spectra*. Analytical Biochemistry, 1987. **161**(1): p. 1-15.
274. Sono, M. and Cady, S.G., *Enzyme kinetic and spectroscopic studies of inhibitor and effector interactions with indoleamine 2,3-dioxygenase. 1. Norharman and 4-phenylimidazole binding to the enzyme as inhibitors and heme ligands*. Biochemistry, 1989. **28**(13): p. 5392-5399.
275. Cady, S.G. and Sono, M., *1-methyl--tryptophan, [beta]-(3-benzofuranyl)--alanine (the oxygen analog of tryptophan), and [beta]-[3-benzo(b)thienyl]--alanine (the sulfur analog of tryptophan) are competitive inhibitors for indoleamine 2,3-dioxygenase*. Archives of Biochemistry and Biophysics, 1991. **291**(2): p. 326-333.
276. Peterson, A.C., Loggia, A.J.L., Hamaker, L.K., Arend, R.A., Fiset, P.L., Ozaki, Y., Will, J.A., Brown, R.R., and Cook, J.M., *Evaluation of substituted β -carbolines as noncompetitive indoleamine 2,3 dioxygenase inhibitors*. Medicinal Chemistry Research, 1993. **3**: p. 473-482.
277. Peterson, A.C., Migawa, M.T., Martin, M.J., Hamaker, L.K., Czerwinski, K.M., Zhang, W., Arond, R.A., Fiset, P.L., Ozaki, Y., Will, J.A., Brown, R.R., and Cook, J.M., *Evaluation of functionalized derivatives and related compounds as competitive inhibitors of indoleamine 2,3-dioxygenase*. Medicinal Chemistry Research, 1994. **3**: p. 531-544.
278. Sono, M., Roach, M.P., Coulter, E.D., and Dawson, J.H., *Heme-Containing Oxygenases*. Chemical Reviews, 1996. **96**(7): p. 2841-2888.
279. Eguchi, N., Watanabe, Y., Kawanishi, K., Hashimoto, Y., and Hayaishi, O., *Inhibition of indoleamine 2,3-dioxygenase and tryptophan 2,3-dioxygenase by [beta]-carboline and indole derivatives*. Archives of Biochemistry and Biophysics, 1984. **232**(2): p. 602-609.
280. Kumar, S., Jaller, D., Patel, B., LaLonde, J.M., DuHadaway, J.B., Malachowski, W.P., Prendergast, G.C., and Muller, A.J., *Structure Based Development of Phenylimidazole-Derived Inhibitors of Indoleamine 2,3-Dioxygenase*. Journal of Medicinal Chemistry, 2008. **51**(16): p. 4968-4977.

281. Brastianos, H.C., Vottero, E., Patrick, B.O., Van Soest, R., Maitainaho, T., Mauk, A.G., and Andersen, R.J., *Exiguamine A, an Indoleamine-2,3-dioxygenase (IDO) Inhibitor Isolated from the Marine Sponge Neopetrosia exigua*. Journal of the American Chemical Society, 2006. **128**(50): p. 16046-16047.
282. Carr, G., Chung, M.K.W., Mauk, A.G., and Andersen, R.J., *Synthesis of Indoleamine 2,3-Dioxygenase Inhibitory Analogues of the Sponge Alkaloid Exiguamine A*. Journal of Medicinal Chemistry, 2008. **51**(9): p. 2634-2637.
283. Carr, G., Tay, W., Bottriell, H., Andersen, S.K., Mauk, A.G., and Andersen, R.J., *Plectosphaeric Acids A, B, and C, Indoleamine 2,3-Dioxygenase Inhibitors Produced in Culture by a Marine Isolate of the Fungus Plectosphaerella cucumerina*. Organic Letters, 2009. **11**(14): p. 2996-2999.
284. Pereira, A., Vottero, E., Roberge, M., Mauk, A.G., and Andersen, R.J., *Indoleamine 2,3-Dioxygenase Inhibitors from the Northeastern Pacific Marine Hydroid Garveia annulata*. Journal of Natural Products, 2006. **69**(10): p. 1496-1499.
285. Gaspari, P., Banerjee, T., Malachowski, W.P., Muller, A.J., Prendergast, G.C., DuHadaway, J., Bennett, S., and Donovan, A.M., *Structure-Activity Study of Brassinin Derivatives as Indoleamine 2,3-Dioxygenase Inhibitors*. Journal of Medicinal Chemistry, 2006. **49**(2): p. 684-692.
286. Yue, E.W., Douthy, B., Wayland, B., Bower, M., Liu, X., Leffert, L., Wang, Q., Bowman, K.J., Hansbury, M.J., Liu, C., Wei, M., Li, Y., Wynn, R., Burn, T.C., Koblisch, H.K., Friedman, J.S., Metcalf, B., Scherle, P.A., and Combs, A.P., *Discovery of Potent Competitive Inhibitors of Indoleamine 2,3-Dioxygenase with in vivo Pharmacodynamic Activity and Efficacy in a Mouse Melanoma Model*. Journal of Medicinal Chemistry, 2009. **52**(23): p. 7364-7367.
287. Matsuno, K., Takai, K., Isaka, Y., Unno, Y., Sato, M., Takikawa, O., and Asai, A., *S-Benzylisothiourea derivatives as small-molecule inhibitors of indoleamine-2,3-dioxygenase*. Bioorganic & Medicinal Chemistry Letters, 2010. **20**(17): p. 5126-5129.
288. Röhrig, U.F., Awad, L., Grosdidier, A.I., Larrieu, P., Stroobant, V., Colau, D., Cerundolo, V., Simpson, A.J.G., Vogel, P., Van den Eynde, B.T.J., Zoete, V., and Michielin, O., *Rational Design of Indoleamine 2,3-Dioxygenase Inhibitors*. Journal of Medicinal Chemistry, 2010. **53**(3): p. 1172-1189.
289. Littlejohn, T., Takikawa, O., Truscott, R., and Walker, M., *Asp274 and His346 Are Essential for Heme Binding and Catalytic Function of Human Indoleamine 2,3-Dioxygenase*. Journal of Biological Chemistry, 2003. **278**(32): p. 29525-29531.
290. Yuasa, H., Takubo, M., Takahashi, A., Hasegawa, T., Noma, H., and Suzuki, T., *Evolution of Vertebrate Indoleamine 2,3-Dioxygenases*. Journal of Molecular Evolution, 2007. **65**(6): p. 705-714.
291. Pyykkö, P. and Atsumi, M., *Molecular Single-Bond Covalent Radii for Elements 1–118*. Chemistry – A European Journal, 2009. **15**(1): p. 186-197.
292. Austin, C.J.D., Moir, M., Kahlert, J., Smith, J.R., Jamie, J.F., Kassiou, M., and Rendina, L.M., *Carborane-Containing Hydroxyamidine Scaffolds as Novel Inhibitors of Indoleamine 2,3-Dioxygenase 1 (IDO1)*. Australian Journal of Chemistry, 2015. **68**(12): p. 1866-1870.
293. Stone, T.W., *Neuropharmacology of quinolinic and kynurenic acids*. Pharmacological Reviews, 1993. **45**(3): p. 309-379.
294. Št'astný, F., Lisý, V., Mareš, V., Lisá, V., Balcar, V.J., and Santamaría, A., *Quinolinic acid induces NMDA receptor-mediated lipid peroxidation in rat brain microvessels*. Redox Report, 2004. **9**(4): p. 229-233.
295. Tavares, R.G., Tasca, C.I., Santos, C.E.S., Alves, L.C.B., Porciúncula, L.O., Emanuelli, T., and Souza, D.O., *Quinolinic acid stimulates synaptosomal glutamate release and inhibits glutamate uptake into astrocytes*. Neurochemistry International, 2002. **40**(7): p. 621-627.
296. Pow, D.V. and Cook, D.G., *Neuronal Expression of Splice Variants of "Glial" Glutamate Transporters in Brains Afflicted by Alzheimer's Disease: Unmasking an Intrinsic Neuronal Property*. Neurochemical Research, 2009. **34**(10): p. 1748-1757.

- 297. Hu, S., Sheng, W.S., Ehrlich, L.C., Peterson, P.K., and Chao, C.C., *Cytokine Effects on Glutamate Uptake by Human Astrocytes*. *Neuroimmunomodulation*, 2000. **7**(3): p. 153-159.
- 298. Alberati-Giani, D. and Cesura, A.M., *Expression of the kynurenine enzymes in macrophages and microglial cells: regulation by immune modulators*. *Amino Acids*, 1998. **14**(1): p. 251-255.
- 299. Heinzelmann, G. and Kuyucak, S., *Molecular Dynamics Simulations of the Mammalian Glutamate Transporter EAAT3*. *PLoS ONE*, 2014. **9**(3): p. e92089.

Publications

Citation	Contribution
Kynurenine-3-monooxygenase: a review of structure, mechanism and inhibitors. <u>Smith, JR.</u> , Jamie, JF., Guillemin, GJ. <i>Drug Discovery Today</i> , 2015, 21(2) p.315-324.	Planned and wrote the manuscript.
Ketimine reductase/CRYM catalyses reductive alkylamination of α -keto acids confirming its function as an imine reductase. Hallen, A., Cooper, AJ., Jamie, JF., <u>Smith, JR.</u> , and Karuso, P. <i>Amino Acids</i> , 2015, 47(11) p.2457-2461.	LC-MS method development. LC-MS analysis of enzyme reactions. Contributed to the manuscript.
Carborane-containing hydroxyamidine scaffolds as novel inhibitors of indoleamine 2,3-dioxygenase 1 (IDO 1). Austin, CJD., Moir M., Kahlert J., Smith, JR., Jamie, JF., Kassiou, M., and Rendina, LM. <i>Aust. J. Chem.</i> , 2015, 68(12) p.1866-1870.	Enzyme production. Design of, and technical assistance with, enzyme assays.
The first indoleamine-2, 3-dioxygenase-1 (IDO1) inhibitors containing carborane. Austin, CJD., Kahlert, J., Issa, F., <i>et al.</i> <i>Dalton Trans.</i> , 43(28) 2014 p.10719-10724.	Molecular modelling of the interactions between IDO1 and naphthoquinone inhibitors. Enzyme production. Design of, and technical assistance with, enzyme assays. Contributed to the manuscript.
Mutation of cysteine residues alters the heme-binding pocket of indoleamine 2, 3-dioxygenase-1. Austin, CJD., Kosim-Satyaputra, P., <u>Smith, JR.</u> , Willows, RD., Jamie, JF. <i>Biochem & Biophys Res Comm</i> , 436(4) 2013 p.595-600.	Molecular modelling of IDO1. Assistance with kinetic analysis.
Natural product-inspired pyranonaphthoquinone inhibitors of indoleamine 2,3-dioxygenase-1 (IDO-1). Bridewell, DJA., Sperry, J., <u>Smith, JR.</u> , <i>et al.</i> <i>Aus. J. Chem.</i> , 66(1) 2013 p.40-49.	Enzyme production. Performance and analysis of inhibition assays.



Kynurenine-3-monooxygenase: a review of structure, mechanism, and inhibitors

Jason R. Smith¹, Joanne F. Jamie¹ and Gilles J. Guillemin²



¹ Department of Chemistry and Biomolecular Sciences, Faculty of Science and Engineering, Macquarie University, Sydney, NSW 2109, Australia

² Department of Biomedical Sciences, Faculty of Medicine and Health Sciences, Macquarie University, Sydney, NSW 2109, Australia

Kynurenine monooxygenase (KMO) is an enzyme of the kynurenine (Kyn) pathway (KP), which is the major catabolic route of tryptophan. Kyn represents a branch point of the KP, being converted into the neurotoxin 3-hydroxykynurenine via KMO, neuroprotectant kynurenic acid, and anthranilic acid. As a result of this branch point, KMO is an attractive drug target for several neurodegenerative and/or neuroinflammatory diseases, especially Huntington's (HD), Alzheimer's (AD), and Parkinson's (PD) diseases. Although a neurological target, administration of KMO inhibitors in the periphery has demonstrated promising pharmacological results. In light of a recent crystal structure release and reports of preclinical candidates, here we provide a concise yet comprehensive update on the current state of research into the enzymology of KMO and related drug discovery efforts, highlighting areas where further work is required.

Introduction

KMO (EC 1.14.13.9) is a flavin adenine dinucleotide (FAD)-containing outer mitochondrial membrane enzyme of the Kyn pathway (KP). This pathway (Fig. 1) is a drug target of several pathological states, especially immunological diseases (e.g., cancer and chronic infection) and neurodegenerative and/or neuroinflammatory diseases (including HD, PD, and AD) [1–4]. It is initiated through the oxidative cleavage of L-tryptophan by indoleamine 2,3-dioxygenases (IDO1, IDO2, E.C. 1.11.13.52), or tryptophan 2,3-dioxygenase (TDO, E.C. 1.13.11.11) to yield N-formyl-L-kynurenine (NFK). Subsequent hydrolysis by formamidase (E.C. 3.5.1.9) yields L-kynurenine (L-Kyn). L-Kyn represents a branch point of the KP because it is the substrate of three enzymes: KMO [producing 3-hydroxy-L-kynurenine (3-HK)], kynureninase (E.C. 3.7.1.3, producing anthranilic acid and L-alanine) and kynurenine amino transferases (KATs, E.C. 2.6.1.7, producing kynurenic acid (KynA)). The end fate of the KP is NAD⁺ biosynthesis.

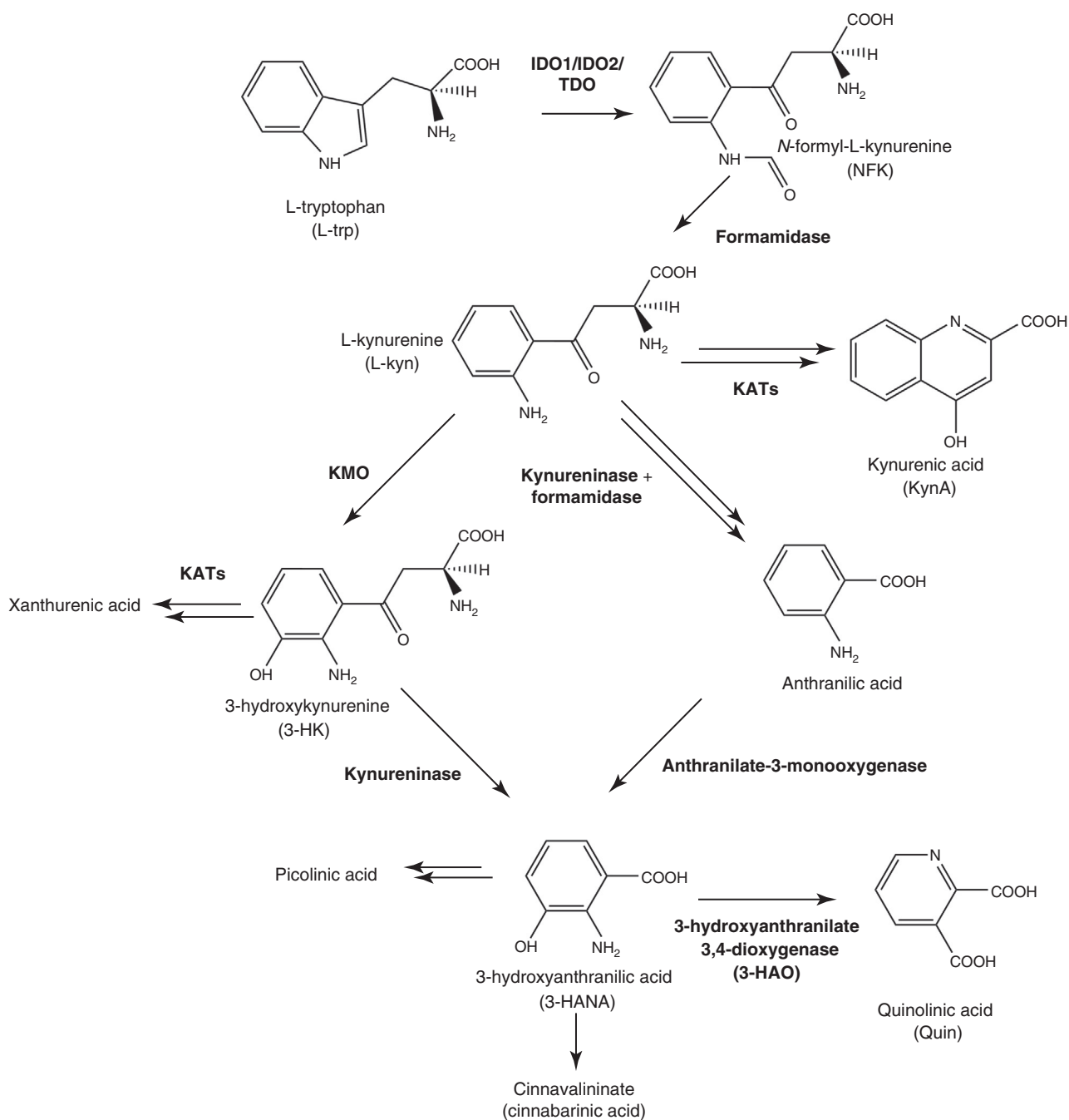
The correlations concerning disease states and KMO expression, activity, and/or KP metabolite concentrations is well outlined and

is only briefly covered here (e.g., [5–11]). A comprehensive review of the molecular properties of KMO, including its kinetics, reaction mechanism, and inhibitor structure–activity relationship (SAR), is not currently available and, thus, is our focus here. In mid-2013, the crystal structure of KMO from *Saccharomyces cerevisiae* was solved [12], sparking greater drug discovery efforts. For example, the pharmaceutical company GlaxoSmithKline recently completed a high-throughput screen of 78 000 chemicals using the Rapid-Fire mass spectrometry system [13], while the not-for-profit organisation CHDI recently reported promising preclinical results from their pipeline [14]. Thus, here we provide a timely review of current KMO biochemical research.

Chemical biology of KP metabolites

More than 95% of tryptophan is metabolised through the KP, with the remainder directed into protein synthesis and serotonin, melatonin, and tryptamine production [15]. Little is known about the biological function of the first KP product, N-formyl-L-kynurenine (NFK), which hydrolyses to L-Kyn spontaneously and enzymatically *via* formamidase and, thus, has a limited lifetime. Proteinaceous tryptophan can be converted to NFK in the presence of light, such as in photosynthetic systems [16,17], and

Corresponding author: Jamie, J.F. (joanne.jamie@mq.edu.au)



Drug Discovery Today

FIGURE 1

Simplified structure of the kynurenine pathway (KP). Some intermediates and enzymes are omitted for clarity. The pathway presented is generalised among mammals, but intertissue and interspecies differences exist. For definitions of abbreviations, please see the main text.

kynurenylation has been demonstrated as a mechanism involved in cataract formation [18,19].

Kyn (among other KP metabolites, such as cinnabarinic acid and KynA) is a ligand of the aryl hydrocarbon receptor (AhR) [20,21], although elucidating the multiple roles of Kyn in the body is largely ongoing [10]. 3-HK and 3-hydroxyanthranilic acid readily oxidise under physiological conditions to form peroxide and hydroxyl radicals [22]. KynA is an inhibitor of NMDA, kainate, AMPA, and α -7 nicotinic acetylcholine (α 7nAChR) receptors [23–25]. It is a

G-protein-coupled receptor 35 (GPR35) [26] and AhR ligand [27] and a scavenger of hydroxyl and superoxide radicals under certain conditions [28]. Quinolinic acid (Quin) is an excitotoxin that selectively activates NMDA receptors (NMDAR) [6,29] and most of its neurological actions can be blocked by NMDAR antagonists [10]. Quin also has a role in iron-dependent oxidative effects, such as the stimulation of lipid peroxidation [30,31] and complexes with ferrous iron; auto-oxidising and producing reactive oxygen species *via* the Fenton reaction [32].

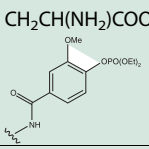
BOX 1

Formatting needs attention beyond what the interface allows.

Reported KMO inhibitors. A number of different reports exist for KMO inhibitors. The diversity of scaffolds to date has centred almost exclusively around substrate mimics and their isosteres. The pyrroloquinolines (**35**), oxopropanitriles (**36**) and the natural product ianthellamide (**37**) are unique exceptions to this.

Table I

Selected SAR of KMO inhibitors with *in vitro* activity.

Scaffold	X	Y	Z	IC ₅₀ μ M/I%, 10 μ M ^a	Source	Compound	Refs.
I	<i>m</i> -Nitro	NH ₂	COOH	0.5	Rat liver	<i>m</i> NBA	[96] ^b
	H	NH ₂	COOH	16	Rat brain	BA	[105]
	3,4-Dichloro	NH ₂	COOH	0.33	Rat brain	1	[96] ^b
		H	COOH	3.9	Rat brain	2	[96] ^b
		OH	COOH	0.42	Rat brain	3	[96] ^b
		CH ₂ Ph	COOH	2.3	Rat brain	4	[96] ^b
		NH ₂	H	None	Rat brain	5	[96] ^b
II	3,4-Dichloro			0.18	Rat brain	UPF-648	[97] ^b
III	3,4-Dimethoxy			0.037	Rat kidney	Ro 61-8048	[56] ^c
	4-Amino			0.040	Rat kidney	6	[56] ^c
	4-Methoxy			0.051	Rat kidney	7	[56] ^c
	4-Chloro			0.084	Rat kidney	8	[56] ^c
	3,4-Dichloro			0.120	Rat kidney	9	[56] ^c
	H			0.200	Rat kidney	10	[56] ^c
	4- <i>iso</i> -propyl			0.990	Rat kidney	11	[56] ^c
IV	3-Chloro	N	N	0.005	Human liver	12	[14] ^c
	3,4-Dichloro	N	N	0.006	Human liver	13	[14] ^c
	H	N	N	0.038	Human liver	14	[14] ^c
	3-Chloro-4-cyclopropoxy	N	N	0.005	Human liver	15	[14] ^c
	3,4-Dichloro	CH	N	0.032	Human liver	16	[14] ^c
	3,4-Dichloro	N	CH	0.090	Human liver	17	[14] ^c
V		Cyclohexyl		19	Rat liver	18	[99] ^c
		Phenyl		30	Rat liver	19	[99] ^c
		<i>p</i> -Chlorophenyl		65	Rat liver	20	[99] ^c
		β -Naphthyl		77	Rat liver	21	[99] ^c
VI	S	N	C	470 nM (IC ₅₀)	Rat kidney	22	[56] ^c
	S	N	N	78	Rat kidney	23	[57]
	N	S	N	72	Rat kidney	24	[57]
	O	CH	N	31	Rat kidney	25	[57]
	NCH ₃	CH	N	0	Rat kidney	26	[57]
VII	3,4-Dichloro	4-CH ₂ COOH		100	Human recombinant from CHO cells	27	[98] ^c
		5-CH ₂ COOH		93	Human recombinant from CHO cells	28	[98] ^c
		4-CH ₂ COOCH ₃		100	Human recombinant from CHO cells	29	[98] ^c
		5-CH ₂ COOCH ₃		88	Human recombinant from CHO cells	30	[98] ^c
VIII	–	–		Not reported		31	[101]
IX	<i>m</i> -Nitro	COOH		0	<i>Pseudomonas fluorescens</i>	32	^d
		CH ₂ CH(NH ₂)COOH		0	<i>P. fluorescens</i>	33	^d
	3,4-Dichloro			17 nM (K _i)	<i>P. fluorescens</i>	34	^d

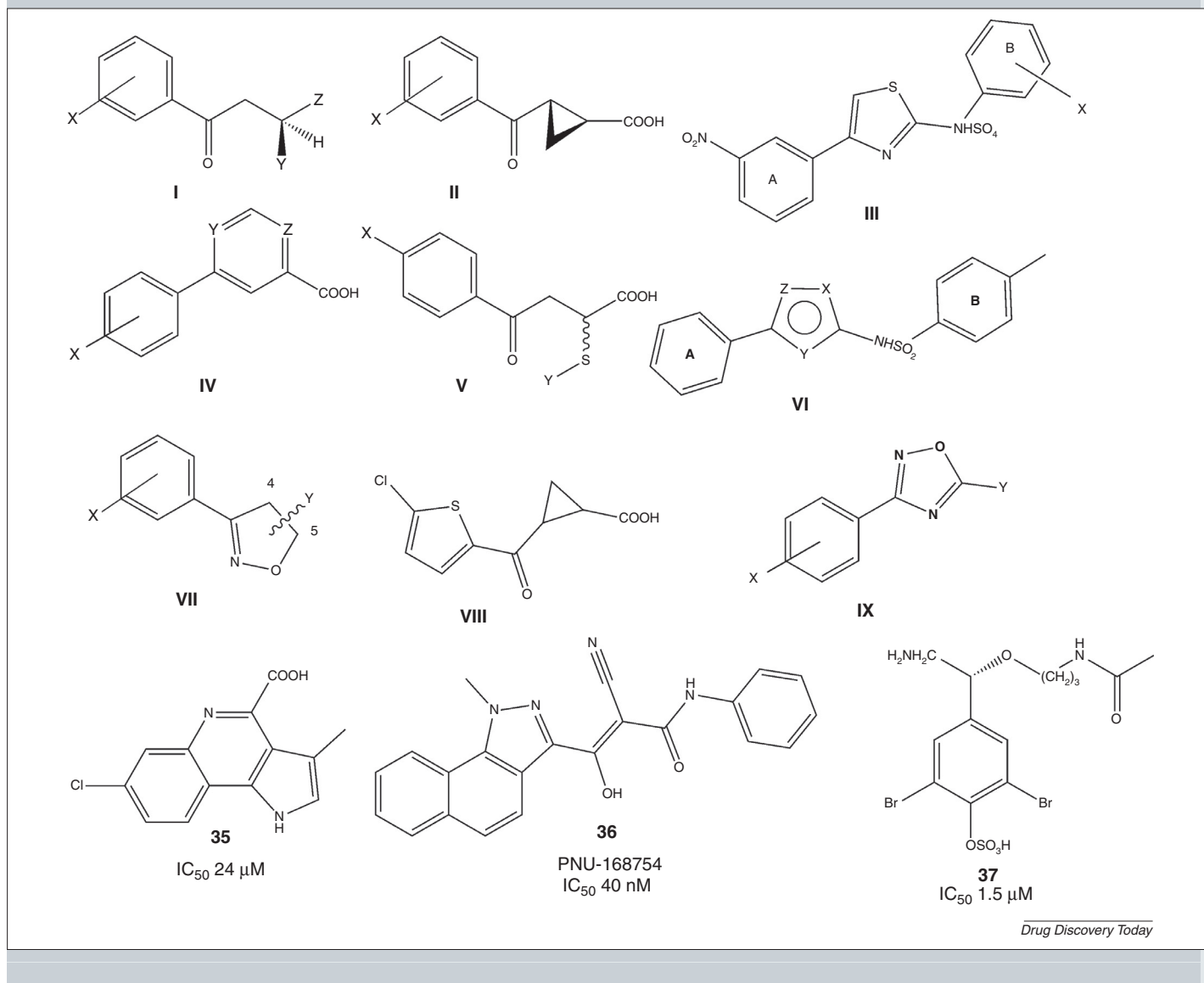
^aFor scaffolds I–IV IC₅₀ μ M data are given; for scaffolds V–IX, data are I%, 10 μ M.

^bL-Kyn at 25 μ M.

^cL-Kyn at 100 μ M.

^dM. Wilkinson, PhD Thesis, The University of Edinburgh, 2013.

Figure 1.



The involvement of KMO in neurodegenerative and/or neuroinflammatory diseases

HD

HD is caused by a mutated form of the huntingtin protein (mHtt) leading to its misfolding and aggregation [33]. Eventually, these toxic structures result in neuronal cell death. In yeast, the toxicity induced by mHtt was rescued through the deletion of its KMO [34]. KMO is localised to the mitochondrial outer membrane and the link between KP dysregulation and HD has been hypothesised to occur at the mitochondrial level [35]. HD is known to affect mitochondrial function [36] and mitochondrial dysregulation has been correlated with decreased KAT activity and increased Quin neurotoxicity [37]. Small-molecule or genetic inhibition of KMO activity in a fruit fly HD model increased the level of neuroprotective KynA, decreased the level of neurotoxic 3-HK, and reduced neurodegeneration [38]. Similar observations were seen upon treatment with KynA and 3-HK, demonstrating the causative role of these molecules. Increased levels of 3-HK and Quin are observed in transgenic mouse HD models and patients

with early-stage HD, and are concomitant with the onset of symptoms in mice [8,39,40]. Mouse models and patients with HD also have reduced KynA levels [41,42]. Quin production and neuronal toxicity can be attenuated through inhibition of KMO in mice [45,46]. There is some debate around the pharmacological result of inhibiting KMO. In one instance, administration of the KMO inhibitor UPF648 (Box 1) saw a lowering of 3-HK without affecting KynA levels [45], whereas the use of the KMO inhibitors Ro-61-8048 [47] or mNBA (Box 1) demonstrated both reduced 3-HK and increased KynA [48].

AD

AD is characterised by the extracellular formation and accumulation of senile plaques comprising misfolded amyloid-β peptides, and also intracellular phosphorylation of tau proteins leading to neurofibrillary tangles [49]. In brain sections from patients with AD, Quin has been shown to co-localise with neurofibrillary tangles in neurons and, *in vitro*, Quin increased tau phosphorylation in a dose-dependent manner [50]. It was also found that Quin increased the

mRNA of ten genes directly associated with AD pathology, including six known to be involved in tau phosphorylation [50]. Increased IDO1, 3-HK, and Quin levels have been correlated with AD stages [51–53]. It has been demonstrated *in vitro* that the amyloid- β peptide can induce IDO1 expression, leading to Quin production by human macrophages and microglia [54]. Zwilling *et al.* demonstrated that treatment with a non-blood–brain barrier (BBB)-penetrating KMO inhibitor in a mouse model of AD significantly ameliorated the symptoms and slowed disease progression [55]. Several other studies demonstrated that peripheral administration of KMO inhibitors could change the concentrations of KP metabolites within the central nervous system (CNS) [14,56–58].

PD

Similar to HD and AD, PD neuropathology is associated with oxidative stress [59], mitochondrial dysfunction [60], protein aggregation [61], excitotoxicity [62], and inflammation; that is, cytokine production [63]. Serum Kyn:Trp ratios and brain 3-HK levels are increased, whereas KynA levels are decreased [64–67]. Pretreatment with KynA reduced chemically induced neuronal cell death in a PD model [68]. Administration of L-Kyn to a PD model with simultaneous inhibition of organic acid transport (to delay clearance of L-Kyn), and inhibition of KMO and kynureninase (using an L-Kyn analogue), protected neurons from Quin-induced toxicity [69,70].

Amyotrophic lateral sclerosis

Neuroinflammation is a hallmark of amyotrophic lateral sclerosis (ALS) [71,72], and the KP is activated during inflammation. Most of the KP metabolites are neuroactive; some being neurotoxic (Quin) and others neuroprotective (KynA). It has previously been demonstrated that the KP is activated in patients with motor neuron disease, leading to an increase in levels of Quin and a decrease of KynA in 150 matching cerebral spinal fluid and serum samples [4,73,74].

Peripheral administration and central effects

The ability for peripheral treatment to yield central effects is theorised to be the result of the presence of selective active transport of KP molecules across the BBB and cell specific expression patterns of KP enzymes. Only three KP metabolites (tryptophan, Kyn, and 3-HK) are actively transported across the BBB [75]. KMO expression is low in the brain, primarily in microglia and infiltrating macrophages, but higher in the liver and kidney [76–79]. Meanwhile, KATII expression is found in astrocytes and neurons [80,81]. Thus, inhibition of peripheral KMO leads to decreased levels of peripheral 3-HK available for BBB transport, and increased levels of L-Kyn that can be centrally converted to neuroprotective KynA [55].

KMO structure and mechanism

KMO is a class A FAD monooxygenase [82]. This class is typified by being encoded by a single gene containing one FAD-binding domain. The FAD in KMO is noncovalently, but tightly, bound [12,83]. Catalysis is dependent upon FAD reduction by NADH or NADPH. Members of this class are often traceable to microbial enzymes responsible for the *ortho*- or *para*-hydroxylation of aromatic rings [84]. Indeed, the KMO of *Pseudomonas fluorescens*

displays 34% identity with human KMO and has been used as a proxy for the more recalcitrant human enzyme in characterisation studies [85,86]. In addition to *P. fluorescens*, the literature has significant contributions from yeast (36% amino acid sequence identity), rodent (76% identity), and human tissue studies, because of the limited availability of high-quality and/or high-quantity recombinant enzymes.

The explicit reaction mechanism of KMO has not yet been formally elucidated; however, evidence suggests that it follows the well-described mechanism of related flavin-dependent mono-oxygenases such as *p*-hydroxybenzoate hydroxylase and phenol hydroxylase (Box 2) [83,85]. After L-Kyn binds, NADPH (preferred over NADH [83]) reduces FAD and leaves as NADP⁺ before oxygen binds and creates an L-Kyn-FAD-hydroperoxide intermediate (Box 2, Figure II) [85]. The oxidation of L-Kyn then proceeds, yielding water and L-3-HK [85]. The reduction rate of FAD is significantly enhanced by the presence of substrate L-Kyn or L-Kyn-like inhibitors, such as benzoylalanine (BA, Box 1) or *m*-nitrobenzoylalanine (*m*NBA, Box 1), a trait commonly observed in bacterial aromatic hydroxylases [87]. The apparent K_D of NADPH is not affected by the presence of these molecules, and neither is the reduction potential (Box 2, Table II) [85]. Bacterial hydroxylases have been proposed to undergo a dynamic shift where the FAD is in an ‘in’ or ‘out’ conformation, and it is only in this ‘out’ conformation that reduction occurs [88]. It has been proposed that the substrate stimulation of FAD reduction occurs as it forces the protein to the ‘out’ form. [89]. No direct evidence of this mechanism exists for KMO, although distinct flavin conformations are found during the catalytic cycle [85].

Low levels of chloride ion have been reported to not only stabilise the protein during *in vitro* kinetic assays, but also inhibit 3-HK production [85]. Spectroscopic data suggest that the chloride forces FAD into a state similar to a 3-HK bound state (although the presence or absence of ligand has not been confirmed) [85]. The chloride ion is either forcing the protein into this conformation (with or without ligand) or, once the protein reaches this conformation through the normal catalytic cycle, is preventing product release. Chloride ions have been seen binding adjacent to the FAD in bacterial flavin-containing mono-oxygenases [88], but it has not yet been investigated whether this conserved kinetic control by monovalent ions of class A mono-oxygenases represents a relevant pharmacological control point in KMO action.

Inhibition by L-Kyn-like molecules, such as *m*NBA, BA, and UPF-648 (Box 1), additionally yield hydrogen peroxide, likely because of the decay of intermediate hydroperoxyflavin [12,85]. At least for *m*NBA, this production is stoichiometric with NADPH loss [85]. These inhibiting molecules are structurally similar to the substrate L-Kyn, and *m*NBA and BA are known to facilitate faster FAD reduction. Therefore, it may become necessary to ensure that therapeutic development is directed towards systems that avoid such peroxide release.

The membrane association of KMO and attempts at recombinant purification

The C terminus of KMO contains a putative outer mitochondrial membrane-targeting sequence [35] and this portion of the molecule is required for both pig and human enzyme function [90,91]. A human polymorphism in this region resulting in an Arg452Cys mutation has been statistically linked to bipolar disorder and

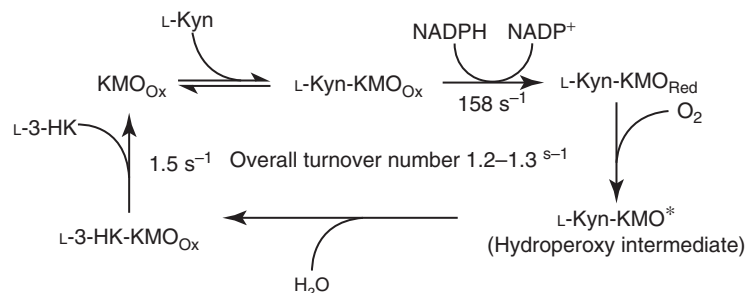
BOX 2

Catalytic mechanism of KMO

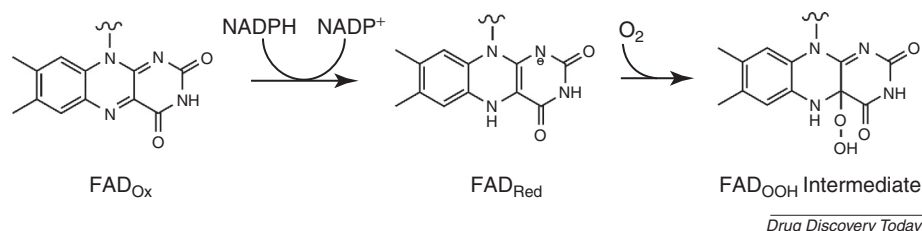
After L-Kyn binding, NADPH (preferred over NADH [83]) binds and quickly reduces the FAD with a rate constant of 158 s^{-1} [85]. NADP⁺ is subsequently released, allowing for dioxygen binding. This likely forms an FAD[•]-superoxide radical pair that rapidly decays to a peroxy-flavin structure capable of acting as the electrophile for L-Kyn oxidation [85]. Rapid dehydration of C4a-hydroxy flavin is thought to yield the oxidised flavin. The final step, 3-HK release, is rate limiting with a rate constant of $\sim 1.5\text{ s}^{-1}$, which is slightly faster than the overall turnover number of the enzyme of $1.2\text{--}1.3\text{ s}^{-1}$ [85,86]. The K_D for NADPH is constant within an order of magnitude regardless of ligand presence, whereas the rate of reduction is enhanced by three orders of magnitude in the presence of saturating L-Kyn [85].

Figure II. (a) Reaction cycle of KMO. **(b)** Probable FAD intermediates during reaction. KMO_{ox} is the oxidised form. KMO_{red} is the reduced form. For definitions of abbreviations, please see the main text.

(a) Reaction cycle of KMO



(b) Probable FAD intermediates during reaction



Drug Discovery Today

Table II

The effect of oxidation state and ligand presence on the NADPH affinity and KMO reduction potential.^a

Complex	$K_D/\mu\text{M}$ (NADPH) [85]	Reduction potential/mV [85]
KMO _{ox}	324	−188
KMO _{ox} -L-Kyn	196	−188
KMO _{ox} -mNBA	346	−188
KMO _{ox} -BA	865	−188
KMO _{ox}	17 (K_D of L-Kyn)	
KMO _{red}	17 (K_D of L-Kyn)	

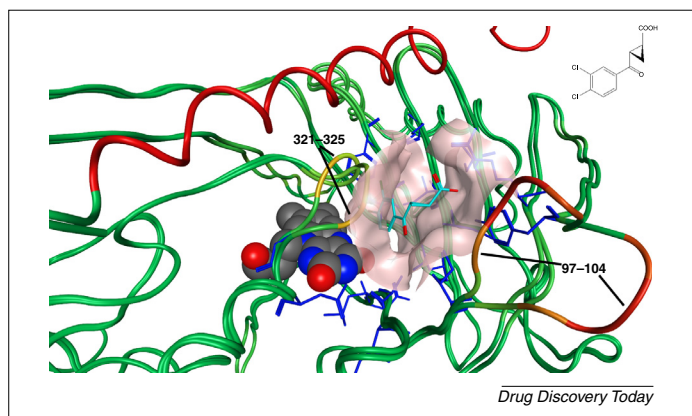
^aAll values are from *Pseudomonas fluorescens*, taken at 5°C.

schizophrenia, with increased central KynA levels and reduced KMO expression [92,93]. Purification attempts by Hirai *et al.* on pig KMO resulted in the co-elution of cytochrome b5 and the β subunit of monoamine oxidase. Attempts at their removal yielded little to no enzyme activity [91]. Likewise, recombinant human KMO expressed in an *E. coli* system co-eluted with the β subunit of tryptophan synthase and an unidentified protein with putative GTP-binding properties [90]. The hydrophobic C terminus of KMO will form complexes or aggregates with other proteins during purification in the absence of an appropriate lipid environment. The inability to remove the proteins with detergents suggests a

particularly tight association, and points to a C-terminal domain that requires a hydrophobic environment to function properly. This is supported by attempts to solubilise the C-terminal domain with a highly hydrophilic 3xFLAG sequence. Most protein was present in the membranous pellet fraction, even after repeated ultracentrifugation and solubilisation steps [90].

Yeast KMO crystal structure

Five KMO structures from *S. cerevisiae* (*E. coli* expressed) were released in 2013 (PDB: 4J2W, 4J31, 4J33, 4J34, and 4J36) [12]. The sequence used was a C-terminal truncation of the full yeast

**FIGURE 2**

Superpositioning of the kynurenine monooxygenase (KMO) structures 4J34 (apo) and 4J36 (holo). The backbone is coloured according to RMSD where green > yellow > orange > red. Active site atoms of 4J36 are shown (dark blue with a pink interaction surface). Co-crystallised UPF-648 is shown with light-blue carbons and red oxygens and also inset. Part of FAD is also shown in space-filling mode with grey carbons, blue nitrogens, and red oxygens. To the immediate left of UPF-648 are the displaced loops 321–325. Immediately to the right of UPF-648 are the loops 97–104. The red alpha helix shown at the top is from 4J34. In 4J36, these residues are unresolved because of displacement by residues 321–325 [12].

KMO, missing the membrane-targeting region. Unlike pig and human KMO, truncated yeast KMO is enzymatically active. Structures 4J34 and 4J36 are most relevant in drug design efforts because they describe the KMO molecules in the absence (apo) and presence (holo) of a bound inhibitor: UPF-648 (also known as PNU-165853), respectively (Fig. 2). Significant structural changes are apparent between the two. In 4J34, the upper roof of the active site, directly above the FAD molecule, comprises the flexible and highly conserved sequence 321-PFYGGQ-325 (*S. cerevisiae* numbering; human and rat PFEGQG). However, in the inhibitor-bound form, this sequence of residues is displaced by the 3,4-dichloro moiety of UPF-648 (Fig. 2). This rotation of the Pro321–Gln325 chain was not evident in a short molecular dynamics simulation involving substrate L-Kyn within the active site of KMO, suggesting an adaptive cavity [12]. A flexible loop exists in the sequence Tyr97–Ile104 close to the active-site entrance. This is conserved among vertebrates with a consensus sequence of YGX₁KX₂QYI. X₁ in particular is almost exclusively a hydrogen bond donor, such as lysine or threonine (a multiple sequence alignment is available in the supplementary information online).

KMO inhibitors

4-Aryl-4-oxobutanoic acids

Early KMO inhibitors were close substrate analogues collectively described as derivatives of 4-aryl-4-oxobutanoic acid. Use of ring deactivating chloro- and nitro- groups yields submicromolar inhibitors (Box 1, *m*NBA and **1**) [94–96]. The carboxyl is obligatory for inhibition (**5**) but the amine is not (**2**), replaceable with a hydroxyl group (**3**) or a methylene bridge (UPF-648) [96,97], suggesting that the amino interaction contributes approximately the same amount of inhibition as the entropic cost of binding the flexible alkyl chain. This alkyl linker between the benzoyl and carboxyl groups can also be replaced with dihydroisoxazole (Box 1, **27–30**) [98]. Replacement of the amine with thioether groups suggests the

presence of a hydrophobic pocket because there is a trend of increasing inhibition with increasing size for these substituents (Box 1) [99,100]. Benatti *et al.* replaced the FAD-binding benzene ring with a thiophene (Box 1, **31**); however, no inhibition data were reported [101]. Carboxyl glycosylation of scaffold **II**, to which UPF-648 belongs, demonstrated unchanged *in vitro* IC₅₀, but improved CNS penetration in rats at 50 mg/kg [58].

Sulfonamides

The sulfonamides are inhibitors with nanomolar IC₅₀s (Box 1) [56,57,102]. They are structural analogues of the substrate L-Kyn, containing an FAD-binding benzene ring (ring A, Box 1), a five- or six-membered aromatic ring as linker, a sulfonamide as amino-acid bioisostere, and an extendable benzene ring (ring B) that might be hitting the same hydrophobic pocket as the thioethers. Significant differences in inhibition are seen with modification of the linking ring, with minimal inhibition from six-membered rings (<25% at 10 μM) [57]. Of the five-membered systems, the thiazole is significantly more potent [56]. The phenylthiazole benzenesulfonamides in particular (Ro 61-8048 and **6–11**) are well explored [56]. Small substituents on both benzene rings are required for optimal *in vitro* binding, with methoxy and smaller groups being preferred. The majority of these inhibitors, such as those listed in Box 1, had equivalent IC₅₀s (within error) of 80–20 nM. They have poor BBB penetration but show evidence that peripheral inhibition is enough to produce pharmacologically relevant results [55].

6-Phenylpyrimidines

The phenylpyrimidines were first investigated after isosteric alignment with the 4-aryl-4-oxobutanoic acid scaffold [14]. The FAD-binding benzene ring is hypothesised to bind in the same manner as the co-crystallised UPF-648, and the 3,4-disubstituted system shows the greatest activity. In particular, 3-chloro-4-alkyl/alkoxy groups show good *in vitro* and in cell activities (Box 1, compare **12–15**) [14]. N4 is needed more than N1 (**16** versus **17**), but both are needed for optimal activity. Peripheral administration of **15** led to an increase of plasma Kyn, KynA, and anthranilic acid, and a concomitant decrease in 3-HK and Quin in rat, as expected from the peripheral inhibition of KMO. BBB penetration of the compound is poor, but was observed in the striatum at levels equivalent to the observed EC₅₀ for rat microglial cells. Increased brain extracellular levels of Kyn, KynA, and anthranilic acid were observed, as was a relatively modest increase in 3-HK, although much smaller than that observed from the administration of exogenous Kyn. This provides indirect evidence that peripheral and central inhibition are both occurring, as it would otherwise be expected that 3-HK levels should increase in a manner similar to that of exogenous Kyn administration [14].

Phenylloxadiazoles

The phenylloxadiazoles were first reported by Milne *et al.* (G. Milne, PhD thesis, University of St Andrews, 2013), and tested further by Wilkinson *et al.* (M. Wilkinson, PhD Thesis, The University of Edinburgh, 2013). Some important differences are observed in the phenylloxadiazoles compared with the structurally similar phenylpyrimidines. In the phenylpyrimidines, carboxylates are highly active, whereas they are inactive in the phenylloxadiazoles (Box 1,

32–33). Activity is not obtained until the carboxylates are converted to benzamides (**34**). In the same study, the benzenesulfonamide Ro 61-8048 gave a much higher K_i of 1 μ M in *P. fluorescens* compared with the nanomolar values reported by Rover *et al.* in rat kidney KMO [56]. This highlights a greater need to investigate the interspecies differences among KMO enzymes for the purposes of drug discovery.

Other scaffolds

Heidempergher *et al.* reported a limited SAR of the modestly active pyrroloquinolines, the strongest of which is shown in Box 1 (**35**) [103]. Removal of the carboxylate group negated inhibition even at 100 μ M. Removal of the pyrrole ring from **35** resulted in negligible activity, as did saturation of the benzene ring. A series of 3-oxo-propanenitrile molecules were also patented and described with 40 nM IC_{50} (Box 1, **36**) [104], although no SAR is available. More recently, the marine sponge amine Ianthellamide A was reported with an IC_{50} of 1.5 μ M in *in vitro* assays and gave a threefold increase in rat brain KynA levels when administered at 200 mg/kg (Box 1, **37**).

Concluding remarks

There is an ever-increasing body of knowledge surrounding the role of the KP in immune and inflammation biology. In particular, the role of L-Kyn, 3-HK, and kynurenic and quinolinic acids has made the KMO branch point of the KP an attractive target for treating neurodegenerative and/or neuroinflammatory conditions. A typical stumbling block in drug development for central targets is the need to cross the BBB to reach the target site; however, peripheral inhibition of KMO has demonstrated pharmacologically relevant, central effects. The recent release of the KMO crystal structure has seen a resurgence of interest in KMO drug discovery, but there are still obstacles to overcome in the areas of human KMO availability, interspecies differences, and the details of KMO dynamics and reaction mechanism.

Appendix A. Supplementary data

Supplementary data associated with this article can be found, in the online version, at <http://dx.doi.org/10.1016/j.drudis.2015.11.001>.

References

- Muller, A.J. *et al.* (2005) Inhibition of indoleamine 2,3-dioxygenase, an immunoregulatory target of the cancer suppression gene Bin1, potentiates cancer chemotherapy. *Nat. Med.* 11, 312–319
- Han, Q. *et al.* (2010) Structure, expression, and function of kynurenine aminotransferases in human and rodent brains. *Cell. Mol. Life Sci.* 67, 353–368
- Pearson, S.J. and Reynolds, G.P. (1992) Increased brain concentrations of a neurotoxin, 3-hydroxykynurenine, in Huntington's disease. *Neurosci. Lett.* 144, 199–201
- Chen, Y. and Guillemin, G.J. (2009) Kynurenine pathway metabolites in humans: disease and healthy states. *Int. J. Tryptophan Res.* 2, 1–19
- Courtney, S. and Scheel, A. (2010) Modulation of the kynurenine pathway for the potential treatment of neurodegenerative diseases. In *Neurodegenerative Diseases*, (Vol. 6) (Dominguez, C., ed.), pp. 149–176, Springer
- Guillemin, G.J. (2012) Quinolinic acid, the inescapable neurotoxin. *FEBS J.* 279, 1356–1365
- Schwarz, M. *et al.* (2013) Increased 3-Hydroxykynurenine serum concentrations differentiate Alzheimer's disease patients from controls. *Eur. Arch. Psychiatry Clin. Neurosci.* 263, 345–352
- Giorgini, F. (2012) Targeting the kynurenine pathway in Huntington's disease. *Adv. Clin. Neurosci. Rehab.* 12, 7–8
- Majláth, Z. and Vécsei, L. (2014) NMDA antagonists as Parkinson's disease therapy: differentiating the evidence. *Neurodegen. Dis. Manage.* 4, 23–30
- Schwarcz, R. *et al.* (2012) Kynurenines in the mammalian brain: when physiology meets pathology. *Nat. Rev. Neurosci.* 13, 465–477
- Vécsei, L. *et al.* (2013) Kynurenines in the CNS: recent advances and new questions. *Nat. Rev. Drug Discov.* 12, 64–82
- Amaral, M. *et al.* (2013) Structural basis of kynurenine 3-monooxygenase inhibition. *Nature* 496, 382–385
- Lowe, D.M. *et al.* (2014) Lead discovery for human kynurenine 3-monooxygenase by high-throughput RapidFire mass spectrometry. *J. Biomol. Screen.* 19, 508–515
- Toledo-Sherman, L.M. *et al.* (2015) Development of a series of aryl pyrimidine kynurenine monooxygenase inhibitors as potential therapeutic agents for the treatment of Huntington's disease. *J. Med. Chem.* 58, 1159–1183
- Takikawa, O. (2005) Biochemical and medical aspects of the indoleamine 2,3-dioxygenase-initiated L-tryptophan metabolism. *Biochem. Biophys. Res. Commun.* 338, 12–19
- Griffiths, H.R. *et al.* (1992) Oxygen radical induced fluorescence in proteins; identification of the fluorescent tryptophan metabolite N-formyl kynurenine, as a biological index of radical damage. *Amino Acids* 3, 183–194
- Dreaden, T.M. *et al.* (2011) N-Formylkynurenine as a marker of high light stress in photosynthesis. *J. Biol. Chem.* 286, 22632–22641
- Parker, N.R. *et al.* (2004) Protein-bound kynurenine is a photosensitizer of oxidative damage. *Free Radic. Biol. Med.* 37, 1479–1489
- Linetsky, M. *et al.* (2014) UVA light-excited kynurenines oxidize ascorbate and modify lens proteins through the formation of advanced glycation end products: implications for human lens aging and cataract formation. *J. Biol. Chem.* 289, 17111–17123
- Opitz, C.A. *et al.* (2011) An endogenous tumour-promoting ligand of the human aryl hydrocarbon receptor. *Nature* 478, 197–203
- Noakes, R. (2015) The aryl hydrocarbon receptor: a review of its role in the physiology and pathology of the integument and its relationship to the tryptophan metabolism. *Int. J. Tryptophan Res.* 8, 7–18
- Goldstein, L.E. *et al.* (2000) 3-Hydroxykynurenine and 3-hydroxyanthranilic acid generate hydrogen peroxide and promote α -crystallin cross-linking by metal ion reduction. *Biochemistry* 39, 7266–7275
- Perkins, M.N. and Stone, T.W. (1982) An iontophoretic investigation of the actions of convulsant kynurenines and their interaction with the endogenous excitant quinolinic acid. *Brain Res.* 247, 184–187
- Parsons, C.G. *et al.* (1997) Novel systemically active antagonists of the glycine site of the N-methyl-D-aspartate receptor: electrophysiological, biochemical and behavioral characterization. *J. Pharmacol. Exp. Ther.* 283, 1264–1275
- Hilmas, C. *et al.* (2001) The brain metabolite kynurenic acid inhibits $\alpha 7$ nicotinic receptor activity and increases non- $\alpha 7$ nicotinic receptor expression: physiopathological implications. *J. Neurosci.* 21, 7463–7473
- Wang, J. *et al.* (2006) Kynurenic acid as a ligand for orphan G protein-coupled receptor GPR35. *J. Biol. Chem.* 281, 22021–22028
- DiNatale, B.C. *et al.* (2010) Kynurenic acid is a potent endogenous aryl hydrocarbon receptor ligand that synergistically induces interleukin-6 in the presence of inflammatory signaling. *Toxicol. Sci.* 115, 89–97
- Lugo-Huitrón, R. *et al.* (2011) On the antioxidant properties of kynurenic acid: free radical scavenging activity and inhibition of oxidative stress. *Neurotoxicol. Teratol.* 33, 538–547
- Stone, T.W. and Perkins, M.N. (1981) Quinolinic acid: a potent endogenous excitant at amino acid receptors in CNS. *Eur. J. Pharmacol.* 72, 411–412
- Ríos, C. and Santamaría, A. (1991) Quinolinic acid is a potent lipid peroxidant in rat brain homogenates. *Neurochem. Res.* 16, 1139–1143
- Štípek, S. *et al.* (1997) The effect of quinolinic acid on rat brain lipid peroxidation is dependent on iron. *Neurochem. Int.* 30, 233–237
- Pláteník, J. *et al.* (2001) Quinolinic acid-iron (II) complexes: slow autoxidation, but enhanced hydroxyl radical production in the Fenton reaction. *Free Radic. Res.* 34, 445–459
- Ross, C.A. and Tabrizi, S.J. (2011) Huntington's disease: from molecular pathogenesis to clinical treatment. *Lancet Neurol.* 10, 83–98
- Giorgini, F. *et al.* (2005) A genomic screen in yeast implicates kynurenine 3-monooxygenase as a therapeutic target for Huntington's disease. *Nat. Genet.* 37, 526–531

- 35 Okamoto, H. *et al.* (1967) On the submitochondrial localization of L-kynurenine-3-hydroxylase. *Biochem. Biophys. Res. Commun.* 26, 309–314
- 36 Orr, A.L. *et al.* (2008) N-terminal mutant huntingtin associates with mitochondria and impairs mitochondrial trafficking. *J. Neurosci.* 28, 2783–2792
- 37 Stone, T.W. and Darlington, L.G. (2002) Endogenous kynurenes as targets for drug discovery and development. *Nat. Rev. Drug Discov.* 1, 609–620
- 38 Campesan, S. *et al.* (2011) The kynurenine pathway modulates neurodegeneration in a Drosophila model of Huntington's disease. *Curr. Biol.* 21, 961–966
- 39 Guidetti, P. *et al.* (2004) Neostriatal and cortical quinolinate levels are increased in early grade Huntington's disease. *Neurobiol. Dis.* 17, 455–461
- 40 Guidetti, P. *et al.* (2006) Elevated brain 3-hydroxykynurenine and quinolinate levels in Huntington disease mice. *Neurobiol. Dis.* 23, 190–197
- 41 Sathyaikumar, K.V. *et al.* (2010) Dysfunctional kynurenine pathway metabolism in the R6/2 mouse model of Huntington's disease. *J. Neurochem.* 113, 1416–1425
- 42 Jauch, D. *et al.* (1995) Dysfunction of brain kynurenic acid metabolism in Huntington's disease: focus on kynurenine aminotransferases. *J. Neurol. Sci.* 130, 39–47
- 43 Amori, L. *et al.* (2009) On the relationship between the two branches of the kynurenine pathway in the rat brain *in vivo*. *J. Neurochem.* 109, 316–325
- 44 Behan, W.M.H. and Stone, T.W. (2000) Role of kynurenes in the neurotoxic actions of kainic acid. *Br. J. Pharmacol.* 129, 1764–1770
- 45 Moroni, F. *et al.* (2005) Kynurenine 3-mono-oxygenase inhibitors reduce glutamate concentration in the extracellular spaces of the basal ganglia but not in those of the cortex or hippocampus. *Neuropharmacology* 48, 788–795
- 46 Moroni, F. *et al.* (2003) Studies on the neuroprotective action of kynurenine mono-oxygenase inhibitors in post-ischemic brain damage. *Adv. Exp. Med. Biol.* 527, 127–136
- 47 Citron, M. (2010) Alzheimer's disease: strategies for disease modification. *Nat. Rev. Drug Discov.* 9, 387–398
- 48 Rahman, A. *et al.* (2009) The excitotoxin quinolinic acid induces tau phosphorylation in human neurons. *PLoS ONE* 4, e6344
- 49 Bonda, D.J. *et al.* (2010) Indoleamine 2,3-dioxygenase and 3-hydroxykynurenine modifications are found in the neuropathology of Alzheimer's disease. *Redox Rep.* 15, 161–168
- 50 Guillemain, G.J. *et al.* (2007) Mass spectrometric detection of quinolinic acid in microdissected Alzheimer disease plaques. *Int. Congress Ser.* 1304, 404–408
- 51 Guillemain, G.J. *et al.* (2005) Indoleamine 2,3 dioxygenase and quinolinic acid immunoreactivity in Alzheimer's disease hippocampus. *Neuropathol. Appl. Neurobiol.* 31, 395–404
- 52 Guillemain, G.J. *et al.* (2003) Aβ1-42 induces production of quinolinic acid by human macrophages and microglia. *NeuroReport* 14, 2311–2315
- 53 Zwilling, D. *et al.* (2011) Kynurenine 3-mono-oxygenase inhibition in blood ameliorates neurodegeneration. *Cell* 145, 863–874
- 54 Rover, S. *et al.* (1997) Synthesis and biochemical evaluation of N-(4-phenylthiazol-2-yl)benzenesulfonamides as high-affinity inhibitors of kynurenine 3-hydroxylase. *J. Med. Chem.* 40, 4378–4385
- 55 Muchowski, P.J. *et al.* Gladstone Institute and University of Maryland. Small molecule inhibitors of kynurenine-3-mono-oxygenase. WO2008/022286
- 56 Benatti, L. *et al.* Newron Pharmaceuticals. Glycoside derivatives of 2-(3,4-dichlorobenzoyl)-cyclopropane-1-carboxylic acid [sic]. EP1475385A1
- 57 Hwang, O. (2013) Role of oxidative stress in Parkinson's disease. *Exp. Neurobiol.* 22, 11–17
- 58 Winklhofer, K.F. and Haass, C. (2010) Mitochondrial dysfunction in Parkinson's disease. *Biochim. Biophys. Acta Mol. Basis Dis.* 1802, 29–44
- 59 Olanow, C.W. and Brundin, P. (2013) Parkinson's disease and alpha synuclein: is Parkinson's disease a prion-like disorder? *Mov. Disord.* 28, 31–40
- 60 Dong, X.-x. *et al.* (2009) Molecular mechanisms of excitotoxicity and their relevance to pathogenesis of neurodegenerative diseases. *Acta Pharmacol. Sin.* 30, 379–387
- 61 Reale, M. *et al.* (2009) Peripheral cytokines profile in Parkinson's disease. *Brain Behav. Immunity* 23, 55–63
- 62 Widner, B. *et al.* (2002) Increased neopterin production and tryptophan degradation in advanced Parkinson's disease. *J. Neural Transmission* 109, 181–189
- 63 Ogawa, T. *et al.* (1992) Kynurenine pathway abnormalities in Parkinson's disease. *Neurology* 42, 1702
- 64 Hartai, Z. *et al.* (2005) Kynurenine metabolism in plasma and in red blood cells in Parkinson's disease. *J. Neurol. Sci.* 239, 31–35
- 65 Gulaj, E. *et al.* (2010) Kynurenine and its metabolites in Alzheimer's disease patients. *Adv. Med. Sci.* 55, 204–211
- 66 Lee, D.Y. *et al.* (2008) Kynurenic acid attenuates MPP⁺-induced dopaminergic neuronal cell death via a Bax-mediated mitochondrial pathway. *Eur. J. Cell Biol.* 87, 389–397
- 67 Silva-Adaya, D. *et al.* (2011) Protective effect of L-kynurenine and probenecid on 6-hydroxydopamine-induced striatal toxicity in rats: implications of modulating kynurenate as a protective strategy. *Neurotoxicol. Teratol.* 33, 303–312
- 68 Miranda, A.F. *et al.* (1997) Protection against quinolinic acid-mediated excitotoxicity in nigrostriatal dopaminergic neurons by endogenous kynurenic acid. *Neuroscience* 78, 967–975
- 69 Beers, D.R. *et al.* (2011) Neuroinflammation modulates distinct regional and temporal clinical responses in ALS mice. *Brain Behav. Immun.* 25, 1025–1035
- 70 McGeer, P.L. and McGeer, E.G. (2002) Inflammatory processes in amyotrophic lateral sclerosis. *Muscle Nerve* 26, 459–470
- 71 Chen, Y. *et al.* (2009) Recent advances in the treatment of amyotrophic lateral sclerosis. Emphasis on kynurenine pathway inhibitors. *Central Nervous Syst. Agents Med. Chem.* 9, 32–39
- 72 Guillemain, G.J. *et al.* (2006) Implications for the kynurenine pathway and quinolinic acid in amyotrophic lateral sclerosis. *Neurodegen. Dis.* 2, 166–176
- 73 Fukui, S. *et al.* (1991) Blood-brain barrier transport of kynurenes: implications for brain synthesis and metabolism. *J. Neurochem.* 56, 2007–2017
- 74 Erickson, J.B. *et al.* (1992) A radiometric assay for kynurenine 3-hydroxylase based on the release of 3H₂O during hydroxylation of L-[3,5-³H]kynurenine. *Anal. Biochem.* 205, 257–262
- 75 Guillemain, G.J. *et al.* (2001) Kynurenine pathway metabolism in human astrocytes: a paradox for neuronal protection. *J. Neurochem.* 78, 842–853
- 76 Guillemain, G. *et al.* (2003) Expression of the kynurenine pathway enzymes in human microglia and macrophages. *Adv. Exp. Med. Biol.* 527, 105–112
- 77 Heyes, M. *et al.* (1997) Different kynurenine pathway enzymes limit quinolinic acid formation by various human cell types. *Biochem. J.* 326, 351–356
- 78 Rzeski, W. *et al.* (2005) Demonstration of kynurenine aminotransferases I and II and characterization of kynurenic acid synthesis in cultured cerebral cortical neurons. *J. Neurosci. Res.* 80, 677–682
- 79 Guillemain, G.J. *et al.* (2007) Characterization of the kynurenine pathway in human neurons. *J. Neurosci.* 27, 12884–12892
- 80 van Berkel, W.J.H. *et al.* (2006) Flavoprotein monooxygenases, a diverse class of oxidative biocatalysts. *J. Biotechnol.* 124, 670–689
- 81 Breton, J. *et al.* (2000) Functional characterization and mechanism of action of recombinant human kynurenine 3-hydroxylase. *Eur. J. Biochem.* 267, 1092–1099
- 82 Moonen, M.J.H. *et al.* (2008) Flavoenzyme-catalysed oxygenations and oxidations of phenolic compounds. *Adv. Synth. Catal.* 344, 1023–1035
- 83 Crozier-Reabe, K.R. *et al.* (2008) Kynurenine 3-mono-oxygenase from *Pseudomonas fluorescens*: substrate-like inhibitors both stimulate flavin reduction and stabilize the flavin-peroxo intermediate yet result in the production of hydrogen peroxide. *Biochemistry* 47, 12420–12433
- 84 Crozier, K.R. and Moran, G.R. (2007) Heterologous expression and purification of kynurenine-3-mono-oxygenase from *Pseudomonas fluorescens* strain 17400. *Protein Expr. Purif.* 51, 324–333
- 85 Chapman, S.K. and Reid, G.A., eds (1999) *Flavoprotein Protocols*, Humana Press
- 86 Montersino, S. *et al.* (2011) Catalytic and structural features of flavoprotein hydroxylases and epoxidases. *Adv. Synth. Catal.* 353, 2301–2319
- 87 Gatti, D. *et al.* (1994) The mobile flavin of 4-OH benzoate hydroxylase. *Science* 266, 110–114
- 88 Wilson, K. *et al.* (2014) Bacterial expression of human kynurenine 3-mono-oxygenase: solubility, activity, purification. *Protein Expr. Purif.* 95, 96–103
- 89 Hirai, K. *et al.* (2010) Dual role of the carboxyl-terminal region of pig liver L-kynurenine 3-mono-oxygenase: mitochondrial-targeting signal and enzymatic activity. *J. Biochem.* 148, 639–650
- 90 Wonodi, I. *et al.* (2014) Influence of kynurenine 3-mono-oxygenase (KMO) gene polymorphism on cognitive function in schizophrenia. *Schizophrenia Res.* 160, 80–87
- 91 Lavebratt, C. *et al.* (2014) The KMO allele encoding Arg452 is associated with psychotic features in bipolar disorder type 1, and with increased CSF KYNA level and reduced KMO expression. *Mol. Psychiatry* 19, 334–341
- 92 Natalini, B. *et al.* (1995) Synthesis and activity of enantiopure (S) (m-nitrobenzoyl) alanine, potent kynurenine-3-hydroxylase inhibitor. *Bioorg. Med. Chem. Lett.* 5, 1451–1454
- 93 Carpenedo, R. *et al.* (1994) Inhibitors of kynurenine hydroxylase and kynureninase increase cerebral formation of kynurenate and have sedative and anticonvulsant activities. *Neuroscience* 61, 237–244
- 94 Giordani, A. *et al.* (1998) 4-Phenyl-4-oxo-butanolic acid derivatives inhibitors of kynurenine 3-hydroxylase. *Bioorg. Med. Chem. Lett.* 8, 2907–2912
- 95 Varasi, M. *et al.* Pharmcia and Upjohn. 2-substituted benzoyl-cycloalkyl-1-carboxylic acid derivatives. WO 98/40344
- 96 Wityak, J. *et al.* CHDI Inc. Certain kynurenine-3-mono-oxygenase inhibitors, pharmaceutical compositions, and methods of use thereof. WO2010/017132

- 99 Autier, V. *et al.* Merck GMBH. Kynurenine 3-hydroxylase inhibitors for the treatment of diabetes. WO2004/060369
- 100 Autier, V. *et al.* Merck GMBH. Use of 4-oxobutanoic acid derivatives in the treatment of pathologies associated with immunological disorders. WO2009/071161
- 101 Benatti, L. *et al.* Newron Pharmaceuticals. Halothenoil-cyclopropane-1-carboxylic acid derivatives. 1 424 333
- 102 Muchowski, P.J. *et al.* Gladstone Institute and University of Maryland. Small molecule inhibitors of kynurenine-3-monooxygenase. WO2008/022281
- 103 Heidempergher, F. *et al.* (1999) Pyrrolo[3,2-c]quinoline derivatives: a new class of kynurenine-3-hydroxylase inhibitors. *Il Farmaco* 54, 152–160
- 104 Pevarello, P. *et al.* Pharmcia and Upjohn. Tricyclic 3-oxo-propanitrile compounds. WO99/16753
- 105 Giordani, A. *et al.* (1995) Enantiospecific synthesis in vitro activity of selective inhibitors of rat brain kynureninase kynurenine-3-hydroxylase. *Adv. Exp. Med. Biol.* 398, 531–534

Pages 210-221 of this thesis have been removed as they contain published material under copyright. Removed contents published as:

Hallen, A., Cooper, A.J.L., Smith, J.R. et al. (2015) Ketimine reductase/CRYM catalyzes reductive alkylamination of α -keto acids, confirming its function as an imine reductase. *Amino Acids*, vol. 47, pp. 2457–2461.

<https://doi.org/10.1007/s00726-015-2044-8>

Austin Christopher J. D., Moir Michael, Kahlert Jan, Smith Jason R., Jamie Joanne F., Kassiou Michael, Rendina Louis M. (2015) Carborane-Containing Hydroxyamidine Scaffolds as Novel Inhibitors of Indoleamine 2,3-Dioxygenase 1 (IDO1). *Australian Journal of Chemistry*, Vol. 68, no. 12, pp. 1866-1870.

<https://doi.org/10.1071/CH15489>

The first indoleamine-2,3-dioxygenase-1 (IDO1) inhibitors containing carborane†

Cite this: *Dalton Trans.*, 2014, **43**, 10719

Christopher J. D. Austin,^a Jan Kahlert,^a Fatiah Issa,^a John H. Reed,^a Jason R. Smith,^b Joseph A. Ioppolo,^a Jennifer A. Ong,^c Joanne F. Jamie,^b David Hibbs^c and Louis M. Rendina^{*a}

Received 12th February 2014,
Accepted 3rd April 2014

DOI: 10.1039/c4dt00444b

www.rsc.org/dalton

Indoleamine-2,3-dioxygenase-1 (IDO1) is a critical immunoregulatory enzyme responsible for the metabolism of tryptophan during inflammation and disease. Based upon a pyranonaphthoquinone framework, the first examples of indoleamine-2,3-dioxygenase-1 (IDO1) inhibitors containing a carborane cage are reported. The novel *closo*-1,2-carboranyl-*N*-pyranonaphthoquinone derivatives display low μM binding affinity for the human recombinant enzyme, with IC_{50} values ranging from 0.78 to 1.77 μM .

Introduction

A lack of structural diversity has been cited as a potential limitation to future drug design.¹ Whilst the element boron currently accounts for approximately 0.5% of framework heteroatoms within the CAS Registry,² the unique chemical properties of this element are worthy of further exploration in medicinal chemistry. Boron clusters, particularly the icosahedral dicarba-*closo*-dodecaboranes (commonly referred to as *closo*-carboranes), have attracted increasing interest from medicinal chemists in recent years as unique pharmacophores.³ With a three-dimensional volume (70–80 Å³) that is comparable to the rotational sweep of a phenyl ring, low toxicity, high kinetic stability to hydrolysis and metabolic degradation, a tunable hydrophobic character, and the possibility of many versatile chemical modifications, carborane clusters offer medicinal chemists a powerful tool to alter shape and charge distribution in both existing and novel drug frameworks.³ Due to the considerable hydrophobicity and unique shape of the *closo*-carboranes, enzyme targets possessing hydrophobic regions in their active sites have been a focus of recent carborane-based drug development.¹ With an active site dominated by two hydrophobic binding pockets,⁴ the haemoprotein indoleamine-2,3-dioxygenase-1 (IDO1; EC 1.13.11.52) is an excellent candidate for a study of carborane–enzyme interactions.

IDO1 is responsible for the first catabolic step (oxidative cleavage of *L*-tryptophan to *N'*-formylkynurenine, Fig. 1) of the 'Kynurenine Pathway', the major pathway for tryptophan metabolism (*ca.* 90%) in mammals. An immunoregulatory enzyme controlled by inflammatory cytokines (principally interferon- γ); during infection and disease increased expression of IDO1 lowers cellular *L*-tryptophan levels, which elicits a range of innate and adaptive immune responses. Most significantly, low tryptophan levels and tryptophan metabolites downstream of *N'*-formylkynurenine affect T-lymphocyte behaviour and communication, resulting in T-cell tolerance and apoptosis.^{5,6} Evolved to suppress autoimmunity during periods of sustained inflammation, IDO1 activity is co-opted by cancer cells (among other pathological conditions) as a mechanism to evade immune detection.^{7,8} Thus, restoration of normal immune response *via* IDO1 enzyme inhibition has been the subject of intense study in recent years due to the potential use of such inhibitors as immunoregulatory chemotherapeutic agents.⁹

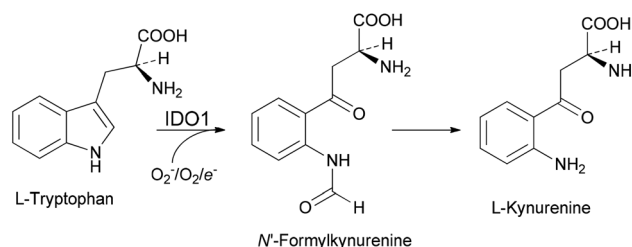


Fig. 1 The first steps of the 'Kynurenine Pathway'. Indoleamine-2,3-dioxygenase-1 (IDO1) cleaves the 2,3-double bond of the *L*-tryptophan indole ring *via* incorporation of O_2 or O_2^- to form *N'*-formylkynurenine. *N'*-Formylkynurenine spontaneously (and *via* enzymatic cleavage) forms *L*-kynurenine.

^aSchool of Chemistry, The University of Sydney, Sydney, NSW 2006, Australia.

E-mail: lou.rendina@sydney.edu.au

^bDepartment of Chemistry and Biomolecular Sciences, Macquarie University, Sydney, NSW 2109, Australia

^cFaculty of Pharmacy, The University of Sydney, Sydney, NSW 2006, Australia

† Electronic supplementary information (ESI) available: X-ray diffraction details of 6. CCDC 967701. For ESI and crystallographic data in CIF or other electronic format see DOI: 10.1039/c4dt00444b

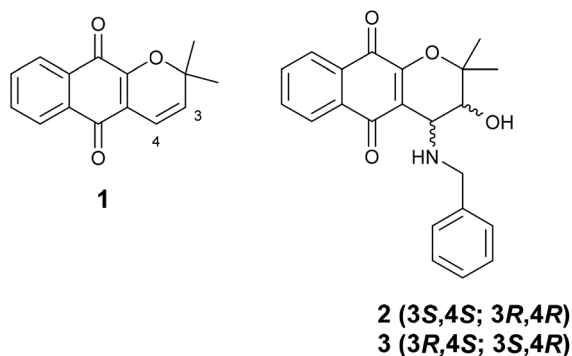


Fig. 2 Dehydro- α -lapachone (**1**); a natural product containing the pyranonaphthoquinone framework which has demonstrated excellent IDO1 inhibition.^{14,15}

Until the human IDO1 structure was determined by means of X-ray crystallography in 2006,⁴ IDO1 inhibitor development was mainly based on alterations of the tryptophan-indole scaffold with the best inhibitors displaying IC_{50} affinities in the μM range.⁹ However, through a greater understanding of the substrate active-site, which is characterised by a large hydrophobic pocket containing the haem *b* catalytic site and a smaller hydrophobic region near the entrance to the active site, significant developments in non-tryptophan related frameworks have been made in recent years,^{10,11} thus improving the potency of IDO1 inhibitors for potential clinical trial assessment.

Following the discovery of pyranonaphthoquinones from marine natural products extracts with potent IDO1 inhibitory properties (Annulin B from *Garveia annulata*¹² and Exiguamine A from *Neopetrosia exigua*¹³), pyranonaphthoquinone frameworks have emerged as promising lead candidates for further synthetic development (**1**).¹⁴ Interestingly, the *cis* diastereomers (3*S*,4*S*/3*R*,4*R*) of the benzylamino-pyranonaphthoquinone derivative (Fig. 2, **2**) are reported to exhibit some of the most potent IDO1 inhibition observed to date.¹⁴

Inclusion of both benzylamino and hydroxyl groups (**2**, **3**) into the pyranonaphthoquinone framework was found to significantly increase IDO1 inhibitor potency over the parent compound **1** (Fig. 2) and structure-activity relationship (SAR) studies of other pyran ring derivatives¹⁴ revealed substitution at the 4-position of the pyran ring was readily tolerated. Given the potential for carboranes to positively modify existing drug frameworks,³ bioisosteric replacement of the benzyl group in **2** and **3** with a *closo*-1,2-carborane cage and an assessment of carborane substitution on inhibiting IDO1 activity was the primary goal of this work. Herein we report the first carborane-based inhibitors which are designed to target the active site of IDO1 and inhibit its catalytic activity.

Results and discussion

Molecular modelling

The essential structural features of IDO1 which govern tolerance for variation at the 4-position of the pyranonaphtho-

quinone framework are not well understood. Molecular modelling of a potent 4-benzyl substituted pyranonaphthoquinone IDO1 inhibitor ((3*S*,4*S*)-**2**)¹⁴ was thus initially undertaken to assess the feasibility of *closo*-1,2-carborane substitution at this position. In order to preclude expulsion of the (3*S*,4*S*)-**2** ligand from the IDO1 active-site during energy minimisations performed as part of a stochastic conformational search, a low-mode molecular dynamics (LMMD) 'what-if' docking was investigated. This method employed a short (*ca.* 1 ps) low-mode molecular dynamics simulation followed by energy minimisation to achieve novel ligand-protein conformations – a process successfully utilised in previous studies to dock other types of IDO1 inhibitors.¹¹ Briefly, poses employing both quinone oxygen atoms (5-oxo, 10-oxo) of (3*S*,4*S*)-**2** were created as haem ligands. The starting position of each LMMD docking run was created by including (3*S*,4*S*)-**2** within the active site of IDO1. (3*S*,4*S*)-**2** was then energy minimised without influence from the IDO1 protein to form a low energy conformation. This conformation was then minimised within the active site while holding the protein and haem group rigid. Finally, the active site and ligand were relaxed through energy minimisation. The resulting relaxed docking pose for (3*S*,4*S*)-**2** within the active site of IDO1 was found to maintain considerable similarity with the starting structure. The ensuing conformation was then used as the starting position of the next pose iteration. LMMD simulations were allowed 700 attempts at finding binding positions. These calculations resulted in 51 unique structures for the 5-oxo (3*S*,4*S*)-**2** ligation pose and 23 structures for the 10-oxo (3*S*,4*S*)-**2** ligation pose (see ESI†). The more likely 5-oxo (3*S*,4*S*)-**2** ligation pose allows the functionalised 3,4-pyran ring to interact with both the haem propanoate arm (*via* the benzylamino group) and the Arg231 residue (*via* both hydroxyl and amino groups) located near the entrance to the IDO1 active-site (Fig. 3). Indeed, in this pose, the 4-benzyl group of (3*S*,4*S*)-**2** extends into the void of the active-site entrance, indicating some degree of clearance for a variety of sterically-bulky groups (*e.g.* a carborane cage) at this position

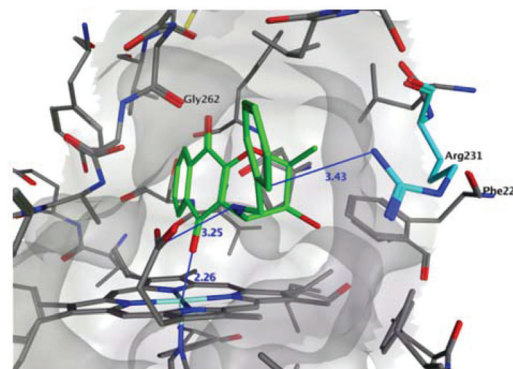


Fig. 3 Example of *in silico* docking of (3*S*,4*S*)-**2** (green) within the active site of IDO1. Atomic distances (Å) – dark blue. Atom colours: grey – IDO1 protein carbon, yellow – sulfur, dark blue – nitrogen, red – oxygen, light blue – iron. Arg231 is highlighted in light blue (right).

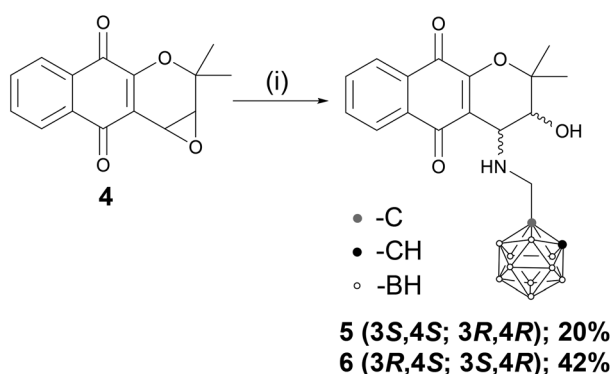
and is in good agreement with the observed data from comprehensive SAR studies.¹⁴

Like many other computer-aided molecular design programs,³ Molecular Operating Environment (2011.10 – the software used to perform LMM docking) does not possess a parameter set for hexavalent boron (a critical atomic property of *closo*-carboranes).¹⁶ As a result, computational modelling of a carborane containing pyranonaphthoquinone was not conducted. However, the modelling of a 4-adamantyl derivative of (3*S*,4*S*)-**2** in which the carbon polycycle possesses similar steric bulk and lipophilicity to a *closo*-carborane cage showed similar docking poses to the benzyl-substituted (3*S*,4*S*)-**2** (see ESI†). Indeed, modelling of both the benzyl- and adamantyl-derivatives confirmed that bulky 4-position substituents can be accommodated readily within the IDO1 active-site entrance void. Given that the molecular environment predicted for pyranonaphthoquinone inhibitors within the IDO1 active-site appears conducive to carborane cage substitution, the synthesis of new *N*-methylamino-*closo*-1,2-carboranylpyranonaphthoquinone derivatives was subsequently undertaken and their *in vitro* inhibition of IDO1 was investigated.

Synthesis

Derivatization of the pyran ring at the 3,4-position of **1** was performed by means of an epoxide ring-opening reaction involving nucleophilic attack of 1-aminomethyl-*closo*-1,2-carborane¹⁷ (or benzylamine) on the epoxide **4** in the presence of a catalytic quantity of InCl₃ in CH₂Cl₂ to afford both *cis* and *trans* diastereomers **5** and **6** after column chromatography and normal phase-HPLC (Scheme 1) in 20% and 42% yield, respectively.^{14,18}

Assignment of the *cis/trans* geometry in these compounds was made by a ¹H NMR coupling constant analysis, and the absolute configuration of (3*R*,4*S*)-**6** was determined by a single-crystal X-ray diffraction study of its *N*-protonated trifluoroacetate salt (Fig. 4 and Table 1). ¹¹B{¹H} NMR studies confirmed that the *closo*-carborane cage remained intact during the preparation of **5** and **6** and no conversion to the *nido* species was observed (*vide infra*).



Scheme 1 The synthesis of *N*-methylamino-*closo*-1,2-carboranylpyranonaphthoquinones. Reagents: (i) 1-aminomethyl-*closo*-1,2-carborane,¹⁷ InCl₃ (5 mol%), CH₂Cl₂.

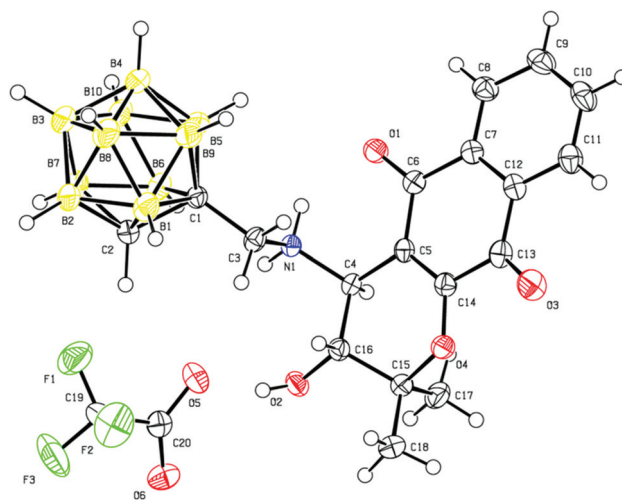


Fig. 4 ORTEP representation of (3*R*,4*S*)-**6** in its *N*-protonated form with trifluoroacetate as a counter-ion.

Table 1 Crystal data for (3*R*,4*S*)-**6**

Crystal data and structure refinement for (3 <i>R</i> ,4 <i>S</i>)- 6	
Identification code	CCDC 967701
Empirical formula	C ₂₀ H ₂₈ B ₁₀ O ₆ NF ₃
Formula weight	543.53
Temperature/K	150
Crystal system	Orthorhombic
Space group	<i>Pbca</i>
<i>a</i> /Å	12.9860(7)
<i>b</i> /Å	19.7953(11)
<i>c</i> /Å	21.0341(12)
α /°	90.00
β /°	90.00
γ /°	90.00
Volume/Å ³	5407.1(5)
<i>Z</i>	8
ρ_{calc} /mg mm ⁻³	1.335
<i>m</i> /mm ⁻¹	0.101
<i>F</i> (000)	2240.0
Crystal size/mm ³	0.2 × 0.1 × 0.1
2 θ range for data collection	3.88 to 52.1°
Index ranges	−13 ≤ <i>h</i> ≤ 15, −24 ≤ <i>k</i> ≤ 24, −25 ≤ <i>l</i> ≤ 25
Reflections collected	37 551
Independent reflections	5324 [<i>R</i> (int) = 0.0445]
Data/restraints/parameters	5324/0/364
Goodness-of-fit on <i>F</i> ²	1.012
Final <i>R</i> indexes [<i>I</i> ≥ 2 σ (<i>I</i>)]	<i>R</i> ₁ = 0.0449, <i>wR</i> ₂ = 0.1070
Final <i>R</i> indexes [all data]	<i>R</i> ₁ = 0.0686, <i>wR</i> ₂ = 0.1203
Largest diff. peak/hole/e Å ⁻³	0.36/−0.26

Additionally, we attempted to prepare the anionic *nido*-7,8-carboranyl species from the *cis* and *trans* *closo*-1,2-carboranyl compounds **5** and **6**, respectively, in order to assess how a dramatic alteration of the hydrophobicity of the carborane cage, whilst preserving much of its steric bulk, affected its interaction with the IDO1 active-site. However, under the conditions of the (mild) deboronation reaction¹⁹ involving CsF and EtOH, the pyranonaphthoquinone ring system was found to be extensively degraded.

Inhibitory constants (IC₅₀) for the new carboranyl derivatives **5** and **6**, along with **1**, **2** and **3**, were determined using

Table 2 Inhibitory activities (IC₅₀) of pyranonaphthoquinone derivatives towards IDO1^a

Compound	IC ₅₀ (μM)
1	1.22 ± 0.08
2	0.35 ± 0.04
3	0.50 ± 0.03
5	0.78 ± 0.02
6	1.77 ± 0.03

^a IC₅₀ (inhibitory concentration 50%) determined with L-tryptophan as the substrate at a concentration of 100 μM. Under the conditions of our assay, the IC₅₀ values of **1**, **2** and **3** were found to be *ca.* 2 to 6-fold higher than those previously reported for the same compounds.¹⁴

recombinant human IDO1^{20,21} in a cell-free assay system, as devised by Takikawa *et al.* with some modifications (Table 2).²² Briefly, ascorbic acid and methylene blue provided the reductive environment necessary for the activation of IDO1 *i.e.* reduction of the Fe³⁺ inactive form to the active Fe²⁺ form of IDO1 that is involved in O₂ binding and metabolism of L-tryptophan to N^ε-formylkynurenine and subsequent conversion to L-kynurenine.²³ Compounds **1**, **2** and **3** were chosen as controls as they represented: the basic pyranonaphthoquinone framework without 4-position modification (**1**) and the equivalent diastereomeric benzyl-substituted pyranonaphthoquinones (**2** and **3**, respectively) to the synthesized *closo*-1,2-carboranyl compounds **5** and **6**.

In accordance with previous studies,¹⁴ the racemic *cis* diastereomer **2** was found to be a significantly more potent inhibitor of IDO1 than the *trans* racemate **3**. The same trend was observed for the *closo*-1,2-carboranyl series (**5** and **6**), indicating that *cis/trans* isomers of both the lipophilic benzyl and *closo*-carboranyl derivatives interact with the IDO1 active site in a similar manner with low μM affinity (Table 2). A minor increase in the IC₅₀ value with *closo*-carborane substitution (*e.g.* *ca.* 2-fold loss of inhibitor potency for **5** when compared to **2**) was observed in our hands. This observation is consistent with the *closo*-1,2-carborane cage slightly diminishing the inhibitor-IDO1 interaction when compared with the analogous benzylamino derivatives **2** and **3**, most likely due to the loss of a cation-π interaction between Arg231 and the benzyl ring, as observed in the molecular modelling for **2** (Fig. 3). Nevertheless, the fact that both *closo*-carboranes **5** and **6** inhibited IDO1 activity at low μM levels (and *closo*-carborane substitution (**5**) enhanced inhibition over the basic pyranonaphthoquinone framework (**1**)) and given the known limited inhibition of IDO1 activity by clinical compounds (*e.g.* 1-methyl-D-tryptophan²⁴ (IC₅₀ > 2.5 mM, Clinical Trial I.D.: NCT00567931)) these results clearly show that second-generation carborane derivatives based on these compounds are an excellent lead for study as potential IDO1 inhibitors.

Experimental

¹H, ¹³C{¹H} and ¹¹B{¹H} NMR spectra were recorded at 300 K on a Bruker AVANCE 400 MHz DRX spectrometer (¹H at

400 MHz, ¹³C at 101 MHz, and ¹¹B at 160 MHz). All NMR signals are reported in ppm. ¹H and ¹³C NMR spectra were referenced to TMS (0 ppm). ¹¹B NMR spectra were referenced according to the IUPAC unified scale (frequency ratio (Ξ) 32.083974). Coupling constants (*J*) are reported in Hz. Peak multiplicities are abbreviated as s (singlet), d (doublet), t (triplet), q (quartet), m (multiplet – unassignable multiplicity or overlapping signals), b (broad). High-resolution ESI-MS were recorded on a Bruker 7 T FTICR mass spectrometer in the positive ESI mode. Normal-phase HPLC was performed on a Waters 2525 binary gradient module equipped with a ZORBAX® RX-SIL column (5 μm, 21.2 mm × 250 mm) and a Waters 2996 photodiode array detector. The results were analysed by means of Waters MassLynx 4.1 software. Solvents and reagents were dried according to literature methods.²⁵ All reactions were performed under an inert atmosphere of nitrogen unless otherwise stated.

General procedure for the synthesis of *N*-methylamino-*closo*-1,2-carboranylpyranonaphthoquinones

To a solution of 2,2-dimethyl-3,4-epoxy-2*H*-naphtho[2,3-*b*]pyran-5,10-dione (**4**) (52.7 mg, 0.22 mmol) in dichloromethane (10 mL) was added 1-aminomethyl-*closo*-1,2-carborane hydrochloride¹⁷ (86 mg, 0.43 mmol) and sodium bicarbonate (36 mg, 0.43 mmol). Subsequently, a catalytic amount of indium(III) chloride (4 mg, 0.018 mmol) was added to the reaction mixture which was left to stir overnight at room temperature. After 14 h, the solvent was removed under reduced pressure to yield a yellow residue that was partially purified *via* flash chromatography (30% EtOAc–hexane) to yield a mixture of two diastereomers (crude 60 mg) which were further separated by preparative normal phase HPLC (isocratic *n*-hexane–isopropanol–trifluoroacetic acid (97 : 3 : 0.1 v/v)).

(**3S,4S/3R,4R**)-4-(1-Aminomethyl-*closo*-1,2-carboranyl)-3-hydroxy-2,2-dimethyl-3,4-dihydro-2*H*-benzo[*g*]chromene-5,10-dione (**5**). Compound **5** was synthesized using the general procedure outlined above in 20% yield (19 mg); mp = 110–112 °C; TLC *R*_f = 0.3 (30% EtOAc–*n*-hexane); *R*_t NP-HPLC (isocratic: *n*-hexane–isopropanol–trifluoroacetic acid (97 : 3 : 0.1 v/v)): 33 min (7 mL min^{−1}); ¹H NMR (CDCl₃) δ: 8.15–8.08 (m, 2H, ArH), 7.82–7.71 (m, 2H, ArH), 4.15 (d, *J* = 4.5 Hz, 1H, HOCH), 4.07 (bs, 1H, BCH), 3.80 (m, 3H, NHCH₂; OH), 3.64 (d, *J* = 13.6 Hz, 1H, NHCH), 3.50 (br s, 1H, NH), 3.0–1.3 (br m, 10H, BH), 1.66 (s, 3H, CH₃), 1.33 (s, 3H; CH₃); ¹³C NMR (CDCl₃) δ: 186.3 (C=O), 178.3 (C=O), 156.2 (O=CCO), 134.9 (ArC), 134.4 (ArC), 131.7 (ArC), 130.9 (ArC), 127.1 (ArC), 126.7 (ArC), 82.1 (HNCH₂), 66.5 (HOCH), 60.2 (C₂H₆CO), 53.3 (BCCH₂), 51.5 (BCH), 24.2 (CH₃), 23.1 (CH₃); ¹¹B NMR (CDCl₃) δ: −2.34 (2B), −4.39 (2B), −9.28 (4B), −13.14 (2B); HR-ESI-MS Calcd for [M + H]⁺ *m/z* 431.29797, Found 431.29799.

(**3R,4S/3S,4R**)-4-(1-Aminomethyl-*closo*-1,2-carboranyl)-3-hydroxy-2,2-dimethyl-3,4-dihydro-2*H*-benzo[*g*]chromene-5,10-dione (**6**). Compound **6** was synthesized using the general procedure outlined above in 41% yield (36 mg); mp = 151–153 °C; TLC *R*_f = 0.3 (30% EtOAc–hexane); *R*_t NP-HPLC (isocratic: *n*-hexane–isopropanol–trifluoroacetic acid (97 : 3 : 0.1 v/v)): 18 min (7 mL min^{−1}); ¹H NMR (CDCl₃) δ: 8.16–8.13 (m, 2H,

ArH), 7.89–7.79 (m, 2H, ArH), 4.28 (d, $J = 14.1$ Hz, 1H, HOCH), 4.16 (m, 3H, NHCH₂; BCH), 3.90 (br s, 1H, OH), 3.82 (d, $J = 14.2$ Hz, 1H, NHCH), 3.50 (br s, 1H, NH), 3.0–1.3 (broad m, 10H, BH), 1.64 (s, 3H, CH₃), 1.33 (s, 3H; CH₃); ¹³C NMR (CDCl₃) δ : 186.7 (C=O), 177.6 (C=O), 156.7 (O=CCO), 135.2 (ArC), 134.9 (ArC), 131.1 (ArC), 130.7 (ArC), 127.3 (ArC), 127.0 (ArC), 110.2 (O=CCCNH), 84.0 (HNCH₂), 69.5 (HOCH), 69.1 (C₂H₆CO), 60.1 (BCCH₂), 58.7 (BCH), 52.1 (CCNH), 25.5 (CH₃), 18.7 (CH₃); ¹¹B NMR (CDCl₃) δ : −1.64 (2B), −3.62 (2B), −8.77 (4B), −12.70 (2B); HR-ESI-MS Calcd for [M + H]⁺ m/z 431.29797, Found 431.29799.

X-ray diffraction studies

Single crystals of (3*R*,4*S*)-6 were grown by means of liquid–liquid diffusion using a DCM–*n*-hexane mixture. A suitable crystal was selected *via* Paratone-N on a Bruker ApexII diffractometer. The crystal was kept at 150 K during data collection. Using Olex2,²⁶ the structure was solved with the ShelXS²⁷ structure solution program using Direct Methods and refined with the ShelXL²⁸ refinement package using Least Squares minimisation.

Molecular modelling (docking) studies

In silico docking studies were performed on (3*S*,4*S*)-2 (or the related 4-adamantyl-substituted pyranonaphthoquinone).¹⁴ All docking was performed on the 2D0T crystal structure.⁴ All molecular mechanics techniques used the CHARMM22 force-field and the Born solvation model, as implemented Molecular Operating Environment version 2011.10 (MOE, Chemical Computing Group, Montreal, Canada). Dielectric constants were set to 4 and 80 for inside and outside the protein, respectively.

The LMMD methodology was employed using MOE's Conformational Search protocol. Default parameters were used except the iteration limit for finding new conformations was 700. The RMSD for defining two poses as equivalent was 0.25 Å and fixed atoms were excluded from this measurement. Flexible species were the ligand, the propanoate arm of haem, and IDO1 amino acid residues: T126, C129, V130, F163, F164, S167, F226, L230, R231, L234, S235, A260, S263, A264, F291, H346, I354 and L384. All backbone atoms of the protein were held fixed. During the 'What-If' analysis,¹¹ the restraint boundaries between iron and the ligating atom were 2.1 and 2.2 Å with a weighting constant of 20 kcal mol^{−1}. RMSD for energy minimisation was 0.005.

IDO1 inhibition assays

Recombinant human IDO1. Recombinant human IDO1 was expressed and purified according to literature procedures.^{20,21}

General assay protocol

The standard reaction mixture (200 μ L) contained 50 mM potassium phosphate buffer (pH 6.5), 10 mM ascorbic acid (neutralised with NaOH), 100 μ g mL^{−1} catalase, 10 μ M methylene blue, 100 μ M L-tryptophan, and 10 nM IDO1. The assay was conducted at 37 °C for 20 min (assay initiated ($T_{\min} = 0$) on the addition of 10 mM ascorbic acid to the pre-warmed mixture)

and stopped by means of addition of 40 μ L of 30% (w/v) trichloroacetic acid. The mixture was then heated at 65 °C for 15 min and 125 μ L of the reaction mixture was transferred into a well of a 96-well microtitre plate and mixed with 125 μ L of 2% (w/v) *p*-dimethylaminobenzaldehyde in glacial acetic acid. The yellow pigment derived from reaction with kynurenine was measured at 480 nm using a Spectramax M5 microtitre plate reader (Molecular Devices).

Inhibitor assessment

For inhibitor assessment, compounds 1, 2, 3, 5 and 6 were added to the standard reaction mixture over a linear concentration range (10 μ M–0.0195 μ M for compounds 5 and 6; 2 μ M–0.0039 μ M for compounds 1, 2 and 3) in DMSO (final concentration of DMSO in standard reaction mixture 2%). DMSO (2%) alone was used as the carrier control (*i.e.* 0 μ M inhibitor). IC₅₀ values were determined by means of non-linear regression analysis employing GraphPad Prism 4® (GraphPad Software).

Conclusion

We have reported a new class of boronated agents that can effectively inhibit IDO1 at low μ M concentrations. The *closo*-carboranes 5 and 6 display IDO1 binding characteristics that are comparable to their corresponding benzyl analogues. As the carborane cage is well tolerated by the IDO1 enzyme in cell-free assays, future work will focus on design of other carborane-based derivatives which engage the large lipophilic IDO1 active site pocket. The results of this work will be reported in due course.

Acknowledgements

We would like to thank Mr Fangzhi Jia and Ms Elizabeth Vleeskens for their contributions to some of the synthetic steps. We thank Dr Nick Proschogo and Dr Ian Luck for assistance with the HR-ESI-MS and NMR spectroscopic studies, respectively. We also thank the ARC and NBCF for funding.

Notes and references

- 1 J. Kahlert, C. Austin, M. Kassiou and L. Rendina, *Aust. J. Chem.*, 2013, **66**, 1118–1123.
- 2 A. H. Lipkus, Q. Yuan, K. A. Lucas, S. A. Funk, W. F. Bartelt, R. J. Schenck and A. J. Trippe, *J. Org. Chem.*, 2008, **73**, 4443–4451.
- 3 F. Issa, M. Kassiou and L. M. Rendina, *Chem. Rev.*, 2011, **111**, 5701–5722.
- 4 H. Sugimoto, S. Oda, T. Otsuki, T. Hino, T. Yoshida and Y. Shiro, *Proc. Natl. Acad. Sci. U. S. A.*, 2006, **103**, 2611–2616.
- 5 P. Puccetti and U. Grohmann, *Nat. Rev. Immunol.*, 2007, **7**, 817–823.

- 6 L. K. Jaspersen, C. Bucher, A. Panoskaltis-Mortari, P. A. Taylor, A. L. Mellor, D. H. Munn and B. R. Blazar, *Blood*, 2008, **111**, 3257–3265.
- 7 M. Friberg, R. Jennings, M. Alsarraj, S. Dessureault, A. Cantor, M. Extermann, A. L. Mellor, D. H. Munn and S. J. Antonia, *Int. J. Cancer*, 2002, **101**, 151–155.
- 8 D. H. Munn, M. D. Sharma, D. Hou, B. Baban, J. R. Lee, S. J. Antonia, J. L. Messina, P. Chandler, P. A. Koni and A. L. Mellor, *J. Clin. Invest.*, 2004, **114**, 280–290.
- 9 S. Löb, A. Königsrainer, H.-G. Rammensee, G. Opelz and P. Ternes, *Nat. Rev. Cancer*, 2009, **9**, 445–452.
- 10 U. F. Röhrig, S. R. Majjigapu, A. I. Grosdidier, S. Bron, V. Stroobant, L. Pilotte, D. Colau, P. Vogel, B. J. Van den Eynde and V. Zoete, *J. Med. Chem.*, 2012, **55**, 5270–5290.
- 11 J. R. Smith, K. J. Evans, A. Wright, R. D. Willows, J. F. Jamie and R. Griffith, *Bioorg. Med. Chem.*, 2012, **20**, 1354–1363.
- 12 A. Pereira, E. Vottero, M. Roberge, A. G. Mauk and R. J. Andersen, *J. Nat. Prod.*, 2006, **69**, 1496–1499.
- 13 H. C. Brastianos, E. Vottero, B. O. Patrick, R. Van Soest, T. Maitainaho, A. G. Mauk and R. J. Andersen, *J. Am. Chem. Soc.*, 2006, **128**, 16046–16047.
- 14 S. Kumar, W. P. Malachowski, J. B. DuHadaway, J. M. LaLonde, P. J. Carroll, D. Jaller, R. Metz, G. C. Prendergast and A. J. Muller, *J. Med. Chem.*, 2008, **51**, 1706–1718.
- 15 H. E. Flick, J. M. LaLonde, W. P. Malachowski and A. J. Muller, *Int. J. Tryptophan Res.*, 2013, **6**, 35–45.
- 16 R. Tiwari, K. Mahasenan, R. Pavlovicz, C. L. Li and W. Tjarks, *J. Chem. Inf. Model.*, 2009, **49**, 1581–1589.
- 17 J. G. Wilson, A. Anisuzzaman, F. Alam and A. Soloway, *Inorg. Chem.*, 1992, **31**, 1955–1958.
- 18 L. R. Reddy, M. A. Reddy, N. Bhanumathi and K. R. Rao, *New J. Chem.*, 2001, **25**, 221–222.
- 19 J. Yoo, J.-W. Hwang and Y. Do, *Inorg. Chem.*, 2001, **40**, 568–570.
- 20 C. J. Austin, J. Mizdrak, A. Matin, N. Sirijovski, P. Kosim-Satyaputra, R. D. Willows, T. H. Roberts, R. J. Truscott, G. Polekhina, M. W. Parker and J. F. Jamie, *Protein Expression Purif.*, 2004, **37**, 392–398.
- 21 C. J. Austin, P. Kosim-Satyaputra, J. R. Smith, R. D. Willows and J. F. Jamie, *Biochem. Biophys. Res. Commun.*, 2013, **436**, 595–600.
- 22 O. Takikawa, T. Kuroiwa, F. Yamazaki and R. Kido, *J. Biol. Chem.*, 1988, **263**, 2041–2048.
- 23 M. Sono, *J. Biol. Chem.*, 1989, **264**, 1616–1622.
- 24 X. Liu, N. Shin, H. K. Koblish, G. Yang, Q. Wang, K. Wang, L. Leffet, M. J. Hansbury, B. Thomas, M. Rupa, P. Waeltz, K. J. Bowman, P. Polam, R. B. Sparks, E. W. Yue, Y. Li, R. Wynn, J. S. Fridman, T. C. Burn, A. P. Combs, R. C. Newton and P. A. Scherle, *Blood*, 2010, **115**, 3520–3530.
- 25 W. L. Armarego and C. Chai, *Purification of laboratory chemicals*, Butterworth-Heinemann, 2012.
- 26 O. V. Dolomanov, L. J. Bourhis, R. J. Gildea, J. A. Howard and H. Puschmann, *J. Appl. Crystallogr.*, 2009, **42**, 339–341.
- 27 G. Sheldrick, University of Göttingen, Germany, 1997.
- 28 G. M. Sheldrick, *Acta Crystallogr., Sect. A: Fundam. Crystallogr.*, 2008, **64**, 112–122.



Mutation of cysteine residues alters the heme-binding pocket of indoleamine 2,3-dioxygenase-1



Christopher J.D. Austin^{a,b}, Priambudi Kosim-Satyaputra^{a,1}, Jason R. Smith^a, Robert D. Willows^a, Joanne F. Jamie^{a,*}

^a Department of Chemistry and Biomolecular Sciences, Macquarie University, Sydney, Australia

^b School of Chemistry, The University of Sydney, Sydney, Australia

ARTICLE INFO

Article history:

Received 24 May 2013

Available online 7 June 2013

Keywords:

Tryptophan metabolism

Kynurenine pathway

Indoleamine 2,3-dioxygenase

Site-directed mutagenesis

Cysteine residues

Altered substrate binding site

ABSTRACT

The hemoprotein indoleamine 2,3-dioxygenase-1 (IDO1) is the first and rate-limiting enzyme in mammalian tryptophan metabolism. Interest in IDO1 continues to grow, due to the ever expanding influence IDO1 plays in the immune response. This study examined the contribution of all individual cysteine residues towards the overall catalytic properties and stability of recombinant human IDO1 *via* mutagenesis studies using a range of biochemical and spectroscopic techniques, including *in vitro* kinetic assessment, secondary structure identification *via* circular dichroism spectroscopy and thermal stability assessment. Upon mutation of cysteine residues we observed changes in secondary structure (principally, shifting from α -helix/ β -sheet features to random coil structures) that produced out of plane heme torsion and puckering, changes to thermal stability (including gains in stability for one mutant protein) and differences in enzymatic activity (such as, increased ability to convert non-natural substrates, *e.g.* D-tryptophan) from wild type IDO1 enzyme.

© 2013 Elsevier Inc. All rights reserved.

1. Introduction

The haemoprotein indoleamine 2,3-dioxygenase-1 (IDO1; EC 1.13.11.52) is an immunoregulatory enzyme responsible for the oxidative cleavage of L-tryptophan to N-formylkynurenine as the first step of the Kynurenine Pathway; the major metabolic pathway for tryptophan breakdown (Fig. 1; Left). Increased expression of IDO1, principally by IFN- γ release due to inflammation resulting from infection and/or disease, elicits both innate and adaptive immune responses that can have both beneficial and detrimental consequences. For example, essential amino acid removal such as tryptophan depletion by increased expression of IDO1 is an ancient, efficient and innate method of slowing the growth of infectious agents that rely on endogenous tryptophan stores for continued metabolic activity [1]. Furthermore, the low tryptophan cellular environment changes adaptive immune mechanisms, altering modulatory signals to/from T-lymphocytes, resulting in both G1-cell cycle arrest and apoptosis. This in turn causes host immunosuppression and is a major mechanism of both tumour immune escape [2] and prevention of maternal foetal rejection [3,4].

In addition, IDO1 activity affects the production of down-stream metabolites of tryptophan (*e.g.* 3-hydroxykynurenine and quinolinic acid), which have been shown to play roles in inflammatory disease symptomology, particularly in the CNS [5,6]. Consequently, IDO1 has received significant research attention as a potential therapeutic target in disease states where the immune system is in a state of dysregulation, for example, ovarian cancer [7]. A greater understanding of how the structural components of human IDO1 interact (*vide infra*), and how alteration of these interactions govern both function and stability, may aid both future drug development and identification and characterisation of possible deleterious single nucleotide polymorphisms [8].

Cysteine residues in proteins are important sites for metal coordination, catalysis and structure stabilisation. Containing a reactive sulfhydryl (–SH) group, the cysteine moiety can act as a nucleophile and forms thiol radicals, making it possible to form both intra- and intermolecular covalent bonds. However, the ease of formation of such covalent bonds depends on the overall redox potential, the spatial environment and pH of the protein and surrounding environment. In IDO1, cysteines are well distributed, mostly in helices. Three cysteine residues are found in the small domain (which contains nine α -helices and two β -sheets) and five in the large domain (comprising 15 α -helices and the catalytic pocket – Fig. 1; Right). IDO1 cysteines do not form disulfide bridges or co-ordinate to the heme iron so their role in the maintenance of activity/structure remains largely unknown. We report here on the contribution of all the individual cysteine residues towards the

* Corresponding author. Address: Department of Chemistry and Biomolecular Sciences, Macquarie University, NSW 2109, Australia. Fax: +61 2 9850 8313.

E-mail address: joanne.jamie@mq.edu.au (J.F. Jamie).

¹ We are particularly grateful for Dr Kosim-Satyaputra's contribution to this research. Sadly, Priambudi passed away before this manuscript could be submitted for publication.

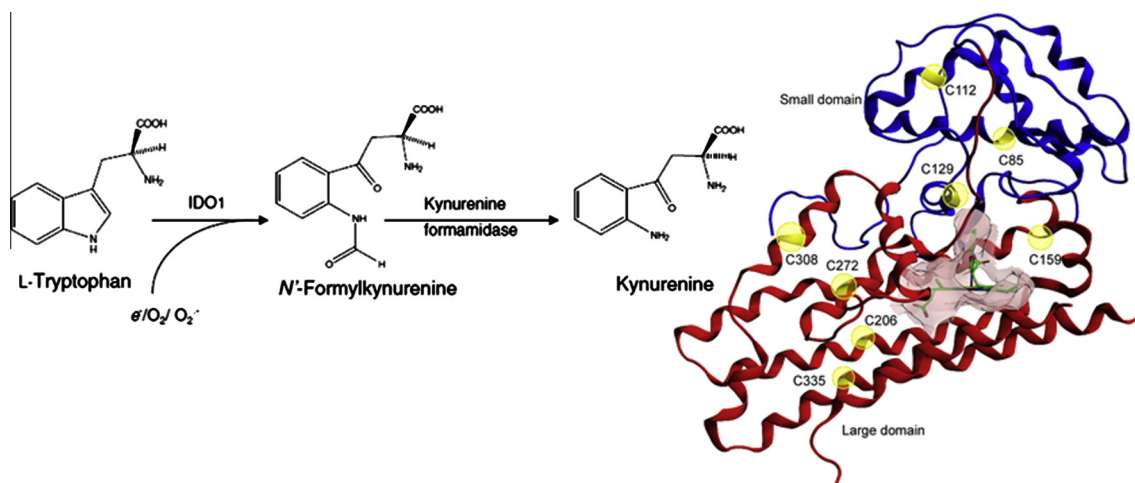


Fig. 1. (Left): initial steps of the Kynurenine pathway. The heme containing enzyme indoleamine 2,3-dioxygenase (IDO) is capable of catalysing this reaction. The cleavage product, *N*-formylkynurenine, is then hydrolysed by kynurenine formamidase, or spontaneously, to form kynurenine. (Right) Crystal structure of human IDO-1 showing positions of all 8 cysteine residues and the active site (PDB: 2D0T, [16]). Active site – pink; heme and co-crystallised phenylimidazole – green. The large and small domains are coloured red and blue, respectively. (For interpretation of the references to colour in this figure legend, the reader is referred to the web version of this article.)

overall catalytic properties, secondary structure, heme environment and stability of human IDO1.

2. Materials and methods

2.1. Materials

All chemicals were of analytical grade unless otherwise specified. A Hi-Trap chelating column and Microspin Sephadex G-25 columns were obtained from Amersham Biosciences. Sephadex G25 (NAP 10) columns were purchased from Pharmacia Biotech. Amicon Ultra 4 mL centrifugal devices were obtained from Millipore. A Superdex 75 PC 3.2/30 column was purchased from Pharmacia LKB Biotechnology. δ -Aminolevulinic acid (ALA), ampicillin, ascorbic acid, catalase (bovine), imidazole, isopropyl- β -D-thiogalactopyranoside (IPTG), L-kynurenine, kanamycin, lysozyme, *p*-dimethylaminobenzaldehyde (*p*-DMAB), phenylmethylsulfonylfluoride (PMSF) and L-tryptophan were obtained from Sigma–Aldrich. Bovine serum albumin (BSA) (Fraction V) was obtained from Amersham. Coomassie blue R250 was purchased from Bio-Rad. DNase and EDTA-free cocktail inhibitor tablets were products of Roche.

2.2. Site-directed mutagenesis of the IDO1 expression plasmid pQE9-IDO1

Plasmid DNA was isolated using a GenElute Plasmid Miniprep Kit (Sigma), according to the manufacturer's instructions. Site-directed mutagenesis of pQE9-IDO1 was undertaken using the QuikChange® site-directed mutagenesis kit (Stratagene) per the manufacturer's instructions. All primers were synthesised by Sigma–Genosys (Castle Hill, Australia). Primers used for site-directed mutagenesis and sequencing are outlined in [Supplementary Data](#). Dye terminator DNA sequence analysis was performed using an ABI-PRISM 377 DNA sequencer (Applied Biosystems) to confirm mutations.

2.3. Bacterial Strain

The *Escherichia coli* strain (EC538, pREP4) used for expression studies has been previously used for the recombinant expression of human IDO1 [9]. Briefly, a single colony of *E. coli* (EC538) cells containing plasmids pQE9-IDO and pREP4 was inoculated in 100 mL LB medium and cultured overnight. The 100 mL culture was added to 900 mL of the same medium and incubated at

30 °C to an optical density of 0.6 at 600 nm. IPTG (100 mM), ALA (500 mM), and PMSF (1 M) were then added at final concentrations of 0.1, 0.5, and 1 mM, respectively. Each culture was incubated for a further 3 h. Cells were collected as a pellet by centrifugation at 5000g for 20 min at 4 °C. The pellet was suspended in 20 mL ice-cold (Dulbecco's) phosphate-buffered saline (PBS) containing 1 mM PMSF and centrifuged at 3000g for 15 min at 4 °C. The bacterial pellet was stored at –20 °C.

2.4. Purification of wild type IDO1 and mutant IDO1 proteins

One litre pellets of bacterial culture, obtained according to the method described above, was suspended in 25 mM tris(hydroxymethyl)methylamine (Tris) buffer at pH 7.4, containing 150 mM NaCl, 10 mM imidazole, 10 mM MgCl₂ and 1 mM PMSF. The suspension was then centrifuged at 5000g for 20 min at 4 °C and the supernatant discarded to remove any residual PBS storage buffer.

The newly washed pellets were resuspended in 20 mL of ice-cold buffer as outlined above, with the addition of EDTA free-cocktail inhibitor tablets ($\times 2$) and DNase (<1 mg). The suspension was French pressed three times at 10,000 p.s.i. and centrifuged at 5000g for 20 min to obtain a clear supernatant and pellet. The clear supernatant (20 mL) was then applied to a 1 mL Hi-Trap chelating column charged with nickel ions; equilibrated with the basal buffer [Tris 25 mM pH 7.4; 150 mM NaCl; 1 mM PMSF] containing 10 mM imidazole. After washing with 18 mL of this buffer, IDO1 (wild type or mutant) protein was eluted on a stepwise gradient incorporating washings at imidazole concentrations of 30, 40, 50, 65, 80 mM, and elution at 190 mM.

The protein collected at the elution step was then buffer-exchanged into 50 mM Tris pH 7.4 using a Sephadex G25 (NAP 10) column. The desalted fractions were pooled and concentrated to a volume of 50 μ L using an Amicon Ultra 4 mL centrifugal device with a 30,000 Da molecular weight cut-off. The concentrated fraction was then applied to a Superdex 75 PC 3.2/30 column according to the manufacturer's instructions, after equilibration with 50 mM Tris pH 7.4. Fractions were collected in 75 μ L aliquots at a flow rate of 60 μ L/min over 3.5 mL. The fractions with the highest 406:280 nm absorbance were pooled for analysis.

2.5. Analysis of wild type IDO1 and mutant IDO1 proteins

Protein concentration was determined with Bio-Rad dye reagent using BSA (0–1 mg/mL) as the standard. The coloured prod-

uct was measured at 595 nm using a Shimadzu UV–Vis spectrophotometer. Proteins were visualised using SDS–PAGE analysis by the method of Laemmli [10]. Ultraviolet (UV) and visible (Vis) spectra of proteins were recorded with a Shimadzu UV–Vis spectrophotometer, with 1 cm pathlength quartz cuvettes. Circular dichroism (CD) spectra were recorded on a JASCO J-810 spectropolarimeter with 1 cm and 1 mm pathlength quartz cuvettes. Sensitivity was 100 millidegrees, and the scanning speed was 50 nm/min for an accumulation of 32 scans. Further analysis of CD data was undertaken using the CDpro and K2D programs according to established protocols [11,12]. Thermal transition curves were measured by monitoring $\lambda = 222$ nm as a function of the increasing temperature over the range 20–99 °C at 1 °C/min. T_m values were determined by finding the first derivative of the thermal transition curve using peak processing software packaged with the JASCO J-810 spectropolarimeter.

2.6. Kinetic studies

IDO1 activity was determined as described by Takikawa et al. [13] with minor modifications. In brief, the standard reaction mixture (200 μ L) contained 50 mM potassium phosphate buffer (pH 6.5), 20 mM ascorbic acid (neutralised with NaOH), 200 μ g/mL catalase, 10 μ M methylene blue, 400 μ M L-tryptophan, and IDO1 (either wild type or mutant protein). The reaction was carried out at 37 °C for 60 min and stopped by the addition of 40 μ L of 30% (w/v) trichloroacetic acid. After heating at 65 °C for 15 min, the reaction mixtures were centrifuged at 11,500g for 7 min. The supernatant (125 μ L) was transferred into a well of a 96-well microtitre plate and mixed with 125 μ L of 2% (w/v) p-DMAB in acetic acid. The yellow pigment derived from kynurenine was measured at 480 nm using a Fluorostar microtitre plate reader (BMG Lab Technologies). A standard curve of L-kynurenine was used to determine product formation, ranging in concentration from 0–500 μ M.

Using this assay, the kinetic activity of wild type IDO1 and the IDO1 mutants was determined against two substrates, i.e. L-tryptophan and D-tryptophan. As IDO1 enzyme samples were a mixture of active holoenzyme (heme-containing IDO1) and inactive apoenzyme (heme-free IDO1), the kinetic parameters were determined as a function of concentration of holoenzyme [14]. The concentration of holoenzyme for each sample was resolved using the extinc-

tion coefficient at 406 nm for rabbit intestinal IDO1 of $\epsilon = 140 \text{ mM}^{-1} \text{ cm}^{-1}$ [15]. The amount of wild type and mutant protein was adjusted to give an initial velocity for each substrate where the percentage of conversion of substrate at each concentration was less than 10%. Apparent Michaelis–Menten constants (K_m , V_{max}) were determined by varying concentrations of L-tryptophan and D-tryptophan with concentration ranges of 0–200 μ M and 0–3000 μ M, respectively. Each reaction was conducted in triplicate.

3. Results and discussion

3.1. Structural analysis of wild type and mutant IDO1 species

Following the purification of the wild type and mutant IDO1 proteins, the products obtained were subjected to SDS–PAGE analysis. For each isolated protein, one homologous band was observed with a molecular mass of ~ 45 kDa (data not shown).

Far UV CD spectra were obtained and analysed using Cdpro and K2D3 deconvolution programs to determine whether Cysteine (C) to Alanine (A) mutations changed the secondary structure of IDO1 when compared to wild type (Fig. 2A). The analyses showed that wild type IDO1 protein exhibited a configuration consisting of 63% α -helical, 4% β -sheet and 33% random coil (Table 1); consistent with the known secondary structure of human IDO1 elucidated from Sugimoto et al.'s crystal structure [16]. The mutant IDO1 proteins differed in structural composition when compared to wild type enzyme (Table 1– 38–71% α -helical, 3–17% β -sheet and 26–44% random coil), however all proteins (with the exception of C335A-IDO) maintained similar proportions of α -helical, β -sheet and random coil structure (i.e. % α -helix > % random coil > % β -sheet). In the case of protein C335A-IDO, the percentage of random coil was higher than both α -helix and β -sheet. Interestingly, the residue C335 is in close proximity to the cofactor entrance flexible loop (residues 360–380 – unresolved by X-ray crystallography) of IDO1. The mutation of C335A appears to alter a segment of the large domain (Fig. 1 – Red) resulting in the increased proportion of random coil observed for this enzyme.

Generally, far UV CD spectroscopy indicated that site-directed mutagenesis of individual cysteine residues had only subtle effects on overall protein secondary structure. Spectra were obtained at high protein concentrations, which allowed greater sensitivity of

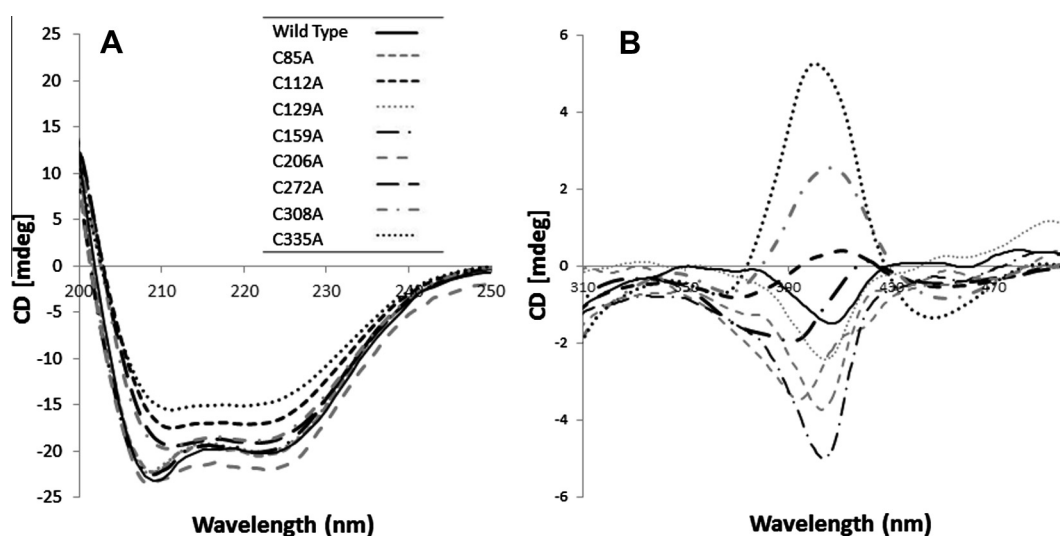


Fig. 2. (A) Circular dichroism spectra of mutant and wild type IDO1 proteins. CD spectra were conducted in 10 mM Tris (pH 7.4) buffer with a 10 mm pathlength cuvette. Protein concentration: 1 mg/mL. The region 200–250 nm is shown. (B) Circular dichroism spectra of mutant and wild type IDO1 proteins. CD spectra were conducted in a 1 mm pathlength cuvette. Protein concentration: 5–10 mg/mL. The region 310–500 nm is shown.

Table 1
Secondary structure analyses of wild type IDO1 and cysteine to alanine IDO1 mutants.

IDO1	α -Helix (%)	β -Sheet (%)	Random coil (%)
Wild Type	62.92	4.24	32.84
C85A	70.48	3.49	26.03
C112A	43.66	14.49	41.85
C129A	70.54	3.43	26.03
C159A	70.68	3.42	25.9
C206A	65.65	3.43	30.92
C272A	49.45	10.93	39.62
C308A	49.72	10.6	39.68
C335A	38.64	17.27	44.09

both the aromatic amino acid side chain and heme environments, respectively. All proteins were oxidised, showing UV–Vis absorbance maxima at 406 nm (Supplementary Data). Overlay of the 310–500 nm CD spectral data reveals measurable changes to mutant IDO1 spectra when compared to wild type, indicating structural changes to the environment of the heme B cofactor (Fig. 2B). For example, C85A-IDO1 shows two distinct peaks at 395 nm and 420 nm – this Soret peak splitting is possibly due to lowered effective symmetry of the heme B group resulting in a lift to the degeneracy of the π^* molecular orbital associated with the Soret transition [17]. Although the present results do not allow us to specify how amino acid substitution affects the heme B moiety (e.g. torsion, doming or out of plane twisting due to indirect structural changes), when viewed in conjunction with substrate kinetic data (see Biochemical Analysis below), the near UV/Soret spectral changes reveal that only subtle changes are required to alter the normal orientation of critical residues and the heme group within the active site.

The thermal transitions of wild type and mutant IDO1 proteins were monitored by measuring molar ellipticity at $\lambda = 222$ nm (α -helix region) as a function of the increasing temperature over the range 20–99 °C (Fig. 3). T_m values for wild type and mutant proteins were determined from the first derivative of the melting curves (Fig. 3 inset). No protein sample refolded upon cooling. A

small global increase in stability was observed in C206A-IDO1 over wild type IDO1, however for all other mutant proteins loss of thermal stability was observed. C206 is located in the large (Fig. 1 – red) IDO1 protein domain and alanine substitution has increased the percentage of α -helix structure within the mutant protein when compared to wild type IDO1 (Table 1). The small increase to highly ordered α -helix may explain the slower rate of denaturation observed in C206A-IDO1.

3.2. Biochemical analysis of wild type and mutant IDO1 species

The enzymatic activity of wild type IDO1 and each mutant-IDO1 protein was analysed using L-tryptophan and D-tryptophan as substrates. The kinetic parameters of wild type and mutant IDO1 for L-tryptophan and D-tryptophan are given in Table 2. For L-tryptophan, all mutants showed a decrease in enzymatic efficiency when compared to the wild type IDO1, with C85A-IDO1 and C206A-IDO1 showing the largest V_{max}/K_m reductions of 86% and 85%, respectively. Interestingly, both these proteins displayed measurable differences in their spectroscopic characteristics (i.e. Soret peak splitting and thermal stability changes, respectively) when compared to wild type IDO1, thus providing supporting data to conclude that cysteine mutation has altered both protein structure and function, particularly in relation to the cofactor binding site. Residue C206, for example, is located on the same α -helix as 'gating' residues F226, F227 and R231, which are critical to IDO1 substrate recognition (Fig. 4A). The loss of L-tryptophan enzymatic activity observed for C206A-IDO1 may be due to an alteration of the hydrophobic interactions and stabilisation bonds provided by F226, F227 and R231 to the heme-binding pocket of wild type IDO1 [16], resulting from mutation of C206 to Alanine. Residue C85 (Fig. 1 – small domain, blue) is located at the cleft joining the large and small domains of IDO1. Due to its spatial position (Fig. 4B), C85 is unlikely to interact directly with substrate, however, the substitution of the bulky aromatic cysteine residue with the simple, smaller alanine residue may change contact/binding between domains by altering hydrophobic interactions, salt

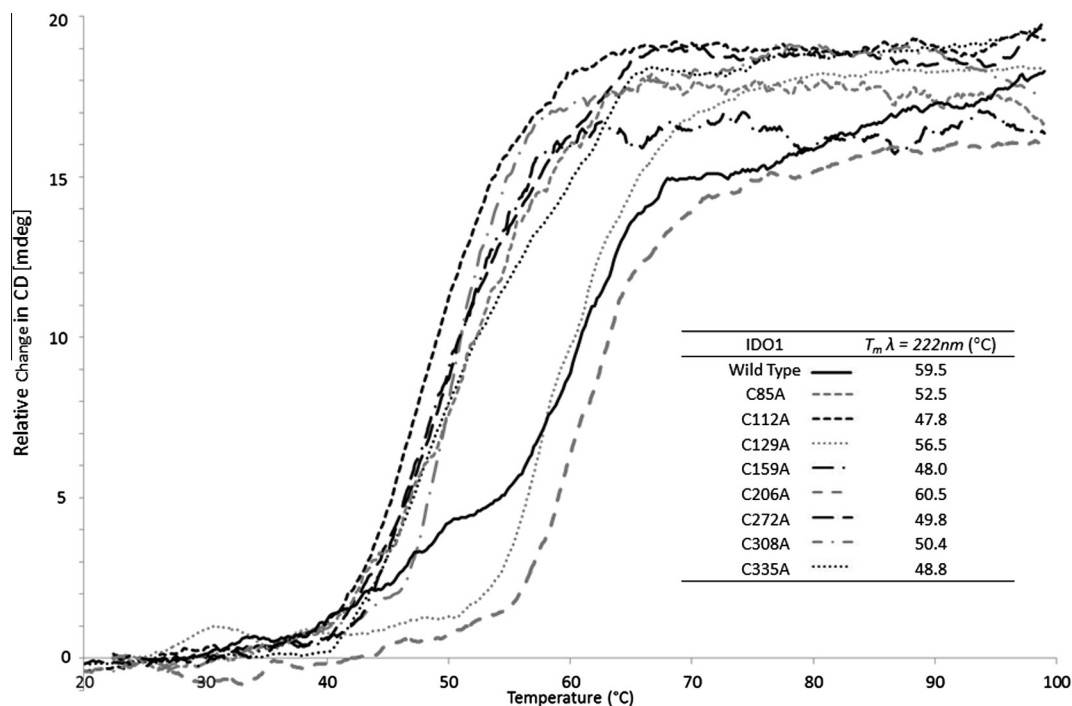


Fig. 3. Thermal transition of mutant and wild type IDO1 proteins at $\lambda = 222$ nm over the range 20–99 °C.

Table 2

Kinetic parameters of wild type and mutant IDO1 for L-tryptophan and D-tryptophan.

IDO1	L-tryptophan			D-tryptophan		
	V_{\max} $\mu\text{M}^{-1}\text{min}^{-1}$	K_m μM	V_{\max}/K_m $\mu\text{M}^{-1}\text{min}^{-1}$	V_{\max} min^{-1}	K_m mM	V_{\max}/K_m $\text{mM}^{-1}\text{min}^{-1}$
Wild type	120	20	6	160	5	32
C85A	30.6 ± 2.0	35.9	0.852	85.3 ± 3.8	2.1	41
C112A	59.8 ± 1.5	18.7 ± 2.0	3.2	109.4 ± 0.6	1.3 ± 0.0	85
C129A	101.1 ± 15.0	42.3	2.39	31.4 ± 1.3	3.7	8.5
C159A	110.4 ± 2.5	75.9	1.45	40.3 ± 3.5	4.4	9.2
C206A	45.5 ± 2.6	50.9	0.894	64.7 ± 3.4	1.7	38
C272A	51.2 ± 0.4	38.1 ± 0.9	1.3	101.0 ± 1.3	3.7 ± 0.2	28
C308A	94.3 ± 2.4	90.3 ± 5.3	1.0	117.5 ± 1.7	3.3 ± 0.2	35
C335A	56.8 ± 0.6	17.1 ± 0.8	3.3	96.1 ± 4.2	9.5 ± 0.9	10.1

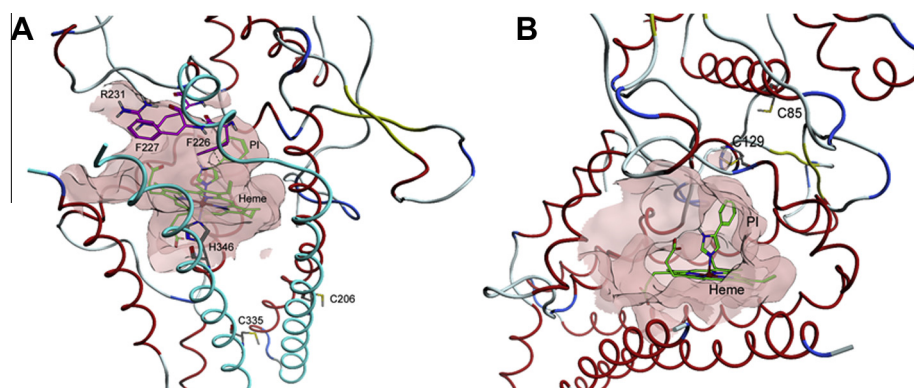


Fig. 4. (A) Crystal structure of wild type IDO-1 showing C206 and C335 relative to the active site (PDB: 2D0T). Carbon atoms of co-crystallised phenylimidazole (PI) and heme are coloured green. Carbon atoms of gating residues F226, F227 and R231 are coloured fuchsia. C206 is directly connected to the gating residues via a rigid alpha helix (colour cyan for contrast). C335 is directly connected to the heme-binding residue H346 (grey carbons, helix also in cyan). With both helices running parallel, structural changes are potentially transmitted to the heme and/or the gating residues via these rigid structures. (B) Crystal structure of wild type rhIDO-1 showing the proximity between C85 and C129 (5.7 angstroms) and the heme active site (PDB: 2D0T, [16]). C129 makes up the roof of the indole binding pocket (occupied here by the phenyl ring of co-crystallised phenylimidazole, PI). (For interpretation of the references to colour in this figure legend, the reader is referred to the web version of this article.)

bridges, or hydrogen bonding resulting in the observed loss of metabolic activity. Any changes to the active site of C85A-IDO1 is likely mediated through C129 (Fig. 4B), which is positioned in-between the heme group and C85, and forms part of the roof of the IDO1 active site.

A large drop (69%) in D-tryptophan metabolism was observed in C335A-IDO1 (Table 2; Fig. 4A). Given the substantial alteration in secondary structure observed for the mutant enzyme C335A-IDO1 (increased proportion of random coil – see *Structural Analysis*), its location on the same long α -helix chain as the proximal co-ordination binding residue (Histidine 346) and proximity to the flexible loop of IDO1 located at the entrance to the cofactor active site, a significant change in substrate efficiency is not unexpected. Interestingly, proteins C85A-IDO1, C112A-IDO1 and C206A-IDO1 showed an increased ability to convert D-tryptophan when measured against the efficiency of the wild-type, with C112A-IDO1 showing the highest increase (265%). This would indicate that while amino acid modification has affected the ability of L-tryptophan to interact with the heme b co-factor, protein structure modification has altered D-tryptophan substrate accessibility. From these results, it is clear that cysteine residues play a role in maintaining the strict geometric complementarity that is required for the formation of the substrate/co-factor complex and the normal enzymatic function of wild type IDO1.

This study is the first to investigate the role cysteine residues play in the metabolic stability of IDO1. While not involved directly in heme b binding or disulphide bond formation, cysteine residues within IDO1 play an important role in the maintenance and stability of normal structure and kinetic behaviour.

Appendix A. Supplementary data

Supplementary data associated with this article can be found, in the online version, at <http://dx.doi.org/10.1016/j.bbrc.2013.05.119>.

References

- [1] H.J. Yuasa, H.J. Ball, Y.F. Ho, C.J. Austin, C.M. Whittington, K. Belov, G.J. Maghzal, L.S. Jermini, N.H. Hunt, Characterization and evolution of vertebrate indoleamine 2, 3-dioxygenases IDOs from monotremes and marsupials, *Comp. Biochem. Physiol. B Biochem. Mol. Biol.* 153 (2009) 137–144.
- [2] M. Friberg, R. Jennings, M. Alsarraj, S. Dessureault, A. Cantor, M. Extermann, A.L. Mellor, D.H. Munn, S.J. Antonia, Indoleamine 2,3-dioxygenase contributes to tumor cell evasion of T cell-mediated rejection, *Int. J. Cancer* 101 (2002) 151–155.
- [3] E.A. Bonney, P. Matzinger, Much IDO about pregnancy, *Nat. Med.* 4 (1998) 1128–1129.
- [4] D.H. Munn, M. Zhou, J.T. Attwood, I. Bondarev, S.J. Conway, B. Marshall, C. Brown, A.L. Mellor, Prevention of allogeneic fetal rejection by tryptophan catabolism, *Science* 281 (1998) 1191–1193.
- [5] G.J. Guillemin, G. Smythe, O. Takikawa, B.J. Brew, Expression of indoleamine 2,3-dioxygenase and production of quinolinic acid by human microglia, astrocytes, and neurons, *Glia* 49 (2005) 15–23.
- [6] N.H. Hunt, J. Golenser, T. Chan-Ling, S. Parekh, C. Rae, S. Potter, I.M. Medana, J. Miu, H.J. Ball, Immunopathogenesis of cerebral malaria, *Int. J. Parasitol.* 36 (2006) 569–582.
- [7] A. Okamoto, T. Nikaido, K. Ochiai, S. Takakura, M. Saito, Y. Aoki, N. Ishii, N. Yanaiharu, K. Yamada, O. Takikawa, R. Kawaguchi, S. Isonishi, T. Tanaka, M. Urashima, Indoleamine 2,3-dioxygenase serves as a marker of poor prognosis in gene expression profiles of serous ovarian cancer cells, *Clin. Cancer Res.* 11 (2005) 6030–6039.
- [8] M. Arefayene, S. Philips, D. Cao, S. Mamidipalli, Z. Desta, D.A. Flockhart, D.S. Wilkes, T.C. Skaar, Identification of genetic variants in the human indoleamine 2, 3-dioxygenase (IDO1) gene, which have altered enzyme activity, *Pharmacogenet. Genom.* 19 (2009) 464–476.

- [9] C.J. Austin, J. Mizdrak, A. Matin, N. Sirijovski, P. Kosim-Satyaputra, R.D. Willows, T.H. Roberts, R.J. Truscott, G. Polekhina, M.W. Parker, J.F. Jamie, Optimised expression and purification of recombinant human indoleamine 2,3-dioxygenase, *Protein Exp. Purif.* 37 (2004) 392–398.
- [10] U.K. Laemmli, Cleavage of structural proteins during the assembly of the head of bacteriophage T4, *Nature* 227 (1970) 680–685.
- [11] C.J. Austin, F. Astelbauer, P. Kosim-Satyaputra, H.J. Ball, R.D. Willows, J.F. Jamie, N.H. Hunt, Mouse and human indoleamine 2,3-dioxygenase display some distinct biochemical and structural properties, *Amino Acids* 36 (2009) 99–106.
- [12] C.J. Austin, B.M. Mailu, G.J. Maghzal, A. Sanchez-Perez, S. Rahlfs, K. Zocher, H.J. Yuasa, J.W. Arthur, K. Becker, R. Stocker, N.H. Hunt, H.J. Ball, Biochemical characteristics and inhibitor selectivity of mouse indoleamine 2,3-dioxygenase-2, *Amino Acids* 39 (2010) 565–578.
- [13] O. Takikawa, T. Kuroiwa, F. Yamazaki, R. Kido, Mechanism of Interferon- γ action; Characterisation of indoleamine 2,3-dioxygenase in cultured human cells induced by interferon- γ and evaluations of the enzyme-mediated tryptophan degradation in its anticellular activity, *J. Biol. Chem.* 263 (1988) 2041–2048.
- [14] T.K. Littlejohn, O. Takikawa, R.J. Truscott, M.J. Walker, Asp274 and his346 are essential for heme binding and catalytic function of human indoleamine 2,3-dioxygenase, *J. Biol. Chem.* 278 (2003) 29525–29531.
- [15] T. Shimizu, S. Nomiya, F. Hirata, O. Hayaishi, Indoleamine 2,3-dioxygenase, purification and some properties, *J. Biol. Chem.* 253 (1978) 4700–4706.
- [16] H. Sugimoto, S. Oda, T. Otsuki, T. Hino, T. Yoshida, Y. Shiro, Crystal structure of human indoleamine 2,3-dioxygenase: catalytic mechanism of O₂ incorporation by a heme-containing dioxygenase, *Proc. Natl. Acad. Sci. USA* 103 (2006) 2611–2616.
- [17] J.S. Felsch, M.P. Horvath, S. Gursky, M.R. Hobaugh, P.N. Goudreau, J.A. Fee, W.T. Morgan, S.J. Admiraal, M. Ikeda-Saito, T. Fujiwara, et al., Probing protein-cofactor interactions in the terminal oxidases by second derivative spectroscopy: study of bacterial enzymes with cofactor substitutions and heme a model compounds, *Protein Sci.* 3 (1994) 2097–2103.

Pages 234-243 of this thesis have been removed as they contain published material under copyright. Removed contents published as:

Bridewell David J. A., Sperry Jonathan, Smith Jason R., Kosim-Satyaputra Priambudi, Ching Lai-Ming, Jamie Joanne F., Brimble Margaret A. (2012) Natural Product-Inspired Pyranonaphthoquinone Inhibitors of Indoleamine 2,3-Dioxygenase-1 (IDO-1)*. *Australian Journal of Chemistry*, vol. 66, 40-49.

<https://doi.org/10.1071/CH12393>



3rd February 2014

Dear Associate Professor Jamie,

Re: "Expression, kinetics and structural studies of recombinant Indoleamine-2,3-dioxygenase (IDO), NADPH:cytochrome-P450 reductase (CPR) and cytochrome b5 (CYB5) and their mutants" (Ref: 5201300881)

Thank you for your Biosafety application. Your application has been reviewed by the Institutional Biosafety Committee (IBC) and approval of the above Exempt Dealing has been granted, effective 3rd February 2014.

Approval has been granted subject to your compliance with the Office of the Gene Technology Regulator's standard conditions for exempt work listed below:

1. The project must be conducted in accordance with the OGTR Guidance Notes for the Containment of Exempt Dealings
(http://www.ogtr.gov.au/internet/ogtr/publishing.nsf/Content/ExemptDealGuideSept11_2-htm)
2. The Guidance Notes are only applicable to exempt dealings conducted under the *Gene Technology Act 2000*. They do not provide guidance for laboratory safety, good laboratory practice or work health and safety issues
For these purposes, refer to AS/NZS 2243.3:2010.
3. You must inform the Institutional Biosafety Committee if you complete or abandon the exempt dealings with GMOs.

Please note the following standard requirements of approval:

1. Approval will be for a period of 5 years *subject to the provision of annual reports*. If, at the end of this period the project has been completed, abandoned, discontinued or not commenced for any reason, you are required to submit a Final Report. If you

complete the work earlier than you had planned you must submit a Final Report as soon as the work is completed. Please contact the Committee Secretary at biosafety@mq.edu.au in order to obtain a report.

A Progress/Final Report for this project will be due on: 1st February 2015

2. If you will be applying for or have applied for internal or external funding for the above project it is your responsibility to provide the Macquarie University's Research Grants Management Assistant with a copy of this email as soon as possible. Internal and External funding agencies will not be informed that you have final approval for your project and funds will not be released until the Research Grants Management Assistant has received a copy of this email.

If you need to provide a hard copy letter of Final Approval to an external organisation as evidence that you have Final Approval, please do not hesitate to contact the Committee Secretary at biosafety@mq.edu.au or by phone 9850 4063.

Please retain a copy of this email as this is your formal notification of final Biosafety approval.

Yours Sincerely

A/Prof Subramanyam Vemulpad

Chair, Macquarie University Institutional Biosafety Committee

Biosafety Secretariat

Research Office

Level 3, Research Hub, Building C5C East

Macquarie University

NSW 2109 Australia

T: +61 2 9850 6848

F: +61 2 9850 4465

<http://www.mq.edu.au/research>



CRICOS Provider Number 00002J

Please consider the environment before printing this email.

This email (including all attachments) is confidential. It may be subject to legal professional privilege and/or protected by copyright. If you receive it in error do not use it or disclose it, notify the sender immediately, delete it from your system and destroy any copies. The University does not guarantee that any email or attachment is secure or free from viruses or other defects. The University is not responsible for emails that are personal or unrelated to the University's functions.